Towards Photosynthetic Hydrogen Production

Thesis submitted to the University of Nottingham for the degree of Doctor of Philosophy

Sean Ross Craig, B.Sc.(Hons)

31/03/2021

Dedication

This work is dedicated to my grandmother, Fiona Craig. You have always been there as a source of inspiration in my life, supporting me through every step I have taken. You have led a life full of love, I can only hope that I have done you proud.

Declaration

The work presented in this thesis was carried out by me unless stated otherwise. No section of this document has been previously submitted for another degree at the University of Nottingham or any other institute of learning.

Sean R. Craig, 31/03/21

Abstract

The need to develop a sustainable energy is crucial and one of the foremost global challenges facing humanity, driven by a continuing global population expansion and anthropogenic climate change. Hydrogen (H_2) is a clean burning fuel which, however production relies on fossil fuels that is both unsustainable and environmentally unfriendly. The current global market is currently estimated at $115.25 Billion and expected to rise to $154.74 Billion by 2022.

Microbes such as cyanobacteria offer a sustainable method of H_2 production platform with minimal environmental impact, making them an extremely attractive proposition. Cyanobacteria can possess two functionally distinct [NiFe] hydrogenases: an uptake enzyme, only capable of hydrogen oxidation and bidirectional enzyme capable of reducing protons to evolve hydrogen. *Synechocystis* sp. PCC 6803 (PCC 6803) and *Synechococcus* sp. PCC 7002 (PCC 7002) encode one bidirectional [NiFe] which is a heteropentameric enzyme composed of a hydrogenase module (HoxH & HoxY), forming the catalytic core and the diaphorase module (HoxE, HoxF & HoxU).

Previously it has been demonstrated that the hydrogenase (Hox) of PCC 6803 is thylakoid associated forming two distinct Hox populations, one dispersed throughout the thylakoid and the other forming distinct puncta which correlate with H_2 evolution (Burroughs *et al*., 2014). An understanding of the interaction partner of each population is key in engineering strains for photobiological hydrogen production. We show that a proportion of the Hox population interacts with the type 1 NAD(P)H dehydrogenase (NDH-1) of the electron transport chain under conditions that support hydrogen evolution suggesting a role of the hydrogenase in modulating redox balance in the plastoquinol pool.

In order to assess the Hox interaction partner at the thylakoid in *Synechocystis* sp. PCC 6803, HoxE and HoxY subunits were tagged with GFP in order to carryout pull downs and assess distribution of Hox. The *hoxYGFP* and *hoxEGFP* strains showed a cytoplasm localisation under photoautotrophic conditions and would localise to the thylakoid under anoxic dark adapted conditions. Pull downs of the *hoxEGFP* strain showed proteins co-eluting with HoxEGFP with similar and unique bands being observed between photoautotrophic growth and anoxic dark adapted conditions.

Hox in *Synechococcus* sp. PCC 7002 is also thylakoid localised, forming similar populations as described in *Synechocystis* sp. PCC 6803. We demonstrate that the hydrogenase puncta of *Synechococcus* sp. PCC 7002 directly interact with the NDH-1 complex which increase upon the addition of glycerol.

The metabolome of *Synechocystis* sp. PCC 6803 strains were compared in a variety of NDH-1 and Hox mutants in order to assess pathways that are implicated in H_2 metabolism. Glutamic acid and lactic acid were shown to be key metabolites that were effect in each mutant relative to wild type, especially under anoxic dark adaptation.

Acknowledgements

I would like to firstly thank my supervisors; Dr Samantha Bryan, Dr Jens Appel and Prof. Nigel Minton for supervision and guidance throughout my PhD. Since arriving in the team I initially found it difficult adapting to the pressures of research and I want to especially thank Sam for all the support that she has given me through the years not only as a supervisor but also as a friend. She has given me the belief by showing confidence in my abilities and without Sams support, I am not sure I would have been able to cross the finishing line. I would also like to extend my gratitude to Jens Appel who hosted me in Germany when taking H_2 measurements. The kindness and hospitality shown by the group is much appreciated.

I am also grateful for all the training that I have received at the University of Nottingham and want to thank the team in SLIM (Especially Robert Markus) for microscopy training and training on image manipulation. I also want to thank Prof. Nigel Burroughs for all the additional help and support for image analysis. I also want to thank everyone in the CAB group (especially Laudina, Salah and Hyun) for LC-MS training and having people to talk to about extraction techniques. I want to single out Laudina to thank her for loading my final samples and analysis of metabolites as COVID-19 restrictions limited my access to the LC-MS instruments.

To the BBSRC DTP for funding this work.

I want to thank all my colleagues for making long shifts in the lab an experience I will take with me forever.

My partner Lizzie McClare has been a rock throughout my PhD and her love has seen me through the hard times of research life.

And finally I would like to thank my parents, grandparents, great grandparents and my step father Wully for all the encouragement throughout the academic journey I have taken.

SHOES! PHIL!

Table of Contents

List of figures

List of tables

Abbreviation

ATP	Adenosine triphosphate
CCM	Carbon concentrating mechanism
CO_2	Carbon Dioxide
CEF	Cyclic electron flow
dNTPs	deoxynucleotide triphosphates
ETC	Electron transport chain
Fd	Ferredoxin
H_2	Hydrogen
NAD-1	Type-1 NAD(P)H dehydrogenase
NADH-1L	NDH-1 isoform responsible for respiration/CEF
NDH-1MS	NDH-1 isoform responsible for CCM
NAD^+	Oxidized nicotinamide adenine dinucleotide
NADH	Reduced nicotinamide adenine dinucleotide
$NAD(P)^+$	Oxidized nicotinamide adenine dinucleotide phosphate
NAD(P)H	Reduced nicotinamide adenine dinucleotide phosphate
O_2	Oxygen
PC	Plastocyanin
PCR	Polymerase chain reaction
PEM	Proton exchange membrane
PQ	Plastoquinone

1 Introduction

1.1 Hydrogen as an Energy Source

The need to develop sustainable, renewable energy is crucial and one of the foremost global challenges facing humanity, driven by population expansion and anthropogenic climate change.

Hydrogen (H_2) is the most abundant element on earth and holds a lot of promise to replace fossil fuels due to the higher energy content and the ability to renewably generate H_2 (Bakenne et al., 2016). H_2 is a clean burning fuel which offers a sustainable alternative to existing liquid fossil reserves representing a growing global market currently worth $115.25 Billion, expected to rise to $154.74 Billion by 2022 (Nagarajan et al., 2017). By replacing current fossil fuel infrastructures with H_2, the transport and energy sectors can be completely decarbonized alleviating the demand for energy from a finite resource and alleviate the adverse effects of climate change caused by excessive carbon dioxide (CO_2) emissions.

1.1.1 The H_2 Fuel Cell

H_2 fuel cells are devices that can generate electrical power by converting H_2 into electricity. An example of the application of a hydrogen fuel cell being used to supply electricity for a building is the SP Group's training centre, being the first 100% zero emission building in South East Asia. In the SP building, renewable energy is used for electrolysis of water and hydrogen is stored and utilized by fuel cells. An overview of the basic schematic of a hydrogen fuel cell is displayed in Figure 1-1.

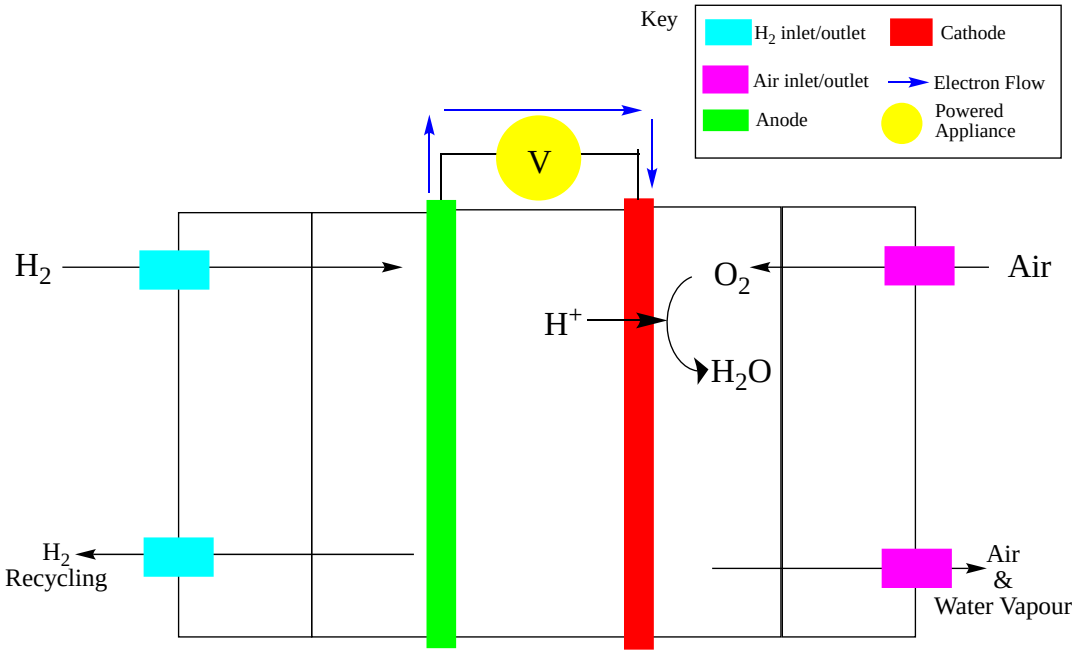

Figure 1-1: Overview of H_2 Fuel Cell.
H_2 enters the fuel cell (black arrows representing gas flow) and is oxidized at the anode. Electrons move towards the powered appliance and protons pass through a proton exchange membrane (PEM) towards the cathode. The protons are reduced and react with oxygen to form water and heat. Notice that unused H_2 can circulate back into the fuel cell.

1.2 H2 Production

H_2 is one of the most abundant elements on Earth and is usually found as a component of other compounds, such as water (Nikolaidis & Poullikkas, 2017). However, unlike conventional fossil fuels, H_2 is not freely available in the environment. H_2 must be extracted from compounds by the input of a primary energy source (e.g. thermal - (Nikolaidis & Poullikkas, 2017)). H_2 can be oxidised in fuel cells in order to generate an electrical current, only generating water as a by-product. The H_2 can then be extracted from compounds such as fossil fuels, water or biomass by a variety of different methods, which will be reviewed in this section.

In the sense of H_2 production methods, each method is characterized by the amount of CO_2 released in the process. Brown/black H_2 production is the oldest method with the highest amount of CO_2 released and involves gasification. Grey H_2 production relies on steam reformation of natural gas releasing a lower amount of CO_2 compared to brown/black methods. Turquoise is a low CO_2-H_2 releasing method which includes electrolysis of water, which can be further divided into groups depending on the primary energy source used for electrolysis.

1.2.1 Brown/Black Techniques utilised in the Manufacturing of H_2

Currently H_2 is manufactured by gasification of organic material and is mostly dependant on fossil fuels (Bakenne et al., 2016). Gasification converts solid based carbonaceous materials to gas at temperatures that exceed 700^{o}C (Kumar et al., 2009). Controlled concentrations of O_2 in the reactor vessels enables the conversion of organic material to CO, CO_2 and H_2 without combustion of the organic feedstock which will ultimately result in H_2 being oxidized to H_2O. The H_2 can be extracted from the gas stream using membrane systems (Poudel et al., 2019).

Replacing coal fossil fuels with biomass can provide a renewable feedstock source for the gasification process as agriculture produces 849 million tonnes of waste per annum (Guo et al., 2010). The cost of H_2 production from biomass ranges from $1.77-2.05/kg in a plant with expected

H_2 output of 139,700 kg/day (Nikolaidis & Poullikkas, 2017). The cost effectiveness of H_2 production varies depending on temperature, catalysts, incubation period and the biomass type used (Nikolaidis & Poullikkas, 2017). Biomass is a renewable source of substrate and the food and agriculture industries could potentially produce enough waste material to support H_2 production (Sancheti & Burange, 2015). However, the high operating temperatures and pressures required for H_2 production from biomass still require a large primary energy input to extract the H_2 from the biomass.

Using thermal conversion of biomass has the benefits of; low reaction times, all of the organic material contributes to H_2 production and the process is the most profitable technique for H_2 production (Duman & Yanik, 2017). The main product of pyrolysis is bio-oil and char (Duman & Yanik, 2017). Bio-oil offers an alternative feedstock for chemical processes, however, undesirable properties (e.g. high water content, corrosiveness, low energy content and high viscosity) limit its application as an energy source.

Another opportunity in processing biomass for H_2 production, particularly lignocellulose waste, is supercritical water gasification (SCWG). SCWG offers rapid reaction times, less impurities in the output gas mixtures and less processing of the biomass as drying is not required (Okolie et al., 2019). It must be noted that a correlation is observed between the cellulose content and H_2 productivity when using such biomass as substrate (Okolie et al., 2019). This technology is promising, however, has not yet reached large scale commercial H_2 production due to complications in reactor design leading to poor thermal distribution in the vessel, poor catalyst recovery and inefficient mixing of reactants (Okolie et al., 2019).

1.2.2 Grey Techniques in the Manufacturing of H_2

Hydrocarbon reformation is currently the preferred technique for large-scale H_2 production (Bakenne et al., 2016). The cost of H_2 production using reformation techniques ranges from $0.75-2.33 per kg of H_2 produced and releases over seven times more CO_2 compared to the H_2 generated (Bakenne et al., 2016).

H_2 is produced by steam reformation using natural gas (CH_4) as a feed stock at high temperatures often using a Ni based catalyst (Equation 1 (Bakenne et al., 2016)). Steam reformation is often followed by dry reformation in order to increase H_2 yields (Equation 2 (Bakenne et al., 2016)). The gas shift reaction can further extract H_2 from CH_4 in the chemical reaction displayed in Equation 3.

$$CH_4 + H_2O \rightleftharpoons CO + 3H_2$$

Equation 1

$$CH_4 + CO_2 \rightleftharpoons 2CO + 2H_2$$

Equation 2

$$CO + H_2O \rightleftharpoons CO_2 + H_2$$

Equation 3

Raw biogas effluent consists of methane (50-75%), CO_2 (25-50%), nitrogen (2-8%) and trace volatile compounds (e.g. H_2, ammonia, sulfides, organic compounds etc) with the composition varying depending on the source (Li et al., 2019). The efficiency of reformation is influenced by gas composition which also dictates the most efficient catalyst to use (Duman & Yanik, 2017). Sources of biogas can range from landfill to the dairy industry (Li et al., 2019), processing of biogas to a defined composition may facilitate the process (Braga et al., 2013) however this comes at a cost given additional processing.

For a sustainable H_2 economy to exist, renewable substrates must be available for the reformation process that can be directly fed into reactors. Using biological systems for extracting H_2 from waste organic material offers a H_2 production platform which can operate at ambient temperature and pressure, thereby reducing the need to maintain high operating temperatures which add to cost and the carbon footprint. In terms of cyanobacteria as a H_2 production chassis, H_2 can be evolved in conjunction with CO_2 fixation potentially offering a negative net carbon foot print for H_2 production.

1.2.3 Turquoise Techniques in the Manufacturing of H_2

Electrolysis of H_2O utilises electricity to split water into molecular H_2 and O_2 in an electrolyser. At the cathode, protons are reduced and H_2 is evolved while at the anode hydroxide ions gather resulting in oxygen evolution.

Considering the primary energy source, electrolysis still utilises fossil fuels, the same issues relating to sustainability and pollution remain. Renewable energy sources coupled to an electrolyser will ensure sustainable electrolysis of water for H_2 production. A study conducted in Iran has shown that photovoltaic systems have the potential to produce 373 t of H_2 annually with optimized solar energy acquisition (Fereidooni et al., 2018). The low efficiency of solar conversion of 12% and the high investment costs associated with the start-up of such a facility (Fereidooni et al., 2018), limit the development of this technology. Considering temperate regions around the globe (such as UK), investment in solar technologies may not be a viable option for supporting growing local H_2 demand, if H_2 is to become the primary energy carrier molecule (Bakenne et al., 2016).

Wind power has also been recently evaluated as a potential route to green H_2 production. A wind power density of 327 W/m^2 has been shown to theoretically produce nearly 40,000 kg of H_2 annually from sea-water (Rezaei et al., 2018). The water had to be desalinised prior to entering the electrolyser, which will inevitably reduce the efficiency of the plant when compared to pure water being used due to issues surrounding ions interfering with electron exchange at the anode and cathode.

Electrolysis of water can be carried out using; alkaline electrolyser (AEL), proton exchange membrane electrolyzer (PEMEL) or solid oxide electrolyzer (SOEL) (Nguyen et al., 2019). AEL is the most mature with large scale H_2 production capabilities already realised (Nguyen et al., 2019). The issues with the technology are; purity of the H_2 stream which is often contaminated with O_2, corrosive electrolytes and low current densities (Vuksic et al., 2014). PEMEL alleviates the O_2 contamination and can be more responsive to activation (Nguyen et al., 2019). However the corrosive, acidic environment and high component cost (due to frequent replacement of

parts) make this process less appealing than AEL (Nguyen et al., 2019; Vuksic et al., 2014). SOEL requires high temperatures to operate, however there is no requirement for catalysts and no corrosive electrolytes used in the process (Nguyen et al., 2019). However the dependency on high temperatures results in a delay in electrolysis (Nguyen et al., 2019).

A developing technique in turquoise H_2 production is methane pyrolysis. In this process, H_2 and solid carbon is produced from methane using either Fe or carbon based catalysts (Sánchez-Bastardo et al., 2020) which eliminates the release of CO_2 from the process. This technology is still at lab scale, however low yields, high operational temperatures and a lack of understanding of the reaction mechanism is holding back the development of this emerging technique (Sánchez-Bastardo et al., 2020).

One of the major problems of classical water electrolysis is the high over potential necessary. Therefore, a lot of the wind energy is lost (around 20 %) and the efficiency is much lower than it could be when using e.g., hydrogenases and photosystem II (PSII) that have no or a very small “over potential”. Furthermore, wind driven electrolysis is not truly sustainable, the blades from the wind turbines end up in landfill and electrolysis requires precious metals/alloys to act as catalysts, which are toxic and unsustainable, given they are often mined from poorer countries. Therefore, a cyanobacteria-based system offers the only truly sustainable alternative, with the added benefit of being able to fix CO_2 thereby having a negative carbon footprint.

1.3 Biological Hydrogen Production

Biological systems offer a H_2 production method at ambient conditions with the potential to generate 12 molecules of H_2 per molecule of glucose consumed (Y. H. P. Zhang et al., 2007). In 1876, Hoppe-Seyeler demonstrated that mixed mud cultures could decompose formic acid and evolve H_2. It was later shown that hydrogenases were responsible for this reaction (Stephenson & Stckland 1932). Since their discovery, hydrogenases have been observed in many microbes catalysing the reversible reduction of protons.

Microbes can produce H_2 using either nitrogenases or hydrogenases. The route for H_2 evolution via the nitrogenase is displayed in Equation 4. One benefit of exploiting the nitrogenase for H_2 production is that the catalysis is unidirectional and the H_2 is oxidized by uptake hydrogenases (Schütz et al., 2004). H_2 is produced as a by-product with the reducing equivalents in the H_2 reaction being consumed by uptake hydrogenases (Tamagnini et al., 2002). Nitrogenases are classified on the metallic composition of their active site (Joerger et al., 1989). Displacing metals at the active site with tungsten has been shown to improve H_2 production by nitrogenases (Siemann et al., 2003). H_2 evolution via nitrogenases is summarised in Equation 4 (Tamagnini et al., 2002).

$$N_2 + 8H^+ + 8e^- + 16\ ATP \rightarrow NH_3 + H_2 + 16\ ADP + 16\ Pi$$

Equation 4

Nitrogenases are multi-subunit metalloprotein complexes that utilize multiple substrates for catalysis (Tamagnini et al., 2002). An overview of nitrogenase structure and subunit function is shown Figure 1-2. The nitrogenase is split into 2 functional moieties; the dinitrogenase reductase (NifH) and the dinitrogenase (NifK & NifD) (Tamagnini et al., 2002).

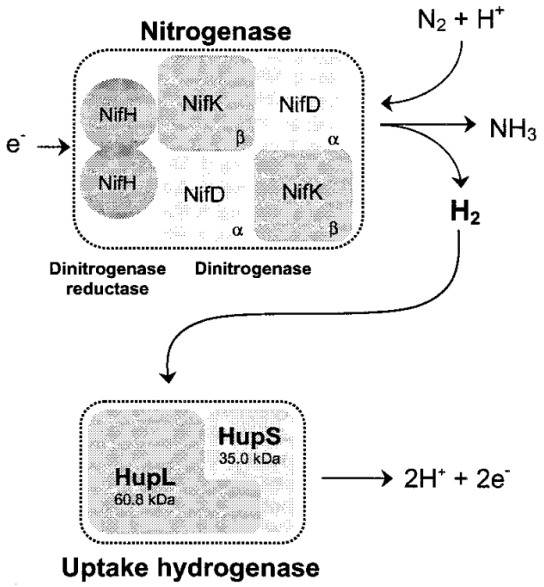

Figure 1-2: Overview of Nitrogenase Structural Genes and Hydrogen Metabolism in Diazotrophs.
The dinitrogenase reductase (NifH dimer) delivers electrons to the dinitrogenase moiety (NifK). ATPase activity of NifH supports this reduction of NifK. The NifD houses the MoFe active site where N_2 reduction to NH_4^+ is catalyzed. Uptake hydrogenases oxidize H_2 and return the reducing equivalents back into the electron transport of the diazotroph. Figure taken from (Tamagnini et al., 2002).

The disadvantage of using nitrogenases as a means of H_2 evolution is the dependancy of ATP to drive the reaction forward. Hydrogenases on the other hand produce H_2 through the simplest of reactions as displayed in Equation 5. The H^+ reduction in hydrogenases is a reversible reaction. The focus of this work is on the biological production of H_2 and therefore hydrogenases will be the focus in this section.

$$2H^+ + 2e^- \rightleftharpoons H_2$$

Equation 5

1.3.1 Hydrogenase Classification

Hydrogenases can also be classed depending on their metallic composition (Vignais et al., 2001). There are three classes of hydrogenase; [Fe], [FeFe] and [NiFe] which are unrelated in protein sequence.

The [Fe] hydrogenases are found in archaea. The [Fe] hydrogenase contains a single Fe atom ligated to the S atom of a cysteine residue on the

structural protein and a guanylylpyridinol cofactor (Shima et al., 2008). The [Fe] hydrogenase is not a redox enzyme and utilises an organic electron carrier (e.g., methyltetrahydromethanopterin), which is used in the biosynthesis of methane from CO_2 and H_2.

[FeFe] hydrogenases are found in the eubacteria and lower eukaryote domains of life and have been shown to have the highest catalytic activity, making them an attractive prospect for biotechnological applications (Winkler et al., 2013). However, the [FeFe] hydrogenases can be extremely sensitive to oxygen and strict anaerobic conditions are required for hydrogenase activity.

The [NiFe] hydrogenases are the oldest and most abundant of the hydrogenases found only in eubacteria and archaea. These hydrogenases are heterodimeric complexes composed of a large and small subunit (Tamagnini *et al*., 2002). The active site of the [NiFe] hydrogenase is ligated to four S atoms on cysteine residues of the large subunit. The Ni and Fe atoms interact via two cysteine residues. The Fe is also ligated to two cyanide and a CO molecule. The structure of the active sites of Fe, [FeFe] and [NiFe] hydrogenases are summarized in Figure 1-3.

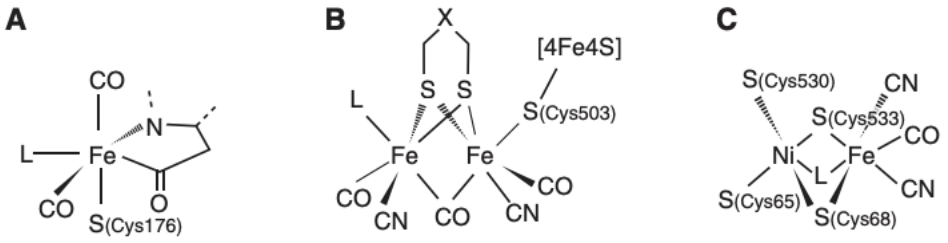

Figure 1-3: Active Site Structure of Hydrogenases Based on Metallic Composition. A) [Fe] Hydrogenase from *Methanocaldococcus jannaschii* (3F47). B) [FeFe] Hydrogenase from *Clostridium pasteurianum* (3C8Y). X is an identified ligand. C) [NiFe] hydrogenase from Desulfovibrio gigas (1YQ9). L is variable depending on the state of the active site. Figure was taken from (Shomura & Higuchi, 2013).

The [NiFe] hydrogenases are further characterised by physiological function. Group 1 [NiFe] hydrogenases are membrane bound linking the

oxidation of H_2 directly to the reduction of substrate, e.g., the membrane bound hydrogenase of *Cupriavidus necator*. Group 2 [NiFe] hydrogenases are uptake hydrogenases, which remain localised in the cytoplasm. Group 3 [NiFe] hydrogenases are heterodimeric often associating with a sub-complex enabling the reversible reduction of protons (for example the *hox* locus in *Synechocystis*). Group 4 [NiFe] hydrogenases are membrane bound multimeric complexes involved in reducing protons from water, resulting in the alleviation of reducing equivalents (e.g., hydrogenase 3 from *E. coli* oxidizing formate to carbon dioxide and H_2 hydrogen).

1.3.2 H_2 Metabolism in Prokaryotes

Under anoxic condition, H_2 is evolved by organisms utilizing protons as an electron sink (Gray & Gest, 1965). Under fermentative conditions, H_2 is evolved via pyruvate-ferredoxin hydrogenase or pyruvate-formate lyase with the eledctrons being derived from organic substrate (McDowall et al., 2014). The oxidation of pyruvate to acetyl-CoA and CO_2 by pyruvate ferredoxin oxidoreductase (PFOR) generates the reduced ferredoxin for H_2 evolution and is the route primarily found in strict anaerobic bacteria such as *Clostridia* sp. (Thauer et al., 1977). The oxidation of formate to CO_2 and H_2 is carried out by facultative anaerobes such as *E. coli* (Thauer et al., 1977).

In facultative anaerobic bacteria such as *E. coli*, the maximum theoretical yield is 2 moles of H_2 per mole of glucose consumed, this is due to mixed acid fermentation being the only route for H_2 production (Trchounian 2015). H_2 is evolved by the formate hydrogen lyase and hydrogenase-3 complex (Hyd-3), which alleviates formate build up in the cytoplasm (Trchounian 2015). **Error! Reference source not found.** shows an overview of the pathway in *E. coli*, with the main engineering strategies for increasing the cytoplasmic concentration of formate to improve H_2 production (Trchounian 2015).

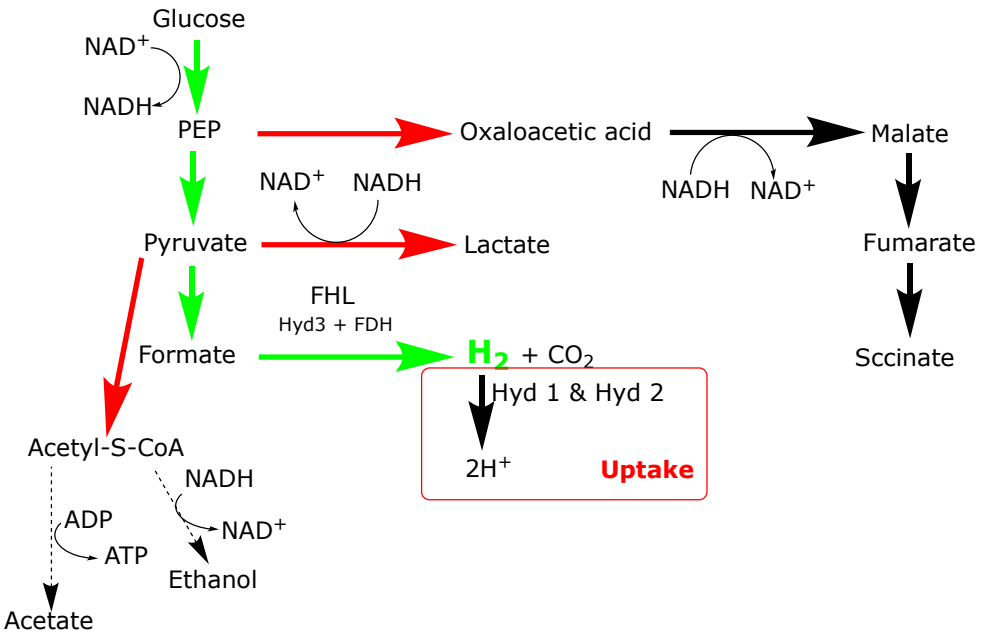

Figure 1-4: Overview of H_2 Metabolism in *E. coli*.
Under anaerobic fermentation conditions, glucose is catabolised and forms formate. The formate is oxidized by the formate hydrogen lyase complex releasing H_2 and CO_2. Reducing equivalents from H_2 can be reintroduced into respiration by oxidation by Hydrogenase 1 (Hyd 1) and hydrogenase 2 (Hyd 2) highlighted in the red box. The competing pathways of phosphoenol pyruvate (PEP) entering into the TCA and pyruvate being converted to lactate are competing pathways in these organisms (highlighted by red arrows).

Glucose is not abundant in waste material; however, *E. coli* has been engineered to utilise treated switch grass as a sole carbon source (Bokinsky et al., 2011). Substrate availability of the *E. coli* hydrogenase 3 was enhanced by the fusion of ferredoxin to HycB resulting in proton reduction being directly coupled to pyruvate oxidation (Lamont et al., 2017). The low theoretical yield of 2 moles of H_2 per mole of consumed glucose must be overcome for *E. coli* to become an economically viable option for biohydrogen production.

In anaerobic fermentation, the [FeFe] hydrogenase is supported by reduced ferredoxin or NADH (Calusinska et al., 2010; Schuchmann et al., 2018). Ferredoxin is reduced by; pyruvate through the pyruvate:ferredoxin oxidoreductase (PFOR) or NADH:ferredoxin oxidoreductase (X. Chen et al., 2006). The trimeric forms of the [FeFe] hydrogenase can oxidise ferredoxin and NADH under low partial pressures of H_2 that would otherwise deem the reaction unfavourable (Calusinska et al., 2010; Schuchmann et al., 2018). Figure 4 depicts an overview of H_2 production in *Clostridia* sp.

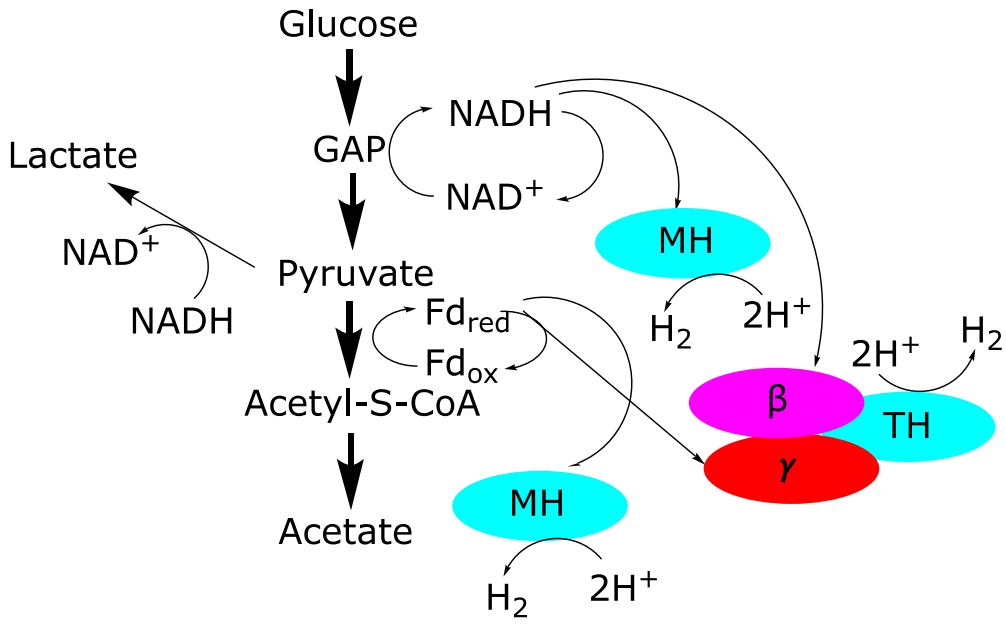

Figure 1-5: Overview of H_2 Metabolism in *Clostridia* sp..
Reducing equivalents are transferred to monomeric hydrogenases (MH) by reduced ferredoxin (Fd_{red}) or NADH derived from oxidation of glyceraldehyde 3-phosphate (GAP) or pyruvate. Both Fd_{red} and NADH can supply reducing equivalents to trimeric hydrogenases (TH). The production of lactate is a competing pathway for reducing equivalents to hydrogenases.

Clostridia thermocellum has been shown to utilise delignified wood producing up to 1.6 moles of H_2 per glucose unit (Levin et al., 2008), which is comparable to 1.7-1.9 moles of H_2 per mole of hexose utilising sucrose as a substrate (Hussy et al., 2005). It was shown that limiting the carbon sources can improve H_2 evolution (Levin et al., 2008). Constant harvesting of H_2 is needed in order to limit the partial pressure of H_2 and will therefore inhibit the hydrogenase (Calusinska et al., 2010).

Glycerol is another waste product with 2 million tonnes being reliably produced on an annual basis (Sytar et al., 2013). *Clostridium acetobutylicum* ATCC 824 was shown to produce 0.27 moles of H_2 per mole of crude glycerol consumed (Dams et al., 2016). As fermentations were all carried out in a volume of 100 mL, scale up may prove challenging as methanogenic bacterial populations need to be stringently controlled in order to maximise H_2 production.

The theoretical maximum yield of H_2 from glucose in anaerobic bacteria is 4 molecules of H_2 per molecule of glucose consumed given that acetate is the only organic acid being produced (Thauer et al., 1977). Organic acids are produced which give the effluent a high biochemical oxygen demand, requiring further treatment before being released. This offers the opportunity to extract more H_2 from the waste organic acids (C. Y. Chen & Chang, 2006).

Considering a two-step process where dark fermentation is followed by photo fermentation by purple non-sulphur (PNS) bacterium, the treatment of the effluent organic acids could provide a carbon source for PNS allowing for more H_2 to be extracted. PNS bacteria evolve H_2 via nitrogenases as opposed to hydrogenases. In conjunction with nitrogen fixation, CO_2 fixation via RuBisCO can fix up to 68% of CO_2 released from anaerobic fermentation (McKinlay & Harwood, 2010) and is further highlighted by exploitation of RuBisCO null strains expressing mutant nitrogenases that are active under nitrogen repletion (Hallenbeck, 2011). *Rhodobacter palustris* Wp 3-5 was shown to produce 3.56 molecules of H_2 per molecule of acetate consumed, which accounts for 60 % of the theoretical yield (C. Y. Chen & Chang, 2006) showing the potential of two stage fermentation treatment. However, cyanobacteria have the capability of H_2 evolution by direct photolysis and therefore circumvent the issue surrounding the loss of H_2 to organic acids in fermentation.

An alternative to using photofermentation to increase the yield of H_2 in the dark fermentation process, is the use of microbial electrolysis cells (MECs). The anode of the MECs can be colonized by anode respiring bacteria (ARB) such as *Shiwanella* sp.which oxidize organic acids and donate electrons thus generating a current. Combining MEC with dark fermentation, a potential of 9 molecules of H_2 could be produced per glucose molecule (H. Liu et al., 2005).

The voltage for water electrolysis is +0.82 V and given the maximum theoretical applied voltage by ARB utilizing acetate as an electron source is -0.28 V, the additional voltage must be met by an external energy source

supplying between 0.6-1.2 V (Lee et al., 2010). Many factors such as the resistance of material (e.g. biofilm) limit the efficiency of MECs (Lee et al., 2010). Therefore, for this process to be energetically beneficial, the externally applied current must be below 0.6 V (Lee & Rittmann, 2010). In order to drive down capital costs and make this technology accessible, much higher production rates are needed as the the current highest rates of H_2 production are 0.13 L of H_2/L/hr applying 0.8 V compared to dark fermentation resulted in a production rate of 7 L of H_2/L/hr applying (Lo et al., 2009).

The issue with using electrolysis of water is the difference in the energy required to electrolyze water and the stored energy in the H_2. The use of biological systems overcomes energy lost in water electrolysis. With respect to energy efficiency in biological H_2 production, hydrogenases offer the most promise as there is no dependency on ATP levels. Pyruvate-ferredoxin hydrogenases are the most efficient means of H_2 evolution producing 4 molecules of H_2 per glucose consumed (Thauer et al., 1977). The cyanobacterial bidirectional hydrogenase (Hox) can efficiently utilise reduced ferredoxin derived from catabolism of glucose or directly from photosynthesis (Appel et al., 2000; Cournac et al., 2002; Gutekunst et al., 2014) permitting the exploitation of multiple metabolic pathways for green H_2 production.

1.4 Cyanobacteria as a Potential Chassis for Photobiological H_2 Production

Cyanobacteria are the oldest, diverse and most abundant organisms on earth, occupying many ecological niches owing to the successful coupling of respiration and photosynthetic electron flow (Vermaas 2001). Figure 1-6 A shows the overall architecture of the Gram-negative cyanobacterial cell (variable Gram staining due to peptidoglycan content of the cell wall). These cells can form filaments (e.g., *Anabaena* sp. B), discrete single cells (e.g., *Synechocystis* sp. PCC 6803 C – here after referred to as PCC 6803) or a colonial arrangement (e.g., *Microcystis* D). The single cells can adopt spherical (as observed in sp. PCC 6803) or rod shaped (*Synechococcus* sp. 7002 E– here after referred to as PCC 7002) morphology.

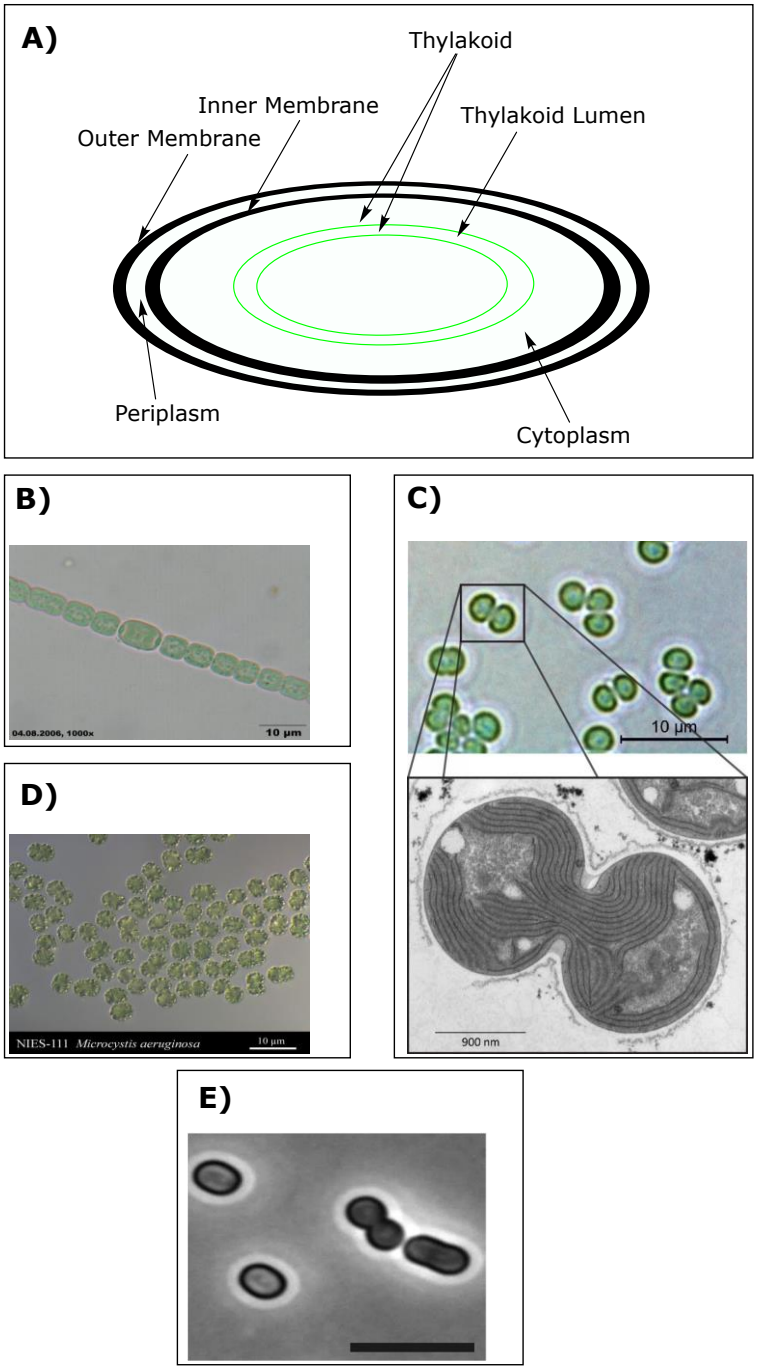

Figure 1-6: Cyanobacterial Cell Architecture.
The general cellular architecture of cyanobacteria follows that of Gram-negative bacteria with an outer and inner membrane. A) photoautotrophic growth cyanobacteria have an extensive intracellular membrane system termed the thylakoid which enable cells to convert light energy into chemical energy by the oxidation of water. Figure is adapted from Vermaas, 2001. B) *Anabaena* image from Dr. Ralf Wagner (http://www.dr-ralf-wagner.de/index-englisch.htm), C) *Synechocystis* sp. PCC 6803 image from Alexander Klotz (https://www.bioregio-stern.de/en/news/how-dead-bacteria-return-to-life), D) *Microcystis auregenosa* image from NIES culture collection (https://shigen.nig.ac.jp/algae/images/strainsimage/nies-0111.jpg) and E) PCC 7002 image from (Frigaard, 2018).

1.4.1 General Features of Cyanobacteria

Cyanobacteria are capable of oxygenic and anoxygenic photosynthesis, offering both a renewable and sustainable means of H_2 production. In oxygenic photosynthesis, the oxidation of water results in the release of molecular oxygen and protons, which have been influential on the atmospheric composition of earth (Vermaas 2001). In anoxygenic photosynthesis, reducing equivalents from respiration can support the reducing power to the plastoquinone pool to support growth (Cooley & Vermaas, 2001). The reducing power generated from the oxidation of water is utilised by the carboxysome to fix carbon and generate biomass (Price & Badger, 1991). Tapping into electrons derived from water oxidation can offer a renewable source of H_2 which is not likely to compete with arable lands for generating feedstocks for fermentations.

H_2 metabolism is an important outlet for excess electrons (Appel et al., 2000; Gutekunst, 2018a) and an important H_2 uptake pathway exists in diazotrophic cyanobacteria in order to make use of excess reducing equivalents in the form of H_2 derived from nitrogenases (Tamagnini et al., 2002). It is of biotechnological interest to understand the flow of electrons to the Hox in species such as PCC 6803 and PCC 7002 in order to exploit this metabolism to make photobiological H_2 production accessible, sustainable, renewable and economically viable.

1.4.2 The Cyanobacterial Bi-directional Hydrogenase (Hox)

Hox acts as an electron valve, which alleviates excessive reducing equivalents in cyanobacteria (Appel et al., 2000). Reduced ferredoxin is oxidised by Hox in order to maintain optimal electron flow (Appel et al., 2000; Gutekunst et al., 2014). Increasing the reduced ferredoxin pool is critical for H_2 evolution in non-diazotrophic cyanobacteria (Cournac et al., 2002, 2004; Gutekunst et al., 2014) promoting H_2 evolution by Hox in order to combat the dangerous over reduction of soluble electron carriers (Appel et al., 2000).

The structural genes for the bi-directional hydrogenase are constitutively expressed in PCC 6803 as a polycystronic unit (Appel et al., 2000; Gutekunst et al., 2005). Hox is localized to the thylakoid membrane, it does not span the membrane as it lacks a transmembrane domain

(Tamagnini et al., 2002) and is instead anchored to the thylakoid by the HoxE subunit (Burroughs et al., 2014). In wild type PCC 6803, the Hox complex forms 2 populations in the thylakoid; diffusely spread or puncta at the thylakoid(Burroughs et al., 2014).

The HoxE subunit is not essential for H_2, however deletion reduces the H_2 evolution rate by 30% when compared to the wild type PCC 6803 (Eckert et al., 2012). In the ∆*hoxE* strain a population of Hox was found to be localized to cytoplasm (Burroughs et al., 2014) which accounts for the reduced hydrogenase activity (Eckert et al., 2012). It is not clear how Hox interacts with the electron transport chain at the thylakoid membrane, however, the influence of HoxE on localization at the thylakoid and potential interactions with an electron partner at the thylakoid accounts for the lower hydrogenase activity observed in the Δ*hoxE* strain (Burroughs et al., 2014; Eckert et al., 2012).

1.4.2.1 Hox Structural Architecture

The cyanobacterial [NiFe] bidirectional hydrogenase (Hox) is a heteropentameric complex (Eckert et al., 2012). The complex is divided into two functional sub-complexes; a hydrogenase sub-complex with the characteristic large and small subunits which is represented by HoxH and HoxY respectively (Appel & Schulz, 1996). The second functional module is the diaphorase moiety, which is composed of HoxE, HoxF and HoxU (Appel & Schulz, 1996). The hydrogenase sub-complex catalyses the reversible reduction of H^+ to H_2 with the diaphorase sub-complex providing the source/sink of electrons for the catalysis (Eckert *et al*., 2012; Gutekunst *et al*., 2014). The Hox complex is summarised in Figure 1-7.

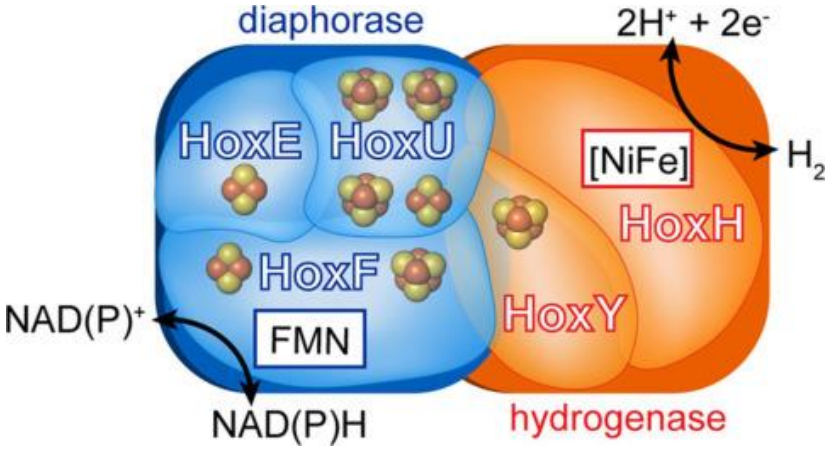

Figure 1-7: Subunit Composition of the Cyanobacterial Bi-Directional Hydrogenase The hydrogenase moiety subunits are highlighted in orange and composed of a large sub-unit (HoxH) and a small sub-unit (HoxY). It is this sub-complex which catalyses the reversible reduction of protons. Both C-terminally processed and unprocessed HoxH can associate with the entire complex (Eckert et al., 2012) however it remains unclear as to whether this interaction is part of the maturation process. The diaphorase sub-complex is highlighted by the blue subunits and composed of HoxEFU. The E subunit has been shown to be dispensable for hydrogenase activity albeit at a lower rate (Burroughs et al., 2014; Eckert et al., 2012). The diaphorase sub-complex is the source/sink of electrons for the Hox complex. Figure taken from (Artz et al., 2020).

Fast protein liquid chromatography studies have shown that the Hox complex can be purified as a number of subcomplexes; HoxEFUYH, HoxEFU or HoxFU (Eckert *et al*., 2012). The HoxE sub-unit was shown to elute as either a single unit or as part of the complex, which led the authors to conclude that HoxE has weak affinity to the Hox complex. The HoxE sub-unit of PCC 6803, PCC 7002 and *Synechococcus* sp. PCC 7942 all have a predicted [4Fe4S] binding motif (Nakao *et al*., 2010) which suggests a role in shuttling electrons to and from electron donors at the thylakoid. In PCC 6803, the HoxEFU complex was shown to be able to oxidize NADH with a Vmax of 2.5 μmol min^{-1} mg^{-1} and NAD(P)H at a Vmax of 5.7 μmol min^{-1} mg^{-1} (Artz et al., 2020). With whole cell lysate, NAD(P)H was unable to induce H_2 evolution where NADH was shown to produce H_2 (Gutekunst et al., 2014) which contradicts the NAD(P)H oxidase activity. It has been shown that reduced ferredoxin does have the ability to reduce $NAD(P)^+$ and NAD^+ (Artz et al., 2020) which highlights the dexterity of the diaphorase subunits. The maximum amount of H_2 produced in the lysate assay was with ferredoxin (Gutekunst et al., 2014) and it has been demonstrated that ferredoxin makes

physical contact with all diaphorase subunits (Artz et al., 2020) which demonstrates that reduced ferredoxin is a major source of reducing equivalents for H_2 evolution.

For enhanced H_2 evolution, saturating the reduced ferredoxin pool is the most successful strategy coupled to a reduction in the competing electron pathways, resulting in reduced ferredoxin and increased H_2 yields (Baebprasert et al., 2011; Gutthann et al., 2007). Hox is essential when PCC 6803 is grown photomixotrophically under nitrate limited conditions (Gutekunst et al., 2014) with a higher rate of H_2 evolution (Gutekunst, personal communication) further highlighting the need to direct electron flux towards Hox for improved H_2 production.

The *hoxE* mutant showed a 70% reduction in hydrogenase activity of wild type PCC 6803 (Eckert et al., 2012). The puncta formation is a physiological stimulus from redox sensing in the cell and is independent of HoxE, with HoxE influencing the localization of the puncta (Burroughs et al., 2014). The localization plays an important function in the turnover of reduced ferredoxin (Burroughs et al., 2014; Gutekunst et al., 2014) which in turn explains the decreased hydrogenase activity (Eckert *et al*., 2012).

1.4.3 Electron Transport of Cyanobacteria

An overview of photosynthetic electron transport is shown in Figure 1-8. Photosynthetic electron flow starts in photosystem II (PSII), where water is oxidised (Vermaas 2001). Electrons from water enter the plastoquinone pool (Vermaas 2001). Plastoquinol is oxidised by the cytochrome b_6f (Cyt b_6f) complex, which reduces the soluble electron carrier plastocyanin (Vermaas 2001). The plastocyanin can be oxidised by terminal oxidases or by photosystem I (PSI) (Vermaas 2001). PSI reduction of ferredoxin is mediated by ferredoxin NAD (P) reductase (FNR) completing linear electron flow with the reducing equivalents consumed by the Calvin-Benson cycle (Vermaas 2001). The Calvin-Benson carbon fixation cycle requires 2 NAD(P)H and 3 ATP molecules to fix 1 CO_2 molecule (Vermaas 2001). Cyclic electron flow (CEF) drives proton translocation for ATP synthesis (Vermaas 2001). Reduced ferredoxin is oxidised directly by the NAD(P)H dehydrogenase

(NDH1) complex (He *et al*., 2015). By decoupling CEF, more electrons would be available for H_2 evolution due to the specific ratio of NAD(P)H and ATP required to drive carbon fixation.

Hox fits into the electron transport chain by acting as a buffer for excess reducing equivalents (Appel et al., 2000). The metabolic dexterity of Hox has been highlighted with the ability of the diaphorase to oxidise multiple soluble electron carriers (namely ferredoxin, flavodoxin, NADH and NAD(P)H) (Artz et al., 2020; Gutekunst et al., 2014). The possibility that Hox can oxidise the plastoquinol pool is limited by the lower H_2 evolution rate observed in M55 (Δ*ndh-1*) (Gutthann et al., 2007). There is a lack of understanding as to how Hox may interact with the electron transport chain to modulate plastoquinol oxidation with the most plausible interaction partner being NDH-1 due to the homology observed between HoxEFU and NuoEFG (Appel & Schulz, 1996) combined with the reduced H_2 evolution rate (Gutthann et al., 2007).

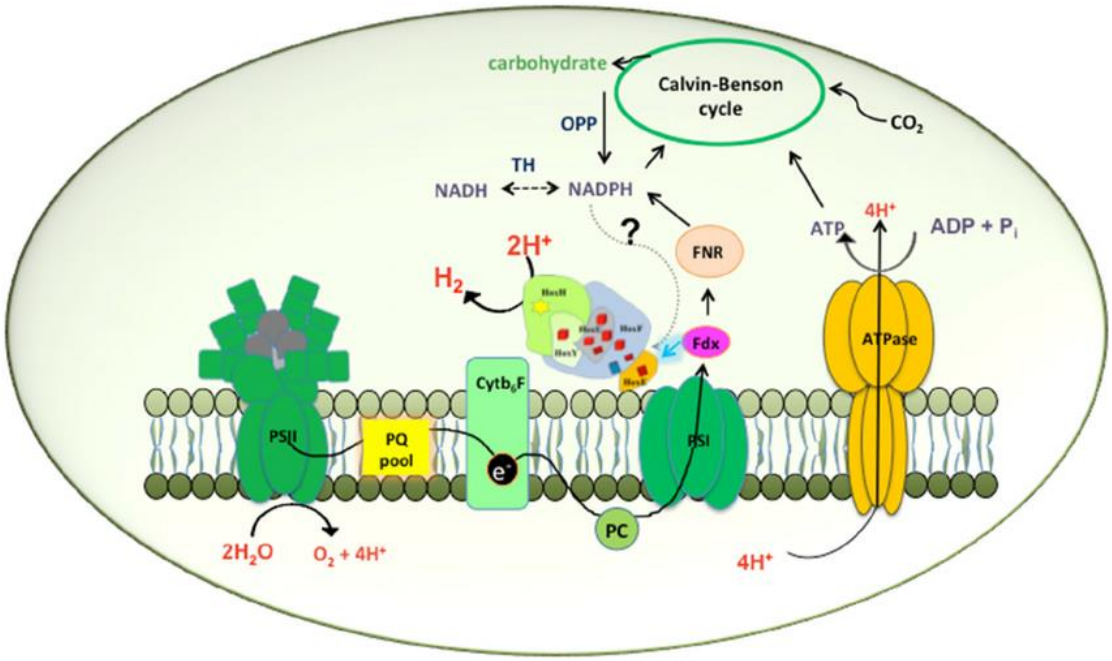

Figure 1-8: Overview of Photosynthetic Electron Flow in Cyanobacteria.
The reducing equivalents in the electron transport chain are passed to ferredoxin. Ferredoxin can be oxidized by the diaphorase moiety of Hox (Gutekunst et al., 2014). There are a number of competing pathways at this point for reducing equivalents for pathways such as nitrate/sulphate metabolism and CO_2 fixation. Figure adapted from (Khanna & Lindblad, 2015).

The metabolic dexterity of Hox has been highlighted with the ability of the diaphorase subunits to oxidise multiple soluble electron carriers (namely ferredoxin, NADH and NAD(P)H) (Artz et al., 2020; Gutekunst et al., 2014). Hox utilizes reduced ferredoxin (Gutekunst et al., 2014) in a similar manner as *Clostridial* sp. under anoxic conditions, which is often referred to as indirect photolysis (Yu & Takahashi, 2007). Photomixotrophic growth using glucose increases H_2 yields significantly when O_2 is removed from the culture (Appel et al., 2020). As the pyruvate pool increases there is a subsequent increase in electron flux towards Hox. Thisstrategy results in the production of 4 molecules of H_2 per molecule of glucose catabolised (Thauer et al., 1977). The dependency of reduced ferredoxin for fermentative and direct photolysis for H_2 evolution is absolutely critical (Gutekunst et al., 2014). Figure 1-9 summarises the respiratory electron transport chain.

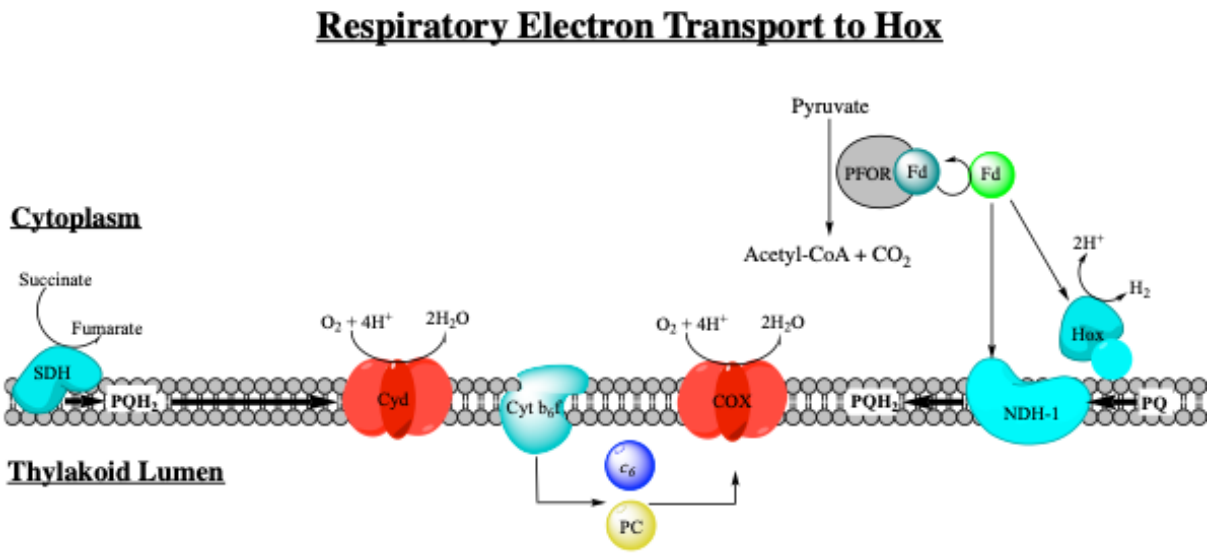

Figure 1-9: Respiratory Electron Transport inthe Thylakoid Under Microaerobic Dark Adapted Conditions.
Electrons enter the plastoquionone pool via succinate dehydrogenase(SDH) and type I NAD(P)H dehydrogenase (Cooley & Vermaas, 2001). The plastoquinol pool is oxidized by cytochrome quinol oxidase (Cyd). The phycocyanin is oxidised by cytochrome c oxidase (COX). For H_2 evolution under fermentative conditions, saturating the soluble electron transport chain with PFOR demonstrated to be the major source of reduced ferredoxin to Hox (Gutekunst et al., 2014).

However, following the onset of photosynthesis in anoxic dark adapted cells, there is a large increase in the reduced ferredoxin pool giving rise to a short period of H_2 evolution (Cournac et al., 2002, 2004) which is referred to

as direct photolysis as photosynthetic electrons are diverted to Hox. The direct photolysis circumvents the loss of H_2 in fermentation products. For this technology to be truly applied, a greater understanding of how Hox interacts with the electron transport chain is vital. The photosynthetic electron transport chain is summarised in **Error! Reference source not found.**.

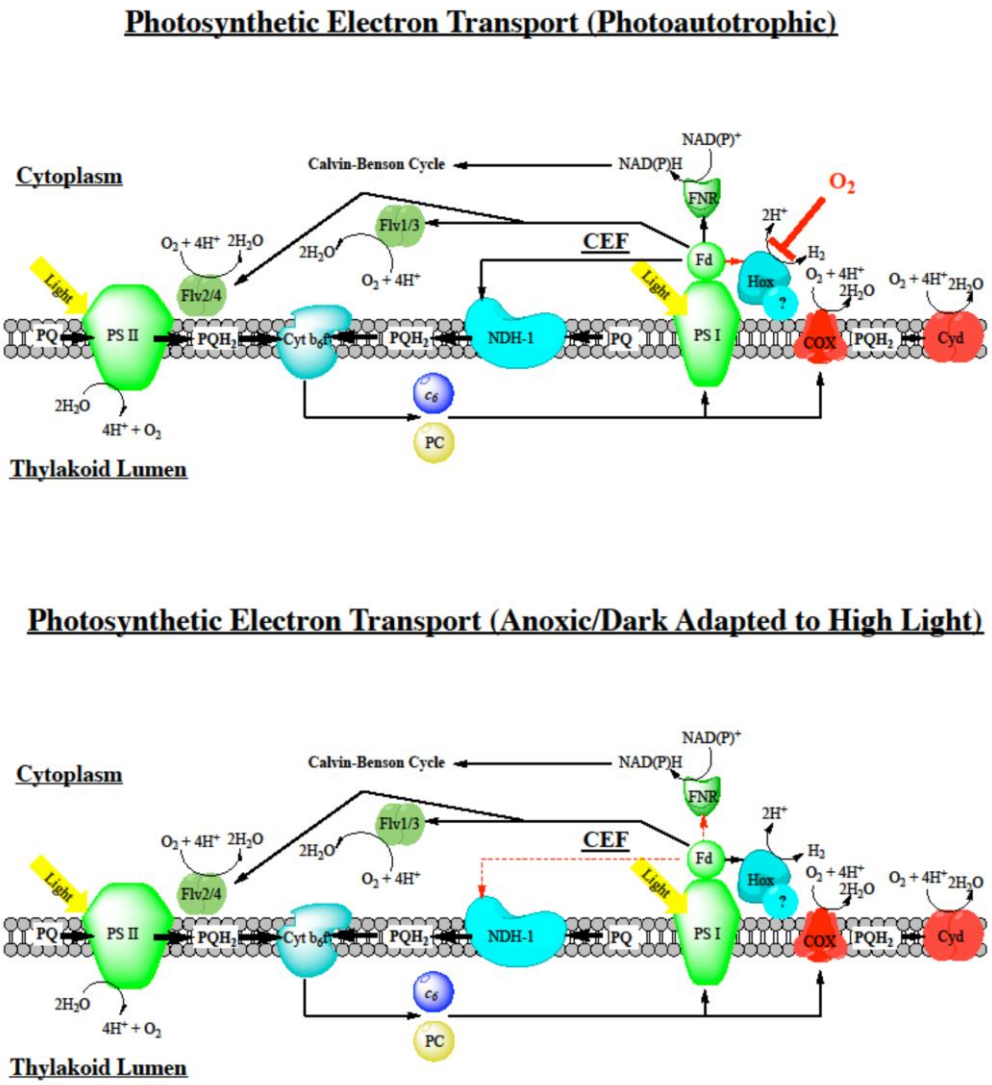

Figure 1-10: Photosynthetic Electron Transport Chain.
Under anoxic dark adapted conditions, the Calvin-Benson cycle is not fully active (indicated by broken red arrow) due to the lack of reducing equivalents from PS I driving CO_2 fixation. Once the activity of PS II and PS I drives photosynthetic electron flow there is a sharp increase in the reduced ferredoxin pool that is dissipated by Hox accounting for the initial burst in H_2 evolution (Appel et al., 2000; Cournac et al., 2002). As cells acclimatize to the light, H_2 is consumed re-entering the photosynthetic electron transport accounting for a period of H_2 oxidation (Appel et al., 2000; Cournac et al., 2002). As more water is oxidised, O_2 increases within the cells resulting in Hox being reversibly inactive.

1.5 Competing Electron Pathways to Hox

1.5.1 Potential Hox Interaction Partner with NAD(P)H Dehydrogenase 1 Complex (NDH-1)

Phylogenic analysis of type 4 membrane bound [NiFe} hydrogenases has hinted they share a universal common ancestor with complex 1 of the respiratory electron transport chain (Marreiros et al., 2013). Hox is closely related to group 4 [NiFe] hydrogenases (Vignais & Billoud, 2007) which highlights the divergence of respiratory complexes (Gutekunst, 2018b).

The NDH-1 complex is homologous to complex 1 of eubacteria and the mitochondria (Appel & Schulz, 1996). Sequence analysis has shown the diaphorase subunits of Hox are homologous to the NADH binding motif of complex 1 (Appel & Schulz, 1996). However, Hox is not essential for CEF in PCC 6803 as *hox* mutants do not show the same phenotype as the CEF deficient mutant Δ*ndhD1/ndhD2* (Ohkawa, Pakrasi, et al., 2000). Structural data has demonstrated that ferredoxin can directly reduce the plastoquinone pool (C. Zhang et al., 2020).

In conjunction with a critical role in CEF (Ohkawa, Pakrasi, et al., 2000), NDH-1 has a role in the carbon concentrating mechanism (CCM) in cyanobacteria (Ohkawa, Dean Price, et al., 2000). NDH-1 has 4 isoforms composed of unique NdhD/NdhF subunits with 2 responsible for CEF and 2 responsible for CCM (Battchikova et al., 2011). Figure 1-11 gives an overview of the different isoforms of NDH-1 highlighting the different subunits.

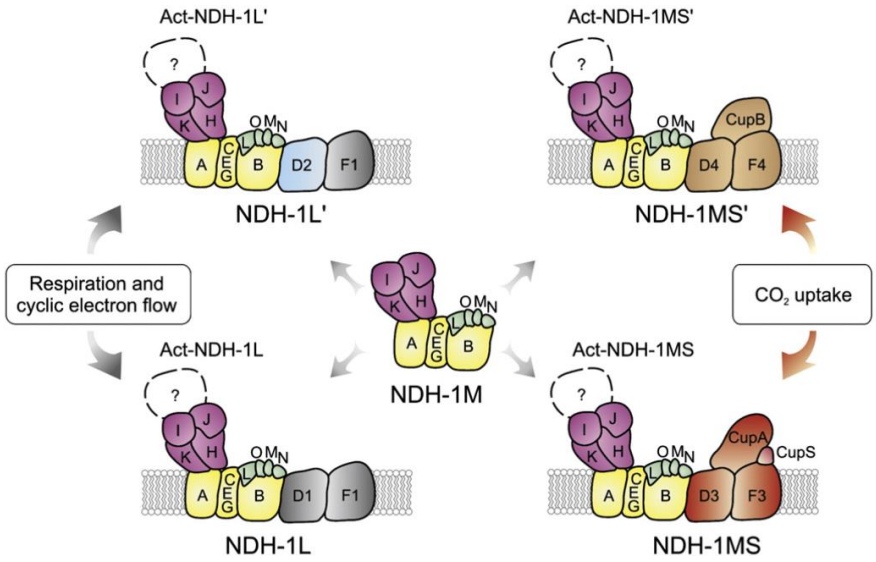

Figure 1-11: An overview of NDH-1 Isoforms.
All NDH-1 isoforms have common subunits that shown in the centre of the figure. The NDH-1L & NDH-1L' isoforms are involved in CEF. The NdhD1 subunit is unique to NDH-1 with NdhD2 being unique to NDH-1L'. NDH-1MS and NDH-1MS' are responsible for the CCM by converting CO_2 to HCO_3^-. The subunits unique to NDH-1MS are; NdhD3, NdhF3, CupA and CupS. The subunits NdhD4, NdhF4 and CupB are unique to NDH-1MS'. It has been demonstrated that NDH-1L' and NDH-1MS' contribute little to the respective functions (Ohkawa, Dean Price, et al., 2000; Ohkawa, Pakrasi, et al., 2000). Figure taken from (Battchikova et al., 2011).

The NDH-1 complex has been visualised in *Synechococcus* sp. PCC 7942 and puncta were observed in conditions where the plastoquinone pool becomes oxidised (L. N. Liu et al., 2012). Blocking oxidation of the plastoquinol pool resulted in limited H_2 uptake (Dutta & Vermaas, 2016) similar to what was observed in the PCC 6803 mutant strain completely lacking the NDH-1 complex (M55) (Cournac et al., 2004). Together these experiments suggest a potential interaction between the Hox and NDH-1 in H_2 oxidation.

It is still unclear whether Hox can evolve H_2 at the expense of reducing equivalents directly from the plastoquinol pool. There is a reduction in hydrogenase activity in M55 (Gutthann et al., 2007), however the total amount of H_2 produced in M55 is significantly higher when compared to wild type (Gutthann et al., 2007). The loss of a functional NDH-1 complex may account for the reduced hydrogenase activity but this still remains unclear as it has been noted that NDH-1 is not required for thylakoid localization of Hox and not all cells express Hox in the M55 *hoxFGFP* strain (Burroughs et al., 2014).

1.5.2 Oxygen as an Electron Sink

Besides CO_2 fixation, O_2 reduction is the second most important electron sink in photoautotrophic organisms (Gutthann et al., 2007). O_2 reduction by the photosynthetic electron transport chain is carried out by terminal oxidases or specialised flavoproteins (Helman et al., 2003). It has been estimated that 40% of the electrons entering the plastoquinol pool from PS II are consumed by the photoreduction of O_2 (Helman et al., 2005).

Terminal oxidases in cyanobacteria have two main sources of reductants; the plastoquinol pool or reduced plastocyanin (Hart et al., 2005). The plastoquinol pool can be oxidized by cytochrome quinol oxidase (Cyd) and phycocyanin can be oxidised by cytochrome c oxidases (COX) (Hart et al., 2005). Terminal oxidases in cyanobacteria have been demonstrated to be critical for the acclimatization of cells to varying light intensities as mutations in the terminal oxidases result in severe photosynthetic and growth defects (Lea-Smith et al., 2013).

In the absence of O_2, excessive reducing equivalents are dissipated by Hox (Appel et al., 2000; Cournac et al., 2002, 2004). Studies have shown that under continuous dark growth Hox is essential (De Rosa et al., 2015), highlighting the significant contribution Hox plays in the electron transport chain. It is not clear whether the essential role under these conditions is simply dissipating excessive reducing equivalents as H_2 or by modulating the stoichiometry of soluble electron carriers (Artz et al., 2020).

1.5.3 Ferredoxins Role in Central Metabolism

Ferredoxins play a critical role in distributing reducing equivalents derived from PS participating in essential redox chemical reactions in cyanobacteria (Mondal & Bruce, 2018). According to KEGG, there are 9 different ferredoxins encoded in the genome of PCC 6803 with surface charges of ferredoxin isoforms playing a role in protein-protein interactions (Kapoor et al., 2018) suggesting that sequence variation allows the ferredoxin isoforms to deliver electrons from PS I to meet the metabolic demands of the cell.

Ferredoxin reduced by PS I plays an essential role in the fixation of CO_2 by donating electrons to $NAD(P)^+$ via the ferredoxin-NAD(P) reductase (FNR) (Forti & Bracale, 1984). This is an essential reaction in photoautotrophic organisms as it is impossible to isolate a fully segregated FNR mutant (Gutekunst et al., 2014). A merodiploid Δ*fnr* mutant in PCC 6803 was characterised showing that photobiological H_2 evolution was significantly higher in Δ*fnr* with a lower H_2 uptake (Gutekunst et al., 2014). Demonstrating that H_2 evolution is dependent on the supply of reduced ferredoxin and that H_2 oxidation requires a significant electron sink. It is worth noting that the Δ*fnr* strain was selected through photomixotrophic growth and this strain has yet to be fully characterised (Gutekunst et al., 2014). Emerging synthetic biology tools in cyanobacteria (Yao et al., 2020), will all the temporal fine tuning of competing pathways.

Nitrate is an important electron sink for cyanobacteria and strategies for improved H_2 productivity often involve nitrate limitation (Baebprasert et al., 2011; Gutthann et al., 2007; McNeely et al., 2010, 2011, 2014). Nitrate is actively transported into the cytoplasm by nitrate transporters (NTR) (Flores et al., 2005). Nitrate reductase (NarB) reduces nitrate to nitrite and the nitrite is reduced to form ammonia by the nitrite reductase (NirA) (Flores et al., 2005). Nitrate reduction to ammonia is a sequential process requiring a total of 8 electrons (Flores et al., 2005) which could potentially be diverted to Hox. Using ammonia as a sole N-source is not economically feasible given H_2 is used in the manufacturing of ammonia (Bakenne et al., 2016), however some success has been achieved by using urea as a sole nitrogen source (Veaudor et al., 2018) which offers both phytoremediation and green H_2 production.

1.6 Aims and Objectives

Biomanufacturing using microorganisms has several advantages over conventional petrochemical-based processes including renewability, sustainability, and carbon neutrality. The commercial goal for bio H2 production is 0.30 USD/kg/H2 (Goswami et al., 2021), to achieve this goal we need to fundamentally understand the role of Hox in the cell and how it interacts with key components of the electron transport chain e.g. NDH-1.

This project aims to provide a comprehensive understanding of the functional activity of Hox, directly linking cellular localization of Hox to electron transport and H_2 metabolism in the cell. **Objectives**

1. Determine the spatiotemporal dynamics and function of Hox and NDH1 under photoautotrophic, mixotrophic, nitrate limiting mixotrophic growth and following anoxic dark adaptation *in vivo* in PCC 6803.
2. Determine the spatiotemporal dynamics and function of Hox and NDH1 under photoautotrophic, dark adaptation and mixotrophic growth in vivo in PCC 7002.
3. Determination of the spatiotemporal dynamics of the Hox subunits and identification of Hox interaction partners in vivo under photoautotrophic and dark adaptation.
4. Characterisation of H_2 metabolism under photoautotrophic, dark adaptation and mixotrophic growth

Appel *et al* demonstrated that a Hox fusion to Photosystem I (PSI) in PCC 6803 was able to generate 500 µM of H_2 under anaerobic conditions in the light (Appel et al., 2020); a significant improvement on the nmol levels (18-300 nmol H_2) previously reported, thus, clearly establishing the importance of efficient electron flux in increasing H_2 productivity. The metabolic engineering challenge is to manipulate the microbial biochemical and regulatory pathways to enable efficient photo-energy conversion to fuel.

However, to solve this challenge and design novel microbial systems, a fundamental understanding of how Hox interacts with key players in the electron transport chain and the metabolic networks that regulate H_2 productivity in the subcellular environment must be understood. This thesis provides a framework for this understanding.

Chapter 3 presents the investigation of the distribution of Hox and NDH-1 in PCC 6803 under phototrophic, mixotrophic and mixotrophic nitrate conditions, addressing the lack of electrons being supplied to Hox.

The interaction partner of Hox and the *in-vivo* assembly intermediates still remain unclear. **Chapter 4** addresses the interaction partner of Hox at the thylakoid.

With a lot of work focussing on H_2 metabolism in PCC 6803, **Chapter 5** addresses the distribution of Hox and NDH-1 in PCC 7002. This will attempt to investigate whether observations in PCC 6803 are in fact transferrable to other cyanobacteria.

The metabolome and photosynthetic performance of PCC 6803 with respect to conditions that support H_2 metabolism and in various mutants associated with H_2 metabolism was investigated in **Chapter 6**. An understanding in the carbon flux of these conditions and mutants will support engineering strategies for designing a cyanobacterial chassis for H_2 production.

2 Materials and Methods

2.1 Culture Growth and Maintenance

2.1.1 Media and Antibiotic Concentrations

Escherichia coli strains were routinely grown in lysogeny broth (LB, Sigma-Aldrich®) medium (BERTANI, 1951) in order to propagate plasmids. For solid media growth, LB was supplemented with 12 g/L of agar (Difco™ agar). When required, antibiotics were used to supplement LB, with final concentrations as shown in Table 2-1. *E. coli* strains were stored long term at -80 ^{o}C using microbeads (Microbank™ bacterial and fungal preservation system). Strains were revived by inoculating 10 mL of LB containing the appropriate antibiotic (Table 2-1) and routinely grown at 37 ^{o}C with shaking at 200 rpm.

Table 2-1: Working Concentration of Antibiotics

Antibiotic	*E. coli*	Cyanobacteria	Abbreviation
Ampicillin/Carbenicillin	100 μg/mL	N/A	Amp/Carb
Kanamycin	50 μg/mL	50 μg/mL	Km
Spectinomycin	50 μg/mL	50 μg/mL	Spec
Apramycin	50 μg/mL	25 μg/mL	Apra
Hygromycin	N/A	200 μg/mL	Hyg
Erythromycin	N/A	25 μg/mL	Ery
Gentamycin	N/A	25 μg/mL	Gent

2.1.2 BG11 Media for Cyanobacteria

Cyanobacteria were grown at 30 ^{o}C, at a light intensity of 10 μE m^{-2} s^{-1} in BG11 (Stanier et al., 1971) for routine maintenance. BG11 media was prepared by mixing the stock solutions (**Error! Reference source not found.** & Table 2-3) adding MilliQ water to the appropriate volume and autoclaving at 121 ^{o}C for 15 minutes. For PCC 7002, vitamin B_{12} was added prior to

inoculation at a final concentration of 0.4 μg/mL (Stevens et al., 1973). For strains with antibiotic selectable markers, antibiotics were added to the final concentrations shown in Table 2-1. For $BG11_0$ media, nitrate was omitted from the BG11 solution prior to autoclaving.

Table 2-2: BG11 Stock Solutions.

Chemical	Stock (g/L)	Dilution
$NaNO_3$	150	100
K_2HPO_4	8	200
$MgSO_4.7H_2O$	15	200
$CaCl_2.2H_2O$	36	1,000
Trace Elements		1,000

Table 2-3: Trace Element Solution for BG11.

Chemical	**Concentration (g/L)**
H_3BO_3	2.86
$MnCl_2.4H_2O$	1.81
$ZnSO_4.7H_2O$	0.222
$NaMoO_4.2H_2O$	0.391
$CuSO_4.5H_2O$	0.079
$Co(NO_3)_2.6H_2O$	0.049
Citric Acid	6
Ferric Ammonium Citrate	6
EDTA (disodium salt)	1

Cells were sub-cultured every month. For long-term storage, 10 mL of stationary phase culture was spun down, re-suspended in 300 μL of 7 % (vol/vol) DMSO in BG11 and stored at -80 °C. For growth on solid BG11, a solution of 2x concentrated BG11 and 3 % agar (Difco™ agar) were autoclaved separately and subsequently mixed in equal parts. Solid BG11 plates were supplemented with 10 mM $NaHCO_3$.

2.1.3 Medium A+ Media for Cyanobacteria

PCC 7002 was grown in Medium A+ (Stevens et al., 1973) supplemented with 2 μM $NiCl_2$ (McNeely et al., 2010) for physiological and microscopy studies. All stock solutions

Table 2-4and Table 2-5 were made in MilliQ water and the Medium A+ stock solution was autoclaved prior to use.

Table 2-4: Medium A+ Stock Solution (100*).

Chemical	Mass (g/L)
KCl	60
$NaNO_3$	100
$CaCl_2.2H_2O$	37
Na_2EDTA	3
KH_2PO_4	5

Table 2-5: Medium A+ Trace Element Stock Solution (1,000*).

Chemical	Mass (g/L)
H_3BO_3	2.86
$MnCl_2.4H_2O$	1.81
$ZnSO_4.2H_2O$	0.222
MoO_3 (85%)	0.03
$CuSO_4.5H_2O$	0.079
$CoCl_2.6H_2O$	0.0403

NaCl and $MgSO_4 \cdot 7H_2O$ were dissolved in 980.7 mL of MilliQ water, the Medium A+ stock, Tris buffer and the trace elements solutions were added in the proportions shown in Table 2-6, prior to autoclaving for 15 minutes at 121°C. After the Medium A+ had cooled to 55°C, filter sterilised $FeCl_2$ was added to a final concentration of 24 μM. Vitamin B_{12} was added to a final concentration of 4 μg/mL prior to inoculation. For solid media, a 2x Medium A+ solution and 3 % agar (Difco™ agar) were autoclaved separately and subsequently mixed, with vitamin B_{12} added prior to pouring agar into sterile Petri dishes.

Table 2-6: Medium A+ Media Recipe.

Chemical	Quantity (per L)
NaCl	18 g
MgSO4.7H2O	5 g
100* A+ Solution	10 mL
Tris (125 g/L), pH = 8	8.3 mL
Trace Elements Solution	1 mL

Table 2-7: Medium A+ Trace Elements Solution

Chemical	Mass (g/L)
H_3BO_3	2.86
$MnCl_2.4H_2O$	1.81
$ZnSO_4.2H_2O$	0.222
MoO_3 (85%)	0.03
$CuSO_4.5H_2O$	0.079
$CoCl_2.6H_2O$	0.0403

2.1.4 General Chemicals

Unless otherwise stated, all chemicals were purchased from Sigma-Aldrich.

2.2 Biological Manipulation

2.2.1 Bacterial Strains and Plasmids.

All strains and plasmids used in this study are shown in Table 2-8. Primers used for plasmid construction and strain screening are displayed in **Appendices**, Table S1.

Table 2-8: Strain and Plasmid Table

Name	Relevant Genotype	Source
E. coli		
DH5α	F– Φ80*lac*ZΔM15 Δ(*lac*ZYA-*arg*F) U169 *rec*A1 *end*A1 *hsdR*17 (rK–, mK+) *pho*A *sup*E44 λ– *thi*-	CRG Culture Collection

	1gyrA96 relA1	
C2987	*fhu*A2 D(*argF-lacZ*) U169 *pho*A *gln*V44 f80D(*lacZ*)M15 *gyrA*96 *rec*A1 *rel*A1 *end*A1 *thi*-1 *hsdR*17	NEB, Ipswitch, USA
***Synechocystis* sp. PCC 6803 (Glucose Tolerant)**		
wt	wt	Teruo Ogawa
Δ *hox*	*hox::hph*	Teruo Ogawa
Δ *hoxYH*	*hoxYH::KanR2*	(Eckert et al., 2012)
Δ hoxE	*hoxE::aac3ia*	(Eckert et al., 2012)
Δ hoxW	*hoxW::SpecR*	Jens Appel (unpublished)
Δ howW hoxFGFP	*hoxW::SpecR ,hoxFC_egfp-aac(3)IV*	This study
Δ hoxYH hoxFGFP	*hoxYH::KanR2, hoxFC_egfp-acc(3)IV*	(Burroughs et al., 2014)
Δ ndhD1/ndhD2	*ndhD1::KanR, ndhD2::CmR*	(Ohkawa, Dean Price, et al., 2000)
hoxFGFP	*hoxFC_egfp-acc(3)IV*	(Burroughs et al., 2014)
ndhMYFP	*ndhMC_eyfp-aadA*	this study
hoxFGFP/ndhMYFP	*hoxFC_egfp-aac(3)IV, ndhMC_eyfp-aadA*	this study
hoxEGFP	*hoxEC_egfp-aadA*	this study
HoxYGFP	*hoxYC_GFP-acc(3)IV*	this study
Synechococcys sp. PCC 7002		
wt	*wt*	Pasteur Cyanobacterial Culture Collection
hoxFGFP	*hoxFC_egfp-acc(3)IV*	this study
ndhMYFP	*ndhMC_eyfp-aadA*	this study
hoxFGFP/ ndhMYFP	*hoxFC_egfp -acc(3)IV, ndhMC_eyfp-aadA*	this study
Plasmids		
pGEM T-Easy	*f1, lacZa, bla, KanR,*	Promega
pIJ778	*P1-FRT-oriT-aadA-FRT-P2*	(Gust et al., 2003)
pIJ786	*egfp-P1-FRT-oriT-aac(3)IV-FRT-P2*	(Gust et al., 2004)
pIJ778-eYFP	*eyfp-P1-FRT-oriT-aadA-FRT-P2*	This study

2.3 DNA Manipulation Procedures

2.3.1 Chromosomal DNA Extraction

Genomic DNA was isolated from *Synechocystis* sp. PCC 6803 and PCC 7002 using the Zymogen Quick-gDNA™ MiniPrep kit as per manufacturer's guidelines. Bead milling was carried out for 5 minutes.

2.3.2 Plasmid DNA Extraction from *E. coli*

Plasmid DNA was extracted from *E. coli* by the QIagen Spin MiniPrep kit with minor modifications, as follows: 10 mL of overnight cultures were used instead of 5 mL, a 5 minute incubation on ice was carried out between neutralisation of the alkaline lysis and centrifugation (in order to facilitate pelleting of cell debris), the optional PB buffer wash step was always carried out and an empty column spin was performed after washing with the PE buffer, to remove excess ethanol.

2.3.3 In-vitro DNA Amplification

All polymerase chain reactions (PCRs) were carried out in 0.2 mL flat cap PCR Sapphire tubes using an Eppendorf Mastercycler Nexus X2 thermal cycler. PCRs were analysed at their end point by agarose gel electrophoresis.

2.3.3.1 Primer design for Fluorescent Protein Tagging of Target Genes

Individual subunits of complexes were tagged with fluorescent proteins in order to visualise the entire complex. Sequences were obtained from Cyano Base (http://genome.microbedb.jp/cyanobase) and cross-referenced with the NCBI database. Primers for HiFi cloning were designed with 25 bp overhangs, using the NEBuilder® website (https://nebuilder.neb.com/) and fragments assembled to generate a suicide vector, as per manufacturer's protocols (NEB).

For C-terminal tagging of selected subunits, primers were designed to amplify the open reading frame plus 1 kb of upstream sequence, excluding the stop codon. Primers were designed to amplify the fluorescent proteins with linkers and the antibiotic resistance cassette from standard vectors (pIJ778-yfp or pIJ786 for GFP). Primers were designed to amplify 1 kb

downstream of the open reading frame to be tagged with fluorescent proteins.

2.3.3.2 Primer design for Gene Deletions

In order to create in-frame gene deletions, suicide vectors were assembled using primers designed to amplify 1 kb up- and downstream of the target gene, including both the start codon and stop codons, respectively. Primers were designed to amplify the spectinomycin resistance cassette from pIJ778 (Gust et al., 2003), with overhangs complementary to the up- and downstream target regions, to replace the open reading frame. HiFi assembly of amplified fragments used as a backbone the pGEM (Promega) vector, linearized by SacI and PstI restriction digestion.

2.3.3.3 High Fidelity PCR Amplification for Cloning

PCR amplification was performed using the NEB® Q5® 2X Master Mix in 50 µL reactions, as described in Table 2-9. The thermal cycling conditions are displayed in Table 2-10. After thermal cycling was completed, 8 µL of 6× NEB® purple loading buffer were added to PCR amplicons, for subsequent analysis by agarose gel electrophoresis.

Table 2-9: High-Fidelity PCR Constituents

Solution	Quantity
2× Q5 Master Mix	25 µL
Forward/Reverse Primer (10 µM)	1 µL
Template DNA	~ 5 ng
Nuclease Free water	top up to 50 µL
Reaction Final Volume	**50 µL**

Table 2-10: Thermal Cycling Conditions for High-Fidelity PCRs

Step	Temperature		Duration
Initial Denaturation		98°C	2 mins
10 cycles	Denaturation	98°C	30 sec
	Annealing	60°C	30 sec
	Elongation	72°C	30 sec/kb
15 cycles	Denaturation	98°C	30 sec
	Annealing	65°C	30 sec
	Elongation	72°C	30 sec/kb
Final Extension		72°C	10 mins
Soak	Holding temperature	10°C	∞

2.3.3.4 Screening Transformants by Colony PCR

Colony PCR was used to screen transformants from successful cloning, transformations or integrations, employing Promega GoTaq® 2× Master Mix, in 15 μL reactions. *E. coli* or cyanobacterial transformants were screened by suspending a single colony, isolated with a sterile toothpick, in 10 μL of nuclease free water in a 0.2 mL PCR tube and incubating in a thermal cycler at 99 °C for 10 minutes. Following this incubation, colonies were spun down to pellet cell debris. An aliquot of 2 μL of boilate was then added to a pre-made master mix containing Promega GoTaq® 2× Master and appropriate primers (Table 2-11). For large numbers of colony PCRs, a volume of master mix was generated by proportionately increasing the volume according to the number of samples, adding 2 extra reactions to account for pipetting errors and subsequently dividing into 13 μL aliquots. Thermal cycling conditions are indicated in Table 2-12.

Table 2-11: Screening PCR Constituents.

Solution	Quantity
2× GoTaq Master Mix	7.5 µL
Forward/Reverse Primer (10 µM)	1 µL
Template DNA	2 µL
Nuclease Free water	4.5 µL
Reaction Final Volume	**15 µL**

Table 2-12: Screening PCR Thermal Cycling Conditions.

Step	Temperature		Duration
Initial Denaturation		94°C	2 mins
10 cycles	Denaturation	94°C	30 sec
	Annealing	50°C	30 sec
	Elongation	72°C	30 sec/kb
15 cycles	Denaturation	95°C	30 sec
	Annealing	55°C	30 sec
	Elongation	72°C	30 sec/kb
Soak	Holding temperature	10°C	∞

2.3.3.5 Restriction Endonuclease Digestion of Plasmid and PCR Amplicon DNA

All restriction enzymes used were FastDigest® from Thermo-Fisher Scientific®. All reactions were carried out in Sapphire 0.2 mL flat cap PCR tubes in a final volume of 10 µL (Table 2-13) and incubated in a water bath for 1 hour. Reactions were analysed by agarose gel electrophoresis.

Table 2-13: Restriction Endonuclease Reaction Constituents.

Solution	Quantity
Green 10× Buffer	1 µL
DNA	1 µg
Restriction Enzyme A	1 µL
Restriction Enzyme B (if required)	1 µL

Nuclease Free Water	Variable
Reaction Volume	**10 µL**

2.3.3.6 DNA Analysis by Agarose Gel Electrophoresis

Agarose gels were prepared by melting 1 % (wt/vol) of technical grade agarose in 1 × TAE buffer (40 mM Tris base, 0.1 % (vol/vol) glacial acetic acid and 1 mM EDTA) on medium heat for approximately 10 minutes. For DNA visualization, Sybr Safe DNA (Invitrogen) was added to a final concentration of 0.01 % (vol/vol) and the agarose was set in a caster (BioRad). Samples were loaded and the gel was run in 1× TAE buffer at 110 V for 30 minutes. Gels were visualized in an UV transilluminator (G:Box XRQ gel doc system), with amplicon sizes determined by comparing to NEB® 2-log ladder.

2.3.3.7 DNA Purification from Agarose Gels

DNA bands of appropriate size were excised from agarose gels using a scalpel, on a UV transilluminator (Syngene). The excised band was placed in a 1.5 mL Eppendorf® microcentrifuge tube and the QIAquick® Gel Extraction kit was used to extract DNA, with minor modifications to the protocol. Briefly, 400 µL of QG buffer were added to the excised band and incubated at 55 ºC until complete dissolution of the agarose. 200 µL of propan-2-ol were added to the dissolved agarose solution and the tube was inverted several times before being applied to the column. The column was washed three times with 500 µL of PE buffer and DNA was eluted in 13 µL of nuclease free water, pre-heated to 55 ºC.

2.3.3.8 DNA Quantification

DNA quantification was carried out using a BioMate™ 3S spectrophotometer (ThermoFisher Scientific). Blanking was established by using 1 µL of the same nuclease free water used in the elution step, by measuring OD_{260} and OD_{280}. Each sample was loaded and quantified, with the quality control measure that 260 nm:280 nm ratios should be ~1.8, as an indication of purity for the eluted DNA (Sambrook et al., 1989).

2.3.3.9 DNA Ligation

2.3.3.9.1 Cut and Paste Cloning

Two DNA fragments were ligated at the 5'-phosphate and the 3'-hydroxyl group of the insert with NEB®T4 Ligase, via complementary ssDNA overhangs. Ratios of the insert:vector ratio were set to 2:1 as stated in

Table 2-14, with ratio calculations carried out in accordance with (Engler & Richardson, 1982), as shown in Equation 6. All ligations were transformed into prepared chemically competent *E. coli* DH5α cells, by transferring 5 µL of the ligation mixture into an aliquot of 50 µL of competent cells.

$$\frac{(\text{ng Vector} \times \text{Insert size (kb)})}{\text{Vector size}} \times \text{Molar Ratio} \left(\frac{\text{Insert}}{\text{Vector}}\right)$$

Equation 6

Table 2-14: Cut and Paste Cloning Ligation Reaction Constituents.

Solution	Quantity
Vector DNA	50 ng
Insert DNA	variable
10× T4 DNA Ligase Buffer	1 µL
T4 DNA Ligase	1 µL
Nuclease Free Water	Top to 10
Reaction Volume	**10 µL**

2.3.3.9.2 HiFi Assembly of DNA Fragments

The HiFi assembly strategy was used to generate plasmids for protein tagging with FPs as well as deletion vectors. Amplicons and linearized vectors were incubated with NEBuilder® HiFi DNA Assembly Master Mix, with ratios of insert: vector set to 2:1 as described in 2.3.6.1, and incubated at 50 °C for 1 hour (reaction components shown in Table 2-15). All HiFi assembly reactions were transformed into NEB® 5-α competent cells

(C2987), using 5 µL of the assembly mix per transformation and following the manufacturer's guidelines.

Table 2-15: HiFi Assembly Reaction Constituents.

Solution	Quantity
Vector DNA	50 ng
Insert DNA 1	variable
Insert DNA 2	variable
Insert DNA 3	variable
2× HiFi Assembly Master Mix	1 µL
Nuclease Free Water	variable
Reaction Volume	**10-20 µL**

2.4 Transferring DNA into Bacterial Strains

2.4.1 Preparation of Chemically Competent Escherichia coli DH5α

E. coli DH5α cryostocks were streaked onto non-selective LB agar and incubated at 37 ^{o}C overnight. A single colony was used to inoculate 10 mL of SOB (Hanahan's Broth, Sigma-Aldrich) and was grown overnight at 37 ^{o}C shaking at 200 rpm.

An aliquot of the overnight culture was used to inoculate 500 mL of SOB to an OD_{600} of 0.1. The 500 mL culture was grown at 30 ^{o}C, with shaking at 200 rpm, to an OD_{600} of 0.35-0.45, at which stage cells were aliquoted into 50 mL Falcon tubes and incubated on ice for 30 minutes.

Cells were harvested by centrifugation at 6,000 rpm in a pre-chilled centrifuge (at 4 ^{o}C) for 5 minutes. The supernatant was decanted and the pellets combined by resuspending in 20 mL of an ice-cold 100 mM $MgCl_2$ solution. Cells were harvested by centrifugation as described above.

The 100 mM $MgCl_2$ solution was decanted and the pellet was resuspended in an ice-cold 100 mM $CaCl_2$ solution and the cell suspension was incubated on ice for a further 30 minutes. Cells were harvested by centrifugation as previously described and the supernatant decanted. The

cell pellet was resuspended in 20 mL ice-cold 85 mM $CaCl_2$ 15% (vol/vol) glycerol. Cells were harvested by centrifugation as previously described and re-suspended in 2 mL of an ice-cold 85 mM $CaCl_2$, 15% (vol/vol) glycerol solution and separated into aliquots of 50 μL in pre-chilled 1.5 mL Eppendorf's. For long-term storage, cells were snap-frozen in liquid nitrogen and stored at -80°C (Sambrook et al., 1989).

For transformation of chemically competent *E. coli* DH5α, plasmids or ligation reactions were incubated with 50 μL of cells on ice for 30 minutes. Cells were heat shocked at 42 °C in a water bath for 1 minute and returned to ice for 2 minutes. Recovery was carried out by adding 950 μL of LB media and incubating for 1.5 hours at 37 °C shaking at 200 rpm. An aliquot of 50 μL was plated on LB agar containing appropriate antibiotics before concentrating the remaining cells by centrifugation (1 minute, 3 000 g, room temperature), decanting 900 μL of supernatant and plating the re-suspended cells on LB agar containing appropriate antibiotics.

2.4.2 Preparation of Cyanobacterial Competent Cells

The preparation of naturally competent cyanobacterial cells was based on (Williams, 1988). 50 mL cultures were grown to stationary phase at a light intensity of 20 μE m^{-2} s^{-1}. Cells were washed twice in BG11 and resuspended in 1 mL of BG11 supplemented with 10 mM $NaHCO_3$. In the case of *Synechococcus* sp. PCC 7002, BG11 was also supplemented with 0.4 μg/mL of vitamin B_{12}.

Suicide vectors were constructed in *E. coli* as described in the previous sections. To each plasmid (5 μg) 150 μL of cells were added, cells and plasmid were thoroughly mixed by pipetting several times and cells were grown at 200 μE m^{-2} s^{-1} for 5 hours in continuous light and plated on BG11 plates. Plates were incubated at 30 °C, at a light intensity of 20 μE m^{-2} s^{-1}, for 24 hours.

Antibiotic was applied after 24 hours, by pipetting 1 mL of the appropriate antibiotic at the concentration displayed in Table 2-1 under the agar in each plate. Plates were incubated at 30 °C under continuous 20 μE

m^{-2} s^{-1} light, for approximately 3 weeks. Colonies were picked and patched on BG11 agar (0.75% wt/vol) containing the appropriate antibiotic and supplemented with 10 mM $NaHCO_3$. Clones were patched twice and potential mutants were screened by colony PCR.

2.5 Cyanobacterial Pigment Composition

2.5.1 Scanning Whole Cell Absorption Spectra

At each time point, the pigment content of the cyanobacterial strains were assessed by whole cell absorption. The samples were standardised to OD_{750} = 0.2 and the whole cell absorption spectra was measured. The data was standardised to the absorption at 750 nm, averaged and plotted using the Prism (version 8, GraphPad) software. The variance of the spectrum was analysed by calculating the phycocyanin:chlorophyll *a* ratios, as displayed in Equation 7..

$$\text{Phycocyanin: Chlorophyll } a = \frac{\text{Absorbance 631 nm}}{\text{Absorbance 682 nm}}$$

Equation 7

2.5.2 Quantification of Chlorophyll *a* Concentration

Chlorophyll *a* concentrations were determined by extraction of chlorophyll *a* from 1 mL of cell cultures, pelleted and re-suspended in 1 mL of methanol. Cell suspensions were incubated at 60 ^oC for 5 minutes and cell debris was removed by centrifugation prior to transferring the methanol extract to a 1 mL cuvette. The absorbance of the solution was measured at a wavelength 665 nm and chlorophyll *a* concentration was determined by (OD_{665}- OD_{750}) * 13.9 (Mackinney, 1941).

2.6 Oxygen Evolution Rate

Photoinhibition curves were carried out based on a previously published method (Mannan & Pakrasi, 1993), with the adaptation of increasing light intensity from 0-450 μE. The Chlorolab 2+ system (Hansatech) was used to measure dissolved oxygen. The instrument was calibrated before every use using air-saturated (using vigorous bubbling) cyanobacterial growth media,

pre-warmed at 30 ^{o}C, in order to establish the oxygen saturation current. Sodium dithionite was added to establish the base current for no dissolved oxygen, with currents measured for a minimum of 5 minutes for each calibration.

Cells from exponentially-grown liquid cultures (OD_{750} between 0.4 and 0.6) were harvested by centrifugation at 6,000 rpm for 5 minutes at room temperature. Pellets were re-suspended in fresh medium supplemented with 10 mM $NaHCO_3$, to a chlorophyll *a* concentration of 5 μg/mL. Standardized cultures were dark-adapted for 5 minutes prior to recording of respiration measurements and the light intensity was increased every 5 minutes.

Oxygen evolution rates were determined by calculating the slope of the curve in the linear range. All measurements were carried out in triplicate and the means of measurements from 3 independent cultures calculated using Prism (version 8, graph pad).

2.7 Hydrogen Measurements

Hydrogenase activity measurements were carried out using Oxygraph+ system (Hansatech). The polarity of the electrode disc was reversed by submerging the Ag/ Pt components in H_2SO_4 and passing a current through the electrode until the Ag component becomes light brown in colour.

For calibration of the instrument, H_2 gas was bubbled through BG11 at 28^{o}C for 10 mins, with H_2 concentration is 74 nM at these conditions. The chamber was maintained at 28^{o}C with 950 µL of BG11, 50 µL of H_2 saturated BG11 was added.

The maximum H_2 evolution measurements were taken by adding 850 µL of exponentially grown cells standardized to OD_{750} = 0.5. 50 µL of 20 mM methylviologen followed by 100 µL of 20 mM sodium dithionite in order to remove oxygen and directly reduce the HoxYH subunits. The slope of the line was used to calculate the maximum hydrogenase activity.

2.8 Microscopy Techniques

2.8.1 Sample Preparation

Cyanobacterial cultures were grown at varying light intensities and culturing media, with agitation at 150 rpm. A 10 μL aliquot of each culture was spotted onto BG11 agar, smeared into a patch of approximately 0.5 cm^2 and left to dry. Agar cubes of approximately 1 cm^2 were cut and placed on a 35 mm glass bottom dish (MatTek Life Sciences).

2.8.1.1 Photoautotrophic Growth of PCC 6803

For photoautotrophic growth, PCC 6803 strains on plate was inoculated in 5 mL of BG11 and grown at a light intensity of 20 μE m^{-2} s^{-1}. Sub culturing was carried out at the light intensity of each experimental condition investigated. Anoxic conditions were achieved by adding 2 mM sodium dithionite.

2.8.1.2 Mixotrophic Growth of PCC 6803

For mixotrophic growth, PCC 6803 strains on plate was inoculated in 5 mL of BG11 supplemented with 10 mM of glucose and grown at a light intensity of 20 μE m^{-2} s^{-1}. Sub culturing was carried out at the light intensity of the experiment investigated. Anoxic conditions were achieved by adding 2 mM sodium dithionite.

2.8.1.3 Mixotrophic Nitrate Limiting Growth of PCC 6803

For mixotrophic nitrate limited growth, PCC 6803 strains on plate was inoculated in 5 mL of $BG11_0$ supplemented with 10 mM of glucose and 5 mM arginine, grown at a light intensity of 20 μE m^{-2} s^{-1}. Sub culturing was carried out at the light intensity of the experiment investigated. Anoxic conditions were achieved by adding 2 mM sodium dithionite.

2.8.1.4 Photoautotrophic Growth of 7002

PCC 7002 was inoculated in 5 mL of medium A+ supplemented with 0.4 μg/mL vitamin B_{12} and grown at 50 μE m^{-2} s^{-1}. For dark adapted anoxic conditions, cultures were washed twice in medium A+ lacking nitrate (supplemented with 0.4 μg/mL vitamin B_{12}) and resuspended to an OD_{750} of 0.7 as described in (McNeely et al., 2010). Anoxic conditions were achieved by adding 2 mM sodium dithionite.

2.8.1.5 Mixotrophic Growth of 7002

PCC 7002 was inoculated in 5 mL of medium A+ supplemented with 0.4 μg/mL vitamin B_{12} and 0.1% glycerol (vol/vol) and grown at 50 μE m^{-2} s^{-1}. For dark anoxic conditions, cultures were washed twice in medium A+ lacking nitrate, supplemented with 0.4 μg/mL vitamin B_{12} and 0.1% glycerol (vol/vol) and resuspended to an OD_{750} of 0.7 as described in (McNeely et al., 2010). Anoxic conditions were achieved by adding 2 mM sodium dithionite.

2.8.1.6 High light treatment of *Synechococcus* sp. 7002

Cells were adapted to dark anoxic conditions for 30 mins as described above, prior to spotting 10 μL on a medium A+ plate. The plate was dried while at a light intensity of 600 μE m^{-2} s^{-1}. For treatment with DCMU, 20 μM of DCMU was added prior to dark adaptation. For treatment with DBMIB, 5 μM of DBMIB was added prior to dark adaptation (Burroughs et al., 2014). For growth on urea, medium A+ was modified by replacing nitrate with 10 mM urea (Ludwig & Bryant, 2012a).

2.8.2 Scanning Conditions

Cells were imaged using ZEISS Elyra 7 using a 63× water immersion objective lens, measuring chlorophyll *a* fluorescence by exciting at 633 nm and recording the emission spectra between 695nm-720 nm. Wavelengths for GFP and YFP excitation were 488 nm and 514 nm and fluorescence spectra were measured between 498-517 and 525-544 nm, respectively. An initial pre-bleached image was captured followed by image bleaching by exposing samples to full power 488 nm for 10 seconds and capturing a bleached image.

2.8.3 Image Processing and Analysis

Images were processed using the Fiji software. The wild type images were tabulated first, to establish the background fluorescence and set the thresholds for colocalization. The image channels were split; the post-bleached fluorescent protein images were subtracted from the pre-bleached image in order to generate a composite image. The contrast settings in the fluorescent protein channels were set to optimise visualisation and the contrast settings were applied to all other images for that channel.

In PCC 6803 images, colocalization was quantified by assessing the fluorescence intensity of each pixel relative to the individual channels, using the co-localisation function in Fiji. In order to express the degrees of colocalization, Manders coefficients were used which expresses the percentage of pixels in each channel that have values above the set threshold (5,000) in the same pixel.

For PCC 7002 images, tabulated images were assessed for the formation of puncta. A mask with a threshold of 5,000 (au) was applied to each image in order to highlight specific regions of higher fluorescence. Puncta were determined by areas of 5x5 pixels above the threshold intensity. Colocalization was determined by overlap of the puncta in the fluorescent channels. Data was analysed by non-parametric testing (Mann-Whitney U test) using SPSS (IBM).

2.9 Metabolomics

2.9.1 Growth Conditions

Cultures were grown photoautotrophically at 30 ^{o}C, 150 rpm and under a continuous light intensity of 60 μE m^{-2} s^{-1}. For assessing metabolome changes in response to dark adaptation, 20 mL of culture were aliquoted into a 50 mL Falcon tube and stored in the dark at 30 ^{o}C for 3 days. To study the dark to high light response, 20 mL of culture were concentrated by centrifugation and re-suspended in fresh BG11 media to an OD_{750} of 1.5. Dark adaptation was carried out for 3 days, followed by exposure to a light intensity of 600 μE m^{-2} s^{-1} for 5 minutes. All handling of dark-adapted cultures was carried out in a dark room under green light and extraction was carried out immediately after the respective treatments.

2.9.2 Metabolite Extraction

For metabolic quenching, cells were harvested by centrifugation at 6,000 rpm for 5 minutes at 4^{o}C and 500 μL of pre-cooled -80 ^{o}C absolute methanol (HPLC Grade, Sigma) was used to resuspend the pellet. Metabolites were extracted from pellets using a biphasic extraction protocol (Prasannan et al., 2018), with chloroform as the non-polar solvent at a 1:1

MeOH:CHL ratio. Extractions were incubated at room temperature with shaking (120 rpm) for 1 hour.

The polar and non-polar phases were separated by centrifugation at 14,000 rpm at 4^{o}C for 30 minutes and each phase was evaporated in separate vials overnight at room temperature. Samples were stored at -80 ^{o}C and metabolites were reconstituted in 100 μL 1:1 MeOH:dH_2O prior to LC-MS analysis.

2.9.3 LC-MS Running Method

Chromatography was performed using a Dionex U3000 UHPLC system (Thermo Fisher Scientific, Hemel Hempstead, UK) with a ZICpHILIC column (4.6 × 150 mm, 5μm particle size, Merck Sequant, Watford, U.K.). The column was maintained at 45^{o}C with a flow rate of 300 μL/min. A quality control (QC) sample was generated by pooling all samples to be analysed. At the beginning of the run, the QC was injected 6 times at the beginning of the analysis to equilibrate the column to the samples. Samples (n=6 for each condition) were randomized in the sequence for untargeted metabolomic analysis.

The mobile phase was composed of solution A (20 mM ammonium carbonate) and B) acetonitrile. A gradient of 20% solution A was increased to 95% over 8 minutes with the composition returning to 20% solution A over 2 minutes. The column was left to re-equilibrate at 400 μL/min for 4 minutes. The flow rate was then reduced to 300 μL/min for 1 min, with the entire run being 15 minutes per sample.

Samples were maintained at 4^{o}C during the analysis with a 5 μL injection per sample being introduced to the column. An orbital trap mass spectrometer (QExactive-Orbitrap, Thermo Fisher Scientific, Hemel Hempstead, UK) was used to identify m/z using electrospray ionization (ESI) + and ESI – modes for full LC-MS profiling. Data was generated dependent on MS/MS (ddMS/MS) accurate mass spectra for identification, with the top 5 hits for each spectrum being used.

The ESI+ parameters were; spray voltage 4.5 kV and capillary voltage was 20 V. The ESI- parameters were; spray voltage of -3.5 kV and a capillary voltage of -20 V. The sheath, auxiliary and sweep gas flow rates were; 40, 5 and 1 (au) respectively for both ESI modes. The capillary and heater temperatures were maintained at 275^{o}C and 150^{o}C respectively. Data acquisition was carried out in full scan mode with a resolution of 70,000 with a *m/z* range 70-1050. The top 5 ddMS/MS scans was performed on QC samples (n=3) with 17,500 resolution and stepped normalized collision energy of 10, 20 and 40.

2.9.4 Data Processing and Metabolite Identification

Data was exported and analysed using Compound Discoverer 3.1 SP1 (Thermo Fisher Scientific). Metabolite identification was based on the accurate mass and retention time of standards (268 standards co-analysed in the run, Table S2). Data was also cross referenced with mzCloud and mzVault for accurate mass and ddMS/MS. Accurate masses were further cross referenced with the metabolome of PCC 6803 in the Biocyc database.

The analytical performance of the LC-MS/MS run was assessed using pooled QC samples followed by unsupervised principal component analysis (PCA). PCA provides an unbiased overview of trends within the data acquired. For analysis of identified metabolites from each strain and condition, the metabolites were exported and normalized to OD_{750} for multivariant analysis (MVA) using Simca P+13 (Umetrics AB, Sweden). Each of the datasets were mean-centred and Pareto scaled. Orthogonal partial least squares discriminant analysis (OPLS-DA) was used to analyse the differences in metabolite profile between the strains and conditions investigated (Want et al., 2010).

The leave one out method (1 out of 6) was used to evaluate the robustness of the generated models by monitoring the fitness of the model (R^2Y) and predictability of the models (Q^2) (Eriksson et al., 2006). Values are displayed in Table S2. Individual metabolites of each data set were analysed for significance by variable importance in the projection (VIP) of the OPLS-DA models comparing 2 classes at a time. The VIP scores estimate the

importance of each metabolite in the projection used to form the OPLS-DA, with a score above 1 being considered to be significant in the model. Student *t*-tests were adjusted to reduce false discovery rates using the Benjamini-Hochberg approach for multiple testing problem were performed across all peaks intensities detected in the 2 classes. In order to statistically analyse the differences in metabolites between the classes, an adjusted *p*-value > 0.05 and VIP > 1 would be considered a significant change in metabolite abundance. The data was represented in a 2-fold log change table.

3 Distribution and Colocalisation of Hox and NDH-I in *Synechocystis* sp. PCC 6803

3.1 Introduction.

Cyanobacteria offer a truly sustainable route to H_2 production, with significant potential to revolutionise the H_2 economy once the 2 key bottlenecks are resolved - electron supply and oxygen tolerance of the hydrogenase (Hox) enzymes. To substantially increase H_2 yield in cyanobacteria we need to understand the fundamental role Hox plays in the cell and how it interacts with key members of the electron transport chain (ETC). This will be essential in allowing the rerouting of electrons to Hox.

Previous work carried out in PCC 6803 demonstrated that Hox forms two distinct populations associated with the thylakoid membrane; one population is uniformly distributed around the thylakoid and the other is localized in puncta, which is thought to correlate with hydrogenase activity (Burroughs et al., 2014; Cournac et al., 2004; Gutthann et al., 2007). These puncta do not respond directly to redox mediated signalling as evidenced by the localization pattern, which remained unchanged following addition of the photosynthetic electron transport inhibitors DCMU and DBMIB (Burroughs et al., 2014), suggesting that the main physiological control could be dissolved oxygen. It is also unclear how Hox directly or indirectly interacts with the electron transport chain at the thylakoid membrane including NDH-1, SDH, cytochrome b6f, the respiratory terminal oxidases, ferrodoxin and the ferredoxin-oxido-reductase (FNR).

Considering the interaction partners at the thylakoid membrane, NDH-1 was shown to be the major route for H_2 oxidation (Dutta & Vermaas, 2016). Sequence analysis of the genomic DNA from PCC 6803 demonstrated that NDH-1 has 11 subunits (Kaneko et al., 1996), but lacks a homologue of the N-module involved in the binding of NADH in *E. coli* (*nuoE-G*). It has been demonstrated through bioinformatics analysis that HoxE, HoxF and HoxU share homology with the NuoE, NuoF and NuoG subunits respectively (Appel & Schulz, 1996), with the Hox diaphorase subunits providing the missing domains from the cyanobacterial NDH-1 complex. However, diaphorase

subunit mutants had no observable differences in respiration rates (Boison et al., 1998) suggesting that Hox does not mediate electron transport to NDH-1.

Structural studies have recently demonstrated that ferredoxin 1 can doc directly with NDH-1 (C. Zhang et al., 2020) indicating that Hox is not essential for mediating cyclic electron flow (CEF). The potential interaction between Hox and NDH-1 has not been investigated *in-vivo*, however previous studies have demonstrated that photoH_2 production and fermentative H_2 production in PCC 6803 are directly coupled via ferredoxin/flavodoxin to PSI and PFOR (pyruvate:flavodoxin/ferredoxin oxidoreductase) (Gutekunst et al., 2014). However, there is still some speculation that NDH-1 may also act as an electron donor for Hox, given NDH-1 couples the electron transport from ferredoxin (Fd) to the plastoquinone pool (PQ) (Pan et al., 2020).

In **Chapter 3**, the question of whether Hox directly interacts with NDH-1 under conditions that support H_2 evolution will be addressed. In order to fully investigate this interaction, varying conditions were used with cultivations carried out in photoautotrophic, mixotrophic and mixotrophic nitrate limiting conditions. Guterkunst *et al*., (personal communication) have shown that mixotrophic growth coupled with arginine addition (removing the nitrate electron sink) significantly increased H_2 evolution under anoxic conditions. Furthermore, Hox was found to be essential under these conditions.

3.2 Generating PCC 6803 Hox and NDH-1 Fluorescent Protein Tagged Strains.

Previous research had demonstrated that a GFP fusion to the C-terminus of HoxF did not impact on Hox function in the cell, e.g. H_2 evolution and complex assembly (Burroughs et al., 2014). The PCC 6803 *hoxFGFP* strain was recreated utilising recombineering and transformed into PCC 6803, strains were then screened via colony PCR (**Error! Reference source not found.**).

Localization of the NDH-1 complex in PCC 7942 was previously achieved through the utilization of a GFP tag to the C-terminus of NdhM (L. N. Liu et al., 2012). YFP was fused to the C-terminus of the NdhM homologue (*slr1623*) in PCC 6803. Strains were screened by PCR in order to test for integration and segregation. The *hoxFGFP* construct was then transformed into the *ndhMYFP* background to generate the double mutant strain. Both the individual *hoxFGFP* and *ndhMYFP* strains and the double mutant were shown to be fully segregated (**Error! Reference source not found.**).

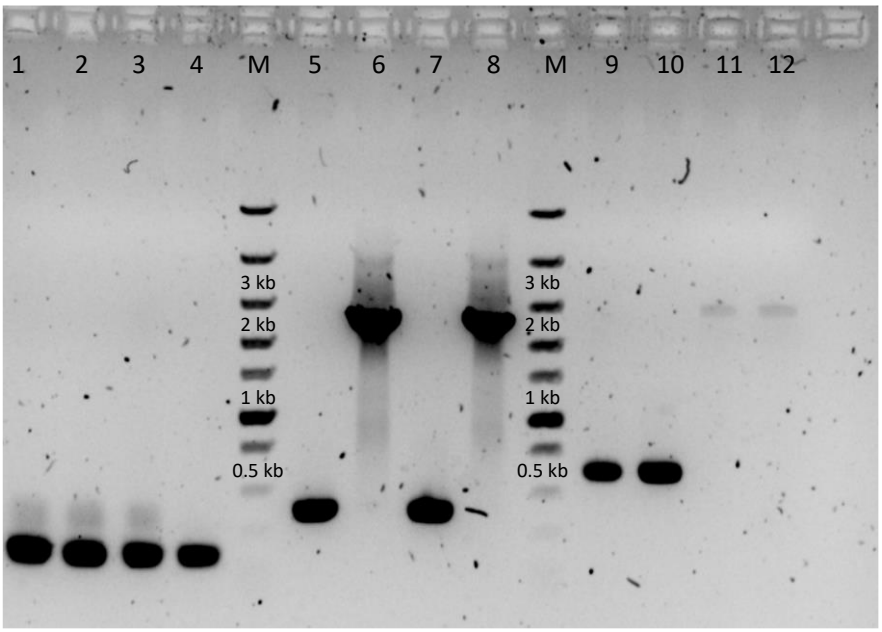

Figure 3-1: PCR Screen of PCC 6803 Strains.
Agarose gel results of the PCR screen of PCC 6803 strains. Lanes 1-4 are various templates amplified using the 6803PsaFSC. DNA template used; 1 – PCC 6803 WT, 2 – PCC 6803 *hoxFGFP*, 3 – PCC 6803 *ndhMYFP* and 4 – PCC 6803 *hoxFGFP ndhMYFP*. Lanes 5-8 are various templates amplified using the 6803HoxFSC. DNA template used; 5 – PCC 6803 WT, 6 – PCC 6803 *hoxFGFP*, 7 – PCC 6803 *ndhMYFP* and 8 – PCC 6803 *hoxFGFP ndhMYFP*. Lanes 9-12 are various templates amplified using the 6803NdhMSC. DNA template used; 9 – PCC 6803

3.3 Microscopy Growth Conditions

In order to verify previous observations and establish a base line for Hox localization in PCC 6803, the cells were initially grown photoautotrophically in BG11 media (Burroughs et al., 2014). Localization of the NDH-1 complex has never been assessed in PCC 6803. The distribution of both Hox and the NDH-1 complex were assessed under photoautotrophic growth using a range of light intensities (20, 60 and 200 $\mu E\ m^{-2}\ s^{-1}$). Following photoautotrophic growth, cells were subject to anoxic dark adaptation to assess the impact on localization of the complexes under conditions which promote H_2 evolution.

Mixotrophic growth has been shown to significantly increase H_2 evolution under anoxic conditions (Appel et al., 2020). Given the increased H_2 evolution the distribution of both Hox and NDH-1 was assessed under these conditions.

It has been previously demonstrated through targeted genetic engineering and media supplementation that removing nitrate from the cell

can improve yields of H_2 (Baebprasert et al., 2011; Gutthann et al., 2007). Hox is essential in PCC 6803 under mixotrophic nitrate limiting growth conditions (Gutekunst et al., 2014) with a significant amount of H_2 being produced under these conditions when anoxia is achieved (Gutekunst, unpublished).

Therefore, all of the above conditions are associated with H_2 evolution and establishing key interactions between NDH1 and Hox under these conditions will enable a better understanding of how Hox functions within the ETC.

3.4 Distribution of Hox and NDH-1 Folowing Photoautotrophic Growth at 20 μE.

3.4.1 Photoautotrophic Growth at 20 μE m^{-2} s^{-1}

For low light growth, cultures were grown at 20 μE m^{-2} s^{-1} in accordance with previous Hox studies in PCC 6803 (Appel et al., 2000). Wild type PCC 6803 was utilised as a control for background chlorophyll fluorescence. There was no significant autofluorescence detected in the PCC 6803 (Figure 3-2).

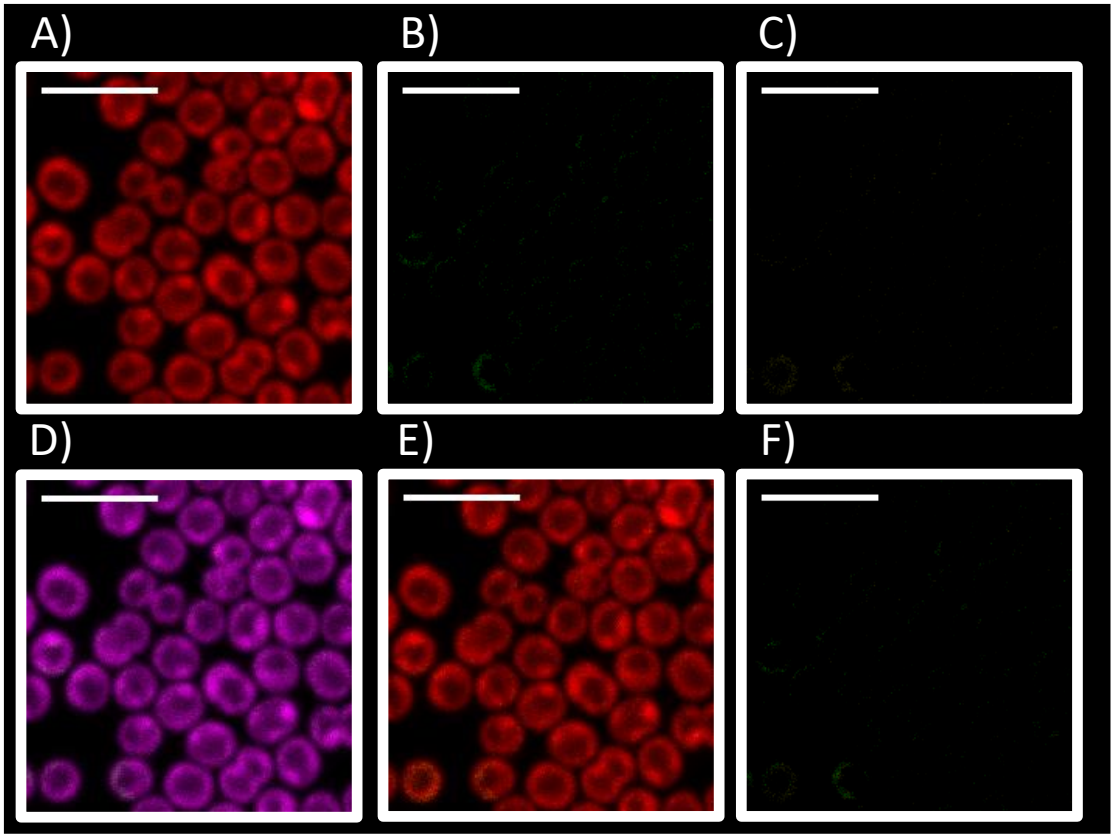

Figure 3-2: Photoautotrophically Grown PCC 6803 WT at 20 μE.
A) Chlorophyll *a* channel. B) GFP channel. C) YFP channel. D) chlorophyll *a* (magenta) and GFP channels merged. E) Chlorophyll *a* and YFP (Cyan) channels merged. F) GFP and YFP (magenta) channels merged. The scale bar represents 5 μm.

Under photoautotrophic growth at 20 μE m^{-2} s^{-1}, 2 populations of Hox were observed; dispersed and puncta, both associated with the thylakoid, similar to those seen in previous studies (Burroughs et al., 2014). NDH-1 was localized to the thylakoid similar to the distribution seen in PCC 7942 (L. N. Liu et al., 2012). The population was either dispersed or localised in puncta at the thylakoid. In the *hoxFGFP ndhMYFP* strain there appeared to be populations of the Hox puncta which were not colocalized with the NDH-1 puncta (Figure 3-3 B-F green arrow) and vice versa (Figure 3-3**Error! Reference source not found.** B-F magenta arrow). There was also a population of Hox and NDH-1 puncta which were colocalized (Figure 3-3 B-F white arrow). The dispersed populations of Hox and NDH-1 also showed a degree of colocalization. Together this is the first time that Hox and NDH-1 has been shown to interact together *in-vivo*. There was no significant difference between the distribution of Hox and NDH-1 in the individually tagged strains vs the *hoxFGFP ndhMYFP* strain (data not shown).

Manders coefficients (M) show the proportion of pixels that were colocalized in each of the channels. Hox colocalized with the chlorophyll *a* fluorescence under photoautotrophic growth at 20 μE m^{-2} s^{-1} (M=0.7762), which agrees with previous observations in PCC 6803 (Burroughs et al., 2014). NDH-1 colocalized to the chlorophyll *a* fluorescence (M=0.7721) which agrees with observations in PCC 7942 (L. N. Liu et al., 2012). Together this shows that Hox and NDH-1 are localized to the thylakoid. Hox and NDH-1 showed colocalization (M=0.407).

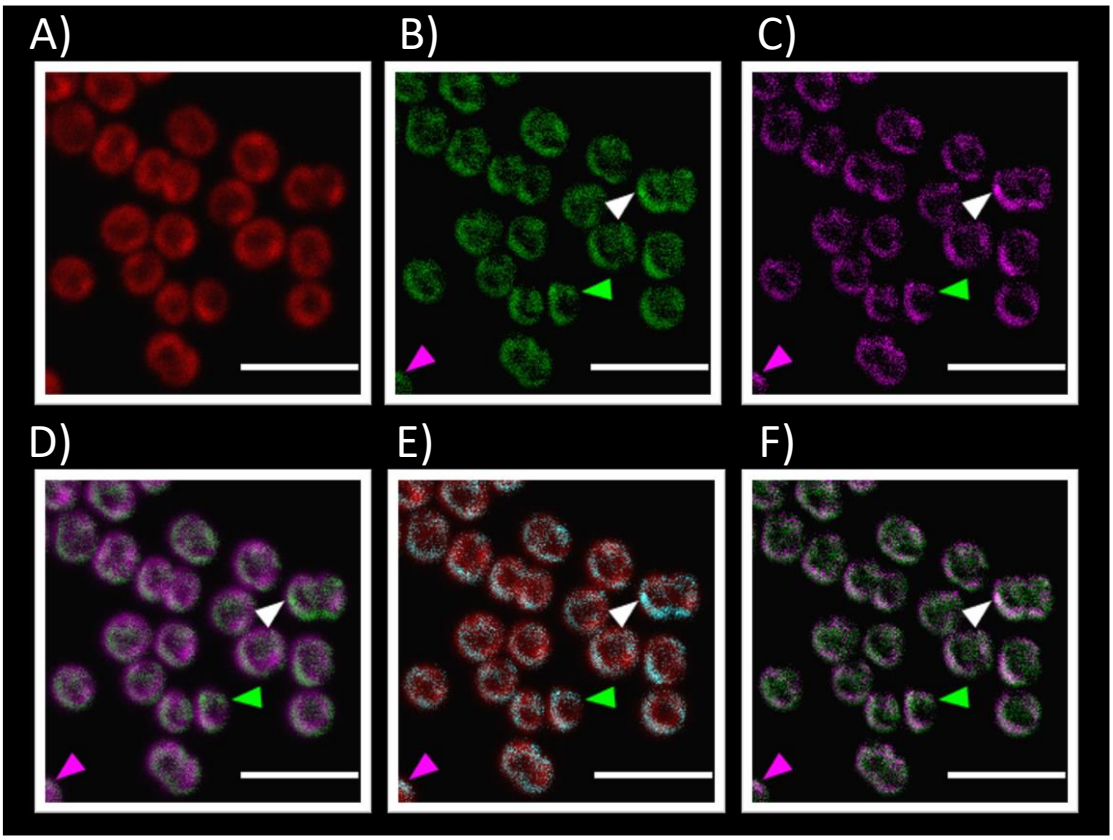

Figure 3-3: Photoautotrophically Grown PCC 6803 *hoxFGFP ndhMYFP* at 20 μE.
A) Chlorophyll *a* channel. B) GFP channel. C) YFP channel. D) chlorophyll *a* (magenta) and GFP channels merged. E) Chlorophyll *a* and YFP (Cyan) channels merged. F) GFP and YFP (magenta) channels merged. The magenta arrow indicates NdhMYFP not co-localized with HoxFGFP. The white arrow indicates the distribution of HoxFGFP and NdhMYFP that is co-localized. The Green arrow indicates HoxFGFP that is not co-localized with NdhMYFP. The scale bar represents 5 μm.

3.4.2 Anoxic Dark Adaptation following photoautotrophic growth at 20μE

H_2 evolution is predominantly observed under anoxic conditions this is primarily due to the sensitivity of the Hox enzyme to oxygen (Cournac et al., 2002, 2004). The cultures were dark adapted, and oxygen was removed by supplementing the cultures with 2 mM sodium dithionite. Under anoxic dark-adapted conditions there was no significant autofluorescence observed in the wild type strain (data not shown).

Figure 3-4 shows that there are similar populations of Hox and NDH-1 as observed in photoautotrophic growth. The Hox formed either dispersed or puncta populations that colocalized with the chlorophyll *a* channel (M=0.7244) which suggests thylakoid localization. NDH-1 was shown to form dispersed and puncta populations that colocalized with the chlorophyll *a*

channel (M=0.9867) which suggests localization to the thylakoid. The Hox puncta population showed colocalization with NDH-1 (Figure 3-4 B-F white arrows) and the formation of discrete populations (Figure 3-4 B-F green arrow). The NDH-1 puncta also showed discrete populations (Figure 3-4 B-F magenta arrows). The total Hox and NDH-1 populations showed a degree of colocalization (M=0.539). There was no significant difference observed in NDH-1 or Hox distribution in PCC 6803 *hoxFGFP ndhMYFP* compared to the single fluorescent tagged strains.

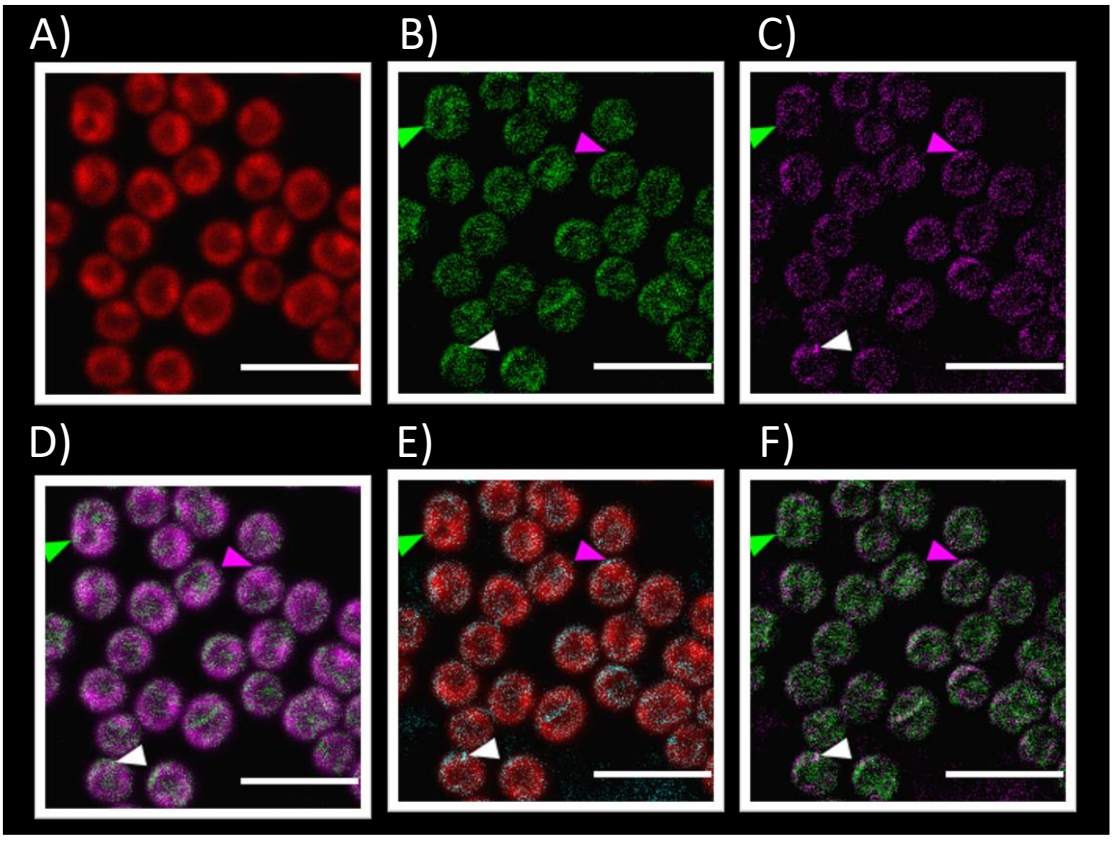

Figure 3-4: Anoxic Dark Adapted Photoautotrophically Grown PCC 6803 *hoxFGFP* at 20 μE.
A) Chlorophyll *a* channel. B) GFP channel. C) YFP channel. D) chlorophyll *a* (magenta) and GFP channels merged. E) Chlorophyll *a* and YFP (Cyan) channels merged. F) GFP and YFP (magenta) channels merged. The magenta arrow indicates NdhMYFP not co-localized with HoxFGFP. The white arrow indicates the distribution of HoxFGFP and NdhMYFP that is co-localized. The Green arrow indicates HoxFGFP that is not co-localized with NdhMYFP. The scale bar represents 5 μm.

3.4.3 Pigment Comparison of PCC 6803 Strains Grown at 20 μE m^{-2} s^{-1}

The pigment composition of each strain was compared under photoautotrophic growth conditions at 20 μE $m^{-2}s^{-1}$. The individually tagged PCC 6803 *hoxFGFP*, *ndhMYFP* strains and double fluorescent tagged strain

showed a slightly reduced photopigment composition compared to the wild type (Figure 3-5)

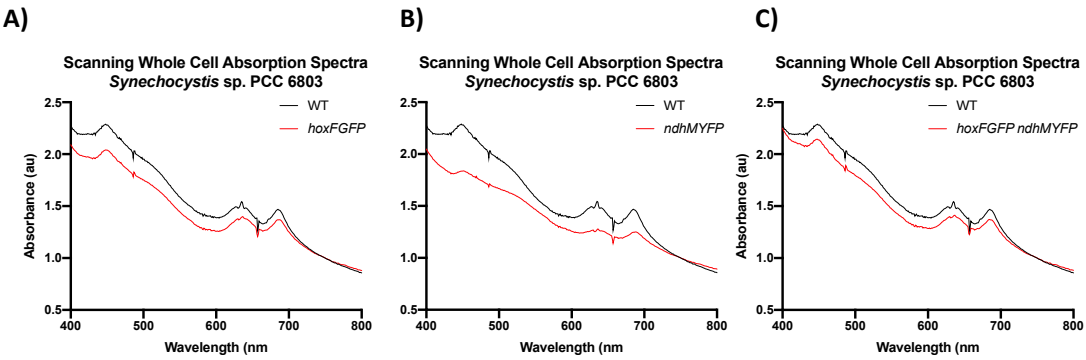

Figure 3-5: Scanning Whole Cell Absorption Spectra of PCC 6803 Strains Grown Photoautotrophically at 20 μE $m^{-2}s^{-1}$.
The scanning whole cell absorption spectra of PCC 6803 growth under photoautotrophic conditions at 20 μE. A) PCC 6803 WT (black line) compared to *hoxFGFP* (red line). B) Wild type (black line) compared to *ndhMYFP* (red line). C) WT (black line) compared to *hoxFGFP ndhMYFP* (red line). Each spectrum represents a biological triplicate (n=3).

3.4.4 Photoautotrophic Growth at 60 μE m^{-2} s^{-1}

Light intensity was increased to 60 μE $m^{-2}s^{-1}$ in order to investigate the distribution of Hox and NDH-1 with higher photosynthetic electron flux. In photoautotrophic growth at 60 μE, no signiificant autofluorescence was detected in wild type PCC 6803 (data not shown).

Both Hox and NDH-1 were localised in the two characterisitc populations, dispersed and puncta (Figure 3-6). A subset of the Hox population, the puncta population were colocalised with the NDH-1 puncta (Figure 3-6 white arrow). A population of the Hox puncta did not colocalise with NDH-1 (green arrow). There was also a small NDH-1 puncta population which did not co-localize with HoxFGFP (magenta arrow).

Hox was shown to be colocalized with chlorophyll *a* (M=0.8131) and is therefore thylakoid localized. The NDH-1 was also colocalized with chlorophyll *a* (M=0.9954). Both Hox and NDH-1 were colocalized and localised to the thylakoid membrane (M=0.6311).

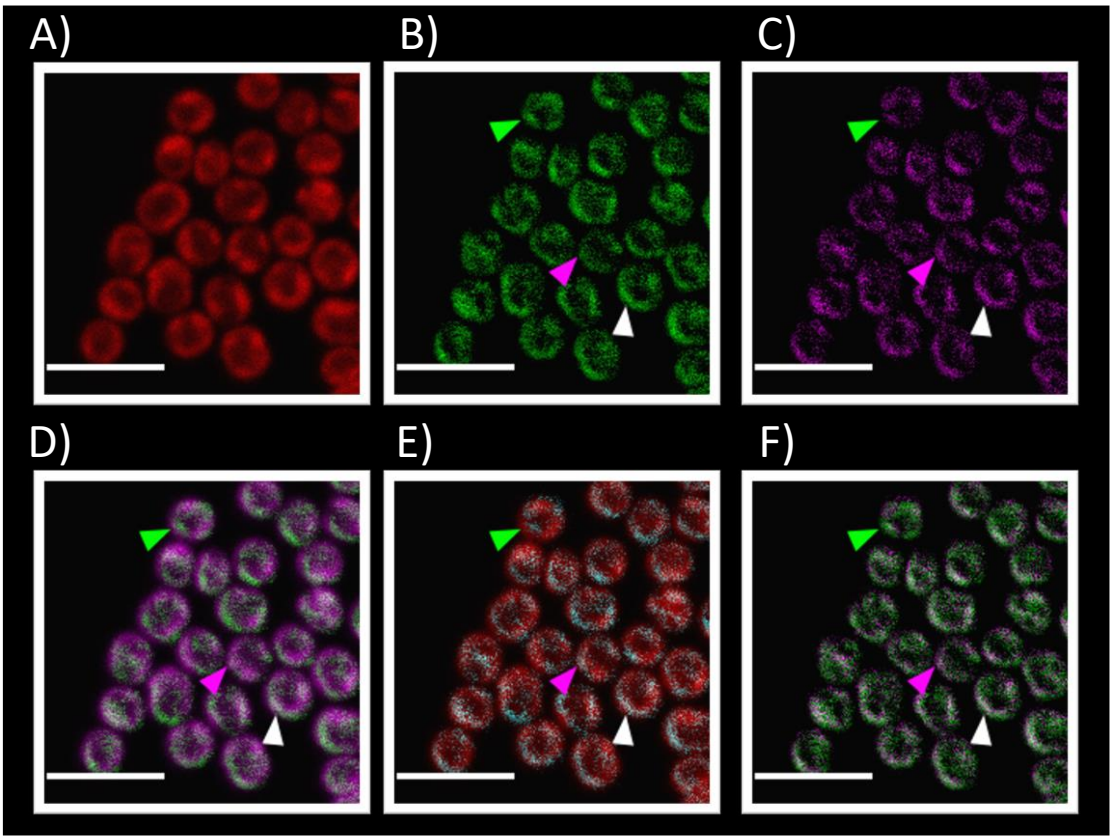

Figure 3-6: Photoautotrophically Grown PCC 6803 *hoxFGFP ndhMYFP* at 60 μE.
A) Chlorophyll *a* channel. B) GFP channel. C) YFP channel. D) chlorophyll *a* (magenta) and GFP channels merged. E) Chlorophyll *a* and YFP (Cyan) channels merged. F) GFP and YFP (magenta) channels merged. The white arrow indicates a population of HoxFGFP and NdhMYFP puncta co-localized. The green arrow indicates a population of HoxFGFP not co-localized with NdhMYFP. The magenta arrow indicates a population of NdhMYFP not co-localized with HoxFGFP The scale bar represents 5 μm.

3.4.5 Anoxic Dark Adaptation following photoautotrophic growth at 60 μE $m^{-2}s^{-1}$

The individual PCC 6803 strains were all dark adapted under anoxic conditions. The anoxic dark adapted PCC 6803 *hoxFGFP ndhMYFP* cells showed that both Hox and NDH-1 were localized to the thylakoid (Figure 3-7 D). It was observed that Hox was either dispersed at the thylakoid or in puncta that were colocalized with the NDH-1 puncta (Figure 3-7 white arrow). Hox also formed a puncta population which was once again not localized with NDH-1 (Figure 3-7 green arrow).

Hox was shown to be colocalized with chlorophyll *a* (M=0.7349) and is therefore thylakoid localized. The NDH-1 was also colocalized with chlorophyll *a* (M=0. 8784). Both Hox and NDH-1 were colocalized and localised to the thylakoid membrane (M=0.5725).

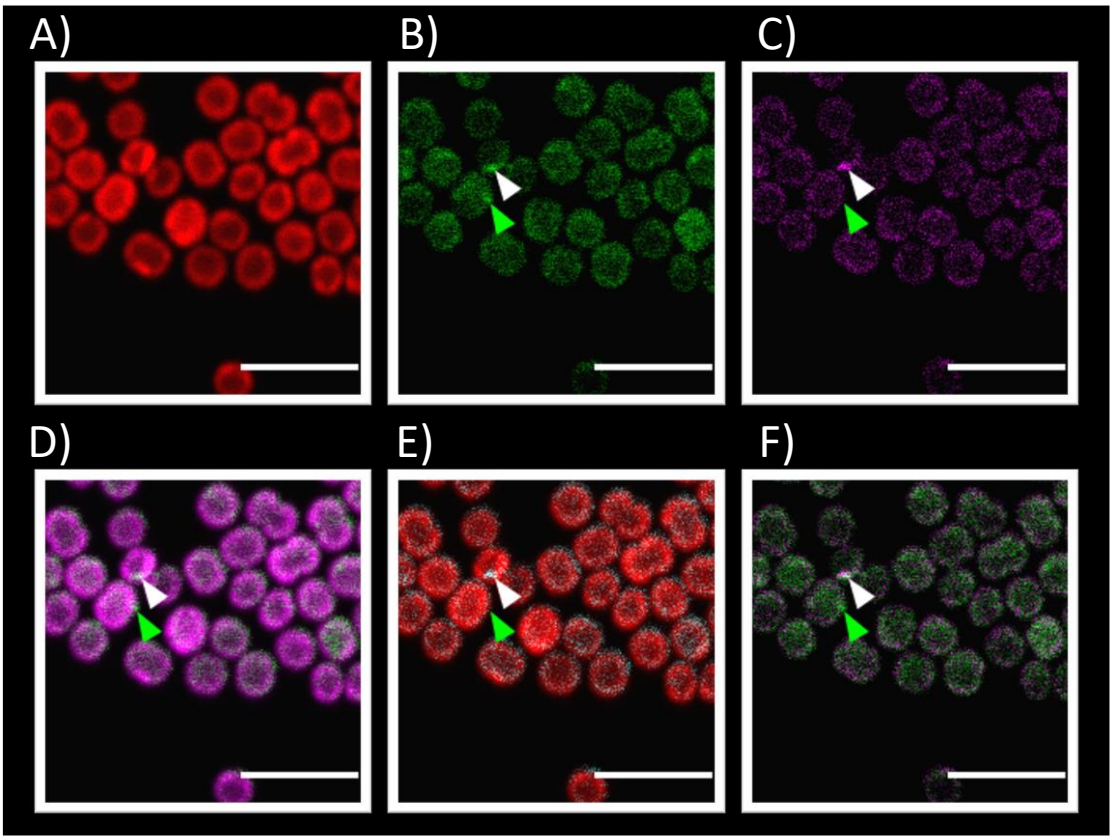

Figure 3-7: Anoxic Dark adapted Photoautotrophically Grown PCC 6803 *hoxFGFP ndhMYFP* at 60 μE.
A) Chlorophyll *a* channel. B) GFP channel. C) YFP channel. D) chlorophyll *a* (magenta) and GFP channels merged. E) Chlorophyll *a* and YFP (Cyan) channels merged. F) GFP and YFP (magenta) channels merged. The green arrow indicates HoxFGFP puncta not co-localized with NdhMYFP. The white arrow indicates HoxFGFP and NdhMYFP puncta co-localized. The scale bar represents 5 μm.

3.4.6 Pigment Comparison of PCC 6803 Strains Grown at 60 μE m^{-2} s^{-1}.

The pigment composition of each of the tagged strains of PCC 6803 were compared under photoautotrophic growth at 60 μE $m^{-2}s^{-1}$. Both the PCC 6803 *hoxFGFP* and the double fluorescently tagged strain showed no difference in the photopigment composition compared to the wild type (Figure 3-8 A & C). The PCC 6803 *ndhMYFP* strain had a higher chlorophyll *a* and phycocyanin content compared to the wild type.

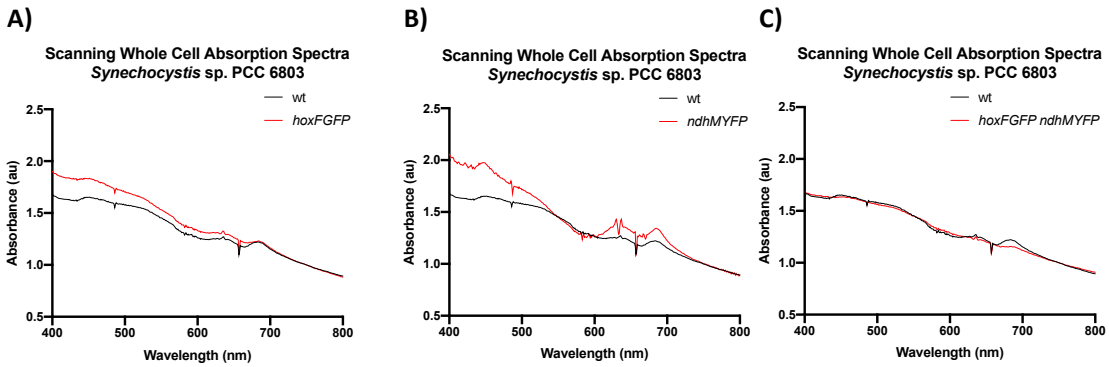

Figure 3-8: Scanning Whole Cell Absorption Spectra of PCC 6803 Strains Grown Photoautotrophically at 60 μE $m^{-2}s^{-1}$.
The scanning whole cell absorption spectra of PCC 6803 growth under photoautotrophic conditions at 60 μE. A) PCC 6803 WT (black line) compared to *hoxFGFP* (red line). B) WT (black line) compared to *ndhMYFP* (red line). C) WT (black line) compared to *hoxFGFP ndhMYFP* (red line). Each spectrum represents a biological triplicate (n=3).

3.4.7 Photoautotrophic Growth Images at 200 μE m^{-2} s^{-1}

The PCC6803 strains were grown at 200 μE m^{-2} s^{-1}. In the PCC 6803 *hoxFGFP ndhMYFP* strain both Hox and NDH-1 had the characteristic two populations,dispersed and puncta with the puncta mostly showing colocalization (Figure 3-9 F white arrow).

Hox was shown to be colocalized to the chlorophyll *a* (M=0.8592) which indicates a localization to the thylakoid. The NDH-1 population showed strong overlap with the chlorphyll *a* channel (M= 0.9442) that demonstrates a localization in the thylakoid. The entire population of Hox showed a high Manders coefficient with the whole NDH-1 population (M=0.9643).

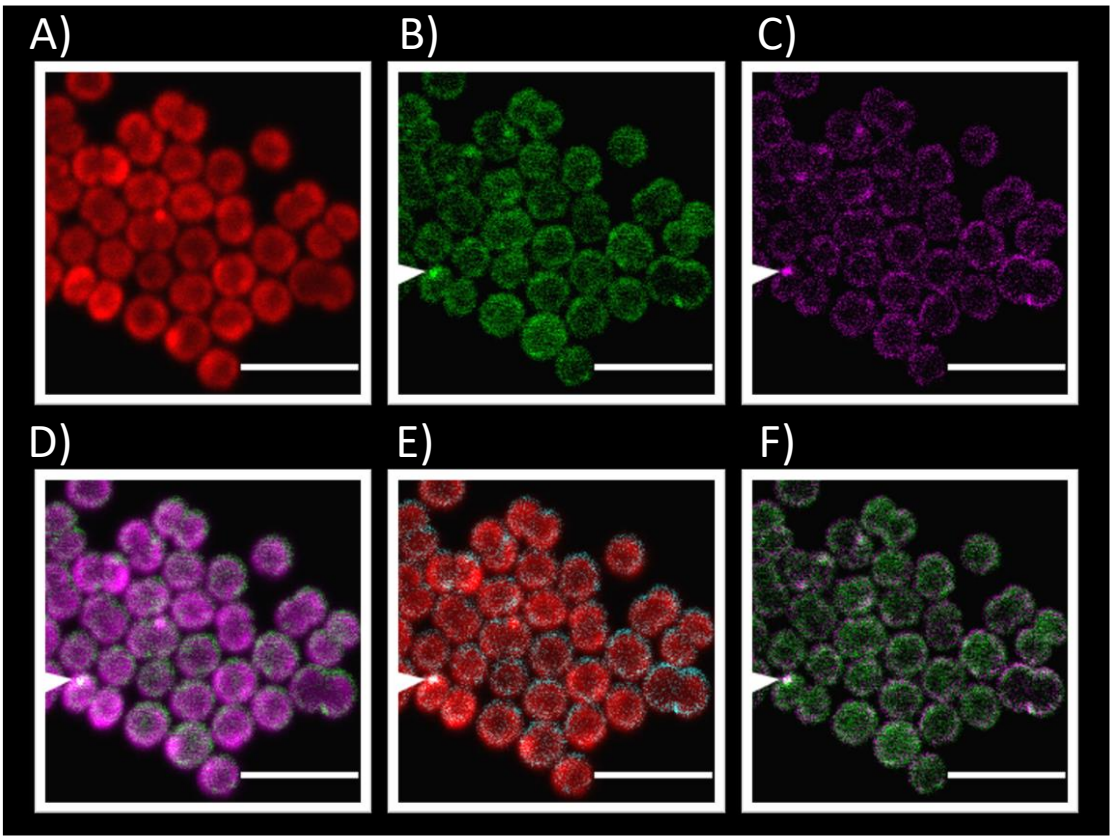

Figure 3-9: Photoautotrophically Grown PCC 6803 *hoxFGFP ndhMYFP* at 200 μE.
A) Chlorophyll *a* channel. B) GFP channel. C) YFP channel. D) chlorophyll *a* (magenta) and GFP channels merged. E) Chlorophyll *a* and YFP (Cyan) channels merged. F) GFP and YFP (magenta) channels merged. The white arrow indicates a population of HoxFGFP and NdhMYFP puncta co-localized. The scale bar represents 5 μm.

3.4.8 Anoxic Dark Adaptation following photoautotrophic growth at 200 μE m^{-2} s^{-1}

Upon anoxic dark adaptation, the Hox and NDH-1 showed 2 distinct populations; dispersed and puncta (Figure 3-10). The Hox puncta population localized in distinct foci (green arrows) or colocalized with NDH-1 puncta (white arrows). The NDH-1 puncta did not form distinct foci and predominantly colocalized with the Hox puncta (white arrows).

The entire Hox population was shown to colocalize with the chlorophyll *a* channel (M=0.8756), entailing that Hox was localized to the thylakoid. The populations of NDH-1 showed colocalization with chlorophyll *a* (M= 0.8587) and therefore showing a localization in the thylakoid. Hox showed colocalization with NDH-1 (M=0.7862).

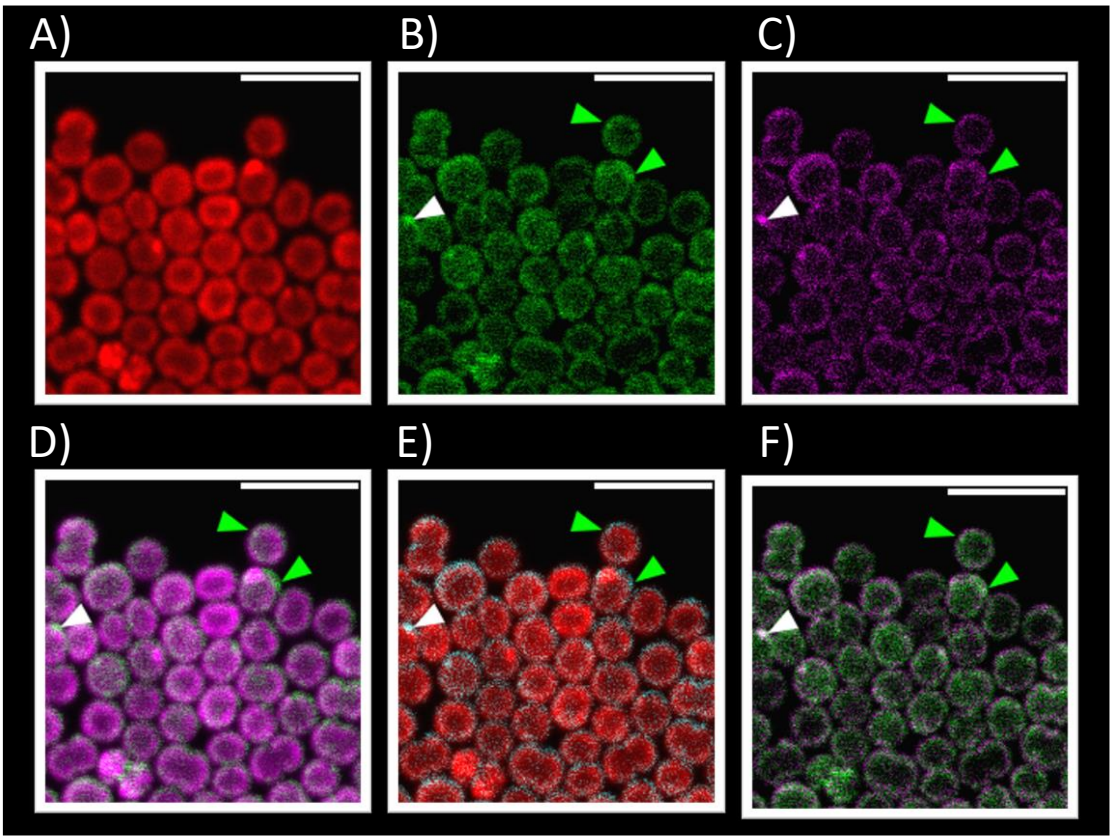

Figure 3-10: Anoxic Dark Adapted Photoautotrophically Grown PCC 6803 *hoxFGFP ndhMYFP* at 200 μE.
A) Chlorophyll *a* channel. B) GFP channel. C) YFP channel. D) chlorophyll *a* (magenta) and GFP channels merged. E) Chlorophyll *a* and YFP (Cyan) channels merged. F) GFP and YFP (magenta) channels merged. The white arrow indicates a population of HoxFGFP and NdhMYFP puncta co-localized. The green arrows represent populations of HoxFGFP not co-localized with NdhMYFP. The scale bar represents 5 μm.

3.4.9 Pigment Comparison of PCC 6803 Strains Grown at 200 μE m^{-2} s^{-1}

The pigment composition of each of the tagged strains of PCC 6803 were compared under photoautotrophic conditions at 200 μE $m^{-2}s^{-1}$ Figure 3-11. The individually tagged PCC 6803 *hoxFGFP, ndhMYFP* strains and double mutants had a higher carotenoid and phycocyanin content compared to the wild type. No difference in chlorophyll *a* content was observed between the PCC 6803 strains.

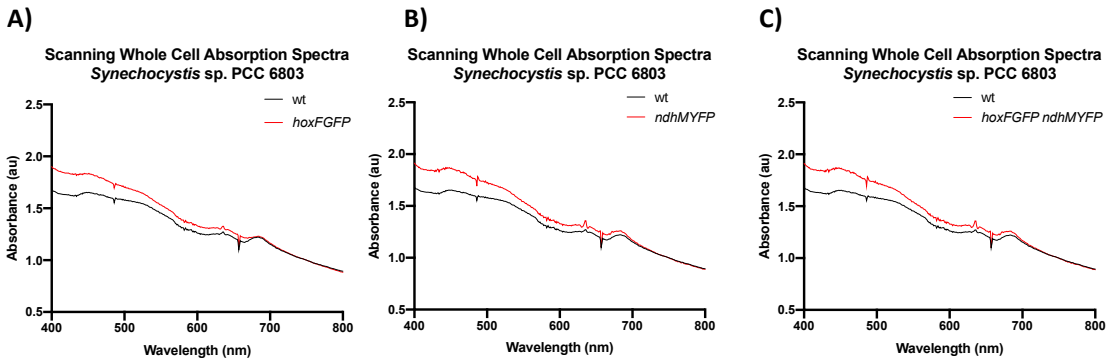

Figure 3-11: Scanning Whole Cell Absorption Spectra of PCC 6803 Strains Grown Photoautotrophically at 200 μE $m^{-2}s^{-1}$.
The scanning whole cell absorption spectra of PCC 6803 growth under photoautotrophic conditions at 200 μE. A) PCC 6803 WT (black line) compared to *hoxFGFP* (red line). B) WT (black line) compared to *ndhMYFP* (red line). C) WT (black line) compared to *hoxFGFP ndhMYFP* (red line). Each spectrum represents a biological triplicate (n=3).

3.5 Distribution of Hox and NDH-1 in PCC 6803 Grown Mixotrophically.

3.5.1 Mixotrophic Growth at 20 μE m^{-2} s^{-1}

Cells were grown mixotrophically with 10 mM glucose at 20 μE m^{-2} s^{-1} (Figure 3-12), in order to compare the distribution of Hox and NDH-1 with photoautotrophic growth. Hox and NDH-1 formed 2 distinct populations; puncta and dispersed (Figure 3-12 B & D). The Hox puncta either colocalized with NDH-1 (magenta arrows) or at foci distinct from NDH-1 (green arrows). A small population of Hox was observed to be localized to the cytoplasm (cyan arrow). The NDH-1 was observed to be dispersed or form puncta. There was a small population of NDH-1 puncta that were not colocalized with Hox (magenta arrows).

Hox was shown to be colocalized with chlorophyll *a* (M=0.7717) which indicates a predominant thylakoid localization. The NDH-1 was shown to colocalize with chlorophyll *a* (M=0.8736) which also shows a thylakoid localization. The total Hox and NDH-1 populations showed colocalization (M=0.6897).

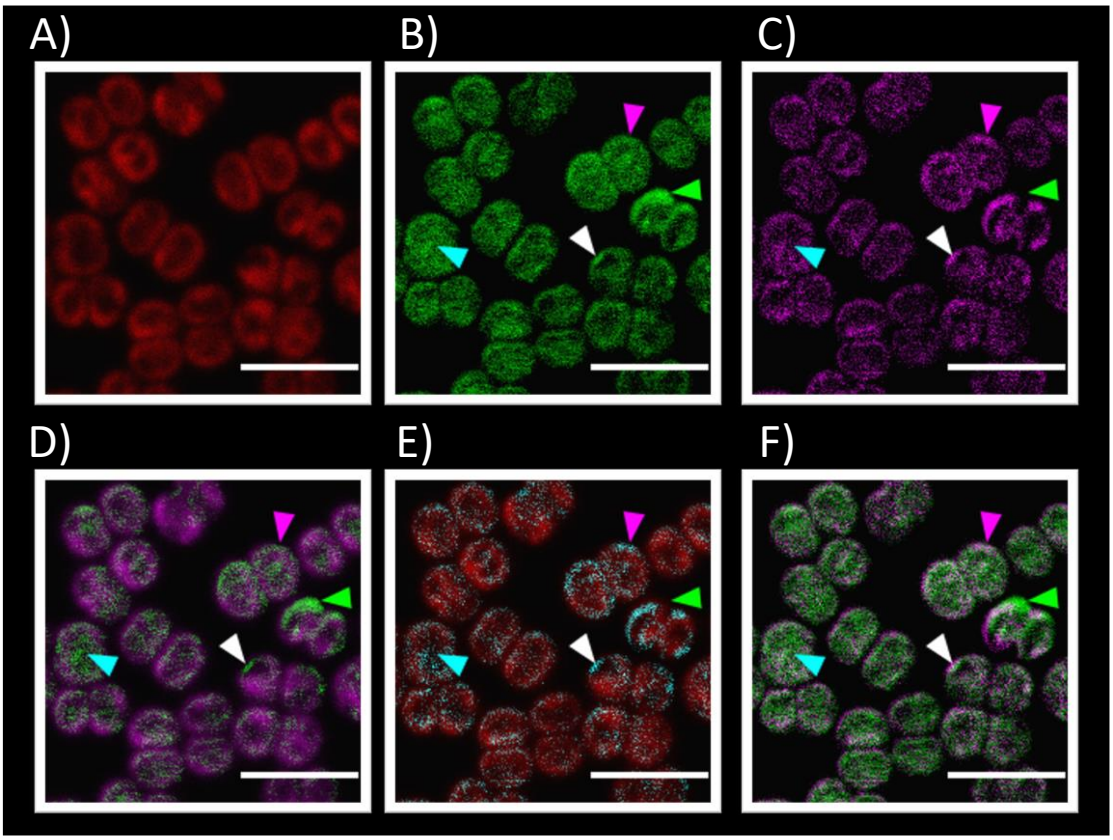

Figure 3-12: Mixotrophically Grown PCC 6803 *hoxFGFP ndhMYFP* at 20 μE.
A) Chlorophyll *a* channel. B) GFP channel. C) YFP channel. D) chlorophyll *a* (magenta) and GFP channels merged. E) Chlorophyll *a* and YFP (Cyan) channels merged. F) GFP and YFP (magenta) channels merged. The magenta arrow indicates NdhMYFP not co-localized with HoxFGFP. The white arrow indicates the distribution of HoxFGFP and NdhMYFP that is co-localized. The Green arrow indicates HoxFGFP that is not co-localized with NdhMYFP. The cyan arrow indicates a population of HoxFGFP localized to the cytoplasm. The scale bar represents 5 μm.

3.5.2 Anoxic Dark Adaptation following photoautotrophic growth at 20uE

After anoxic dark adaptation, the Hox population in the cytoplasm appears to be lost (Figure 3-13 B & D). Hox showed a distribution pattern of dispersed and puncta. NDH-1 was observed to be dispersed or in puncta co-localized with Hox puncta (white arrows).

The entire Hox population was shown to colocalize with chlorophyll *a* (M=0.9264) which shows a localization to the thylakoid. NDH-1 showed colocalization with chlorophyll *a* (0.8161) entailing that NDH-1 is localized in the thylakoid. The entire Hox and NDH-1 was shown to be colocalized (M=0.7923).

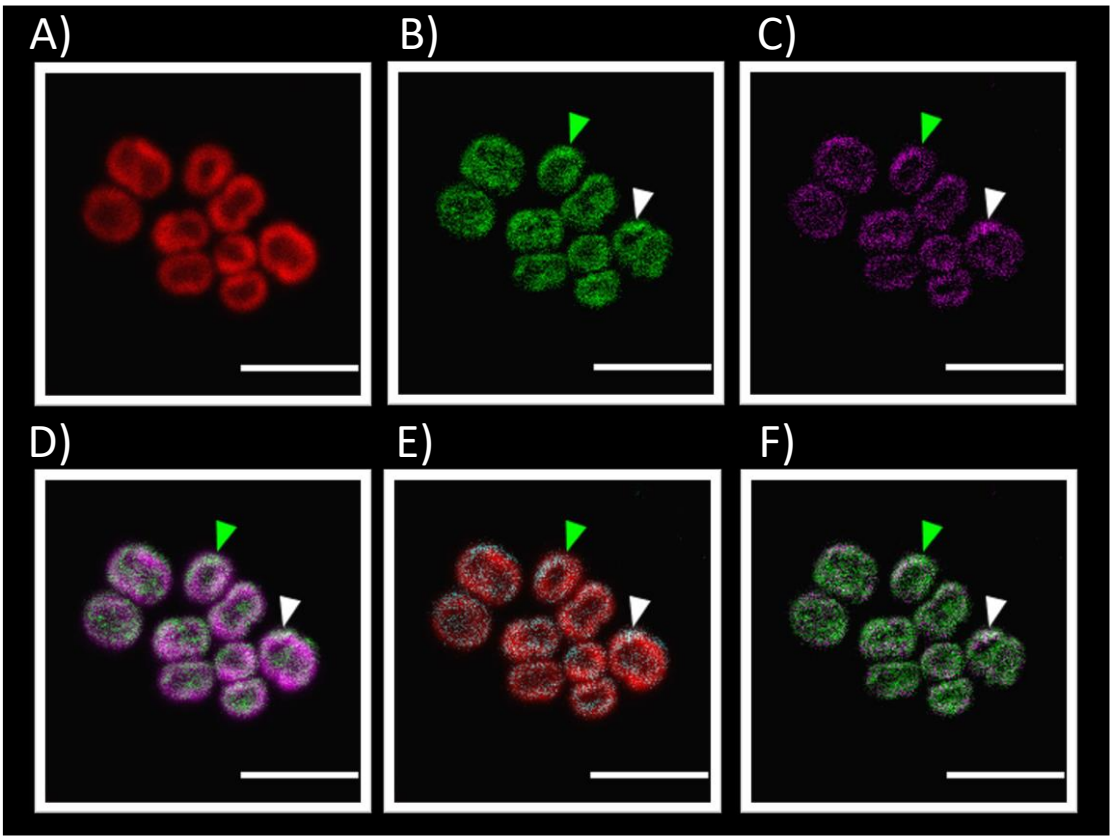

Figure 3-13: Anoxic Dark Adapted Mixotrophically Grown PCC 6803 *hoxFGFP ndhMYFP* at 20 μE.
A) Chlorophyll *a* channel. B) GFP channel. C) YFP channel. D) chlorophyll *a* (magenta) and GFP channels merged. E) Chlorophyll *a* and YFP (Cyan) channels merged. F) GFP and YFP (magenta) channels merged. The white arrow indicates the distribution of HoxFGFP and NdhMYFP that is co-localized. The Green arrow indicates HoxFGFP that is not co-localized with NdhMYFP. The scale bar represents 5 μm.

3.5.3 Pigment Comparison of PCC 6803 Strains Grown Mixotrophically at 20 μE m^{-2} s^{-1}

The pigment composition of each of the tagged strains of PCC 6803 were compared under mixotrophic conditions at 20 μE $m^{-2}s^{-1}$ (Figure 3-14). Both the PCC 6803 *hoxFGFP* and *ndhMYFP* strains and the double mutant had a lower carotenoid content compared to the wild type. No difference in chlorophyll *a* and phycocyanin content was observed between the PCC 6803 strains grown mixotrophically at 20 μE $m^{-2}s^{-1}$.

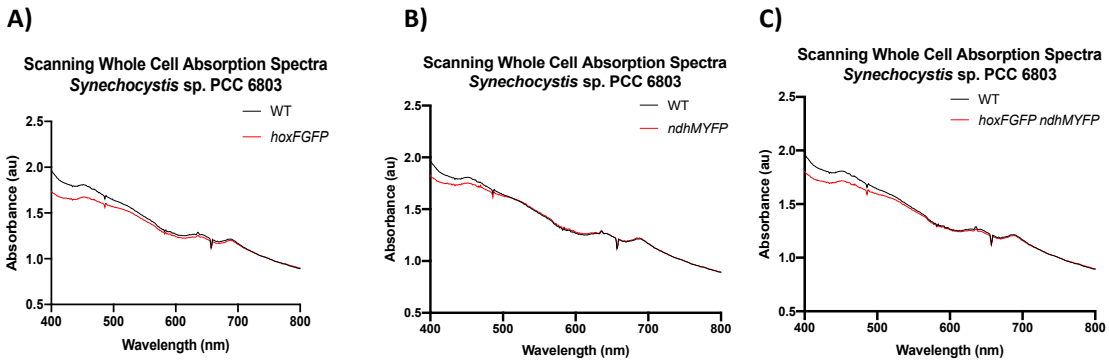

Figure 3-14: Scanning Whole Cell Absorption Spectra of PCC 6803 Strains Grown Mixotrophically at 20 μE $m^{-2}s^{-1}$.
The scanning whole cell absorption spectra of PCC 6803 growth under mixotrophic conditions at 20 μE. A) PCC 6803 WT (black line) compared to *hoxFGFP* (red line). B) WT (black line) compared to *ndhMYFP* (red line). C) WT (black line) compared to *hoxFGFP ndhMYFP* (red line). Each spectrum represents a biological triplicate (n=3).

3.5.4 Mixotrophic Growth at 60 μE m^{-2} s^{-1}

The light intensity under mixotrophic growth was increased to 60 μE m^{-2} s^{-1} in order to compare the distribution of Hox and NDH-1 with photoautotrophic grown cultures. In the *hoxFGFP ndhMYFP* strain Hox was predominantly distributed in the cytoplasm, this was in stark contrast to the distribution of Hox in the same strain grown at 20 μE m^{-2} s^{-1} (Figure 3-15 D cyan arrow). The NDH-1 showed dispersed and puncta populations. There was still a population of Hox which appeared to be localized to the thylakoid (green arrow) and was still associated with NDH-1 (white arrow).

The Hox population showed colocalization with chlorophyll *a* fluorescence (M=0.621) indicating that a population of Hox is still localized to the thylakoid. NDH-1 was colocalized to chlorophyll *a* (M=0.7744) and was therefore thylakoid localized. Hox showed colocalization with NDH-1 (M=0.486). The distribution of Hox in the mixotrophically grown PCC 6803 *hoxFGFP ndhMYFP* was similar to that observed in the *hoxFGFP* strain (data not shown).

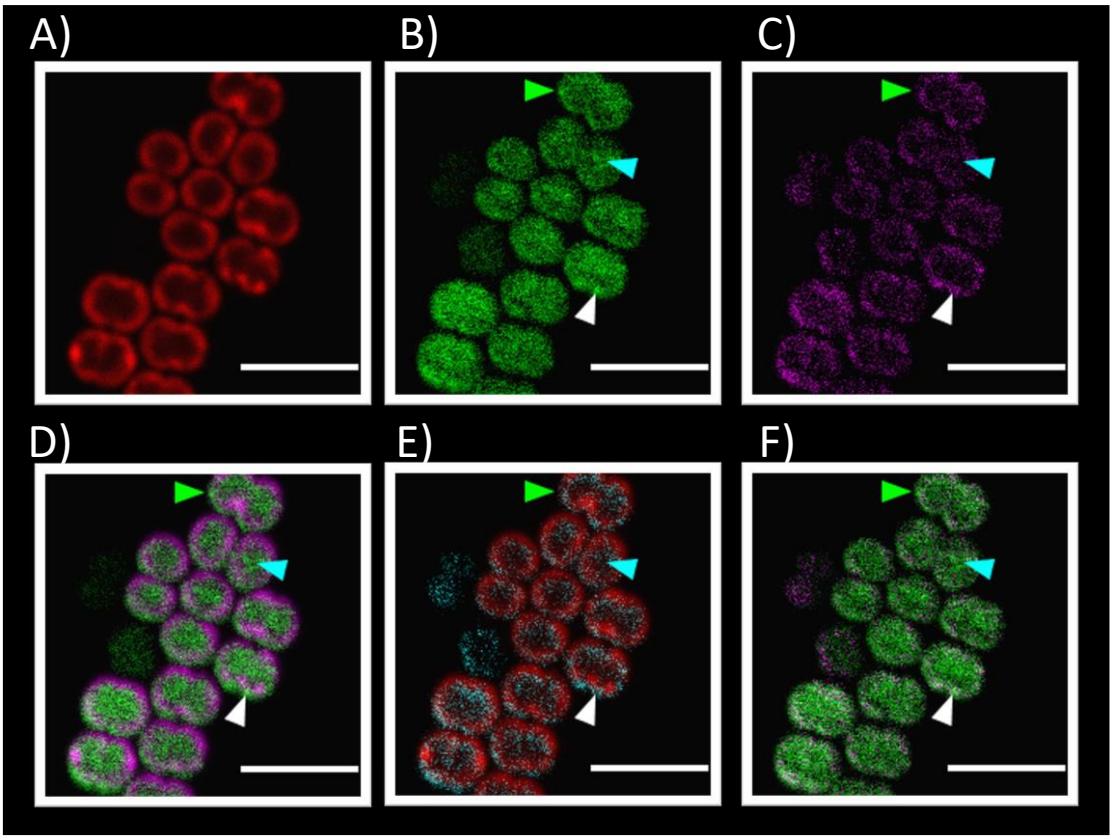

Figure 3-15: Mixotrophically Grown PCC 6803 *hoxFGFP ndhMYFP* at 60 μE.
A) Chlorophyll *a* channel. B) GFP channel. C) YFP channel. D) chlorophyll *a* (magenta) and GFP channels merged. E) Chlorophyll *a* and YFP (Cyan) channels merged. F) GFP and YFP (magenta) channels merged. The white arrow indicates a population of Hox and NDH-1 puncta colocalized. The Green arrow indicates a Hox population forming a distinct puncta at the thylakoid. The cyan arrow indicates Hox localization to the cytoplasm. The scale bar represents 5 μm.

3.5.5 Anoxic Dark Adaptation following Mixotrophic Growth at 60 μE m^{-2} s^{-1}

Anoxia was shown to result in H_2 evolution in mixotrophic growth (Appel et al., 2020), the distribution of Hox and NDH-1 was visualized under these conditions. The majority of Hox puncta did not co-localize with NDH-1 (Figure 3-16 green arrow). The YFP channel was very weak but there were populations of NDH-1 that did not colocalize with Hox (Figure 3-16 magenta arrow).

Hox colocalized with chlorophyll *a* (M=0.8744) demonstrating that the Hox population was capable of redistributing from the cytoplasm to the thylakoid. NDH-1 remained colocalized with chlorophyll *a* (M=0.823) in the thylakoid. Both Hox and NDH-1 showed colocalization (M=0.5791) as a total of all populations.

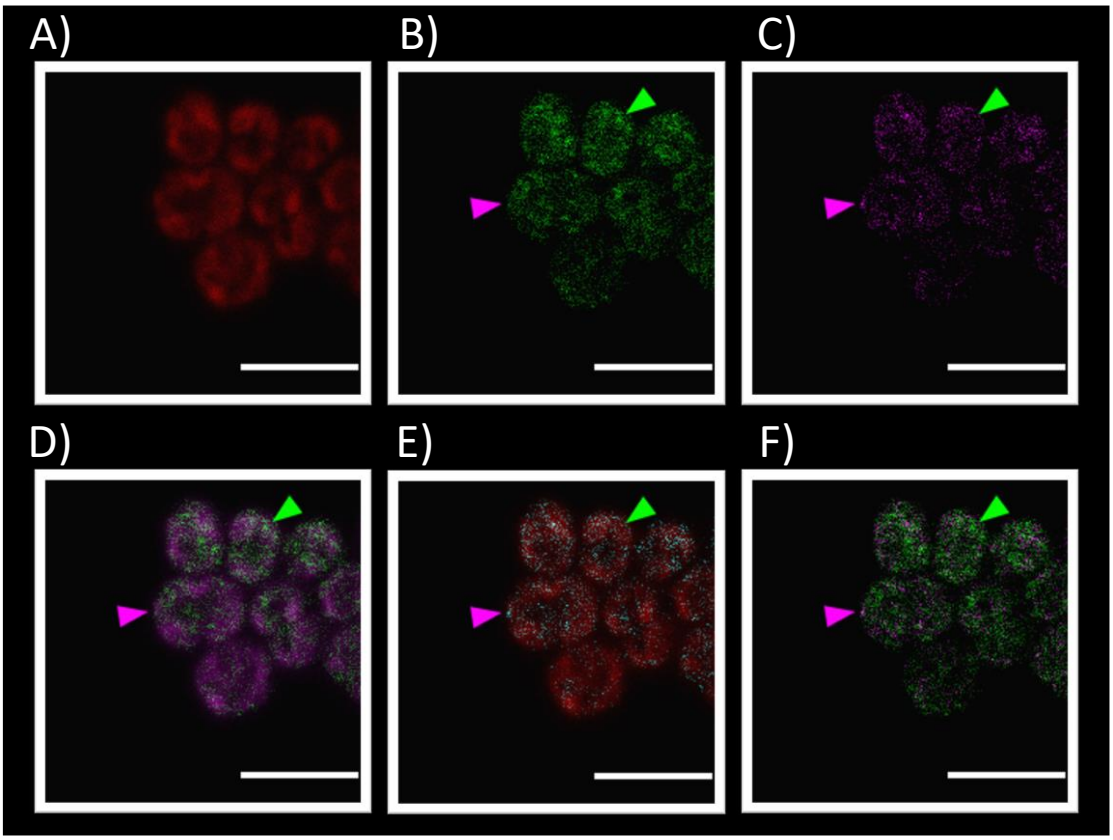

Figure 3-16: Anoxic Dark Adapted Mixotrophically Grown PCC 6803 *hoxFGFP ndhMYFP* at 60 μE.
A) Chlorophyll *a* channel. B) GFP channel. C) YFP channel. D) chlorophyll *a* (magenta) and GFP channels merged. E) Chlorophyll *a* and YFP (Cyan) channels merged. F) GFP and YFP (magenta) channels merged. The white arrow indicates a population of Hox and NDH-1 puncta colocalized. The Green arrow indicates a Hox population forming a distinct puncta at the thylakoid. The scale bar represents 5 μm.

3.5.6 Pigment Comparison of PCC 6803 Strains Mixotrophically Grown at 60 μE m^{-2} s^{-1}

The pigment composition of each of the tagged strains of PCC 6803 were compared under mixotrophic conditions at 60 μE $m^{-2}s^{-1}$ (Figure 3-17). The PCC 6803 *hoxFGFP* strain had an increase in carotenoid content but no difference in phycocyanin or chlorophyll *a* content when compared to wild type. The *ndhMYFP* strain had a higher carotenoid, phycocyanin and chlorophyll *a* content compared to wild type. The *hoxFGFP ndhMYFP* strain showed no difference in the phycocyanin or chlorophyll *a* content but a small decrease was seen in the carotenoids.

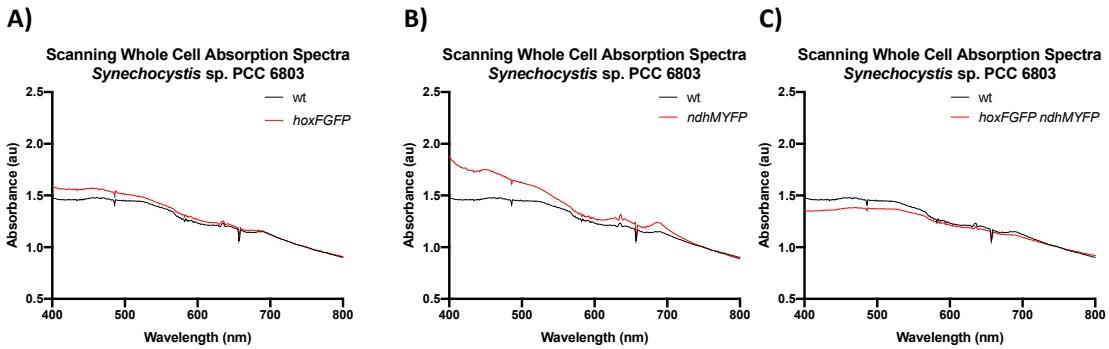

Figure 3-17: Scanning Whole Cell Absorption Spectra of PCC 6803 Strains Grown Mixotrophically at 60 μE $m^{-2}s^{-1}$.
The scanning whole cell absorption spectra of PCC 6803 growth under mixotrophic conditions at 60 μE. A) PCC 6803 WT (black line) compared to *hoxFGFP* (red line). B) WT (black line) compared to *ndhMYFP* (red line). C) WT (black line) compared to *hoxFGFP ndhMYFP* (red line). Each spectrum represents a biological triplicate (n=3).

3.5.7 Mixotrophic Growth at 200 μE m^{-2} s^{-1}

The Hox distribution was predominantly dispersed (Figure 3-18). NDH-1 was shown to be in 2 populations; dispersed and puncta at foci where Hox also colocalizes (white arrows).

Although Hox appeared to be localized to the cytoplasm, a proportion was colocalized to chlorophyll *a* (M=0.46) indicating that Hox still localizes at the thylakoid. NDH-1 was shown to colocalize with chlorophyll *a* (M=0.9511) indicating thylakoid localization. At the thylakoid Hox colocalized with NDH-1 (M=0.4431).

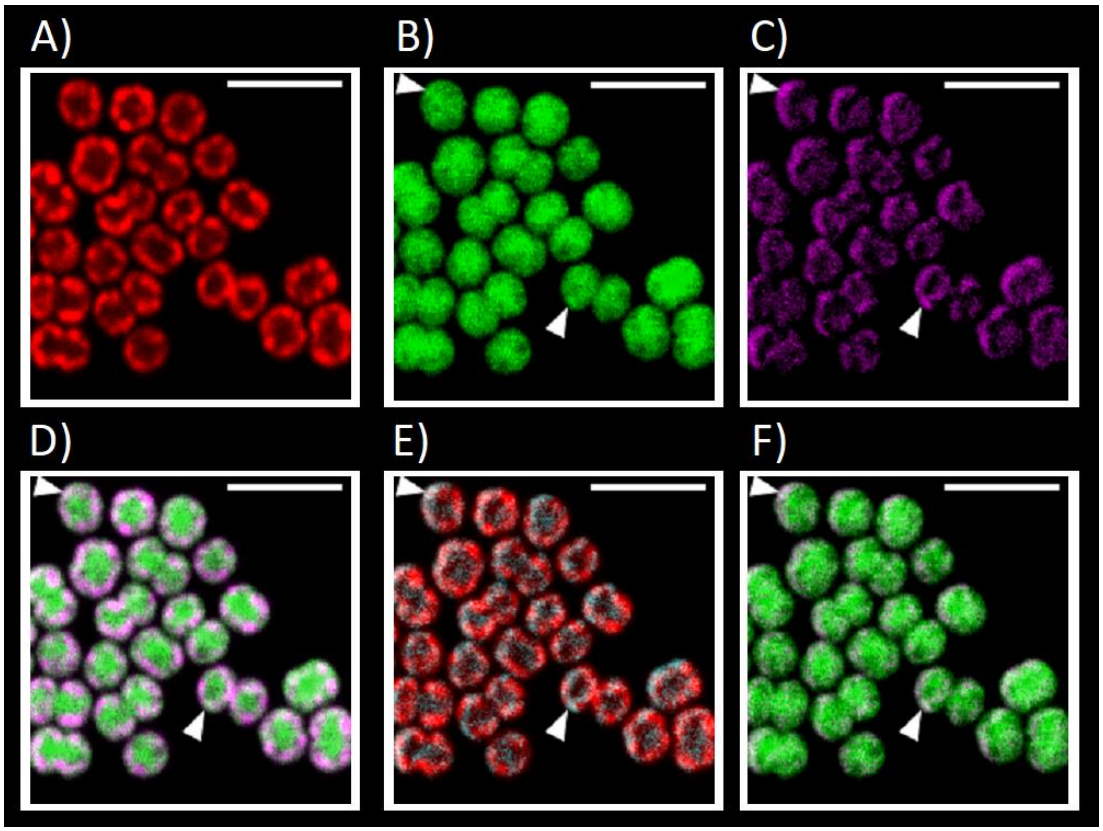

Figure 3-18: Mixotrophically Grown PCC 6803 *hoxFGFP ndhMYFP* at 200 μE.
A) Chlorophyll *a* channel. B) GFP channel. C) YFP channel. D) chlorophyll *a* (magenta) and GFP channels merged. E) Chlorophyll *a* and YFP (Cyan) channels merged. F) GFP and YFP (magenta) channels merged. The white arrow indicates a population of HoxFGFP and NdhMYFP puncta co-localized. The scale bar represents 5 μm.

3.5.8 Anoxic Dark Adaptation following Mixotrophic Growth at 200 μE m^{-2} s^{-1}

Anoxic dark adaptation caused the Hox population to be dispersed or forming puncta at distinct foci or colocalized with NDH-1 puncta (Figure 3-19 green and white arrows respectively). NDH-1 also showed a dispersed or puncta population with the puncta colocalized with Hox puncta (Figure 3-19 white arrow).

The distribution of anoxic dark adapted cells caused a larger proportion of Hox to colocalize with chlorophyll *a* (M=0.997) (Figure 3-19) that was similar to the observations at 60 μE m^{-2} s^{-1}. NDH-1 was shown to colocalize with chlorophyll *a* (M=0.9992) indicative of thylakoid localization. The total Hox and NDH-1 populations showed colocalization (M=0.854).

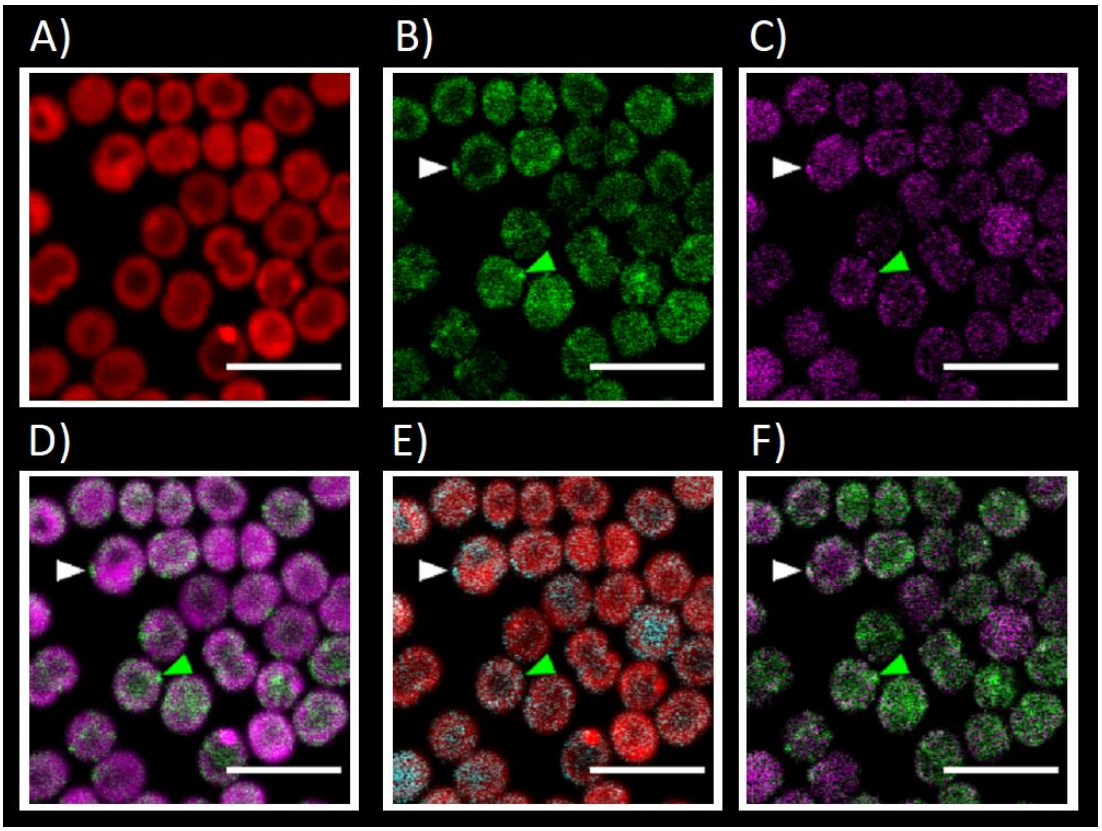

Figure 3-19: Anoxic Dark Adapted Mixotrophically Grown PCC 6803 *hoxFGFP ndhMYFP* at 200 μE.
A) Chlorophyll *a* channel. B) GFP channel. C) YFP channel. D) chlorophyll *a* (magenta) and GFP channels merged. E) Chlorophyll *a* and YFP (Cyan) channels merged. F) GFP and YFP (magenta) channels merged. The white arrow indicates a population of HoxFGFP and NdhMYFP puncta co-localized. The gren arrow represents a population of HoxFGFP not co-localized with NdhMYFP. The scale bar represents 5 μm.

3.5.9 Pigment Comparison of PCC 6803 Strains grown Mixotrophically at 200 μE m^{-2} s^{-1}

The pigment composition of each of the tagged strains was compared under mixotrophic conditions at 200 μE m-2s-1 (Figure 3-20). The hoxFGFP strain had an increased carotenoid content with no real difference in the phycocyanin or chlorophyll a content when compared to the wild type. The ndhMYFP strain had a higher carotenoid, phycocyanin and chlorophyll a content compared to wild type. The hoxFGFP ndhMYFP strain had no difference in either the phycocyanin or chlorophyll a content but there was an

increase in carotenoids.

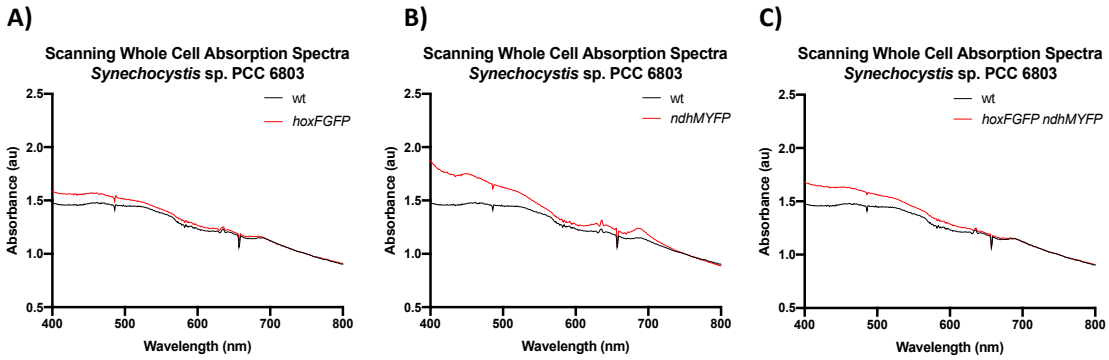

Figure 3-20: Scanning Whole Cell Absorption Spectra of PCC 6803 Strains Grown Mixotrophically at 200 μE $m^{-2}s^{-1}$.
The scanning whole cell absorption spectra of PCC 6803 growth under mixotrophic conditions at 200 μE. A) PCC 6803 WT (black line) compared to *hoxFGFP* (red line). B) WT (black line) compared to *ndhMYFP* (red line). C) WT (black line) compared to *hoxFGFP ndhMYFP* (red line). Each spectrum represents a biological triplicate (n=3).

3.6 Distribution of Hox and NDH-1 grown in Mixotrophic Nitrate Limiting Conditions.

3.6.1 Mixotrophic Nitrate Limited Growth at 20 μE m^{-2} s^{-1}

It is important to highlight changes in the interaction between Hox and NDH-1 under conditions where Hox is essential for the growth of PCC 6803 (Gutekunst et al., 2014). Hox was shown to form 2 distinctive populations; dispersed or puncta. The YFP from NDH- was extremely weak (Figure 3-21 C), making analysis more difficult. It was noted that regions of NDH-1 localization, Hox puncta formed foci (white arrow).

Hox showed colocalization with chlorophyll *a* (M=0.8753) indicating Hox localization to the thylakoid. NDH-1 showed colocalization with chlorophyll *a* (M=0.8091) indicated that NDH-1 is localized to the thylakoid. The Hox and NDH-1 showed a degree of colocalization (M=0.6862).

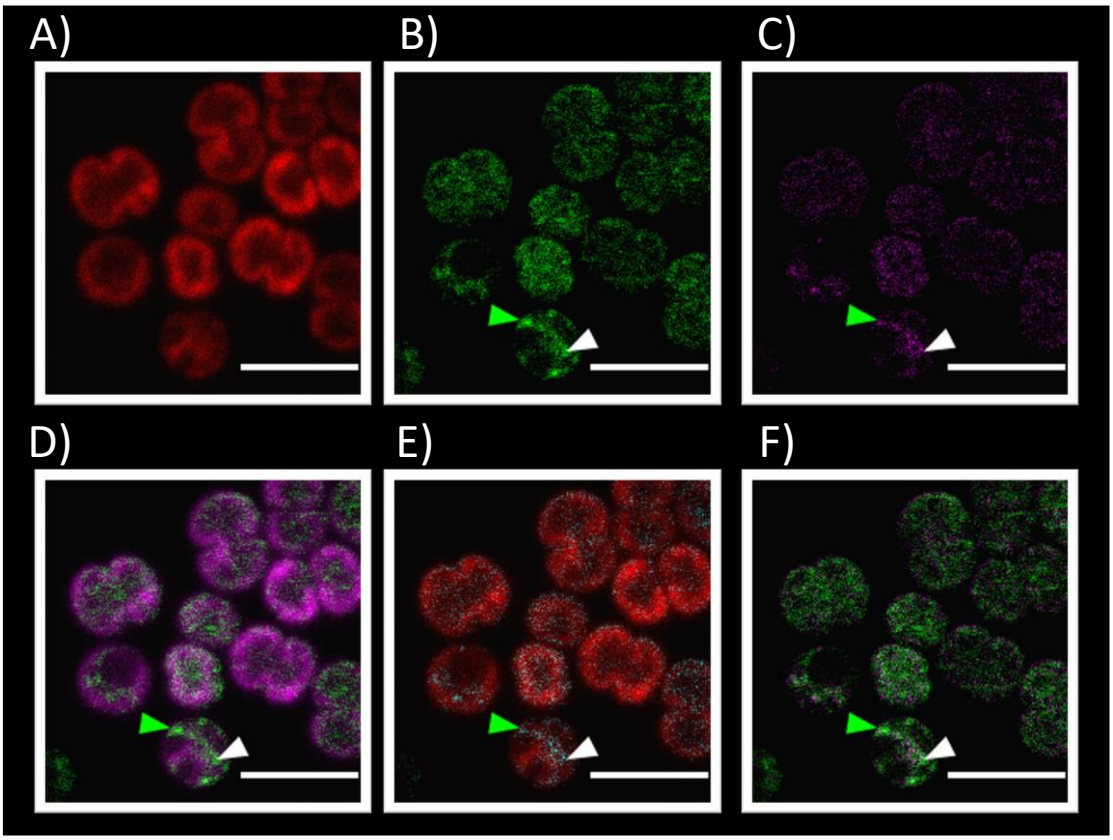

Figure 3-21: Nitrate Limited Mixotrophically Grown *Synechocystis* sp. PCC 6803 *hoxFGFP ndhMYFP* at 20 μE.
A) Chlorophyll *a* channel. B) GFP channel. C) YFP channel. D) chlorophyll *a* (magenta) and GFP channels merged. E) Chlorophyll *a* and YFP (Cyan) channels merged. F) GFP and YFP (magenta) channels merged. The magenta arrow indicates NdhMYFP not co-localized with HoxFGFP. The white arrow indicates the distribution of HoxFGFP and NdhMYFP that is co-localized. The Green arrow indicates HoxFGFP that is not co-localized with NdhMYFP. The cyan arrow indicates a population of HoxFGFP localized to the cytoplasm. The scale bar represents 5 μm.

3.6.2 Anoxic Dark Adaptation Following Mixotrophic Nitrate Limited Growth at 20 μE $m^{-2}s^{-1}$

The cells were grown mixotrophically under nitrate limited conditions at 20 μE m^{-2} s^{-1} and then subject to anoxia and dark adaptation. Hox showed dispersed and puncta populations (Figure 3-22). The YFP channel was still extremely weak (Figure 3-22 C), however a population of NDH-1 was co-localized with Hox puncta (Figure 3-22 B-F white arrow). A sub population of the Hox puncta did not colocalize with NDH-1 (Figure 3-22 B-F green arrow).

Hox was shown to colocalize with chlorophyll *a* (M=0.7508) indicating that hox is localized to the thylakoid. NHD-1 colocalized with chlorophyll *a* (M=0.9984) showing that NDH-1 is localized in the thylakoid. Hox and NDH-1 colocalized showed a degree of colocalization (M=0.5409).

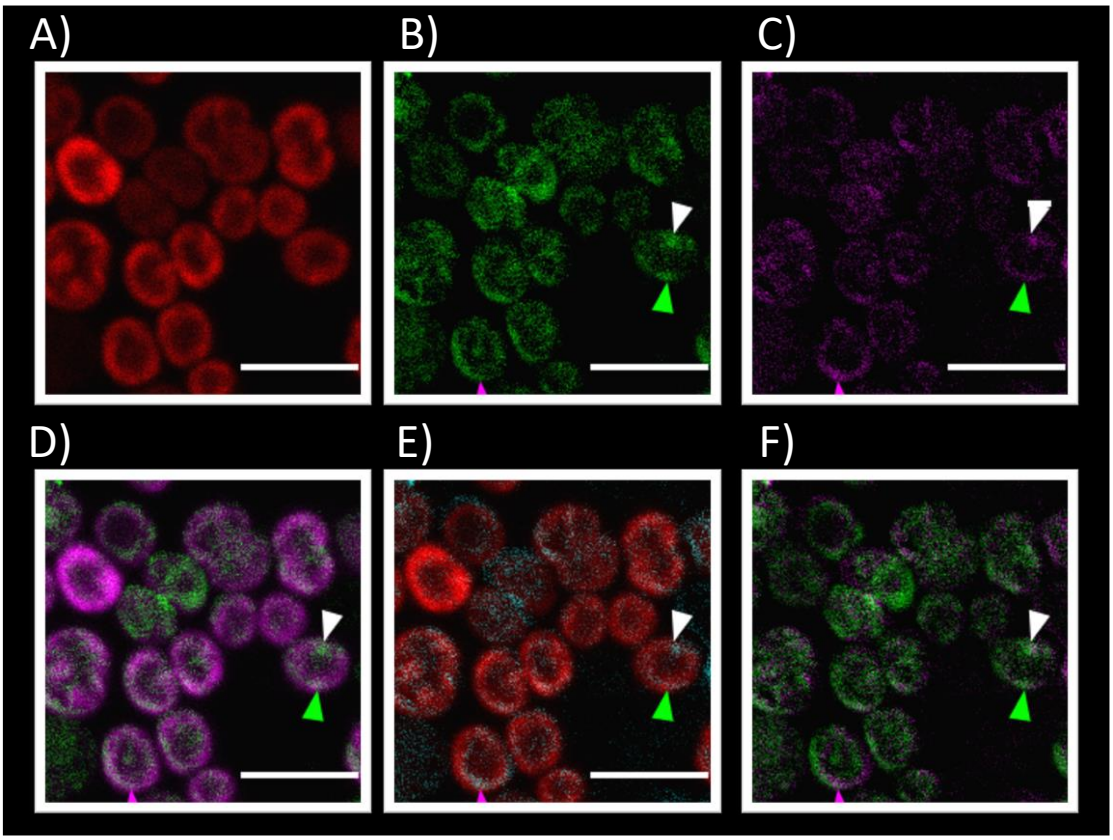

Figure 3-22: Anoxic Dark Adapted Nitrate Limited Mixotrophically Grown PCC 6803 *hoxFGFP ndhMYFP* at 20 μE.
A) Chlorophyll *a* channel. B) GFP channel. C) YFP channel. D) chlorophyll *a* (magenta) and GFP channels merged. E) Chlorophyll *a* and YFP (Cyan) channels merged. F) GFP and YFP (magenta) channels merged. The magenta arrow indicates NdhMYFP not co-localized with HoxFGFP. The white arrow indicates the distribution of HoxFGFP and NdhMYFP that is co-localized. The Green arrow indicates HoxFGFP that is not co-localized with NdhMYFP. The cyan arrow indicates a population of HoxFGFP localized to the cytoplasm. The scale bar represents 5 μm.

3.6.3 Pigment Comparison of the PCC 6803 Strains Grown Mixotrophically under Nitrate Limitation at 20 μE m^{-2} s^{-1}

The pigment composition of each of the tagged strains was compared under mixotrophic conditions at 20 μE $m^{-2}s^{-1}$ (Figure 3-23). The *hoxFGFP* strain had an increased carotenoid content with no real difference in the phycocyanin or chlorophyll *a* content when compared to wild type. The *ndhMYFP* strain also had a higher carotenoid content with no real difference in the phycocyanin or chlorophyll *a* content when compared to wild type. The *hoxFGFP ndhMYFP* strain showed no difference in either the phycocyanin or chlorophyll *a* content but had a decrease in carotenoids.

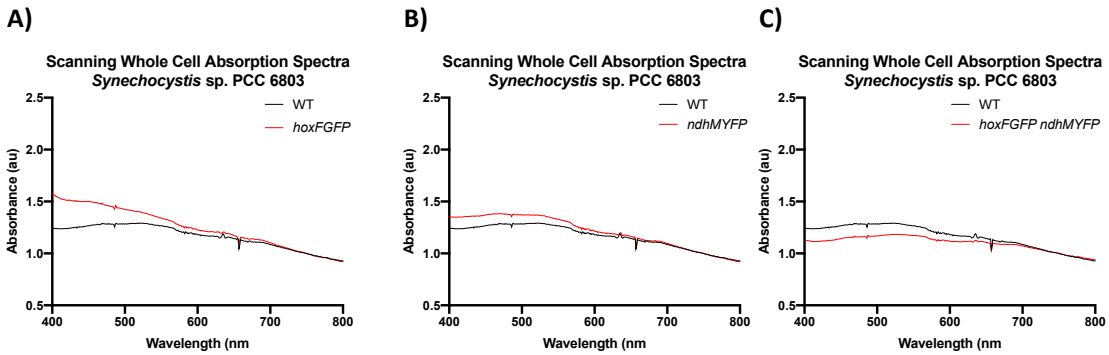

Figure 3-23: Scanning Whole Cell Absorption Spectra of PCC 6803 Strains Grown Mixotrophically Under Nitrate Limiting Conditions at 20 μE $m^{-2}s^{-1}$.
The scanning whole cell absorption spectra of PCC 6803 growth under mixotrophic nitrate limiting conditions at 20 μE $m^{-2}s^{-1}$. A) PCC 6803 WT (black line) compared to *hoxFGFP* (red line). B) WT (black line) compared to *ndhMYFP* (red line). C) WT (black line) compared to *hoxFGFP ndhMYFP* (red line). Each spectrum represents a biological triplicate (n=3).

3.6.4 Mixotrophic Nitrate Limited Growth at 60 μE m^{-2} s^{-1}

Hox was observed to be either dispersed (Figure 3-24 cyan arrow) or in puncta (green and white arrows). NDH-1 was predominantly in a dispersed population with few puncta being observed to be colocalized with Hox puncta (white).

Hox was colocalized with chlorophyll *a* (M=0.8439) therefore localized to the thylakoid. NDH-1 was observed to colocalize to the thylakoid (M=0.6734) and therefore being localized to the thylakoid. Hox showed colocalization with NDH-1 (M=0.6077).

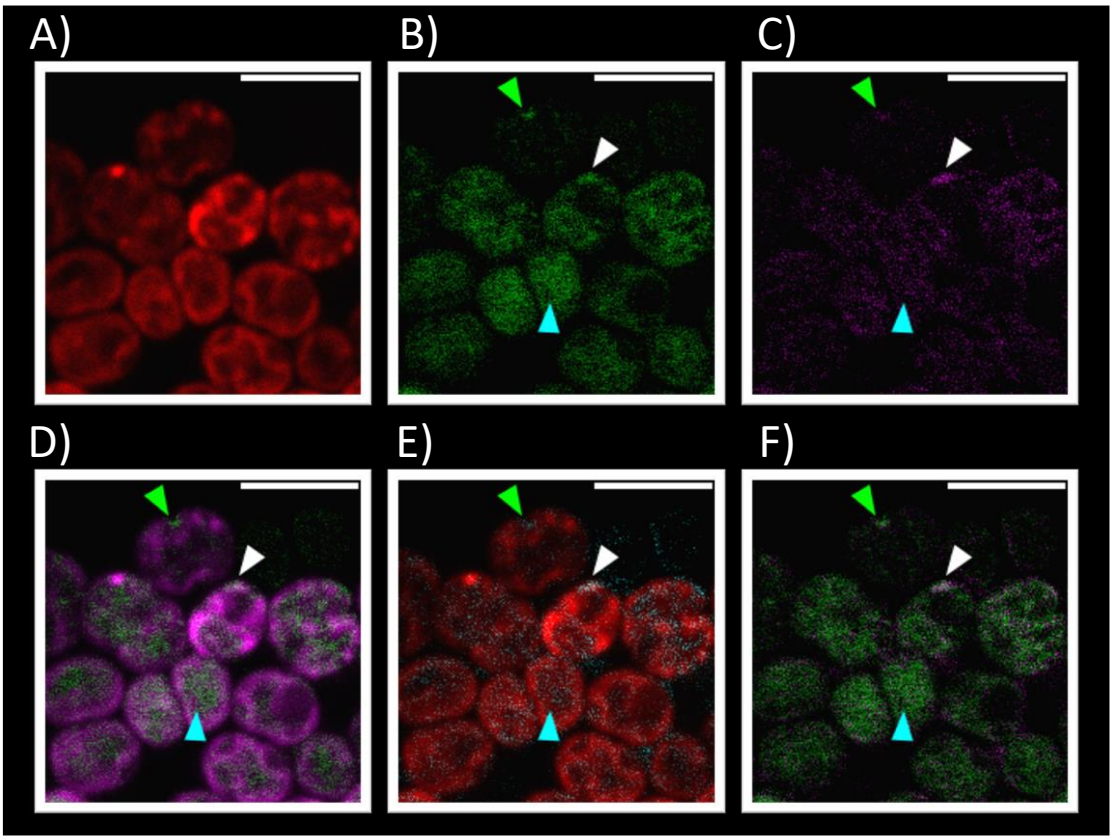

Figure 3-24: Nitrate Limited Mixotrophically Grown PCC 6803 *hoxFGFP ndhMYFP* at 60 μE.
A) Chlorophyll *a* channel. B) GFP channel. C) YFP channel. D) chlorophyll *a* (magenta) and GFP channels merged. E) Chlorophyll *a* and YFP (Cyan) channels merged. F) GFP and YFP (magenta) channels merged. The white arrow indicates a population of HoxFGFP and NdhMYFP puncta co-localized. The Green arrow indicates a HoxFGFP population forming a distinct puncta at the thylakoid. The cyan arrow indicates HoxFGFP localization to the cytoplasm. The scale bar represents 5 μm.

3.6.5 Anoxic Dark Adaptation Following Mixotrophic Nitrate Limited Growth at 60 μE m^{-2} s^{-1}

Under anoxic dark adapted conditions, Hox showed either dispersed or puncta populations. NDH-1 was mostly visible in puncta populations (Figure 3-25 white arrow) that showed colocalization with Hox puncta.

Hox colocalized with chlorophyll *a* (M=0.7859) showing a localization with the thylakoid. NDH-1 was colocalized with chlorophyll *a* (M=0.8057) indicating thylakoid localization. The Hox showed a degree of colocalization with NDH-1 (M=0.69) at the thylakoid.

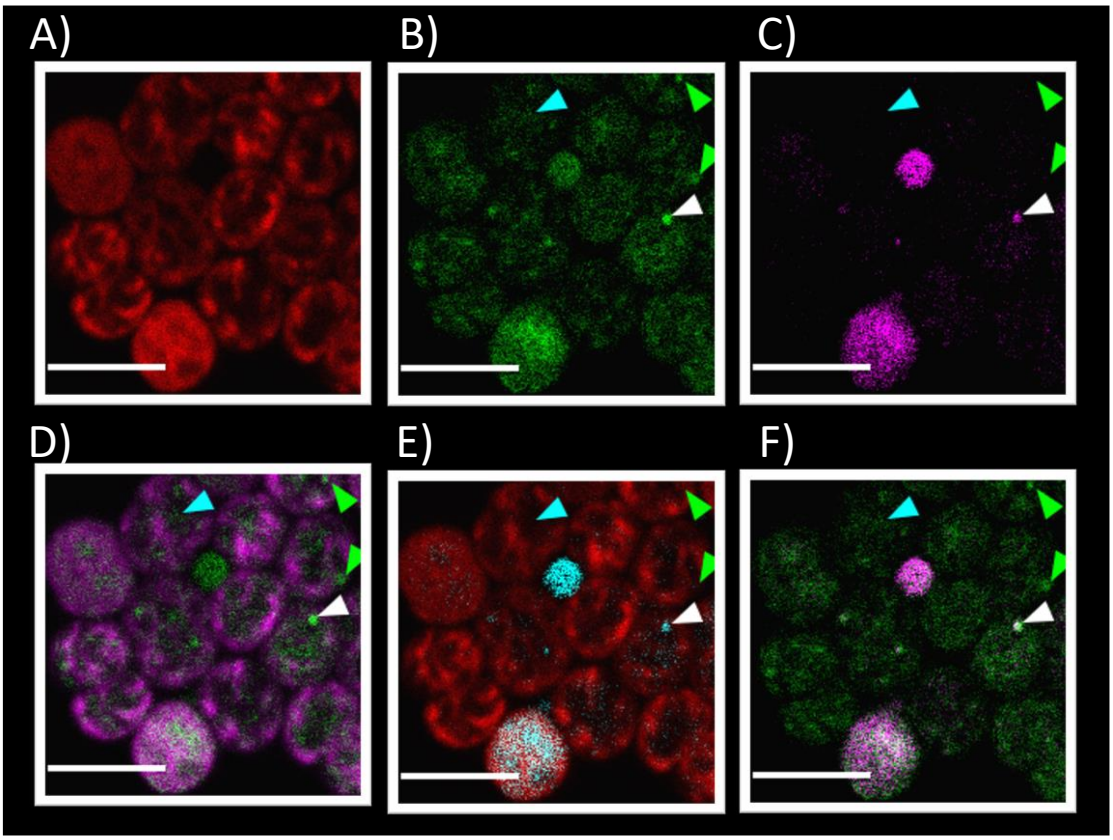

Figure 3-25: Anoxic Dark Adapted Nitrate Limited Mixotrophically Grown PCC 6803 *hoxFGFP ndhMYFP* at 60 μE.
A) Chlorophyll *a* channel. B) GFP channel. C) YFP channel. D) chlorophyll *a* (magenta) and GFP channels merged. E) Chlorophyll *a* and YFP (Cyan) channels merged. F) GFP and YFP (magenta) channels merged. The white arrow indicates a population of HoxFGFP and NdhMYFP puncta co-localized. The Green arrow indicates a HoxFGFP population forming a distinct puncta at the thylakoid. The cyan arrow indicates HoxFGFP localization to the cytoplasm. The scale bar represents 5 μm.

3.6.6 Pigment Comparison of the PCC 6803 Strains Mixotrophically Grown at 60 μE m^{-2} s^{-1}

The pigment composition of each of the tagged strains was compared following mixotrophic growth at 20 μE $m^{-2}s^{-1}$ (Figure 3-26). The *hoxFGFP* strain showed no difference in the levels of carotenoids, phycocyanin or chlorophyll *a* content when compared to wild type. The *ndhMYFP* stain had a reduction in the level of carotenoids, phycocyanin and the chlorophyll *a* content compared to wild type. The *hoxFGFP ndhMYFP* strain showed no real difference in the carotenoid, phycocyanin or chlorophyll *a* content when compared to wild type.

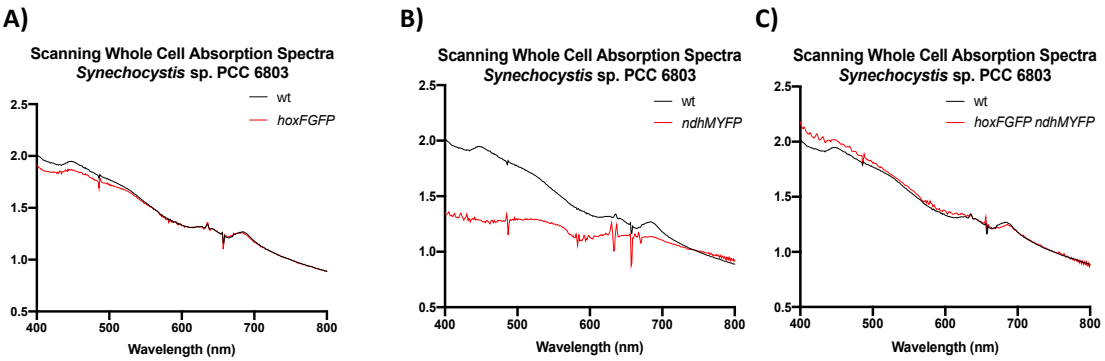

Figure 3-26: Scanning Whole Cell Absorption Spectra of PCC 6803 Strains Grown Mixotrophically Under Nitrate Limiting Conditions at 60 μE $m^{-2}s^{-1}$.
The scanning whole cell absorption spectra of PCC 6803 growth under mixotrophic nitrate limiting conditions at 60 μE $m^{-2}s^{-1}$. A) PCC 6803 WT (black line) compared to *hoxFGFP* (red line). B) WT (black line) compared to *ndhMYFP* (red line). C) WT (black line) compared to *hoxFGFP ndhMYFP* (red line). Each spectrum represents a biological triplicate (n=3).

3.6.7 Mixotrophic Nitrate Limited Growth at 200 μE m^{-2} s^{-1}

Nitrate limited growth at 200 μE m^{-2} s^{-1} led to patchy chlorophyll a fluorescence in the *hoxFGFP ndhMYFP* strain (Figure 3-27 A). Hox populations were either dispersed or in puncta. NDH-1 showed predominantly a dispersed distribution.

Hox was colocalized with chlorophyll *a* (M=0.7081) indicating thylakoid localization. NDH-1 colocalized with chlorophyll *a* (M=0.7728) showing thylakoid localization. Hox colocalized with NDH-1 (M=0.5587).

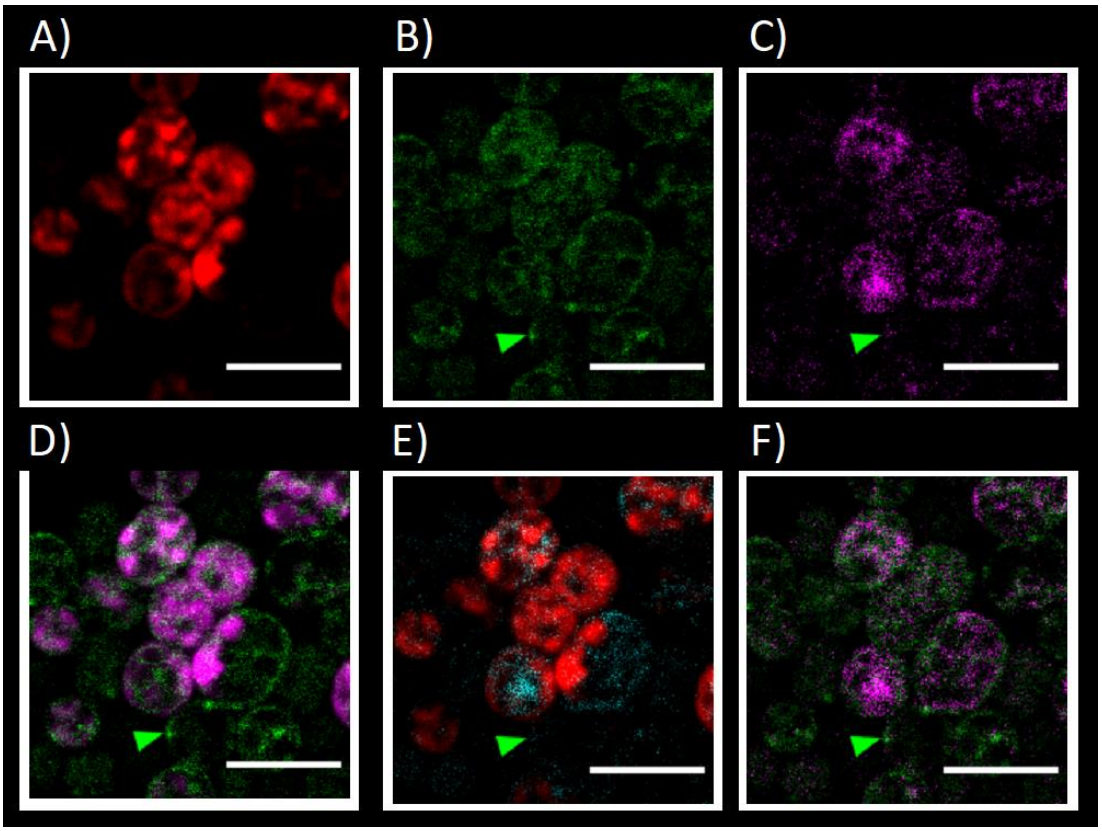

Figure 3-27: Nitrate Limited Mixotrophically Grown PCC 6803 *hoxFGFP ndhMYFP* at 200 μE.
A) Chlorophyll *a* channel. B) GFP channel. C) YFP channel. D) chlorophyll *a* (magenta) and GFP channels merged. E) Chlorophyll *a* and YFP (Cyan) channels merged. F) GFP and YFP (magenta) channels merged. The green arrow indicates a population of HoxFGFP puncta not co-localized with NdhMYFP. The scale bar represents 5 μm.

3.6.8 Anoxic Dark Adaptation following Mixotrophic Nitrate Limited Growth at 200 μE m^{-2} s^{-1}

Following anoxic dark adaptation, the chlorophyll *a* fluorescence was less patchy (compare Figure 3-27 and Figure 3-28 A). Hox had a dispersed and puncta population with the puncta being much more pronounced. NDH-1 showed a dispersed distribution.

Hox colocalized with chlorophyll *a* (M=0.8992) indicating that Hox is localized to the thylakoid. NDH-1 showed colocalization with chlorophyll *a* (M=0.7834) indicating thylakoid localization. Hox colocalized with NDH-1 (M=0.6547).

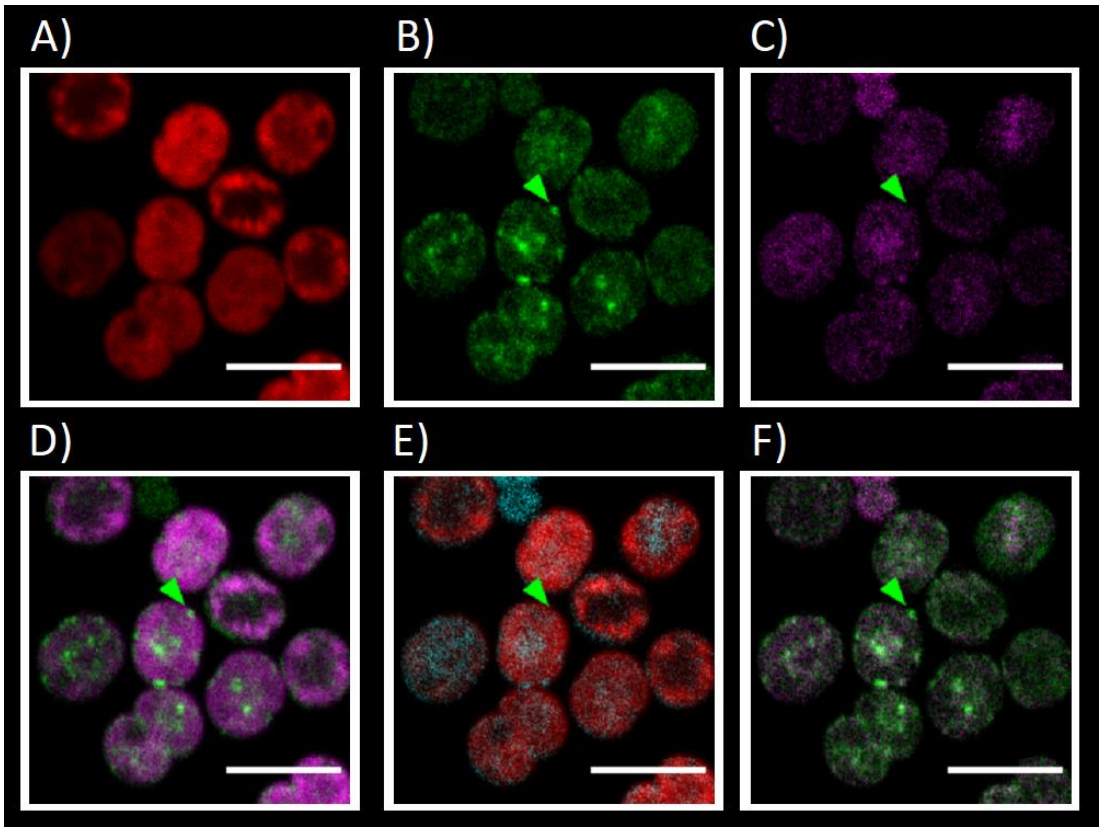

Figure 3-28: Anoxic Dark Adapted Nitrate Limited Mixotrophically Grown PCC 6803 *hoxFGFP ndhMYFP* at 200 μE.
A) Chlorophyll *a* channel. B) GFP channel. C) YFP channel. D) chlorophyll *a* (magenta) and GFP channels merged. E) Chlorophyll *a* and YFP (Cyan) channels merged. F) GFP and YFP (magenta) channels merged. The green arrow indicates a population of HoxFGFP puncta not co-localized with NdhMYFP. The scale bar represents 5 μm.

3.6.9 Pigment Comparison of the PCC 6803 grown Mixotrophically at 200 μE m^{-2} s^{-1}

The pigment composition of each of the tagged strains was compared following mixotrophic growth at 20 μE $m^{-2}s^{-1}$ (Figure 3-29). The *hoxFGFP* strain showed no difference in the level of carotenoids, phycocyanin or chlorophyll *a* content when compared to wild type. The *ndhMYFP* strain had significantly reduced carotenoid, phycocyanin and chlorophyll *a* content when compared to wild type. The *hoxFGFP ndhMYFP* strain showed no real difference in the carotenoid, phycocyanin or chlorophyll *a* content when compared to the wild type.

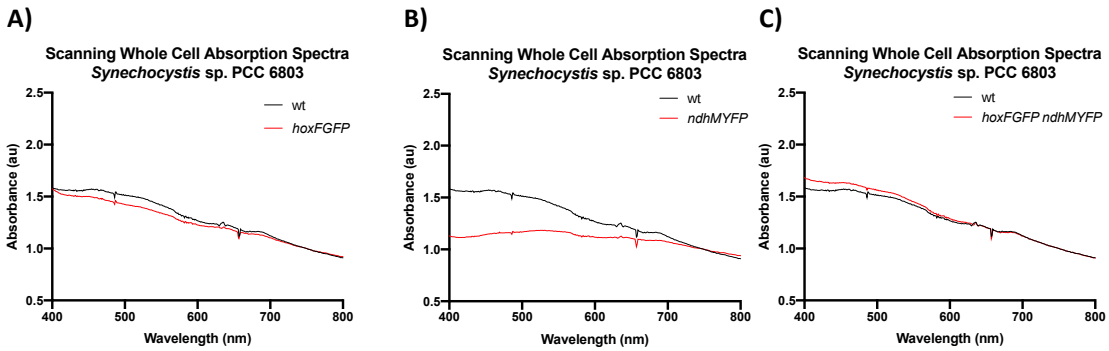

Figure 3-29: Scanning Whole Cell Absorption Spectra of PCC 6803 Strains Grown Mixotrophically Under Nitrate Limiting Conditions at 200 μE $m^{-2}s^{-1}$.
The scanning whole cell absorption spectra of PCC 6803 growth under mixotrophic nitrate limiting conditions at 200 μE $m^{-2}s^{-1}$. A) PCC 6803 WT (black line) compared to *hoxFGFP* (red line). B) WT (black line) compared to *ndhMYFP* (red line). C) WT (black line) compared to *hoxFGFP ndhMYFP* (red line). Each spectrum represents a biological triplicate (n=3).

3.7 Discussion

Error! Reference source not found. summarises the change in Manders coefficients comparing the light intensity of the growth conditions with H_2 measurements (Gutekunst, personal contact).

Table 3-1: Summary of Manders Coefficient and Changes in Hox/NDH-1 Colocalization.

		H2 Production?		Hox Colocalization with NDH-1 (Manders Coefficient)		
Light intensity ($\mu E\ m^{-2}s^{-1}$)	Growth	In Light	Anoxic Dark Adapted	Light	Anoxic Dark Adapted	Change When Anoxiic Dark Adapted
20	Photoautotrophic	No	Yes	0.964	0.786	Decrease
	Mixotrophic	No	Yes	0.854	0.443	Decrease
	Nitrate Limited Mixotrophic	No	Yes	0.559	0.854	Increase
60	Photoautotrophic	No	Yes	0.631	0.573	No Change
	Mixotrophic	No	Yes	0.486	0.579	No Change
	Nitrate Limited Mixotrophic	No	Yes	0.608	0.69	No Change
200	Photoautotrophic	No	Yes	0.539	0.407	No Change
	Mixotrophic	No	Yes	0.69	0.792	Increase
	Nitrate Limited Mixotrophic	No	Yes	0.541	0.686	Increase

Under photoautotrophic conditions, it was observed that Hox and NDH-1 were colocalized. At 20 and 60 $\mu E\ m^{-2}\ s^{-1}$, the colocalization increased when cells were anoxic and dark adapted which may suggest a role for electron transport with Hox/NDH-1 interactions under fermentative conditions. It is still unclear as to whether NDH-1 is facilitating electron delivery to Hox as there are still populations of Hox puncta not colocalized with the NDH-1 puncta. Interestingly, Hox was strongly colocalized to NDH-1 at 200 $\mu E\ m^{-2}\ s^{-1}$ which supports the idea of Hox behaving like an electron valve (Gutthann et al., 2007). There is also evidence to suggest a phenotype in PCC 6803 Hox mutants (Eckert et al., 2012) which was also observed in **Chapter 4** & **Chapter 6**.

The distribution of Hox in PCC 6803 has been studied primarily under photoautotrophic growth (Burroughs *et al*., 2014). Under these conditions, anoxic dark adapted cells exposed to light have the highest hydrogenase activity rate (Cournac *et al*., 2004) which was also shown to have the highest

Hox puncta count per cell at the thylakoid (Burrough *et al*., 2014). As it was shown previously that mixotrophic growth promoted H_2 evolution in PCC 6803 (Appel et al., 2020), it is interesting to observe Hox localized to the cytoplasm (Figure 3-15 & Figure 3-18). This was observed in the presence or absence of NdhMYFP, however there does seem to be a small population of Hox that shows co-localization with NDH-1.

This phenomenon requires further investigation as to the possible physiological role Hox could play in the cytoplasm. A possible role could be acting as an electron valve for the soluble electron carriers, namely NAD(P)H as it has been previously shown in cell lysate that NAD(P)H can act as an electron donor to Hox (Artz et al., 2020; Gutekunst et al., 2014). Interaction partners in the cytoplasm could be identified by carrying out GFP pull downs in PCC 6803 *hoxFGFP.* H_2 production in mixotrophic growth is observed during anoxia (Appel et al., 2020), Hox does redistribute to the thylakoid under anoxic dark adapted conditions (Figure 3-16 & Figure 3-19), which suggests that localization to the thylakoid is crucial in the evolution of H_2 with a correlation between puncta and hydrogenase activity (Burroughs et al., 2014). Comparing all light intensities tested for mixotrophic growth, all show an increase in Hox/NDH-1 colocalization. Comparing the mixotrophic growth with other culturing conditions, 20 and 200 $\mu E\ m^{-2}\ s^{-1}$ show a higher level of colocalization. Under mixotrophy, Hox may be mediating redox poise regulation in the cell (Artz et al., 2020) via NDH-1 (Gutekunst, 2018a) in order to support nitrate metabolism.

Under nitrate limited mixotrophic growth, PCC 6803 cells look sick at higher light intensities. Nitrate is an important electron sink for cyanobacteria competing with Hox for electrons (Baebprasert *et al*., 2011; Gutekunst *et al.,* 2014). Replacing nitrate with arginine eliminates an electron sink and the addition of reducing equivalents from glucose accounts for the increased H_2 evolution (Gutekunst, unpublished). This strategy for increasing H_2 evolution may be limited due to the stress that the cells are under.

One interesting observation is that following anoxic dark adaptation under nitrate limited mixotrophic growth the Hox puncta population appears

to shift from the NDH-1 foci to form independent Hox puncta, which agrees with the notion that NDH-1 is responsible for the majority of H_2 oxidation (Cournac *et al.,* 2004; Dutta & Vermaas 2016), however it is not clear if the remaining Hox puncta interacting with NDH-1 are contributing to H_2 evolution at the expense of plastoquinol.

At 20 $\mu E\ m^{-2}\ s^{-1}$, the colocalization of total Hox/NDH-1 populations decreased under anoxic dark adapted conditions, which could potentially highlight a change in interaction partner. At 60 and 200 $\mu E\ m^{-2}\ s^{-1}$ the colocalization between Hox/NDH-1 increased under anoxic dark adaptation. It is not clear whether this increase in colocalization is within the dispersed population or the puncta. As the puncta populations of Hox (Burroughs et al., 2014) and NDH-1 (L. N. Liu et al., 2012) were shown to correlate with the function of each respective complex, a better understanding of complex localization and interaction is required to tie this to increased H_2 evolution.

4 Distribution of HoxYGFP, HoxEGFP and HoxFGFP in Various Hox Mutants of *Synechocystis* sp. PCC 6803

4.1 Introduction

In the literature there is a lack of understanding of the localization of Hox subunits *in-vivo* with the most detailed studies being carried out in PCC 6803(Burroughs et al., 2014). Recently it has been demonstrated that the purified Hox subcomplex HoxEFU can catalyse redox reactions *in-vitro* independent of the HoxYH subunits (Artz et al., 2020). Ferredoxin 1 and flavodoxin dependant reduction of NAD^+/NAD(P) show that HoxEFU can mediate the redox poise *in-vitro* (Artz et al., 2020), however, it still remains unclear if these redox reactions are being carried out by HoxEFU *in-vivo*.

Artz also demonstrated the binding of ferredoxin 1 to HoxEFU with ferredoxin 1 making contact with each of the subunits. However, a fundamental understanding of how Hox interacts with the photosynthetic electron transport chain is still lacking. By tagging different Hox subunits with GFP and pulling down proteins that interact with the Hox subunits we will gain a better understanding of where exactly in the photosynthetic electron transport chain Hox is interacting and how this changes with localisation. The added benefit of using GFP tagging for pull down experiments is that *in-vivo* localisation of Hox can be determined. This can also allow investigations of sub-complex distribution *in-vivo* as it has been demonstrated that *hox* mutants result in higher rates of Hox turnover as observed in PCC 6803 Δ*hoxYH* (Burroughs et al., 2014; Eckert et al., 2012).

An understanding of the distribution of Hox during maturation may give better insights into strain engineering to maximize the amount of fully mature Hox. A significant proportion of our understanding of [NiFe] hydrogenase maturation has come from genetic/biochemical studies in *E. coli* (M. Blokesch et al., 2002; Lacasse & Zamble, 2016). The Fe atom is ligated to 2 CN and one CO molecules (Shomura & Higuchi, 2013). The metabolic origins of the CO ligand are unknown with the CN ligand being synthesized by HypF from carbomyoylphosphate (Paschos et al., 2002) with HypE transferring the CN ligand to the Fe atom (Melanie Blokesch, Paschos, et al., 2004). It is believed that the $Fe(CN)_2CO$ is inserted into the large hydrogenase subunit after

coordinating the CO and CN ligands to Fe (Löscher et al., 2005; Winter et al., 2005).

The Ni is delivered to the large hydrogenase subunit by HypA and HypB (Maier et al., 1993). The hydrolysis of GTP by HypB promotes the release of Ni via the N-terminus of HypA and subsequent insertion into the large hydrogenase subunit (Melanie Blokesch, Rohrmoser, et al., 2004; Bock, 1995). All of the afore mentioned maturation factors have been identified and genetically confirmed in PCC 6803 (Hoffmann et al., 2006). PCC 6803 was shown to have two *hypA* homologues (*hypA1* [slr1675] & *hypA2* [sll1078]) and two *hypB* genes (*hypB1* [sll1432] & *hypB2* [sll1079]) with *hypA1/hypB1* being specific for HoxH maturation (Hoffmann et al., 2006). The final part of the hydrogenase maturation process involves the cleavage of the C-terminus of the large sub-unit by the protease *hoxW,* which is specific for Hox H (Hoffmann et al., 2006). Figure 4-1 summarizes the Hox maturation process.

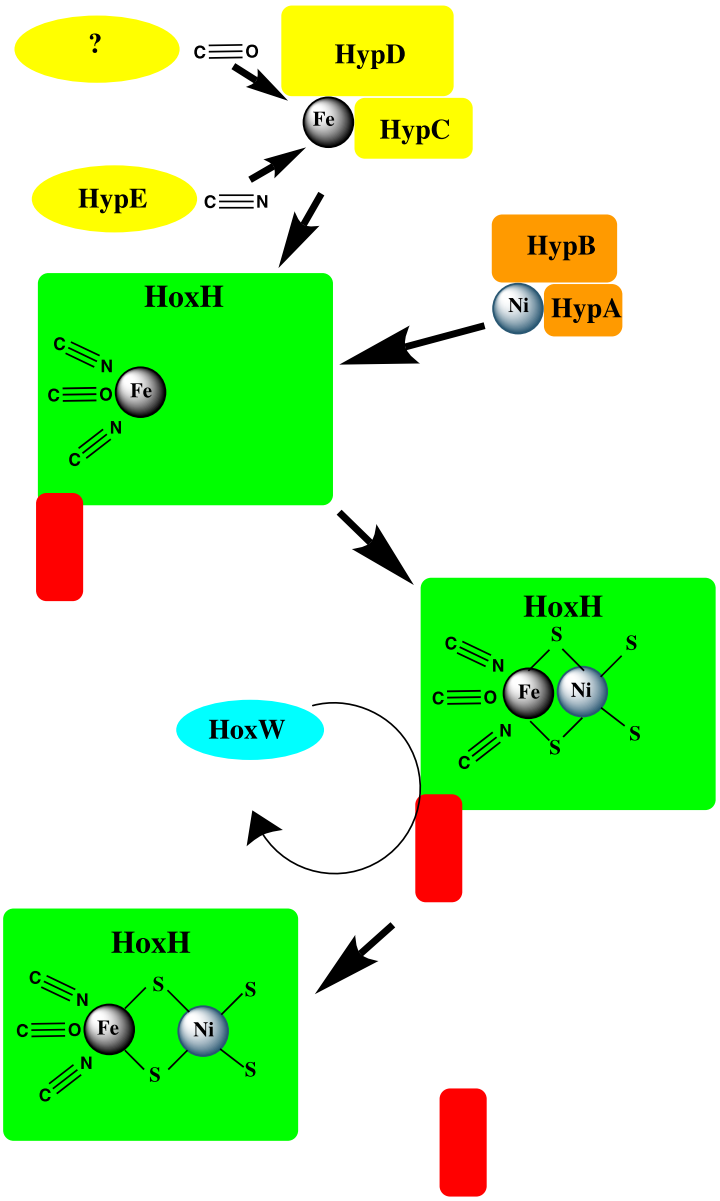

Figure 4-1: [NiFe] Hydrogenase Maturation overview.
The maturation of [NiFe] hydrogenases is carried out in a step-by-step manner. The Fe atom is inserted into the large sub-unit (HoxH - green) after CO and CN coordinate to the Fe atom (HypC [ssl3580], HypD [slr1498] & HypE [sll1462] – yellow). HypF (sll0322) is involved in biosynthesis of CN from carbamoyl phosphate (not shown). The Ni atom is inserted into HoxH (HypA1 [slr1675] & HypB1 [sll1432] – orange) coordinated by S from cysteine residues. HoxH is fully matured by the cleavage of the C-terminus (red) by HoxW (cyan [slr1876]).

The stability of the entire complex is dependent on the presence of other sub-units (Eckert et al., 2012). It was demonstrated that in PCC 6803 wild type, Hox can exist as either an entire complex (HoxEFUYH) or alternatively as either individual subcomplexes; HoxFUYH, HoxEFU, HoxFU or as free protein subunits (Eckert et al., 2012). Previous research has shown that in HoxFGFP fluorescence is significantly reduced in the Δ*hoxYH*

background (Burroughs et al., 2014). The authors hypothesizing that this may be down to reduced stability of the subcomplexes in the absence of functional hydrogenase.

Deletion of the diaphorase subunits *hoxF* and *HoxU* showed no accumulation of subcomplexes highlighting the interdependence of the diaphorase subunits with regards to complex stability (Eckert et al., 2012). Interestingly, though the Δ*hoxE* strain showed an increase in the abundance of Hox subunits in subcomplexes (Eckert et al., 2012). In the Δ*hoxE* strain H_2 evolution was only observed to be 70% of the wild type level, and H_2 was only generated following supplementation with reduced methyl viologen (Eckert et al., 2012). This was shown to correlate directly to localization of Hox (Burroughs et al., 2014).

It has recently been shown that a PsaD-HoxY fusion in PCC 6803 could produce photobiological H_2 (Appel et al., 2020). With the fusion, electrons could be passed directly to HoxY from photosystem I with limited H_2 oxidation (Appel et al., 2020). In this study, the immobilization of HoxYH to photosystem I showed no measurable H_2 uptake and had a lower H_2 evolution rate, suggesting the interaction partner responsible for H_2 oxidation is perturbed and optimization of electron transfer from F_B of PsaC to the 4Fe4S cluster of HoxY is required in order to maximize H_2 production (Appel et al., 2020). This comes with a fitness cost in PCC 6803 as the PsaD-HoxY fusion showed significant growth defects presumably due to the lack of reducing equivalents, derived from PS I entering cellular metabolism (Appel et al., 2020). A greater understanding of how Hox is interacting with the photosynthetic electron transport chain could provide alternative engineering strategies that allow electrons to be redirected to Hox. Engineering based on the localization of Hox rather than direct fusions to PSI may alleviate the growth defect observed in PCC 6803 Δ*psaD-hoxY* (Appel et al., 2020).

In this chapter, the distribution of Hox will be assessed in several Hox mutants in PCC 6803. The distribution of Hox in PCC 6803 Δ*hoxYH* was similar to the distribution previously reported (Burroughs et al., 2014). In the

Δ*hoxW* background, where HoxH is not fully matured, HoxFGFP showed a similar distribution pattern to the Δ*hoxYH* strain.

The hydrogenase subunit (HoxYH) has previously been shown to accept electrons directly from photosystem I (Appel et al., 2020) and could potentially form HoxYH sub-complexes (Eckert et al., 2012) which have different interaction partners compared to HoxFGFP. HoxYGFP distribution was investigated to visualize the localization of the HoxYH subcomplex and its interaction partners. The HoxYGFP distribution was similar to the localization seen in the HoxFGFP in the Δ*hoxE* background, e.g., localized to the cytoplasm.

Given the distinct localization seen in the Δ*hoxE* background, e.g., cytoplasmic vs thylakoid, a HoxEGFP strain was generated to identify the specific interaction partners at the two locations through pull-downs. It was shown that the HoxEGFP had a similar distribution as HoxYGFP.

4.2 Physiological Characterisation of *Synechocystis* sp. PCC 6803 Δ*hoxYH* & Δ*hoxW*

Hox activity was measured using a Clark electrode to measure the maximum hydrogenase evolution rate by adding dithionite and methyl viologen to cells in the chamber as previously described (Gutthann et al., 2007; Hoffmann et al., 2006). The maximum H_2 evolution rate was determined by removing oxygen and supplying Hox with electrons using reduced methylviologen as previously described (Gutthann et al., 2007; Hoffmann et al., 2006). The slope of the line was calculated and used to determine H_2 evolution rate. The Hox activity was assessed in both the Δ*hoxW and* Δ*hoxYH* strains, to confirm that neither strain was capable of H_2 evolution. This is essential to ensure that the strains are correct. **Error! Reference source not found.** shows the measured Hox activity of each PCC 6803 strain. As expected, there was no Hox activity detected in Δ*hoxYH* and Δ*hoxW*, verifying the previously published results (Eckert et al., 2012; Hoffmann et al., 2006).

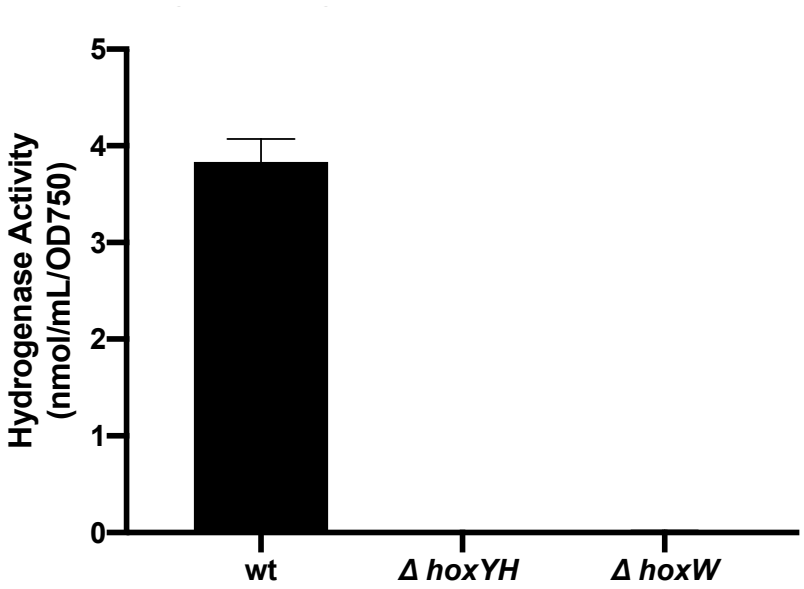

Figure 4-2: Hydrogenase Activity of *Synechocystis* sp. PCC 6803 Strains. Hydrogenase activity of *Synechocystis* sp. PCC 6803 strains determined by SHE and standardized to OD_{750}. Each measurement is a biological triplicate with the error bar representing the standard error of the mean.

To assess the differences in the pigment composition between the strains, scanning whole cell absorption spectra was utilized, to compare the

pigment composition across the strains following 3 days of growth. Figure 4-3 shows there was a small increase in chlorophyll *a and* phycocyanin content in Δ*hoxYH* and Δ*hoxW* compared to the wild type strain (**Error! Reference source not found.**Figure 4-3 A & B). No significant difference was observed between *hoxFGFP* in the different background strains (**Error! Reference source not found.**Figure 4-3 C-E). There was no significant difference in the phycocyanin:chlorophyll *a* ratios observed between the strains (**Error! Reference source not found.**Figure 4-3 F).

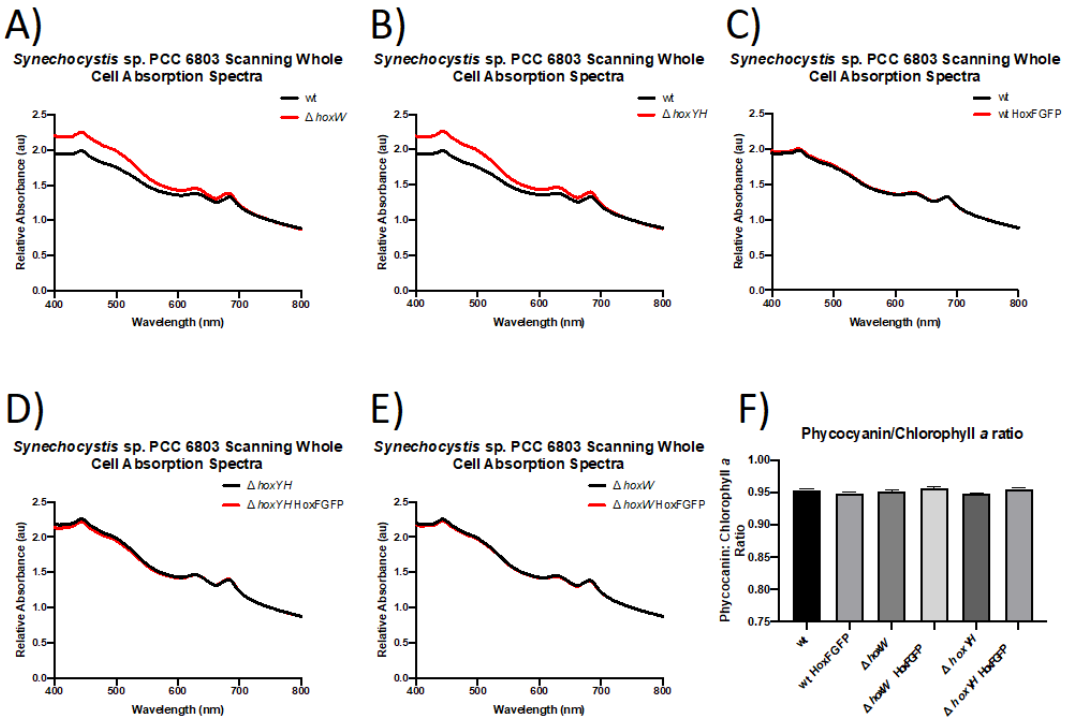

Figure 4-3: Scanning Whole Cell Absorption Spectra and Phycocyanin:Chlorophyll *a* of PCC 6803 strains.
The scanning whole cell absorption spectra of each fluorescent protein tagged Hox subunit was measured prior to microscopy. A) PCC 6803 WT (black line) compared to Δ *hoxW* (red line). B) WT (black line) compared to Δ *hoxYH* (red line). C) WT (black line) compared to *hoxFGFP*. D) PCC 6803 Δ *hoxYH* (black line) compared to Δ *hoxYH hoxFGFP* (red line). WT (black line) compared to Δ *hoxW* (red line). E) PCC 6803 Δ *hoxW* (black line) compared to Δ *hoxW hoxFGFP* (red line). F) Phycocyanin:Chlorophyll *a* ratios of each strain. Error bars represent the standard error of the mean (n=3).

4.3 HoxFGFP Distribution in PCC 6803 Δ*hoxYH* and Δ*hoxW*

4.3.1 Introducing the HoxFGFP Construct into PCC 6803 Δ*hoxW*

The Δ*hoxYH hoxFGFP* strain was obtained from a previous study (Burroughs et al., 2014). The HoxFGFP construct was transformed into the natural *hoxF* locus (sll1221) in the Δ*hoxW* background. The objective being to assess complex stability in the absence of a functional Hox. Given previous data has shown that subunit stability is decreased in both the Δ*hoxH* and Δ*hoxW* strains (Gutekunst, unpublished) similar to Δ*hoxYH* (Eckert et al., 2012).

4.3.2 Spatial Distribution of Hox in PCC 6803 *ΔhoxYH* and *ΔhoxW*

Hox distribution was assessed under photoautotrophic growth at a light intensity of 60 μE m^{-2} s^{-1}. Photoautotrophic growth has previously shown a reduction in fluorescence in the Δ*hoxYH hoxFGFP* strain compared to the *hoxFGFP* (Burroughs et al., 2014). To remove autofluorescence from chlorophyll and other pigments naturally present in PCC 6803, wildtype cells were used as a control with no GFP expression. **Error! Reference source not found.**Figure 4-4 shows that there is no significant autofluorescence detected in the GFP channel.

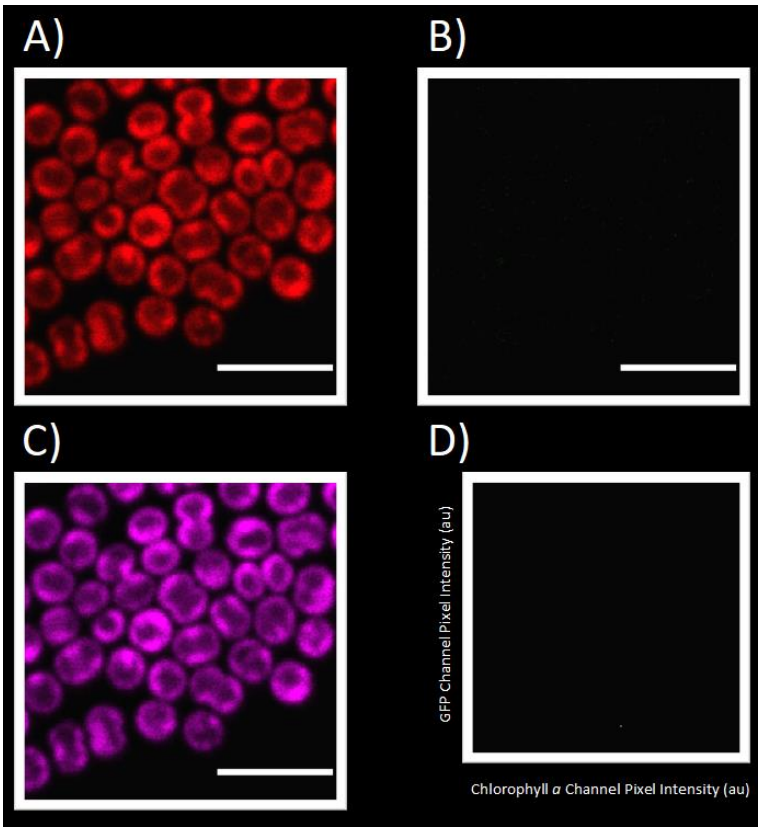

Figure 4-4: PCC 6803 WT Grown Photoautotrophically at 60 μE.
Photoautotrophic growth of PCC 6803 WT A) Chlorophyll *a* channel. B) GFP channel. C) Merge of chlorophyll *a* (magenta) and GFP channels. D) 2D xy-scatter of the co-localized chlorophyll *a* and GFP co-localized pixel intensities. The scale bar represents 5 μm.

Before assessing the distribution of HoxFGFP in the Δ *hoxW* and Δ *hoxYH* backgrounds, the distribution of the hydrogenase complex was assessed under different light conditions. Under photoautotrophic growth in the wild type background, Hox appears to be colocalized with the chlorophyll *a* (**Error! Reference source not found.**Figure 4-5, panels B & C green arrow) and therefore localized to the thylakoid. The Manders coefficient (M) illustrates the proportion of HoxFGFP colocalized with chlorophyll *a* pixels. Hox was shown to be colocalized with chlorophyll *a* (M=0.732). A positive correlation between chlorophyll *a* and HoxFGFP pixel intensity channels was observed (R=0.46) indicating that Hox is localized to regions of the thylakoid that correlate with chlorophyll *a* content. This agrees with the previous publication (Burroughs et al., 2014).

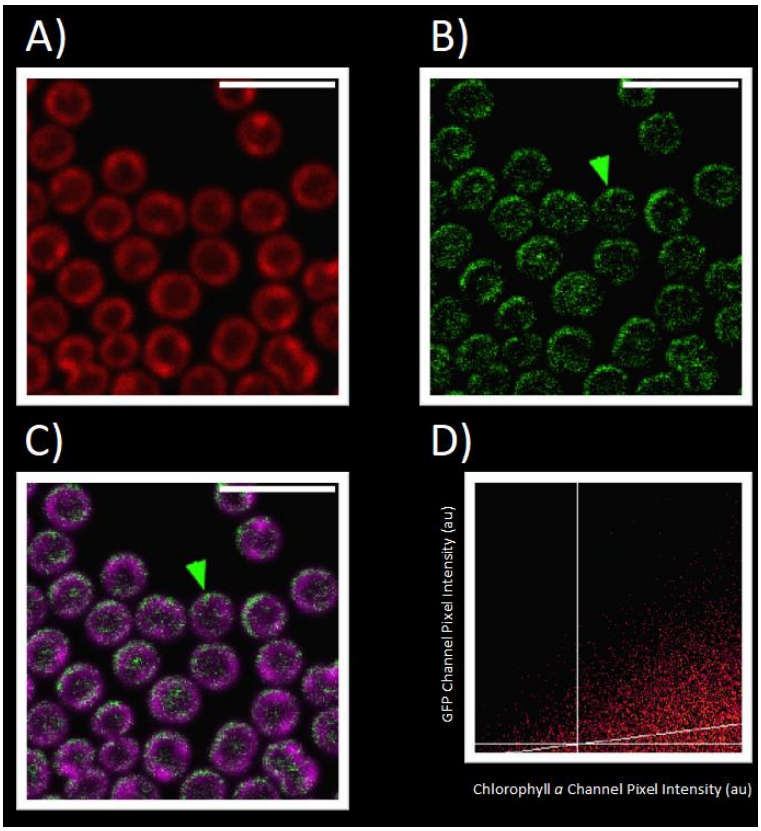

Figure 4-5: PCC 6803 *hoxFGFP* Grown Photoautotrophically at 60 μE.
Photoautotrophic growth of *Synechocystis* sp. PCC 6803 *hoxFGFP*. A) Chlorophyll *a* channel. B) GFP channel. C) Merge of chlorophyll *a* (magenta) and GFP channels. D) 2D xy-scatter of the chlorophyll *a* and GFP co-localized pixel intensities. The scale bar represents 5 μm.

The previous observation that deletion of *hoxYH* causes a decrease in HoxFGFP fluorescence (Burroughs et al., 2014) was presumably a result of Hox complex stability (Eckert et al., 2012), this experiment set out to verify this observation. PCC 6803 Δ*hoxYH* was scanned under the same conditions as above to test if there were any changes in the spectral properties that may need to be accounted for during image analysis. **Error! Reference source not found.** shows that there is no significant autofluorescence detected (**Error! Reference source not found.Error! Reference source not found.** B & C).

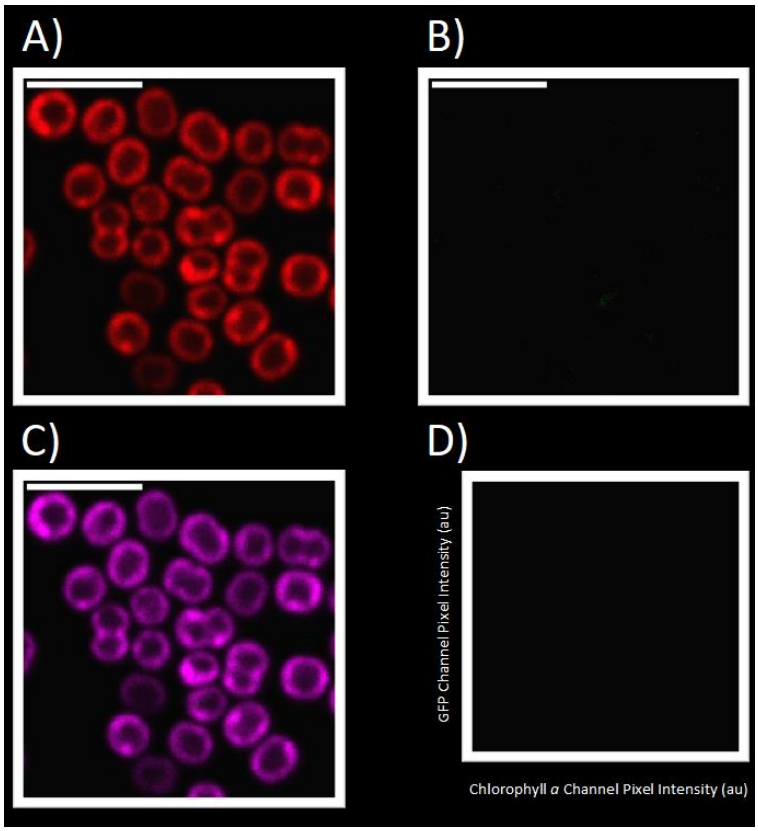

Figure 4-6: PCC 6803 Δ *hoxYH* Grown Photoautotrophically at 60 μE.
Photoautotrophic growth of PCC 6803 Δ *hoxYH*. A) Chlorophyll *a* channel. B) GFP channel. C) Merge of chlorophyll *a* (magenta) and GFP channels. D) 2D xy-scatter of the chlorophyll *a* and GFP co-localized pixel intensities. The scale bar represents 5 μm.

Under photoautotrophic conditions, the HoxFGFP signal in the Δ*hoxYH hoxFGFP* strain was appreciably lower than the signal observed in the wild type background (compare Figure 4-5 **Error! Reference source not found.** panel B with **Error! Reference source not found.**Figure 4-7 panel B). The majority of the HoxFGFP pixels colocalize with chlorophyll *a* (M=0.998) showing a positive correlation (R=0.41). Together these results agree with previous microscopy imaging (Burroughs et al., 2014) and previous proteomic work (Eckert et al., 2012) with the GFP fluorescence from Hox being barely detectable.

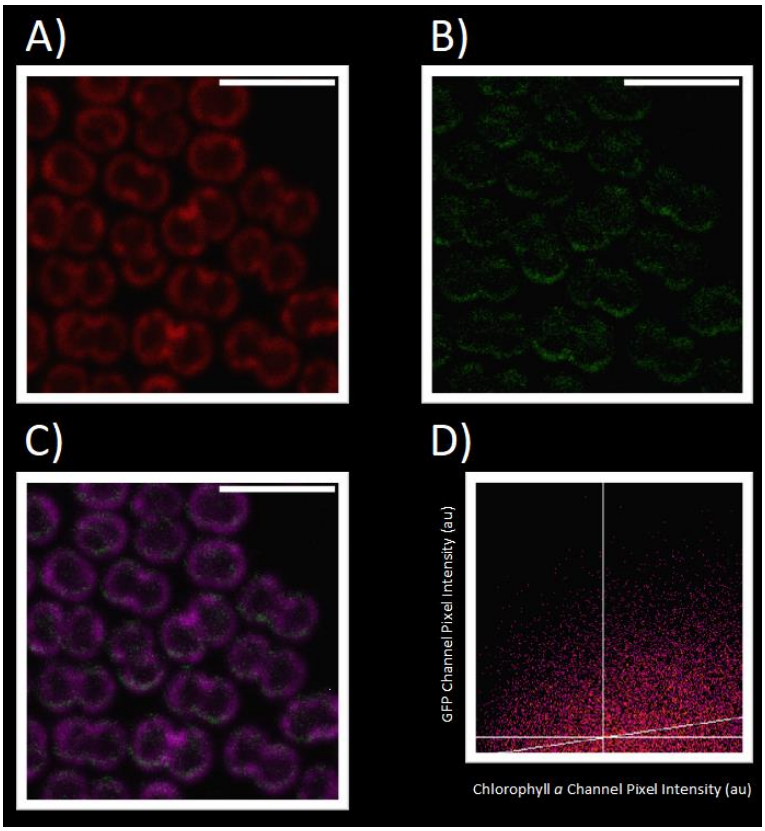

Figure 4-7: PCC 6803 Δ *hoxYH hoxFGFP* Grown Photoautotrophically at 60 μE. Photoautotrophic growth of PCC 6803 Δ *hoxYH hoxFGFP*. A) Chlorophyll *a* channel. B) GFP channel. C) Merge of chlorophyll *a* (magenta) and GFP channels. D) 2D xy-scatter of the chlorophyll *a* and GFP co-localized pixel intensities. The scale bar represents 5 μm.

HoxW functions by proteolytically processing the HoxH subunit generating a mature hydrogenase (Hoffmann et al., 2006). Therefore, to evaluate if impeded maturation impacts on the distribution and fluorescence of Hox, Δ*hoxW* was utilized. Autofluorescence was evaluated as previously stated. **Error! Reference source not found.**Figure 4-8 shows that there was no significant autofluorescence detected in the GFP channel in PCC 6803 Δ*hoxW* (Figure 4-8**Error! Reference source not found.** B & C).

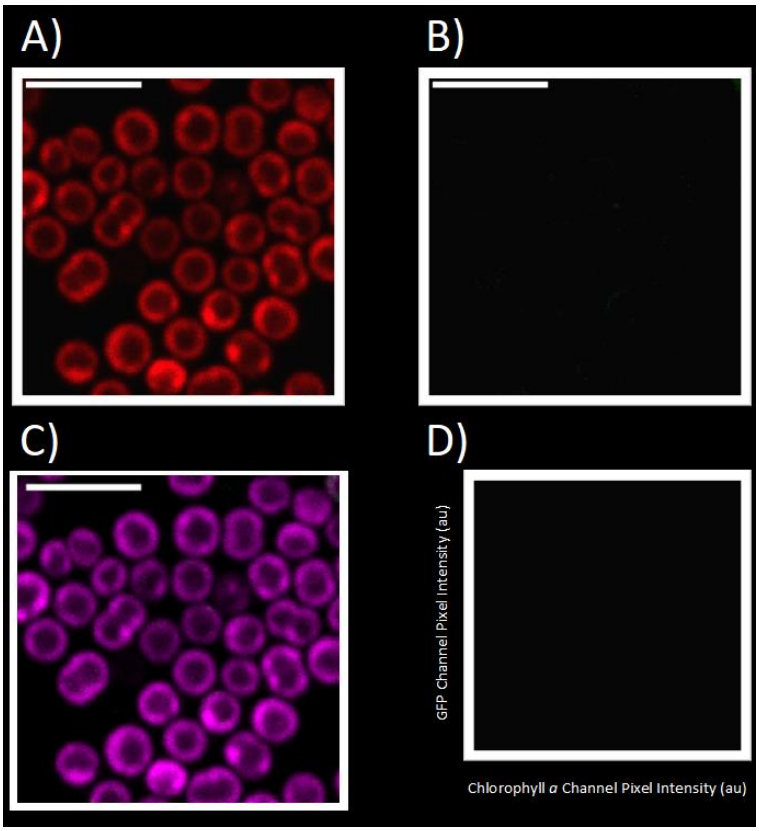

Figure 4-8: PCC 6803 Δ *hoxW* Grown Photoautotrophically at 60 μE.
Photoautotrophic growth of PCC 6803 Δ *hoxW*. A) Chlorophyll *a* channel. B) GFP channel. C) Merge of chlorophyll *a* (magenta) and GFP channels. D) 2D xy-scatter of the chlorophyll *a* and GFP co-localized pixel intensities. The scale bar represents 5 μm.

HoxFGFP in the Δ*hoxW* background had a similar level of fluorescence intensity to the Δ*hoxYH* strain (compare **Error! Reference source not found.** panel B with **Error! Reference source not found.**Figure 4-7 panel B). Hox showed a high level of colocalization with chlorophyll *a* (M=0.915). A positive correlation exists between the HoxFGFP and chlorophyll *a* pixel intensity (R=0.36). Together this data shows that the HoxFGFP in the Δ*hoxW* strain displays a similar distribution and pixel intensity profile as the Δ*hoxYH* strain.

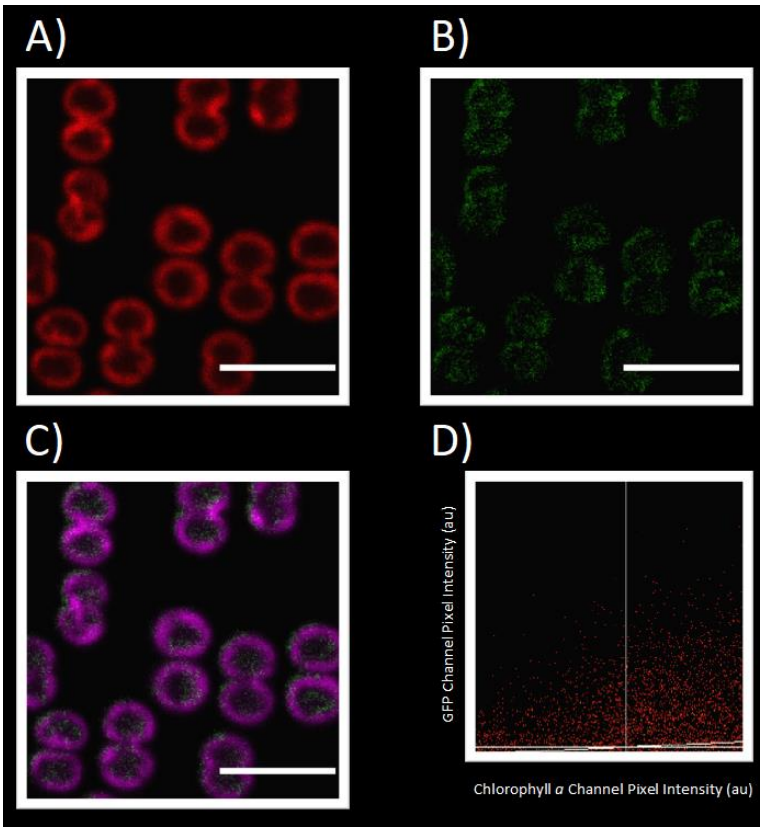

Figure 4-9: PCC 6803 Δ *hoxW hoxFGFP* Grown Photoautotrophically at 60 μE. Photoautotrophic growth of PCC 6803 Δ *hoxW hoxFGFP*. A) Chlorophyll *a* channel. B) GFP channel. C) Merge of chlorophyll *a* (magenta) and GFP channels. D) 2D xy-scatter of the chlorophyll *a* and GFP co-localized pixel intensities. The scale bar represents 5 μm.

4.4 Distribution of HoxEGFP and HoxYGFP in PCC 6803

4.4.1 Pigment Composition and Distribution of HoxEGFP and HoxYGFP

Hox is split into 2 functional moieties; the hydrogenase and diaphorase subunits, therefore both HoxE and HoxY were tagged with GFP to investigate localization differences between the subcomplexes and Hox. HoxY was tagged at the C-terminus with eGFP. The HoxE subunit has been shown to localize Hox to the thylakoid (Burroughs et al., 2014), therefore HoxE was tagged with eGFP for localization and pull downs in order to investigate the specific interaction partners of HoxE at the thylakoid. The added benefit of using a fluorescent protein tag in pull downs is that *in-vivo* localization can be observed under the same conditions that the pull-downs are carried out under.

To assess any differences in pigment composition between the strains prior to microscopic analysis, scanning whole cell absorption spectra was carried out. **Error! Reference source not found.**Figure 4-10 shows that there is no significant difference in the spectra between the strains under these growth conditions.

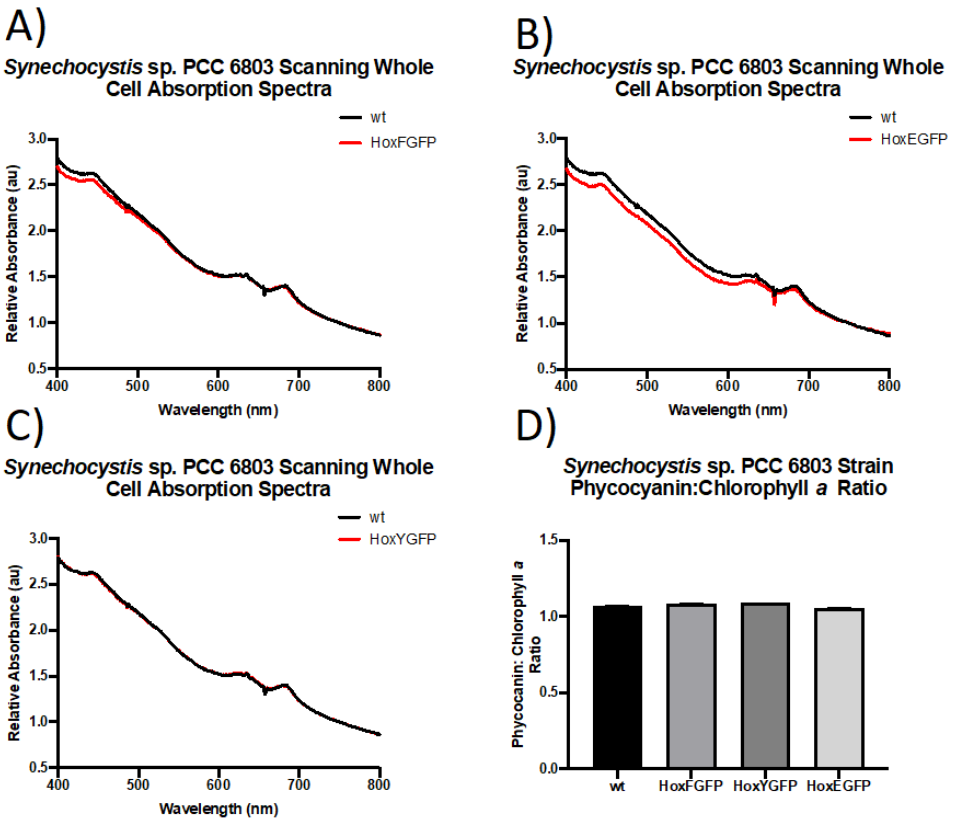

Figure 4-10: Scanning Whole Cell Absorption Spectra and Phycocyanin:Chlorophyll *a* Ratio.
The scanning whole cell absorption spectra of each fluorescent protein tagged Hox subunit was measured prior to microscopy. A) PCC 6803 wild type (black line) compared to HoxFGFP (red line). B) PCC 6803 wild type (black line) compared to HoxEGFP (red line). C) PCC 6803 wild type (black line) compared to HoxYGFP. D) Phycocyanin:Chlorophyll *a* ratios of each strain. Error bars represent the standard error of the mean (n=3).

4.4.2 Spatial Distribution of HoxEGFP and HoxYGFP in PCC 6803 Grown Photoautotrophically at 60 μE m^{-2} s^{-1}.

As a control, the PCC 6803 wild type strain was scanned under the same conditions as the fluorescent protein tagged strains. Figure 4-11 **Error! Reference source not found.** demonstrates that there is no significant fluorescence measured from the wild type cells in the GFP channel.

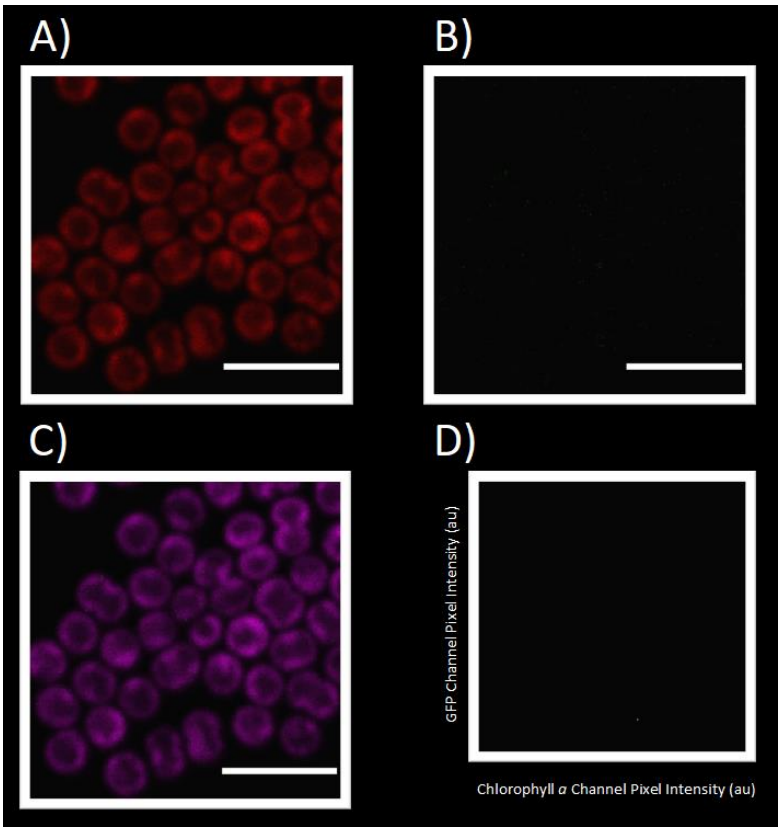

Figure 4-11: PCC 6803 Wild Type Grown Photoautotrophically at 60 μE.
Photoautotrophic growth of PCC 6803 wild type. A) Chlorophyll *a* channel. B) GFP channel. C) Merge of chlorophyll *a* (magenta) and GFP channels. D) 2D xy-scatter of the chlorophyll *a* and GFP co-localized pixel intensities. The scale bar represents 5 μm.

In the *hoxEGFP* strain, Hox is predominantly localized in the cytoplasm (**Error! Reference source not found.**Figure 4-12, panel C, green arrows). This is evident given a lower proportion of Hox is colocalized with chlorophyll *a* (M=0.559) compared to Hox localization in the *hoxFGFP* strain. Considering the pixel intensity, there is a positive correlation between chlorophyll *a* and Hox pixel intensity (R=0.46). There also seems to be small populations of Hox localized to the thylakoid either as puncta (**Error! Reference source not found.**Figure 4-12 yellow arrows) or protein aggregates in large patches of the thylakoid (white arrow).

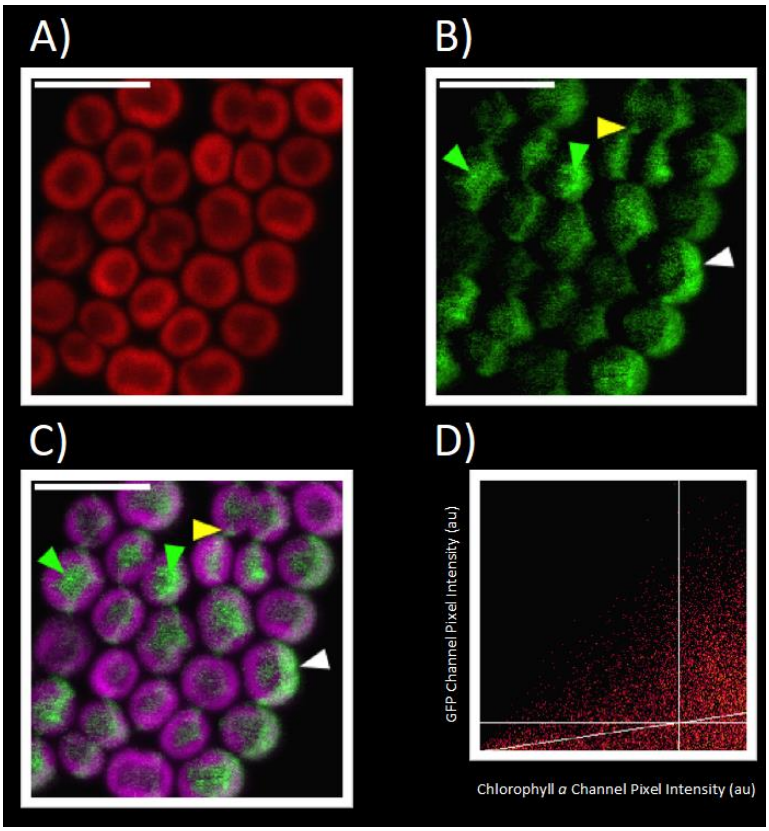

Figure 4-12: PCC 6803 HoxEGFP Grown Photoautotrophically at 60 μE. Photoautotrophic growth of PCC 6803 HoxEGFP. A) Chlorophyll *a* channel. B) GFP channel. C) Merge of chlorophyll *a* (magenta) and GFP channels. D) 2D xy-scatter of the chlorophyll *a* and GFP pixel intensities. The scale bar represents 5 μm.

In the *hoxYGFP* strain Hox is also localized in the cytoplasm (Figure 4-13**Error! Reference source not found.**, panel C, white arrows). There is a lower incidence of Hox and chlorophyll *a* colocalization compared with *hoxFGFP* (M=0.574). The colocalization pixel intensity shows a weak positive correlation between chlorophyll *a* and HoxYGFP pixel intensity (R=0.29).

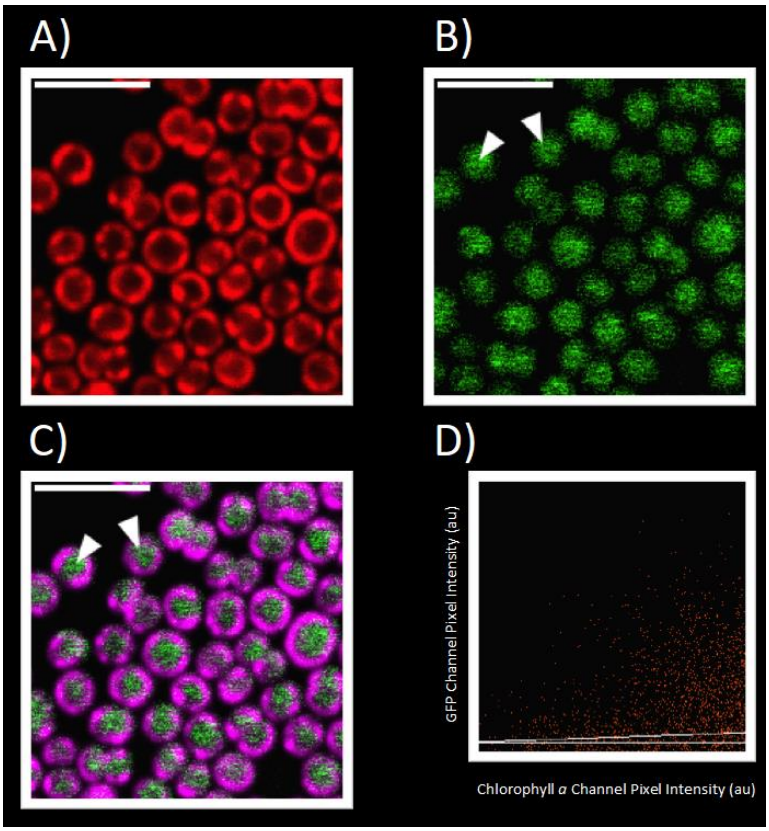

Figure 4-13: PCC 6803 HoxYGFP Grown Photoautotrophically at 60 μE.
Photoautotrophic growth of PCC 6803 HoxYGFP. A) Chlorophyll *a* channel. B) GFP channel. C) Merge of chlorophyll *a* (magenta) and GFP channels. D) 2D xy-scatter of the chlorophyll *a* and GFP pixel intensities. The scale bar represents 5 μm.

4.4.3 Spatial Distribution of HoxEGFP and HoxYGFP in PCC 6803 Under Anoxic Dark-Adapted Conditions

Previous studies showed that in the Δ*hoxE hoxFGFP* strain, photoautotrophic growth at low light resulted in Hox being primarily localized to the cytoplasm. Following dark adaptation and anoxia, the Hox population localized back to the thylakoid, forming puncta, these puncta were localized at different locations at the thylakoid when compared to the *hoxFGFP* strain (Burroughs et al., 2014). Therefore, the *hoxEGFP* strain was subject to dark adaptation and anoxia to investigate whether Hox can return to the thylakoid with similar treatment.

Upon anoxic dark adaptation, some of the Hox population appears to be localized to the thylakoid (Figure 4-14**Error! Reference source not found.**, green arrow). It does seem that a sizeable portion of the Hox remains in the cytoplasm (Figure 4-14**Error! Reference source not found.**, yellow arrow). This is evident with increased colocalization of Hox and

chlorophyll *a* being observed (M=0.725). The pixel intensities of the chlorophyll *a* channel and the HoxEGFP channel show positive correlation (R=0.43), which suggests that a proportion of the Hox population localizes to the thylakoid upon anoxic dark adaptation.

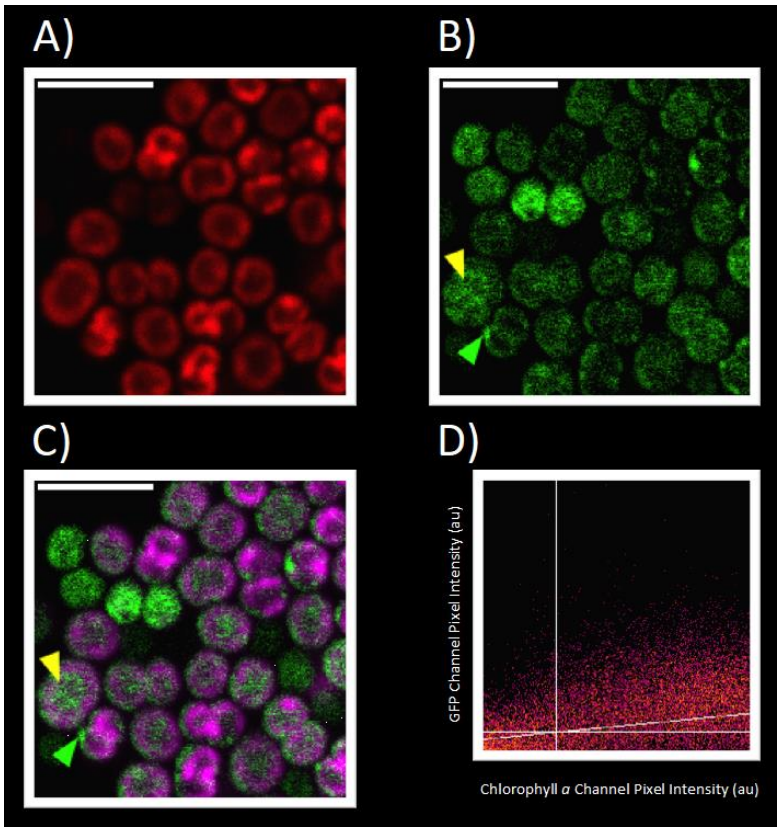

Figure 4-14: PCC 6803 *hoxEGFP* Grown photoautotrophically at 60 μE and Dark Adapted.
Photoautotrophic growth of PCC 6803 HoxEGFP dark adapted and treated to remove oxygen. A) Chlorophyll *a* channel. B) GFP channel. C) Merge of chlorophyll *a* (magenta) and GFP channels. D) 2D xy-scatter of the chlorophyll *a* and GFP pixel intensities. The scale bar represents 5 μm.

In anoxic dark adapted *hoxYGFP*, the Hox population appears to be localized to the thylakoid (M=0.934) (Figure 4-15). A stronger correlation between chlorophyll *a* and Hox pixel intensities is observed in dark adaptation (R=0.63) when compared to light conditions. Together these data show that in the *hoxEGFP*/*hoxYGFP* strains, photoautotrophic conditions result in Hox being localized to the cytoplasm. However, the Hox population relocates to the thylakoid membrane following anoxic dark adaptation similar to the distribution seen in Δ*hoxE hoxFGFP* under similar experimental conditions (Burroughs et al., 2014).

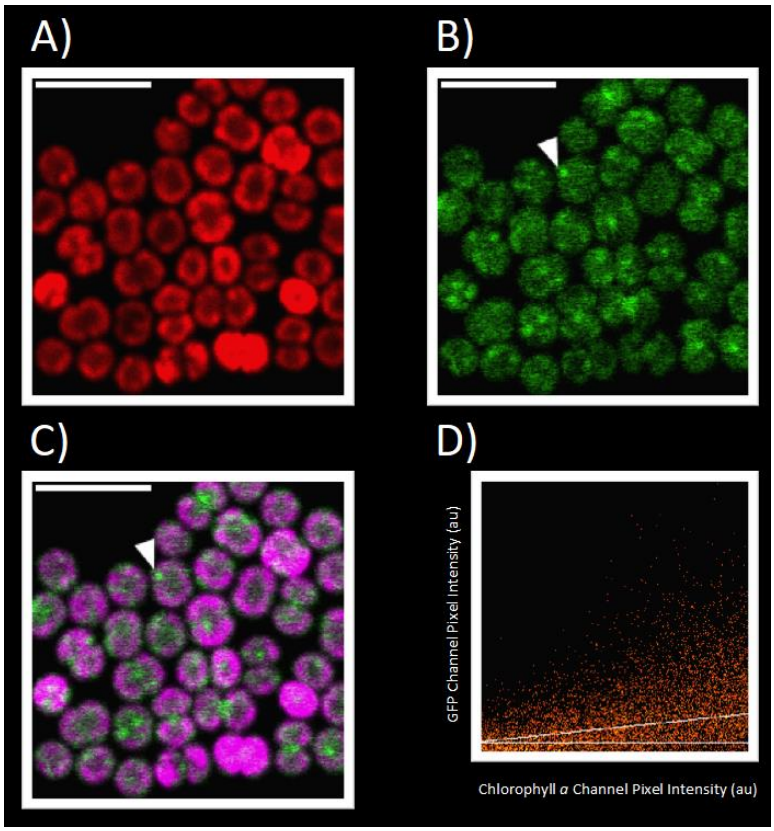

Figure 4-15: PCC 6803 *hoxYGFP* Grown photoautotrophically at 60 μE and Dark Adapted.
Photoautotrophic growth of PCC 6803 HoxYGFP dark adapted and treated to remove oxygen. A) Chlorophyll *a* channel. B) GFP channel. C) Merge of chlorophyll *a* (magenta) and GFP channels. D) 2D xy-scatter of the chlorophyll *a* and GFP pixel intensities. The scale bar represents 5 μm.

4.4.4 Synechocystis sp. PCC 6803 *hoxEGFP* Pull-downs

The HoxE subunit of Hox has been shown to mediate the interaction between Hox and the thylakoid membrane in PCC 6803 (Burroughs et al., 2014). To investigate the composition of the puncta, pull down assays were attempted with magnetic beads functionalized with anti GFP antibodies (Sacharz et al., 2015). Cells were grown under both photoautotrophic and dark-adapted conditions and disrupted in the absence of detergent and fractionated into both soluble and membrane fractions. SDS-PAGE of the associated fractions demonstrated that proteins were pulled down in the soluble fraction when cells were dark adapted. However, following photoautotrophic growth proteins were associated with both the membrane fraction and the soluble fraction (Figure 4-16**Error! Reference source not found.**). Some of the protein bands were present under both conditions, while selected bands were present exclusively in the cells exposed to dark adaptation and photoautotrophic growth (Figure 4-16**Error! Reference**

source not found.). Suggesting these proteins may be either directly or indirectly associate with Hox.

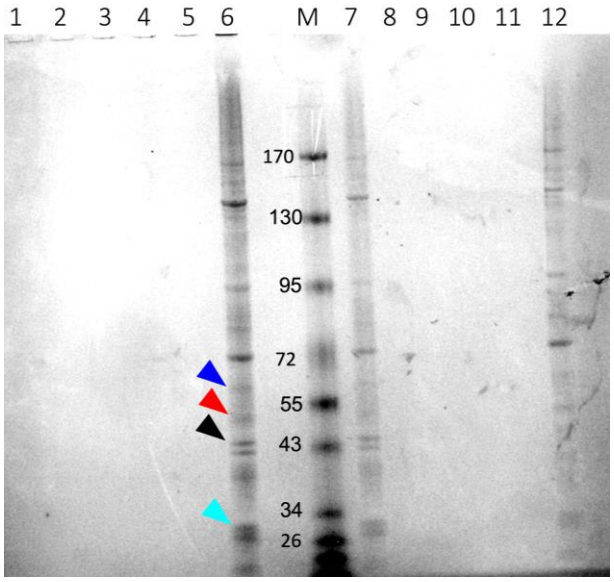

Figure 4-16: Pull-Down of PCC 6803 wild type and *hoxEGFP*.
Elutant from μMacs GFP pull down columns. 1) Crude membrane extract of PCC 6803 *hoxEGFP* anoxic and dark adapted. 2) Crude membrane extract of PCC 6803 WT anoxic and dark adapted. 3) Soluble fraction of PCC 6803 *hoxEGFP* anoxic and dark-adapted wash 2. 4) Soluble fraction of PCC 6803 WT anoxic and dark-adapted wash 2. 5) Soluble fraction of PCC 6803 WT anoxic and dark adapted elutant. 6) Soluble fraction of PCC 6803 *hoxEGFP* anoxic and dark adapted elutant. 7) Crude membrane extract of PCC 6803 *hoxEGFP* grown at 60 μE m^{-2} s^{-1}. 8) Crude membrane extract of PCC 6803 WT grown at 60 μE m^{-2} s^{-1}. 9) Soluble fraction of PCC 6803 *hoxEGFP* grown at 60 μE m^{-2} s^{-1} wash 2. 10) Soluble fraction of PCC 6803 WT grown at 60 μE m^{-2} s^{-1} wash 2. 11) Soluble fraction of PCC 6803 *hoxEGFP* grown at 60 μE m^{-2} s^{-1} elutant. 12) Soluble fraction of PCC 6803 *hoxEGFP* grown at 60 μE m^{-2} s^{-1} elutant. M) marker. Cyan arrow shows expected HoxU size, Black arrow shows expected HoxEGFP size, Red arrow shows expected HoxH size and Blue arrow shows expected HoxF size.

Table 4-1 shows the expected size of subcomplexes of Hox when pulled down in PCC 6803 *hoxEGFP*. A band matching the expected size of HoxEGFP, HoxF, HoxU and HoxH (**Error! Reference source not found.** & Table 4-1) was observed in **Error! Reference source not found.** suggesting that these may form sub-complexes *in-vivo*.

Table 4-1: Expected Hox Subunit Sizes (kDa)

Subunit	Expected Size (kDa)	Present on gel? (Y/N)
HoxEGFP	45.8	**Y**
HoxF	57.8	**Y**
HoxU	26.2	**Y**
HoxY	20	**N**
HoxH	52.9	**Y**

4.5 Discussion

It has previously been demonstrated that Δ*hoxW* is critical for H_2 evolution (Hoffmann et al., 2006). The deletion of the *hoxYH* subunits also completely abolished H_2 evolution in PCC 6803 resulting in reduced subunit abundance (Eckert et al., 2012) which was also observed in a decrease in fluorescence observed in PCC 6803 Δ*hoxYH hoxFGFP* (Burroughs et al., 2014).

Therefore it was expected that Δ*hoxW hoxFGFP* may have a similar Hox distribution as Δ*hoxYH hoxFGFP* (Burroughs et al., 2014). The Δ*hoxW* strain showed a similar Hox subunit abundance as the Δ*hoxH* strain (Gutekunst, unpublished) taken together with the decreased levels of fluorescence in PCC 6803 this suggests that a fully functional and mature HoxYH is essential for Hox stability *in-vivo*. Increased expression of the Hox accessory genes (such as *hoxW*) and supplementation of the media with Fe and Ni have both been shown to improve H_2 yields (Ortega-Ramos et al., 2014; Veaudor et al., 2018), which presumably increases the *in-vivo* quantity of mature Hox and therefore decreases the rate of Hox turnover.

The localization of Hox in the *hoxE* and *hoxY* strains showed a different localization compared to the *hoxFGFP* strain. HoxYH has been demonstrated to be critical in the stability of Hox (Burroughs et al., 2014; Eckert et al., 2012) which suggests that the HoxYGFP assembles into HoxYH. As there was no apparent decrease in fluorescence in *hoxEGFP* and *hoxYGFP* strains points towards the subunits forming stable complexes.

It has been shown that the HoxEFU complex can function as an oxidoreductase independently of HoxYH (Artz et al., 2020). The observation that the *hoxEGFP* and *hoxYGFP* strains showed Hox populations in the cytoplasm suggests that the HoxEFU and HoxYH subcomplexes may not only be an artifact of purification but functional population *in-vivo* (Artz et al., 2020; Eckert et al., 2012). In the Δ*hoxE* strain, it has been previously shown that HoxFUYH and FU form sub complexes (Eckert et al., 2012), however it is unknown if they participate in redox biochemistry within the metabolism of cells. What has been shown in the GFP pull down assays is that HoxE may

directly interact with HoxF, HoxU and HoxH with no direct contact being made with HoxY.

Under photoautotrophic conditions, the HoxEFU subunits may mediate the stoichiometry of reduced ferredoxins and NADH levels as it was shown that HoxEFU has a preference for NAD^+ over $NAD(P)^+$ (Artz et al., 2020). Under anoxic dark-adapted conditions, Hox localizes to the thylakoid, which could function by interacting with NDH-1 in the respiratory electron transport chain (**Chapter 3**). The fact that HoxEFU can oxidize reduced ferredoxins is interesting given that it has demonstrated that ferredoxins can directly bind to NDH-1 (Pan et al., 2020), which may suggest a role of Hox in mediating CEF.

This potential dual role for Hox may have implications in engineering and directed evolution strategies for improved O_2 tolerance and H_2 productivity. As Hox is essential under nitrate limited mixotrophic growth (Gutekunst et al., 2014) with more H_2 produced under these conditions (Gutekunst, unpublished) it would make sense to culture mutant libraries under these conditions. However, as Hox could mediate the stoichiometry of the soluble electron carriers (Artz et al., 2020) with these subcomplexes potentially being observed *in-vivo* (this work and (Eckert et al., 2012)). This culturing strategy may force the enrichment of the mutant library down the reaction route of mediating ferredoxin and NADH stoichiometry as opposed to improving H_2 productivity.

It is evident from the pull down experiments that there are proteins that are eluting with HoxEGFP. Previous work has shown that Hox subunits can be pulled down using HoxH and HoxE His tagged proteins (Eckert et al., 2012). The GFP pull downs developed in Bryan et al., allow localisation to be tied direct protein interactions. Bands were highlighted to be unique (**Error! Reference source not found.**) and common across all treatments were cut from the SDS-PAGE with the aim of identification using MALDI-TOF MS (Sacharz et al., 2015). However, due to time constraints in the project, MALDI-TOF MS was not carried out.

In summary, the distribution of Hox in PCC 6803 Δ*hoxW* is comparable to PCC 6803 Δ*hoxYH,* which indicates a fully mature HoxH is

critical for Hox stability and therefore efforts in engineering cyanobacteria for H_2 production must take this into consideration. Increasing expression of maturation factors (including *hoxW*) has been successfully applied to PCC 6803 for improved H_2 production (Veaudor et al., 2018). HoxE anchors Hox to the thylakoid membrane (Burroughs et al., 2014) and has been shown to also make contact with the subunits HoxU, HoxF and HoxH, further demonstrating how essential HoxE is for Hox localization at the thylakoid. **Error! Reference source not found.** summarizes the findings of **Chapter 4**.

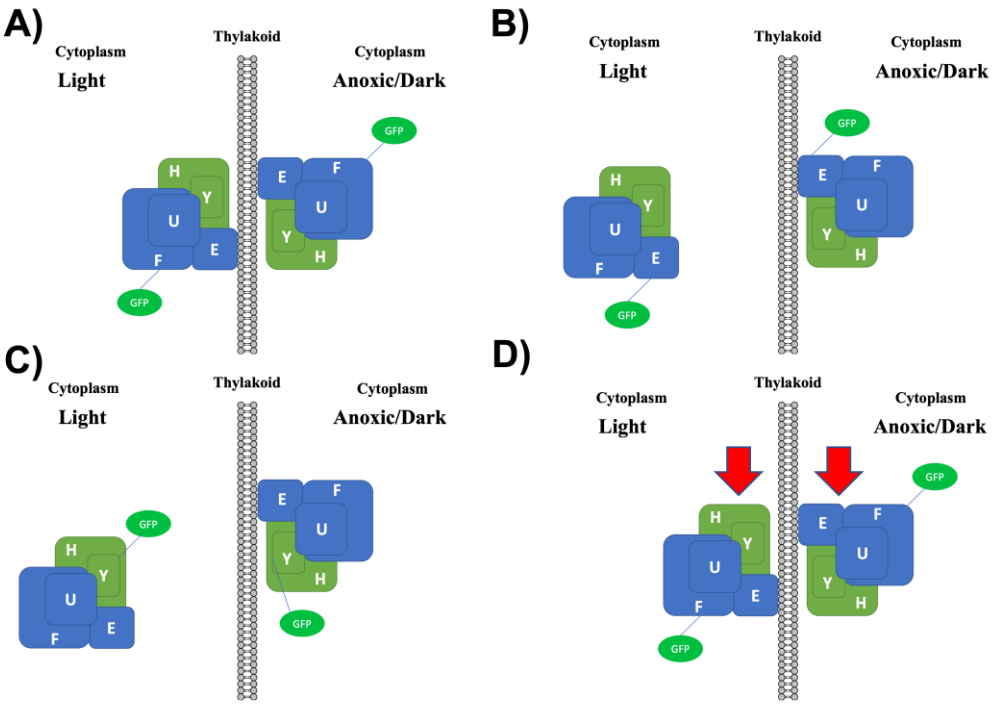

Figure 4-17: Overview of Hox Sub Complex Localization Under Photoautotrophic Growth
A) Under photoautotrophic growth, PCC 6803 *hoxFGFP* Hox was localized to the thylakoid as observed previously (Burroughs et al., 2014). B) In PCC 6803 Δ*hoxYH hoxFGFP* and Δ*hoxW hoxFGFP,* hox distribution was not affected and still localized to the thylakoid however the GFP fluorescence was noticeably lower. C) The distribution of Hox in PCC 6803 *hoxEGFP* was shown to be localized to the cytoplasm under photoautotrophic growth. Under anoxic dark adapted conditions, the Hox distribution in PCC 6803 *hoxEGFP* was localized to the thylakoid forming dispersed and puncta populations. D) Hox distribution in PCC 6803 *hoxYGFP* was localized to the cytoplasm under photoautotrophic growth. When dark adapted under anoxic conditions, Hox was observed to be localized to the thylakoid.

5 Distribution of Hox and NDH-1 in *Synechococcus* sp. PCC 7002

5.1 – Introduction

Our planet is comprised of approximately 71% water, however of this water only 2.5% is fresh water that is predominantly in ground water or in the form of ice (Pimentel et al., 2007). Marine strains are more desirable for photobiological H_2 production as they will not compete with fresh water supplies. The model cyanobacterium PCC 7002 (formerly; *Agmenellum quadruplicatum*) is a euryhaline stain capable of growth in seawater.

Originally isolated from mud samples derived from a fish pen on Magueyes Island (Baalen, 1961) the genome has been fully sequenced (https://www.ncbi.nlm.nih.gov/nuccore/1197208233). PCC 7002 is a non-diazotrophic, unicellular rod shaped cyanobacterium capable of mixotrophic growth on glycerol (Ingram et al., 1973). It can tolerate a wide range of NaCl concentrations, irradiance and has a doubling time of 2.6 hours under optimal conditions (Ludwig & Bryant, 2012a) compared to a doubling time of 5.13 in *Synechocystis* sp. PCC 6803 (Zavřel et al., 2015). Furthermore, it is genetically tractable making it attractive from a biotech perspective.

H_2 production under fermentative conditions in PCC 7002 has been shown to be enhanced through the removal of nitrate from the fermentation media (McNeely et al., 2014; Qian et al., 2016). Nitrate limitation resulted in a metabolic shift from the oxidative pentose phosphate pathway to the Embden–Meyerhof–Parnas (EMP) glycolysis pathway under fermentative conditions (McNeely et al., 2014). This shift resulted in increased reducing equivalent availability in the form of NAD(P)H. Under fermentative conditions, Pyruvate:ferredoxin oxidoreductase (PFOR) is the primary source of reducing equivalents to Hox in the form of reduced ferredoxin (Gutekunst et al., 2014). PFOR is responsible for both the oxidation of pyruvate and reduction of ferredoxin, which has been shown to be essential for H_2 evolution in PCC 6803 under auto fermentative conditions (Gutekunst et al., 2014). However in PCC 7002 it was shown to be influential in the initial onset of H_2 evolution (McNeely et al., 2011). A PFOR deletion mutant resulted in reduced acetate

secretion during mixotrophic growth on glycerol (McNeely et al., 2011). Therefore, an alternative electron source must exist in order to support H_2 evolution under mixotrophic fermentative conditions as the fermentative source of reduced ferredoxin has been eliminated. An understanding of the distribution of Hox and NDH-1 under these conditions will contribute to an overall understanding of H_2 metabolism in PCC 7002.

One bottleneck in using cyanobacteria as a green platform for biological H_2 production is there is not enough electron flux derived from either the respiratory or photosynthetic electron transport chain. In PCC 7002, the phycobilisome to PSI quantum efficiency is the highest measured in cyanobacteria (0.89) (Dong et al., 2009). This feature may prove useful as reducing equivalents from PSI to Hox has been shown to directly become oxidized by Hox in PCC 6803 (Appel et al., 2020; Cournac et al., 2002, 2004). Comparing the phycobilisome to PSI quantum efficiency between PCC 6803 (0.4) (Mullineaux, 1994) and PCC 7002, there is more potential to divert electrons from carbon metabolism to Hox in PCC 7002.

The dark adapted mixotrophic PCC 6803 cultures showed colocalization between Hox and NDH-1 under various conditions, therefore it is important to evaluate if this is unique to individual strains or shared amongst strains. The main focus this chapter is to assess the distribution and colocalization of Hox and NDH-1 under various conditions in PCC 7002. These will include photoautotrophic growth and dark adaption, perturbations to the electron transport chain through the addition of DCMU and DMIB will also be investigated, along with the addition of urea as a nitrogen source.

5.2 Constructing Fluorescent Tagged Hox and NDH-1 PCC 7002 Strains.

To visualize Hox distribution in PCC 7002, GFP was fused with the HoxF subunit, to ensure that there was no effect on the stoichiometry of the Hox complex and to ensure expression was physiologically relevant, the HoxFGFP construct was integrated into the natural *hoxF* locus (SYNPCC7002_A0196). PCR was used to confirm transformants were fully segregated (Figure 5-1)

NDH-1 localisation has already been visualised in PCC 7942 through a GFP fusion to the C-terminus of NdhM, without causing any significant problems with growth and complex assembly (L. N. Liu et al., 2012). A similar strategy was used to construct a YFP fusion to the C-terminus of NdhM in. PCC 7002. The Construct was also integrated into the native locus (SYNPCC7002_A0569). PCR was used to confirm integration of the construct and full segregation (Figure 5-1)

Both the HoxFGFP and NdhMYFP constructs were individually introduced into PCC 7002. The hoxFGFP construct was also transformed into the *ndhMYFP* strain, to generate a strain with both complexes tagged for colocalization. PCR confirmed the construct had integrated and the strains were fully segregated. (Figure 5-1).

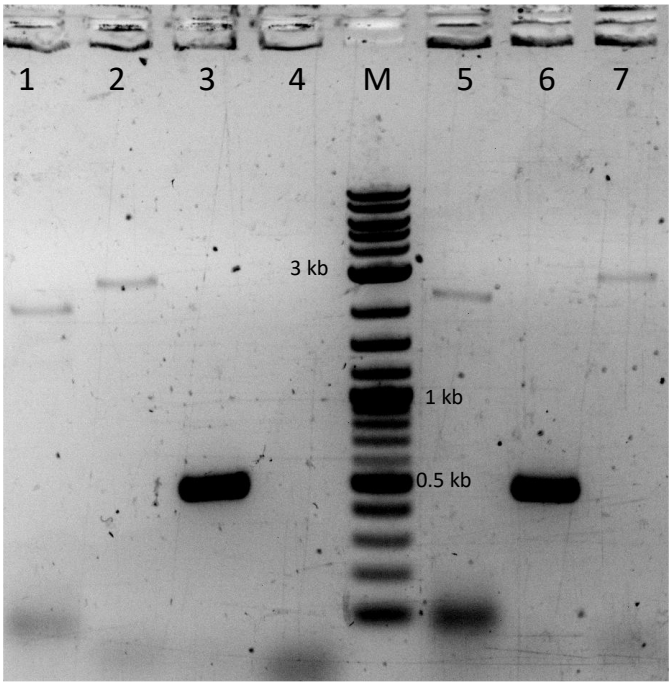

Figure 5-1: PCR Screen of PCC7002 mutants
Boilates were subject to PCR screening to check for integration and segregation. 1) PCC 7002 *hoxFGFP* screened with primer set 7002HoxFsc. 2) PCC 7002 *ndhMYFP* screened with primer set 7002NdhMsc. 3) PCC 7002 *hoxFGFP* screened with primer set 7002PsaFsc. 4). PCC 7002 *ndhMYFP* screened with primer set 7002PsaFsc. 5) PCC 7002 *hoxFGFP ndhMYFP* screened with primer set 7002HoxFsc. 6) PCC 7002 *hoxFGFP ndhMYFP* screened with primer set 7002PsaFsc. 7) PCC 7002 *hoxFGFP ndhMYFP* screened with primer set 7002NdhMsc.

5.3 Growth Conditions Microscopy Imaging Experiments.

Understanding H_2 metabolism in PCC 7002 has primarily focused on fermentative H_2 evolution (McNeely et al., 2010, 2011, 2014). In auto fermentation PCC 7002, cultures were washed twice with medium A+ lacking sodium nitrate and purged with argon to ensure anoxia was achieved (McNeely et al., 2010, 2011, 2014). The removal of nitrate eliminates an electron sink (Gutthann et al., 2007) and also induces the expression of genes involved in glycogen catabolism (Shimmori et al., 2018) which will further enhance the reducing equivalents available for Hox.

Following nitrate limitation, non-diazotrophic cyanobacteria cease proliferation and undergo significant changes to metabolism and morphology (Schwarz & Forchhammer, 2005). Colour changes are also observed in nitrogen starvation as a result of phycobilisome degradation resulting in reduced photosynthetic capacity (Görl et al., 1998). Nitrogen starvation is clearly not a sustainable means of H_2 production, however H_2 measurements

were carried out in PCC 7002 under these conditions (McNeely et al., 2010, 2011, 2014) with the aim of these experiments is to investigate the spatiotemporal dynamics of Hox and NDH-1 under conditions where H_2 evolution is observed to understand the relatiuonship between this interaction and H_2 evolution. To establish the distribution of Hox and NDH-1 under conditions that support H_2 evolution in PCC 7002, these conditions were replicated with the exception that 2 mM dithionite was used in order to remove oxygen as opposed to purging with argon.

Previously, it was demonstrated that the mixotrophic growth of PCC 7002 on glycerol reduces H_2 evolution during fermentative conditions (McNeely et al., 2011). In **Chapter 3**, a significant proportion of Hox was shown to be localized to the cytoplasm under mixotrophic growth in PCC 6803 and therefore this was investigated in PCC 7002. With PCC 7002 unable to utilize glucose as a carbon source, glycerol was used in place of glucose for mixotrophic growth. The distribution of both Hox and NDH-1 has yet to be evaluated in PCC 7002, fermentative conditions were investigated to assess the differences in distribution, comparing anoxic dark-adapted cells that were previously grown under mixotrophic and photoautotrophic growth conditions.

The electron transport inhibitors DCMU and DBMIB have previously been shown to have little impact on the redistribution of the Hox complex in PCC 6803 (Burroughs et al., 2014). However, the NDH-1 complex of PCC 7942 has been shown to respond to the electron transport inhibitors DCMU and DBMIB causing the populations to redistribute (L. N. Liu et al., 2012). Puncta were formed in response to the oxidised plastoquinone pool following DCMU treatment, while the complex remained dispersed following treatment with DBMIB (L. N. Liu et al., 2012). Treatment with DCMU has been shown to enhance H_2 evolution in PCC 6803 by limiting oxygen evolution from PSII, meaning that the reducing equivalents for H_2 evolution is being supported by respiratory electron transport (Appel et al., 2020). Therefore, both DCMU and DBMIB were assessed in PCC 7002 in order to assess if the complexes behave in a similar way to Hox and NDH1 in both PCC 6803 and PCC 7942.

Nitrate is a large electron sink in cyanobacteria (Gutthann et al., 2007) and the removal of nitrate from A+ medium was shown to increase fermentative H_2 production (McNeely et al., 2010, 2011, 2014). Therefore, the presence and absence of nitrate was investigated. Urea was used as a nitrogen source and added at a concentration of 10 mM (Ludwig & Bryant, 2012a, 2012b). As the transition between anoxic dark conditions to high light conditions gives the highest rates of hydrogen production in PCC 6803 (Cournac et al., 2002; Gutthann et al., 2007). However, no data exists for photobiological H_2 production in PCC 7002, therefore the distribution of Hox and NDH-1 was assessed under conditions where dark anoxic cultures were exposed to high light comparing the presence and absence of nitrate.

5.4 Distribution of Hox and NDH-1 Following Anoxic Dark Adapted Conditions following Photoautotrophic Growth.

PCC 7002 cultures were grown photoautotrophically at 50 μE m^{-2} s^{-1} prior to anoxic dark adaptation for 3 days as significant H_2 evolution is observed after 3 days (McNeely et al., 2010). The distribution of both Hox and NDH-1 was assessed under photoautotrophic growth in PCC 7002. In order to demonstrate that no significant autofluorescence was detected, wild type PCC 7002 was imaged following photoautotrophic growth. No significant fluorescence was detected in the wild type cells (Figure 5-2).

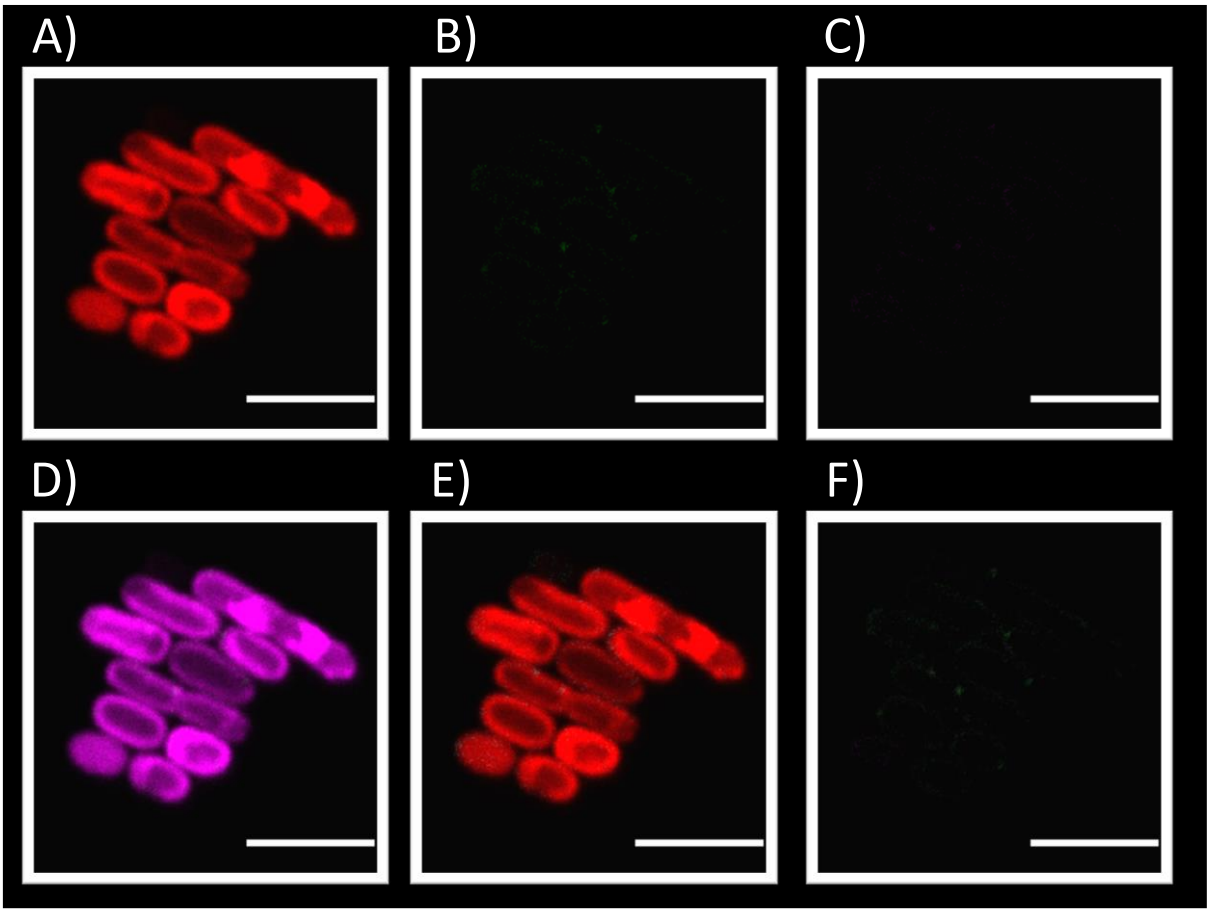

Figure 5-2: Photoautotrophically Grown PCC 7002 Wild Type
A) Chlorophyll *a* channel. B) GFP channel. C) YFP channel. D) chlorophyll *a* (magenta) and GFP channels merged. E) Chlorophyll *a* and YFP (Cyan) channels merged. F) GFP and YFP (magenta) channels merged. The scale bar represents 5 μm.

Hox was shown to co-localize with the chlorophyll *a* fluorescence (Figure 5-3 D) indicating localisation to the thylakoid membrane. Hox was shown to have two distinctive populations (Figure 5-3 B), dispersed and localised in puncta, similar to those already seen in *Synechocystis* sp. PCC

6803 in **Chapter 3** and previous publications (Burroughs et al., 2014). The Hox puncta were observed to be localized to the thylakoid membrane at the poles of the cell.

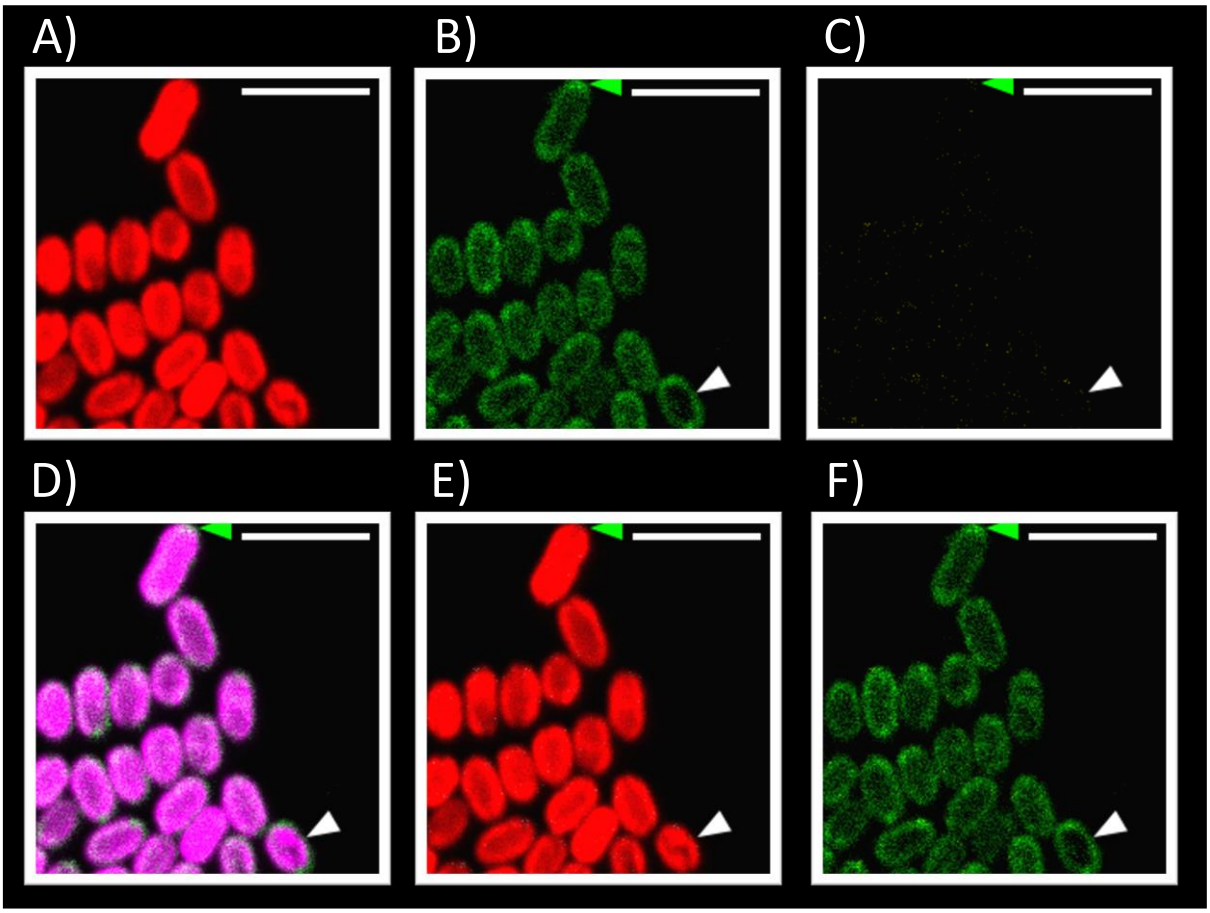

Figure 5-3: Photoautotrophically Grown PCC 7002 *hoxFGFP*
A) Chlorophyll *a* channel. B) GFP channel. C) YFP channel. D) chlorophyll *a* (magenta) and GFP channels merged. E) Chlorophyll *a* and YFP (Cyan) channels merged. F) GFP and YFP (magenta) channels merged. The green arrow represents HoxFGFP. The white arrow highlights the HoxFGFP dispersed population. The scale bar represents 5 μm.

The NDH-1 complex showed co-localisation with chlorophyll *a* fluorescence (Figure 5-4 E) and hence was localised in the thylakoid membrane. The NDH-1 complex was either dispersed around the thylakoid membrane or in puncta (Figure 5-4 magenta arrows) similar to what had already been observed in PCC 7942 (L. N. Liu et al., 2012). The NDH-1 puncta population also appeared to be at the poles of the cell (Figure 5-4 C, E & F magenta arrow).

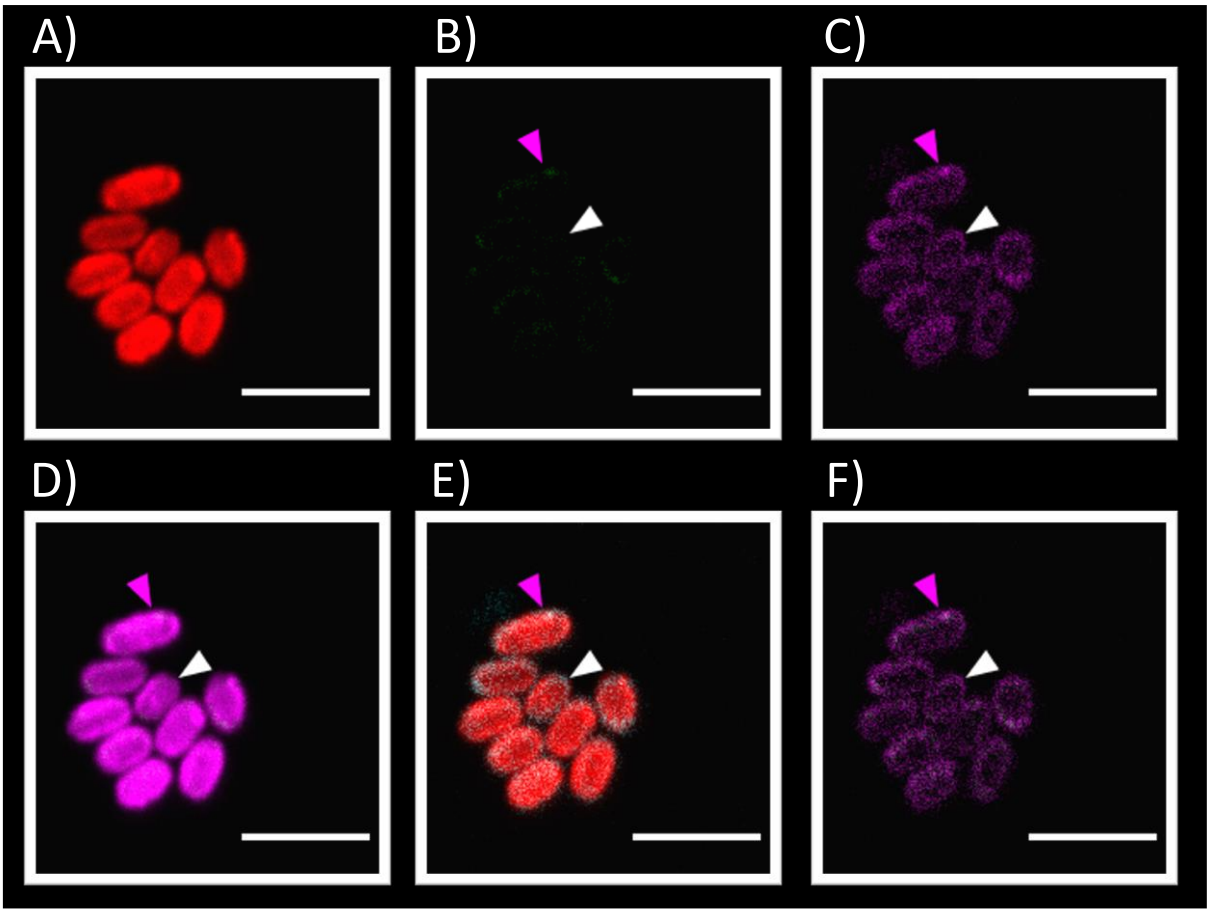

Figure 5-4: Photoautotrophically grown PCC 7002 *ndhMYFP*
A) Chlorophyll *a* channel. B) GFP channel. C) YFP channel. D) chlorophyll *a* (magenta) and GFP channels merged. E) Chlorophyll *a* and YFP (Cyan) channels merged. F) GFP and YFP (magenta) channels merged. Magenta arrow indicates the NdhMYFP population as puncta. The white arrow highlights NdhMYFP dispersed population. The scale bar represents 5 μm.

Colocalization of Hox and NDH-1 was assessed following anoxic dark adaptation after photoautotrophic growth in *hoxFGFP ndhMYFP*. Photoautotrophic growth was not assessed as H_2 is not evolved under these conditions and the removal of nitrate is crucial for H_2 evolution (McNeely et al., 2014). Both Hox and NDH-1 were colocalised with chlorophyll *a* forming either dispersed or puncta populations (Figure 5-5 D & E respectively). The distribution of Hox and NDH-1 was not significantly different to the distribution pattern seen in the single mutants (data not shown). The Hox puncta populations colocalized with the NDH-1 puncta populations (Figure 5-5 white arrows) but also formed discrete puncta (Figure 5-5 green arrows). A similar pattern could be seen for the NDH-1 population with discrete NDH-1 puncta being highlighted by the magenta arrows in Figure 5-5. The Hox and NDH-1

puncta show a high frequency of localisation with most of the puncta populations being localised to the poles of the cells.

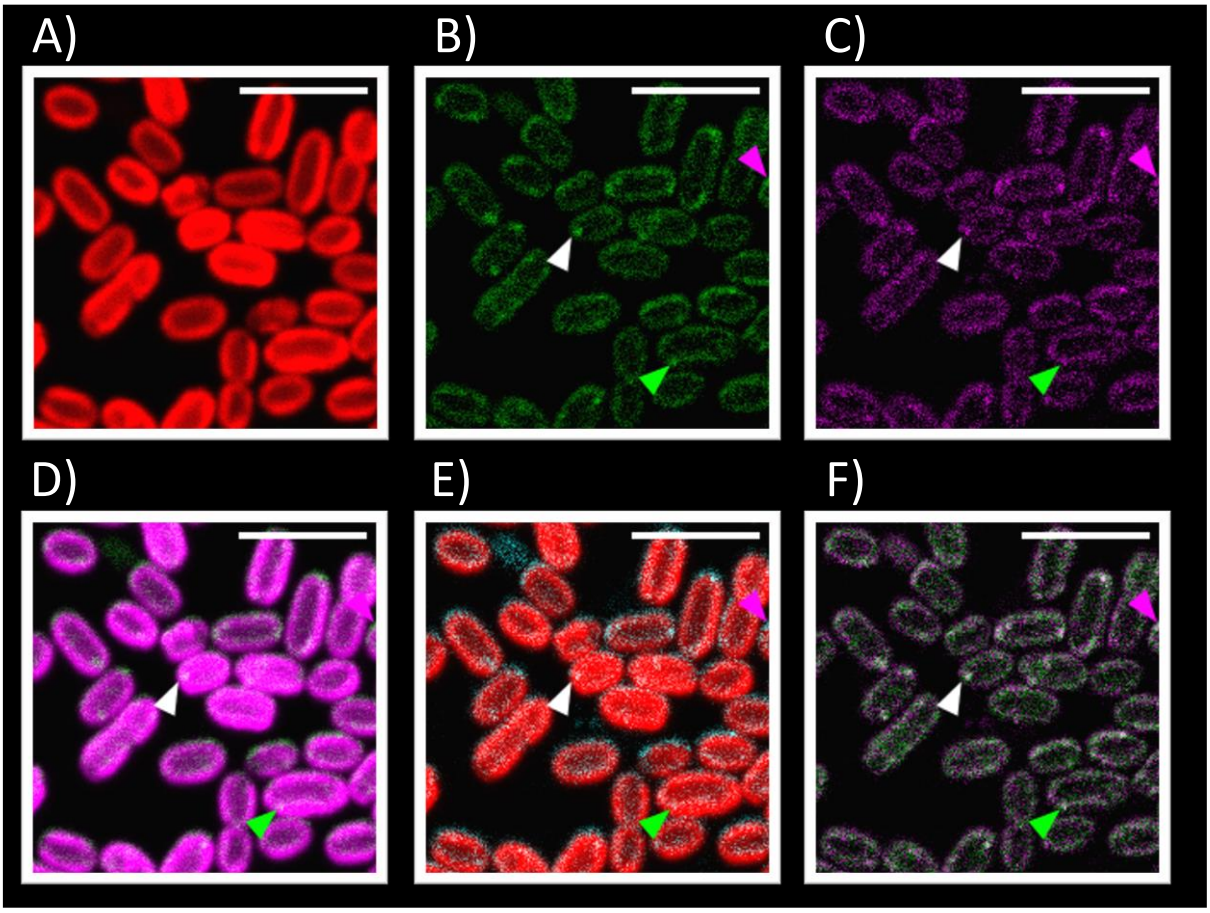

Figure 5-5: Photoautotrophically Grown PCC 7002 *hoxFGFP ndhMYFP.*
A) Chlorophyll *a* channel. B) GFP channel. C) YFP channel. D) chlorophyll *a* (magenta) and GFP channels merged. E) Chlorophyll *a* and YFP (Cyan) channels merged. F) GFP and YFP (magenta) channels merged. The green arrow represents HoxFGFP puncta not co-localized with NdhMYFP puncta. Magenta arrow indicates the NdhMYFP puncta not co-localized with HoxFGFP. The white arrow highlights HoxFGFP NdhMYFP puncta that is co-localized. The scale bar represents 5 μm.

5.5 Distribution of Hox and NDH-1 in PCC 7002 Following Anoxic Dark Adaptation following Mixotrophic Growth.

Following anoxic dark adaptation after mixotrophic growth, PCC 7002 wild type cells showed no significant autofluorescence (data not shown). Both Hox and NDH-1 distribution in PCC 7002 *hoxFGFP ndhMYFP* was not significantly different when compared to the single mutants (data not shown).

NDH-1 colocalised with chlorophyll *a* (Figure 5-6 D & E, magenta and white arrows) which indicates thylakoid localisation. The populations were either dispersed in the thylakoid or in distinct puncta (Figure 5-6, magenta arrows). As in photoautotrophic growth, a large population of NDH-1 puncta were observed to form foci at the poles of the cells.

Hox was localised to the thylakoid, in two distinctive populations, dispersed or puncta (Figure 5-6 B & D), this is comparable to what has already been observed in PCC 6803 with populations being dispersed or forming puncta localized to the thylakoid (Burroughs et al., 2014). The Hox puncta appear to be localized to the poles of the cells as observed in the photoautotrophic growth.

The Hox and NDH-1 puncta showed co-localisation with a tendency to be located at the poles of the cells (Figure 5-6 F).

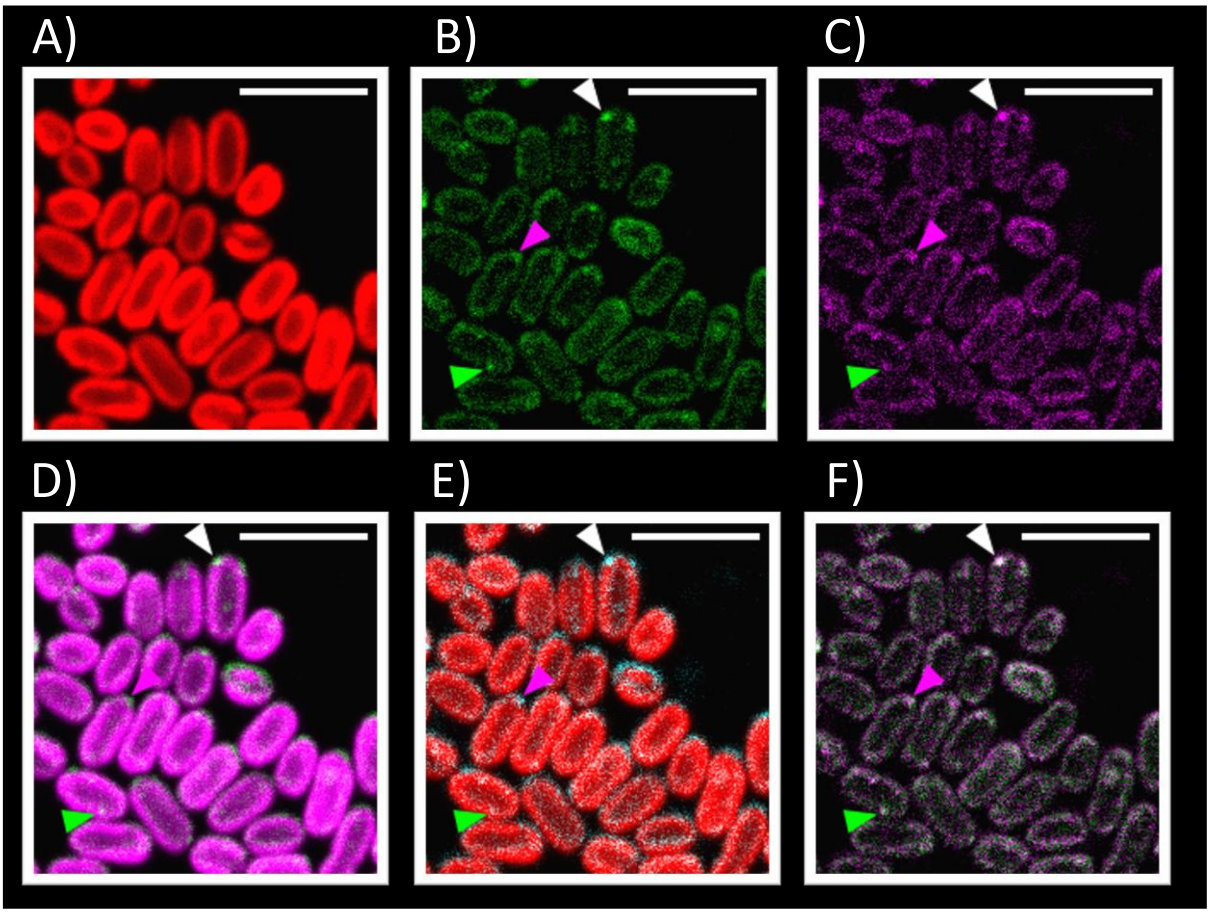

Figure 5-6: Mixotrophically Grown PCC 7002 *hoxFGFP ndhMYFP*
A) Chlorophyll *a* channel. B) GFP channel. C) YFP channel. D) chlorophyll *a* (magenta) and GFP channels merged. E) Chlorophyll *a* and YFP (Cyan) channels merged. F) GFP and YFP (magenta) channels merged. The green arrow represents HoxFGFP puncta not co-localized with NdhMYFP puncta. Magenta arrow indicates the NdhMYFP puncta not co-localized with HoxFGFP. The white arrow highlights HoxFGFP NdhMYFP puncta that is co-localized. The scale bar represents 5 μm.

5.6 Statistical Analysis of Images Comparing Anoxic Dark Adapted Photoautotrophic and Mixotrophic growth

The proportion of NDH-I puncta in PCC 7002 increased significantly under mixotrophic conditions compared to photoautotrophic conditions ($P<0.001$). This would suggest that under mixotrophic growth the demand for increased NDH-1 activity is met by increasing the puncta population as observed in PCC 7942 in order to maintain optimal plastoquinone redox poise (L. N. Liu et al., 2012).

The distribution of Hox in PCC 7002 was shown to be significantly higher in anoxic mixotrophic conditions compared to the photoautotrophic dark-adapted cells ($P<0.001$). This suggests that the Hox population in PCC 7002 shifts from a dispersed population to puncta in response to mixotrophic growth on 0.1% glycerol.

Since the frequency of Hox puncta per cell in PCC 6803 correlates with Hox activity (Burroughs et al., 2014) and the NDH-1 puncta correlate with the plastoquinone reductase activity of NDH-1 (L. N. Liu et al., 2012), the frequency of Hox and NDH-1 puncta co-localisation was scored under anoxic dark adapted photoautotrophic and mixotrophic conditions. The puncta co-localization frequencies per cell for each condition are displayed in Figure 5-7. Dark adapted mixotrophic growth showed an increase in the incidence of Hox and NDH-1 puncta co-localisation ($P<0.001$).

In addition to analysing puncta co-localization in *hoxFGFP ndhMYFP*, puncta which are not colocalised can also be investigated. The incidence of Hox puncta not colocalised with NDH-1 was not significantly different ($P=0.445$). However, there was a significant increase in the population of NDH-1 puncta not colocalised with Hox puncta ($P<0.001$). This would suggest that another interaction partner interacts with NDHI which is located in the thylakoid membrane and has a physiological role in PCC 7002 utilizing glycerol under mixotrophic conditions.

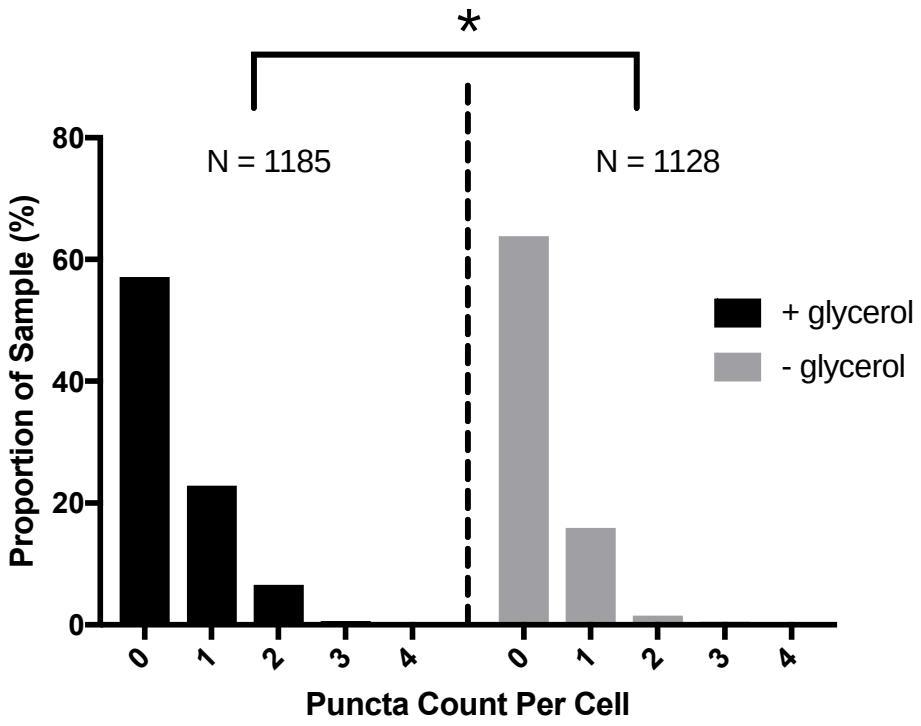

Figure 5-7: Hox/NDH-1 Co-Localization Scores Comparing Anoxic Dark Adapted Mixotrophic and Photoautotrophic Growth.
Frequencies of colocalization between Hox and NDH-1 puncta from biological replicates (n=3).

5.7 Distribution of Hox and NDH-1 Under Anoxic Dark Adaptation to High Light in PCC 7002 Treated with DCMU.

DCMU is a photosynthetic electron transport inhibitor that blocks the interaction between plastoquinone and photosystem II therefore inhibiting the reduction of the plastoquinone pool (Metz et al., 1986). In order to assess the distribution of both Hox and NDH-1 in PCC 7002 under physiological conditions where the plastoquinone pool is oxidised, PCC 7002 was treated with DCMU for 30 minutes prior to high light exposure, limiting the electrons entering the plastoquinone pool from water (600 μE $m^{-2}s^{-1}$).

The distribution of both Hox and NDH-1 in PCC 7002 *hoxFGFP ndhMYFP* was not significantly different compared to the single mutants (data not shown). Hox was distributed in 2 populations, one dispersed and one forming puncta at the thylakoid (Figure 5-8 B & D). NDH-1 also showed dispersed and puncta populations in the thylakoid (Figure 5-8 C & E). The Hox and NDH-1 puncta were co-localised (Figure 5-8 white arrow) forming discrete puncta (Figure 5-8 green and magenta arrows respectively). The puncta were observed to be located at the poles of the cells, although they were slightly less pronounced than in untreated PCC 7002 (data not shown).

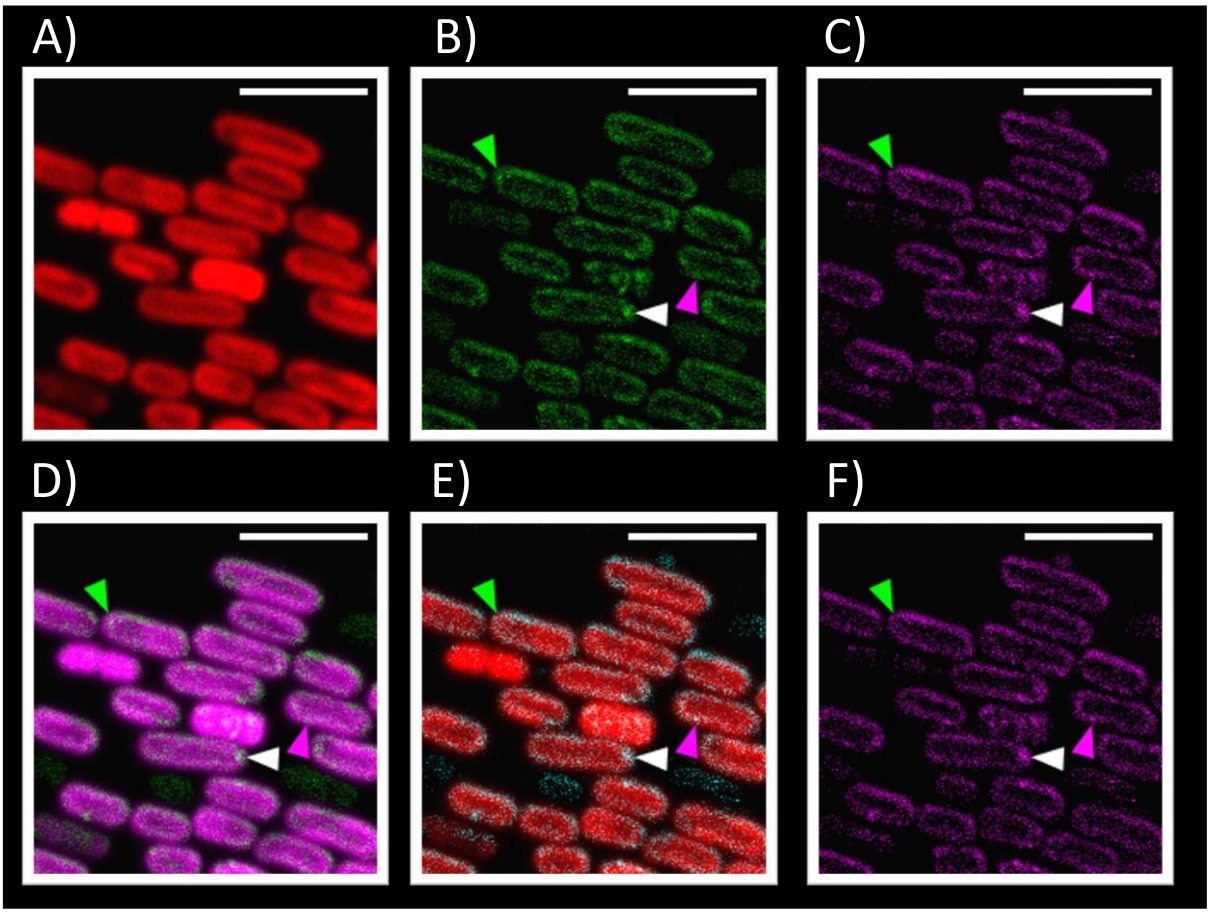

Figure 5-8: Anoxic Dark Adapted to High Light PCC 7002 *hoxFGFP ndhMYFP* Treated with DCMU.
A) Chlorophyll *a* channel. B) GFP channel. C) YFP channel. D) chlorophyll *a* (magenta) and GFP channels merged. E) Chlorophyll *a* and YFP (Cyan) channels merged. F) GFP and YFP (magenta) channels merged. The green arrow represents Hox puncta not colocalised with NDH-1 puncta. Magenta arrow indicates the NDH-1 puncta not colocalised with Hox. The white arrow highlights Hox and NDH-1 puncta that is colocalised. The scale bar represents 5 μm.

5.8 Distribution of Hox and NDH-1 Under Anoxic Dark Adaptation to High Light in PCC 7002 Treated with DBMIB.

The treatment of cells with DBMIB inhibits photosynthetic electron transport from the cytochrome b_6f complex to plastocyanin (Regensburg & Freiburg, 1991), resulting in the over reduction of the plastoquinone pool. In PCC 6803, Hox distribution was not affected by DBMIB (Burroughs et al., 2014), however NDH-1 was mainly dispersed in the thylakoid (L. N. Liu et al., 2012). In this experiment the aim was to investigate the effect of an over reduced plastoquinone pool has on the distribution of Hox and NDH-1 in PCC 7002.

There was no significant autofluorescence detected in PCC 7002 wild type cells (data not shown) with no observable difference in the distribution of Hox or NDH-1 in PCC 7002 *hoxFGFP ndhMYFP* compared to the single mutants (data not shown). PCC 7002 *hoxFGFP ndhMYFP* treated with DBMIB showed a decrease in fluorescence intensity in the fluorescent protein channels (Figure 5-9 B & C). The Hox and NDH-1 puncta appeared to be less pronounced but still localised to the poles of the cell (Figure 5-9 magenta, green and white arrows).

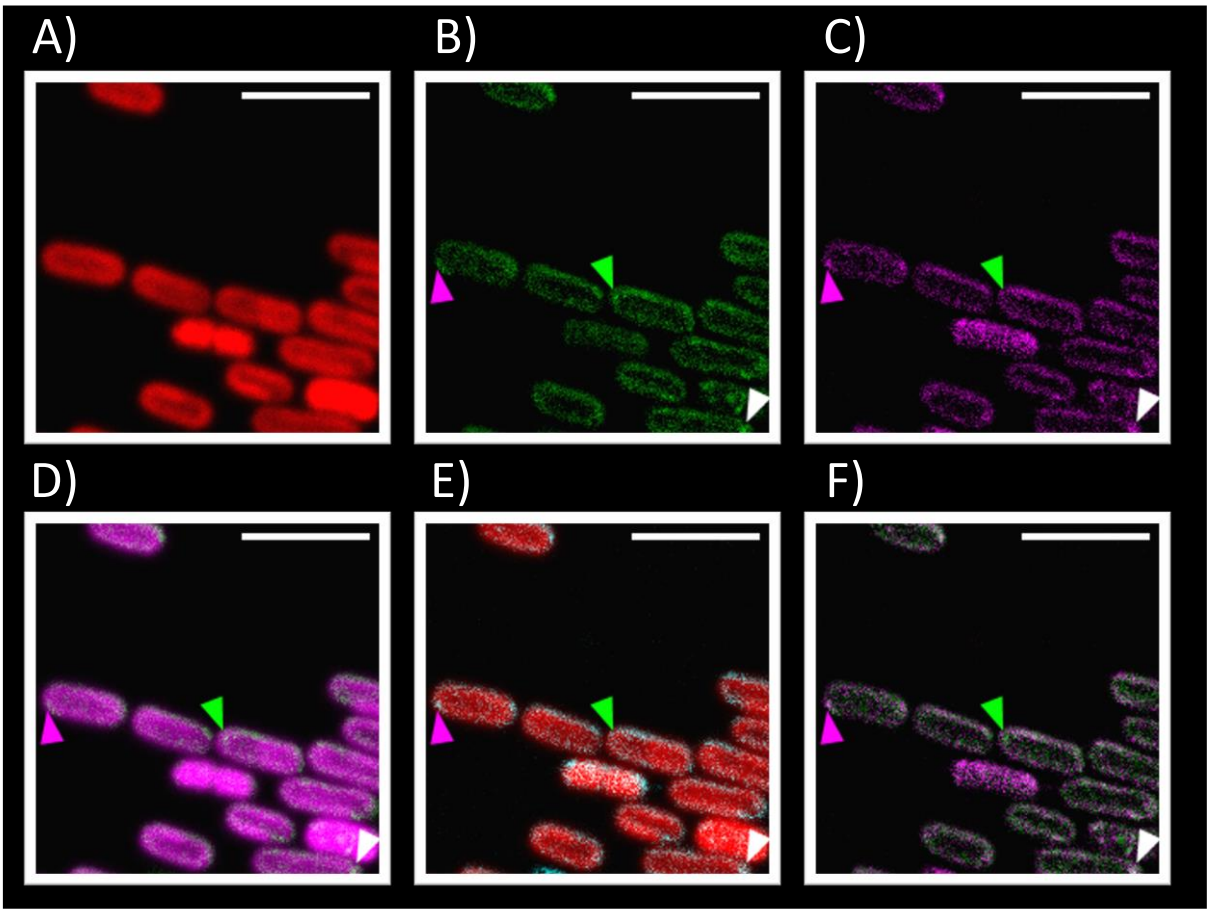

Figure 5-9: Anoxic Dark Adapted to High Light PCC 7002 *hoxFGFP ndhMYFP* Treated with DCMU.
A) Chlorophyll *a* channel. B) GFP channel. C) YFP channel. D) chlorophyll *a* (magenta) and GFP channels merged. E) Chlorophyll *a* and YFP (Cyan) channels merged. F) GFP and YFP (magenta) channels merged. The green arrow represents HoxFGFP puncta not co-localized with NdhMYFP puncta. Magenta arrow indicates the NdhMYFP puncta not co-localized with HoxFGFP. The white arrow highlights HoxFGFP NdhMYFP puncta that is co-localized. The scale bar represents 5 μm.

5.9 Statistical Analysis of the Co-localisation between Hox and NDH-1 in DCMU and DBMIB Treatments.

There was a significant decrease in the NDH-1 puncta following treatment with DCMU (P=0.049) compared to the control. By reducing the plastoquinone pool through DBMIB treatment, the population of NDH-1 puncta was significantly lower when compared to the untreated control (P=0.002). There was no significant difference when comparing the DCMU or DBMIB treatments (P=0.244). In PCC 7942 DCMU treatment increased the number of puncta for NDH-1 and DBMIB treatment almost completely eliminated the NDH-1 puncta population (L. N. Liu et al., 2012). This discrepancy may be a result of differences in the physiology between the two organisms and suggests that another complex, such as succinate dehydrogenase complex (Sdh), could be more influential to the redox poise of the plastoquinone pool in PCC 7002 (L. N. Liu et al., 2012)

DCMU treatment showed no significant difference in Hox puncta when compared to the untreated control (P=0.209). The treatment with DBMIB resulted in a significant decrease in Hox puncta (P=0.046). Treatment of PCC 6803 with either DCMU or DBMIB did not alter the distribution of Hox (Burroughs et al., 2014), however the decrease of Hox puncta in PCC 7002 with DBMIB treatment may highlight the lack of electrons being delivered to photosystem I and therefore limiting Hox from evolving H_2.

To assess colocalization between Hox and NDH-1, the puncta from each complex was scored with the frequencies displayed in Figure 5-10. Treatment of PCC 7002 with both DCMU and DBMIB showed a significant decrease in the incidence of colocalization of the Hox and NDH-1 puncta when compared to untreated images (P=0.029 & P=0.004 respectively). There was no significant difference between the DCMU and DBMIB treatments (P=0.553). The significant decrease in co-localization of the Hox and NDH-1 puncta is most likely due to the decrease in NDH-1 puncta under the treatments.

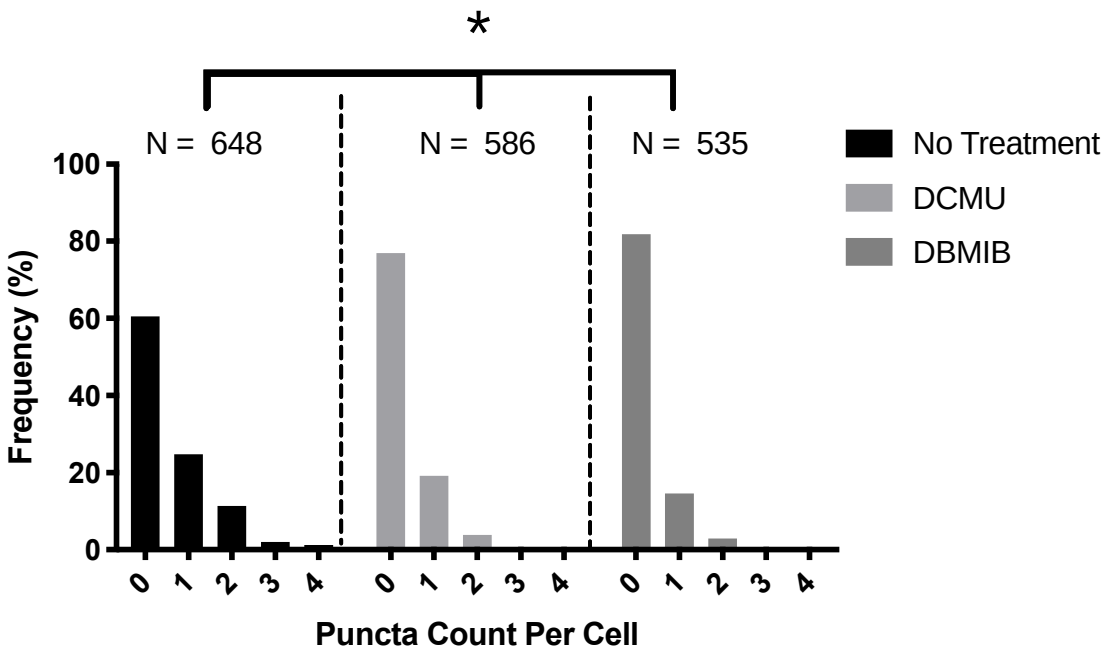

Figure 5-10: Hox/NDH-1 Colocalisation Scores Comparing Photosynthetic Inhibitor Treatment
Frequencies of colocalization between Hox and NDH-1 puncta from biological replicates (n=3).

5.10 Distribution of Hox and NDH-1 Growth on Medium A+ with Nitrate Dark Adapted to Highlight Conditions in PCC 7002.

The removal of nitrate from PCC 7002 cultures that are fermentatively evolving H_2 is critical for improving H_2 productivity (McNeely et al., 2014). Understanding how anoxic dark adapted PCC 7002 transition to highlight is lagging behind observations made in PCC 6803 (Cournac et al., 2002, 2004; Gutekunst et al., 2014; Gutthann et al., 2007). In this experiment, the aim was to investigate the distribution of Hox and NDH-1 in the transition from anoxic dark adapted to high light in the presence and absence of nitrate.

NDH-1 fluorescence was weak but showed co-localisation with chlorophyll *a* fluorescence (Figure 5-11 E). Puncta populations were observed mostly colocalised with Hox puncta populations (Figure 5-11 white arrows). The Hox population was shown to colocalise with the chlorophyll *a* fluorescence (Figure 5-11 D). It was observed that the Hox puncta populations either colocalised with the NDH-1 puncta (Figure 5-11 white arrows) or formed discrete puncta (Figure 5-11 green arrows) suggesting the existence of another interaction partner at the thylakoid.

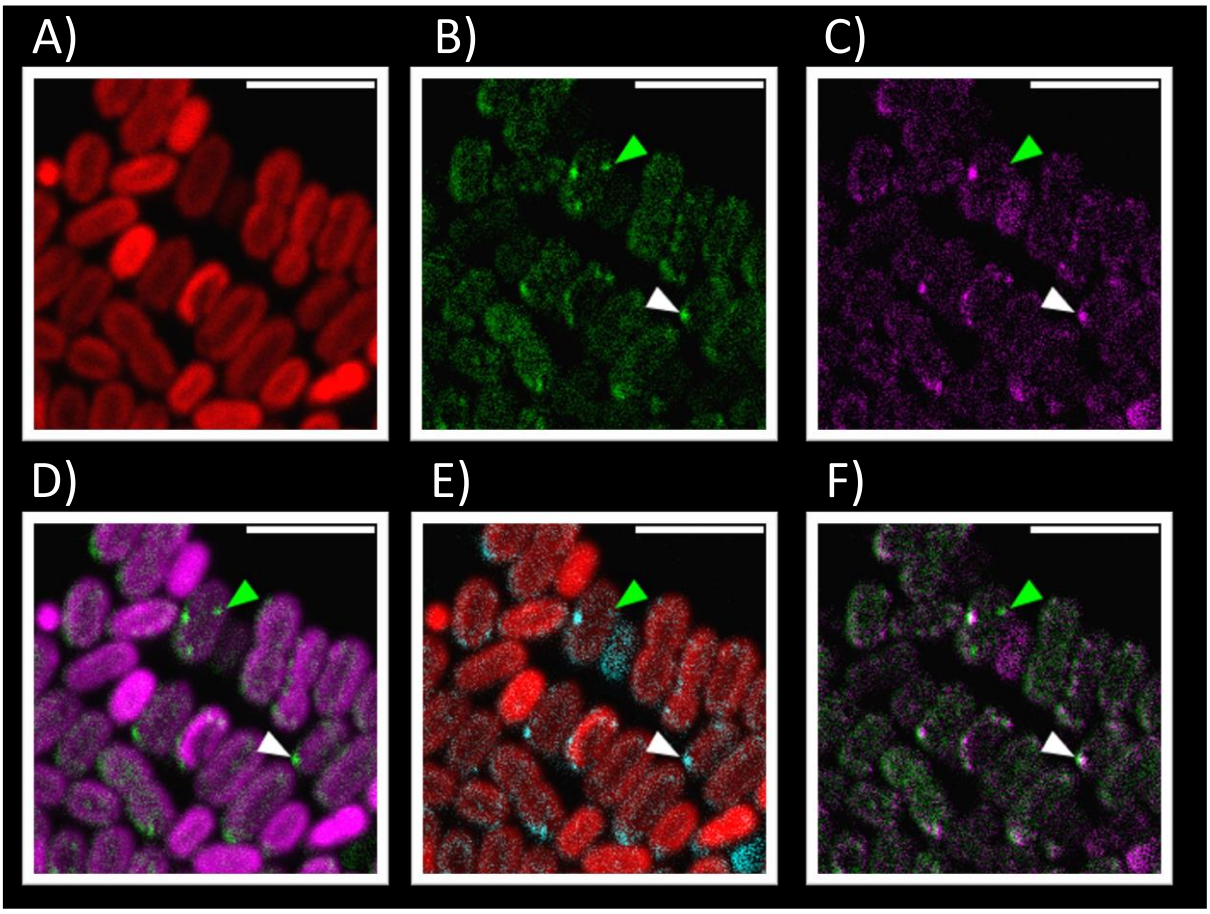

Figure 5-11: Anoxic Dark Adapted to High Light PCC 7002 *hoxFGFP ndhMYFP* in the Presence of Nitrate.
A) Chlorophyll *a* channel. B) GFP channel. C) YFP channel. D) chlorophyll *a* (magenta) and GFP channels merged. E) Chlorophyll *a* and YFP (Cyan) channels merged. F) GFP and YFP (magenta) channels merged. The green arrow represents HoxFGFP puncta not co-localized with NdhMYFP puncta. The white arrow highlights HoxFGFP NdhMYFP puncta that is co-localized. The scale bar represents 5 μm.

5.11 Distribution of HoxFGFP and NdhMYFP following growth on Medium A+ with Urea Dark Adapted to Highlight Conditions in PCC 7002.

In order to fully grasp the competitive nature nitrate metabolism has on H_2 evolution, the distribution of Hox and NDH-1 in PCC 7002 grown in medium A+ was compared to medium A+ with the nitrate being replaced by urea. Cultures appeared to have a larger proportion of dead cells (Figure 5-12). The NDH-1 was weak and showed co-localization to chlorophyll *a* fluorescence (Figure 5-12 E). The NDH-1 puncta population showed a high frequency of co-localisation with the Hox puncta (Figure 5-12 white arrows). The Hox was colocalised to the chlorophyll *a* fluorescence (Figure 5-12 D). The Hox puncta also had a sub population which did not co-localize with the NDH-1 puncta (Figure 5-12 green arrows).

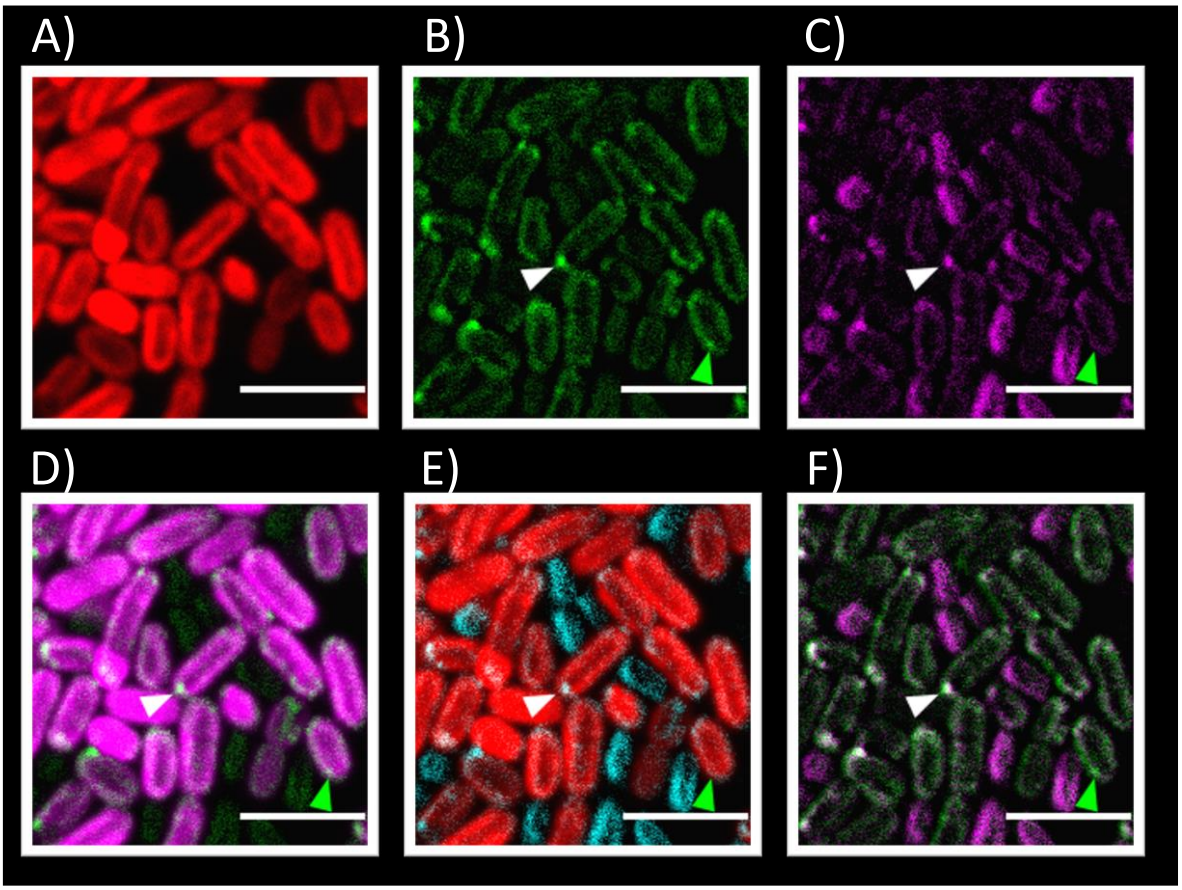

Figure 5-12: Anoxic Dark Adapted to High Light PCC 7002 *hoxFGFP ndhMYFP* in the Absence of Nitrate.
A) Chlorophyll *a* channel. B) GFP channel. C) YFP channel. D) chlorophyll *a* (magenta) and GFP channels merged. E) Chlorophyll *a* and YFP (Cyan) channels merged. F) GFP and YFP (magenta) channels merged. The green arrow represents HoxFGFP puncta not co-localized with NdhMYFP puncta. The white arrow highlights HoxFGFP NdhMYFP puncta that is co-localized. The scale bar represents 5 μm.

5.12 Statistical Analysis of Dark Adapted to Highlight Conditions in PCC 7002 Comparing Nitrate and Urea.

As Hox and NDH-1 showed a similar distribution compared to previous experiments, the puncta populations were scored as either colocalised or not. With respect to the total NDH-1 puncta, there was no significant change in the population when comparing nitrate or urea growth (P=0.81). The proportion of NDH-1 puncta which did not colocalise with Hox did not significantly change when comparing nitrate or urea growth (P=0.793) although this was not common.

The Hox puncta population slightly increased but there was no statistical significance (P=0.068) which translated into no significant increase in the incidence of co-localisation of the Hox/NDH puncta when nitrate was replaced by urea. The population of Hox puncta that was not colocalised with the NDH-1 puncta showed a statistically significant increase (P=0.005) in cultures grown with urea. This result may suggest a change in the Hox interaction partner at the thylakoid in response to nitrate removal and urea supplementation. The frequencies of Hox puncta observed in nitrate compared to urea growth are displayed in Figure 5-13.

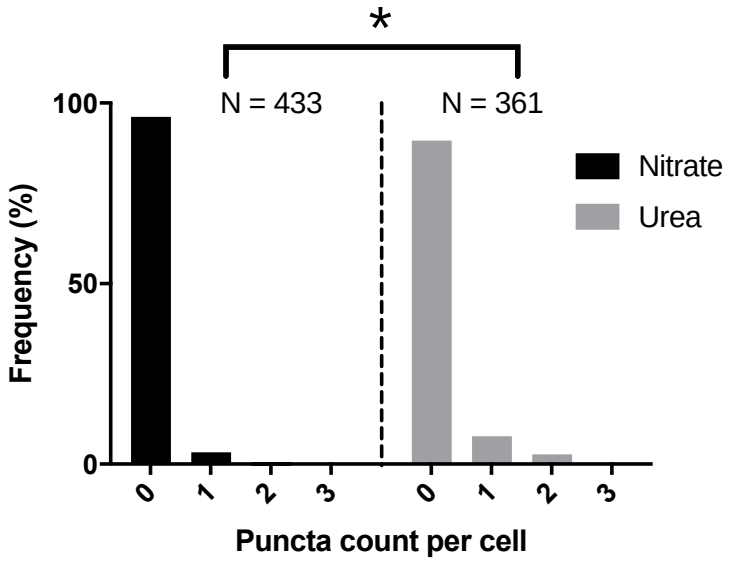

Figure 5-13 Hox Puncta Scores Comparing Nitrate and Urea Growth
Frequencies of Hox puncta from biological replicates (n=3).

5.13 Discussion

The distribution of Hox in PCC 7002 is similar to that observed in PCC 6803, with populations dispersed or forming puncta at the thylakoid (Burroughs et al., 2014). It was noted that a large proportion of Hox puncta were located at the poles of cells. The degradation of carboxysomes has also been shown to take place at the poles of PCC 7942 (Cameron et al., 2013) and PCC 7002 (Hill et al., 2020). This may suggest the presence of a distinct region in the thylakoid membrane involved in the organisation of complexes involved in photoautotrophic growth. Images from this study demonstrated that NDH-1 also had a large proportion of puncta at the poles of the cell. This may have implications on anoxygenic photosynthetic electron flow as it was also noted that NDH-1 has a tendency to form puncta at the poles of PCC 7942 cells (L. N. Liu et al., 2012). Furthermore, NDH-1 is the major route for electrons derived from H_2 oxidation in PCC 6803 (Dutta & Vermaas, 2016). Mixotrophic growth showed a decrease in H_2 evolution (McNeely et al., 2011), with an increased colocalization between Hox and NDH-1, which may suggest a site for anoxygenic photosynthesis where H_2 oxidation is taking place. However the removal of nitrate improves H_2 production (McNeely et al., 2014) and the Hox puncta remained at the poles of the cell which suggests that the poles may be the site of hydrogen metabolism in PCC 7002.

Previous data has shown that the photosynthetic/respiratory electron transport chainin PCC 7942; PSI, PSII and cyt b_6f show a dispersed distribution in the thylakoid membrane with populations forming distinct patches of foci at the poles of the cells (Casella et al., 2017). Each complex was shown to be mobile in the thylakoid (Casella et al., 2017) and the stoichiometry of the complexes was shown to be comparable in both PCC 6803 and PCC 7942 (Casella et al., 2017; Fraser et al., 2013), which indicates similar distribution patterns in these species of cyanobacteria. In this chapter, Hox distribution was observed to be dispersed or in puncta at specific foci similar to PCC 6803 (Burroughs et al., 2014). Interestingly, the populations of Hox and NDH-1 puncta were observed at the poles of PCC 7002 cells. A decrease in the colocalisation of Hox/NDH-1 puncta when

nitrate was replaced by urea suggests there may be a change in the Hox interaction partner. PSI would be a key interaction partner and should be the focus of future work, as PSI is a major source of excessive reducing equivalents in the form of reduced ferredoxin (Appel et al., 2000; Cournac et al., 2002, 2004). Work carried out in PCC 6803 fusing the hydrogenase subunits of Hox to PSI (PsaD-HoxYH) confirms the notion of the interaction between Hox and PSI being key to photoH_2 production in cyanobacteria (Appel et al., 2020).

Comparing photoautotrophically and mixotrophically grown cells under anoxic dark-adapted conditions, the Hox and NDH-1 puncta significantly increased with increased co-localisation of the puncta being observed. Mixotrophic growth of PCC 7002 reduces fermentative H_2 evolution and results in an increase in the excretion of succinate (McNeely et al., 2011). This study also highlighted increased Hox and NDH-1 co-localisation which may further reduce overall H_2 evolution by promoting H_2 oxidation as NDH-1 was shown to be the main route of electrons from H_2 oxidation in PCC 6803 (Dutta & Vermaas, 2016).

Treatment with DCMU blocks electron flow from PS II to the plastoquinone pool, it would therefore be expected that respiration would compensate for electron transport (Cooley & Vermaas, 2001; L. N. Liu et al., 2012). The treatment of PCC 7942 with DCMU increased NDH-1 puncta in order to provide electrons derived from respiration and CEF (L. N. Liu et al., 2012). NDH-1 puncta were observed to decrease when PCC 7002 was treated with DCMU, this may suggest that other complexes (such as succinate dehydrogenase) may play a role in the reduction of the plastoquinone pool by the oxidation of succinate. Considering the Hox puncta in total, there was no significant difference observed between DCMU treated and untreated cultures which was similarly observed in PCC 6803 (Burroughs et al., 2014). DCMU treatment of 6803 did not impede on the rate of photosynthetic H_2 evolution but did reduce the time in which Hox started evolving H_2 when the light was removed, suggesting the respiratory electron transport chain compensate for the lack of electrons derived from the oxidation of water by photosystem II (Cournac et al., 2002). Removing nitrate

(Baebprasert et al., 2011; McNeely et al., 2010, 2011, 2014) or limiting sulphate (Melis et al., 2000) have been culturing strategies applied to improve sustained H_2 evolution in photosynthetic organisms highlighting support from the respiratory electron transport chain to support the hydrogenase (Melis et al., 2000). As the frequency of NDH-1 colocalization is decreased following DCMU treatment, the data suggests that an alternative interaction partner at the thylakoid could be supporting H_2 evolution.

DBMIB blocks the oxidation of the plastoquinone pool by cytochrome b_6f, therefore the plastoquinone is highly reduced. It was observed in PCC 7942 that NDH-1 puncta decreased as a result (L. N. Liu et al., 2012). The treatment of cells with DBMIB showed a decrease in both Hox and NDH-1 puncta populations in PCC 7002. In PCC 6803 the Hox puncta population was not affected following treatment with DBMIB (Burroughs et al., 2014).This may be a result of the inhibition of cytochrome b_6f limiting the flux of electrons to PSI and therefore to Hox. The decrease in the incidence of co-localization between the Hox and NDH-1 puncta could be attributed to limitations in the plastoquinone pool, being further reduced and points to the notion that the observed Hox-NDH-1 interaction is primarily mediating H_2 oxidation (Dutta & Vermaas, 2016).

In PCC 6803 the highest hydrogenase rates were recorded when anoxic dark adapted cells were treated with high light (Cournac et al., 2002; Gutthann et al., 2007). The removal of nitrate and engineering PCC 7002 by inactivation of the nitrate reductase (*narB*) was shown to significantly improve H_2 evolution (Qian et al., 2016). In order to investigate the distribution of Hox and NDH-1 under H_2 evolution, cells were dark adapted with anoxia and switched to high light in either the presence or absence of nitrate. In order to eliminate nitrate the cultures were grown in medium A+ lacking nitrate and supplemented with urea (Ludwig & Bryant, 2012a). With growth on urea, there was no significant difference observed in the Hox and NDH-1 puncta per cell. There was also no significant difference in the co-localisation of the Hox and NDH-1 puncta, however, there was a significant increase in the Hox puncta population that was not colocalised with the NDH-1 puncta. This may result from Hox interacting with an alternative partner at the thylakoid.

Interestingly PCC 7002 did not grow well on urea with a significant increase in the number of sick cells (Sakamoto et al., 1998). If urea is to be used as a sole nitrogen source for H_2 production in cyanobacteria, genetic engineering could offer a solution to the toxicity as demonstrated by inactivation of *ureC* in both PCC 6803 and PCC 7002 (Sakamoto et al., 1998; Veaudor et al., 2018). These results point towards an interaction between Hox and NDH-1 at the site of H_2 oxidation in PCC 7002. This Interaction could be detrimental to H_2 productivity as mixotrophic growth with glycerol followed by anoxic fermentation resulted in decreased H_2 production (McNeely et al., 2011) and removal of nitrate greatly improves H_2 productivity in PCC 7002 (McNeely et al., 2010). The results of **Chapter 5** are summarised in Figure 5-14.

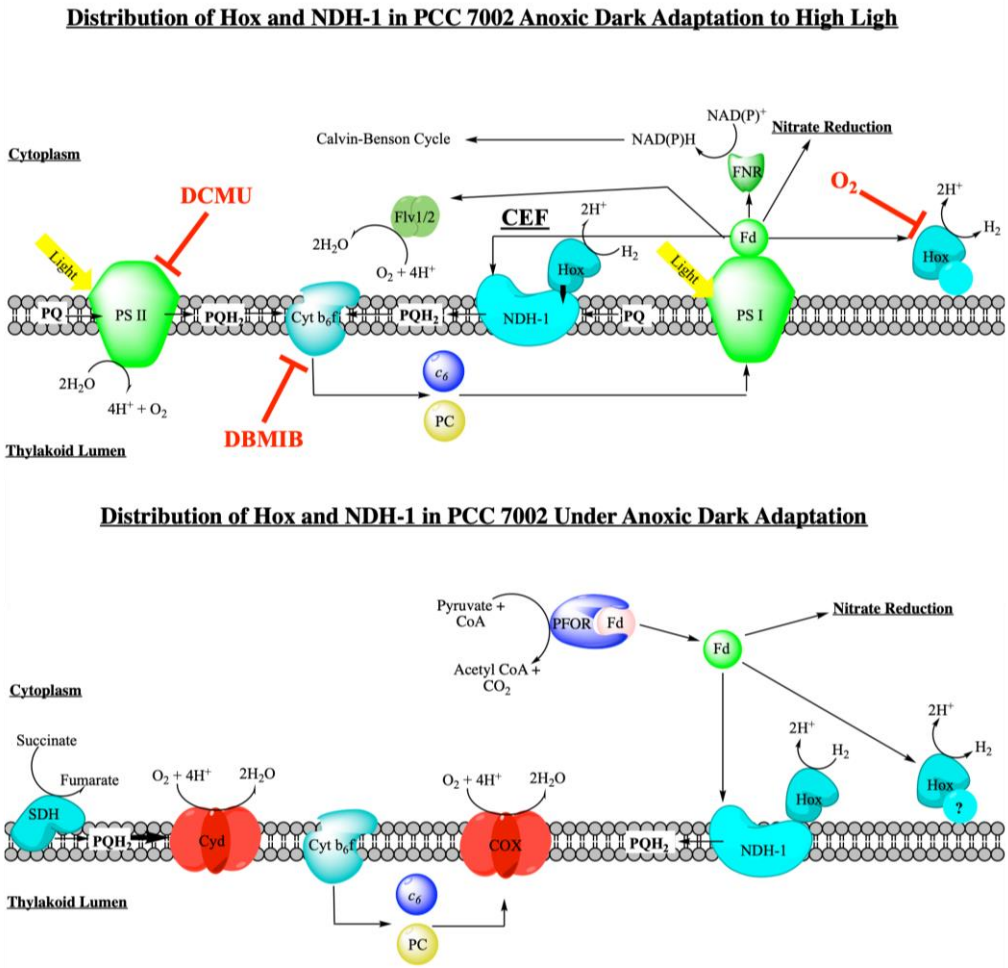

Figure 5-14: Overview of Hox & NDH-1 Interaction in *Synechococcus* sp. PCC 7002
When anoxic dark adapted PCC 7002 cultures are exposed to high light, treatment with DCMU or DBMIB showed a significant decrease in the incidence of NDH-1 puncta which correlated with reduction of the plastoquinone pool. The Hox puncta were unaffected by DCMU treatment however the puncta decreased in DBMIB treatment. Both DCMU and DBMIB treatment resulted in a decreased incidence of Hox and NDH-1 puncta colocalization. Replacing nitrate with urea in PCC 7002 cultures resulted in an increase in Hox puncta that were not colocalized with NDH-1. Under anaerobic dark conditions, the main source of reduced ferredoxin is pyruvate:ferredoxin oxidoreductase (PFOR) which can feed into biosynthetic pathways (such as nitrate assimilation). Removing these pathways may result in more reduced ferredoxin being available for Hox for H_2 evolution. Utilization of glycerol instead of glycogen stores decreases the availability of NADH (McNeely et al., 2014) which in turn means more H_2 oxidation, with the electrons passing into the electron transport chain through NDH-1.

6 Photosynthetic Electron Transport and Carbon Flux Analysis of *Synechocystis* sp. PCC 6803 Strains

6.1 Introduction.

Cyanobacteria have been shown to produce H_2 following anoxic dark adaptation and anoxic dark adaptation shifted to high light (Cournac et al., 2004). H_2 productivity has also been improved by anoxic mixotrophic growth due to the contribution that glucose provides in respiration (Appel et al., 2020), in this study photoautotrophic growth was focussed on in order to get a better understanding of H_2 metabolism and photosynthetic performance.

A major bottleneck in H_2 production in oxygenic photoautotrophs is the sensitivity of Hox to O_2 (Cournac et al., 2004). This issue has been tackled by directly inhibiting oxygen evolution using chemical agents photosystem II (Appel et al., 2020) or by limiting the sulphur in media (Melis et al., 2000). Another more sustainable approach would be to engineer the expression of photosystem II to be repressed under conditions for H_2 production (Batyrova & Hallenbeck, 2017). This approach is problematic in the fact that the reducing equivalents derived from water oxidation by photosystem II would not be available for Hox, removing oxygen from cultures has been applied to cyanobacterial cultures for H_2 production (Khosravitabar & Hippler, 2019) which is a promising alternative as electron flow is not perturbed. In conjunction with targeting the oxygen sensitivity, genetic engineering has been applied to eliminate competing pathways by knocking out *narB* and *nirA* in PCC 6803, significantly improved hydrogen yields 140-times compared to the wild type (Baebprasert et al., 2011).

PCC 6803 has been shown to have 4 electron sinks competing for reductants; Calvin-Benson cycle, protons, oxygen and nitrate (Gutthann et al., 2007). A meroploid knockout of the

Ferredoxin:NAD(P)H reductase in PCC 6803 improved Hox activity, highlighting CO_2 fixation as a major pathway competing for electrons and points towards reduced ferredoxin being a major reductant source for the Hox (Gutekunst et al., 2014).

NDH-1 has 2 distinct isoforms (P. Zhang et al., 2004); NDH-1L involved in CEF (Ohkawa, Pakrasi, et al., 2000) and NDH-1MS responsible for CO_2 concentration (Ohkawa, Dean Price, et al., 2000). M55 is an NDH-1 deficient mutant of PCC 6803 (Ogawa, 1991)) which has neither of the two isoforms (P. Zhang et al., 2004) and is limited in growth through perturbation of CEF and CO_2 concentrating mechanism (Ogawa, 1991; Ohkawa, Dean Price, et al., 2000). NDH-1 has a role in reduction of the plastoquinone pool by respiration (Cooley & Vermaas, 2001) and H_2 oxidation (Dutta & Vermaas, 2016) which in M55 has been shown to enhance photobiological H2 production (Cournac et al., 2004; Gutthann et al., 2007). For an overview on electron transport refer to Figure 6-1.

The M55 strain, has a lower pool of total $NAD(P)^+$ and NAD^+ with the $NAD(P)^+$ pool being completely reduced and the NAD^+ pool showing a similar redox poise to PCC 6803 proving that there is little transhydrogenase activity (Cooley & Vermaas, 2001). Intracellular concentrations of succinate, fumarate and malate were depleted in M55 (Cooley & Vermaas, 2001), this is consistent with the observations in PCC 7002 linking auto fermentative H_2 production to redox poise and succinate oxidation (McNeely et al., 2014). Inhibition of succinate oxidation and respiration resulted in a 40-fold increase in H_2 evolution in PCC 6803 (Burrows et al., 2008), highlighting that diverting electron flux from the plastoquonone pool is a successful strategy for improving H_2 yields in cyanobacteria. However, a greater understanding of comparative flux down the Embden-Meyerhof-Parnas pathway, oxidative

pentose phosphate, Entner-Duodoroff pathways and a complete overview of the tricarboxylic acid cycle in these mutants is critical.

Previous work has shown that Hox behaves as an electron valve in photoautotrophic growth (Appel et al., 2000). This was later shown to be essential under both mixotrophic and nitrate limiting growth (Gutekunst et al., 2014) where no measurable growth phenotype had been observed under photoautotrophic (Appel et al., 2000; Eckert et al., 2012) and mixotrophic growth (Gutekunst et al., 2014). Understanding the physiological basis for when electron flux through the Hox is essential is critical for developing strategies for the sustained H_2 production in a cyanobacterial chassis.

By removing nitrate in PCC 7002 metabolites in the Embden-Meyerhof-Parnas pathway were enriched (McNeely et al., 2014), which ultimately increased the amount of NAD(P)H and therefore increasing the overall reductant poise in metabolism, resulting in excess reductant being converted to H_2 and lactate (McNeely et al., 2014). H_2 productivity has been shown to increased fivefold through deletion of the lactate dehydrogenase gene (McNeely et al., 2010). This strategy has been successfully utilized to improve H_2 yields in heterotrophic bacteria (Tran et al., 2014). With reference to **Error! Reference source not found.**Figure 6-1, lactate is produced by the reduction of pyruvate, which decreases reductant flux towards the bidirectional Hox (Gutekunst et al., 2014; McNeely et al., 2010).

Up to 40% of electrons originate from photosystem II (Helman et al., 2005), which offers a tantalising option for electron sequestration to Hox. The quinol oxidases were knocked out in PCC 6803 (Δ *cyd* Δ *cytI*) which resulted in a reduction in net photosynthesis but a considerable increase in Hox activity but only

a modest increase in total photobiological H_2 evolution (Gutthann et al., 2007).

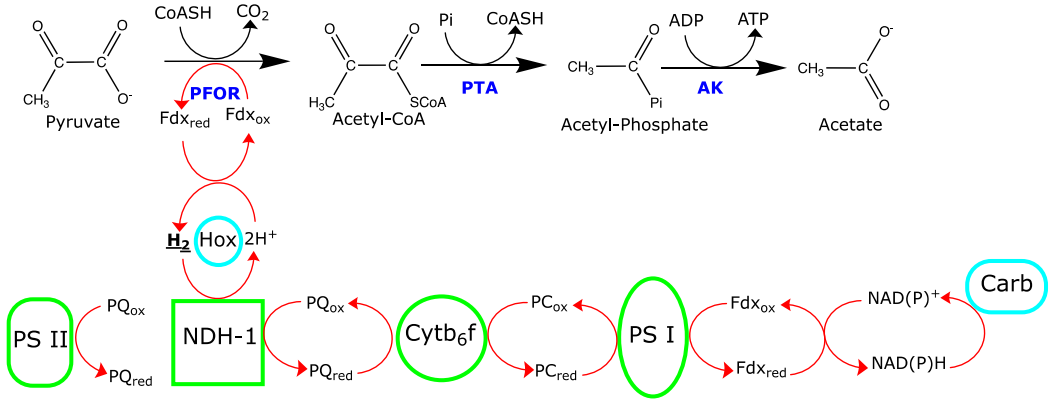

Figure 6-1: Overview of Electron Transport in H_2 Metabolism in Non-Diazotrophic Cyanobacteria.
The electrons derived from intracellular carbon stores feed into H_2 metabolism in dark anoxic conditions via pyruvate:ferredoxin oxidorectase (PFOR), which converts pyruvate to acetyl-CoA, releasing CO2 and reducing ferredoxin (Fdx_{red}). Phosphotransacetylase (PTA) converts the acetyl-CoA into acetyl-phosphate by consuming a phosphate and releasing CoA. Acetate kinase (AK) dephosphorylates the acetyl-phosphate generating acetate and ATP. Fdx_{red} generated by the conversion of pyruvate to acetyl-CoA can be oxidized by Hox resulting in H_2 being evolved and the oxidation of ferredoxin (Fdx_{ox}). H_2 can be oxidized, reducing plastoquinone (PQ_{ox}). Oxidation of the plastoquinol (PQ_{red}) is carried out by the cytochrome b_6f complex ($Cytb_6f$) and reduces the plastocyanin (PC_{ox}) pool. Reduced plastocyanin (PC_{red}) can pass electrons to terminal oxidases (not shown) or in light dependant manner to photosystem I (PSI). In conditions where reducing equivalents can be accepted into the electron transport, Hox can oxidize H_2. Red arrows represent the flow of electrons, black arrows represent the flow of intracellular metabolites, green boxes represent protein complexes localized to the thylakoid membrane, turquoise boxes represent soluble protein complexes and blue labels represent soluble enzymes.

Chapter 6 will focus on electron transport in PCC 6803 with respect to H_2 metabolism. The results agreed with previously published data with regards to photoautotrophic growth of PCC 6803 (Appel et al., 2000; Eckert et al., 2012). During exponential growth, oxygen evolution rates were assayed to assess activity of photosystem II in the photosynthetic electron transport chain. It was demonstrated that Hox null mutants showed a similar oxygen evolution phenotype as observed in the CEF deficient mutants. This chapter will wrap up with the assessment of the metabolome of

PCC 6803 strains under continuous light, anoxic dark adaptation and the transition from anoxic dark-adapted cells to high light.

6.2 Growth Characteristics of Hydrogenase Mutants in PCC 6803.

The growth of PCC 6803 was carried out at 60 μE m^{-2} s^{-1} under photoautotrophic growth conditions in order to compare the data acquired for photoautotrophic growth in **Chapters 3 & 4**. The strain M55 strain (PCC 6803 Δ*ndhB*) was cultured for comparisons due to the increased overall H_2 production in this strain (Cournac et al., 2004). As Hox was shown to colocalize with NDH-1 under a range of growth conditions, the Δ*ndhD1/ndhD2* was also used as a comparison due to the inability of the strain to perform CEF (Ohkawa, Pakrasi, et al., 2000). In order to investigate changes in the metabolism due to the absence of Hox activity, the Δ*hox* strain was used as the entire *hox* operon has been deleted (Eckert et al., 2012). In **Chapter 4** it was demonstrated that the Δ*hoxW* and Δ*hoxYH* strains showed a similar distribution of Hox, both of these strains still have the diaphorase subunit HoxEFU (Eckert et al., 2012) and given the in vitro activity of these subcomplexes these strains were added to the metabolomics analysis (Artz et al., 2020).

Hox null mutants previously showed no appreciable difference between growth rates under photoautotrophic conditions (Appel et al., 2000; Eckert et al., 2012). **Error! Reference source not found.**Figure 6-2 A-E shows the growth curves of PCC 6803 strains. There was no significant difference in the growth rate between the strains (Figure 6-2F), (ANOVA p=0.067).

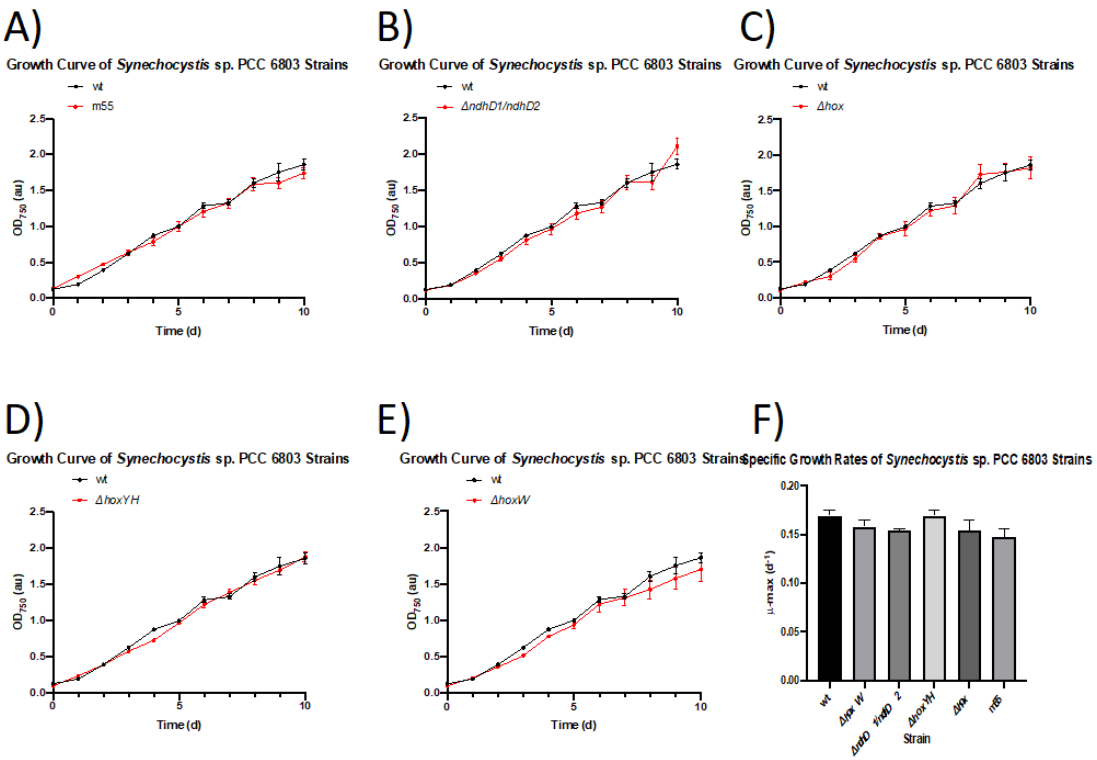

Figure 6-2: Growth Kinetics of Photoautotrophically Grown PCC 6803 Strains. Each of the PCC 6803 strains growth curves were compared to wild type (panels A-E). A) WT compared to M55, B) WT compared to Δ*ndhD1*/Δ*ndhD2*, C) WT compared to Δ *hox*, D) WT compared to Δ *hoxYH* and E) WT compared to Δ *hoxW*. Panel F depicts the specific growth rate (μ-max) of all strains. Error bars represent the standard error of the mean (n=6). Where error bars are not shown, the error bars overlap the data point symbol.

6.3 Photosynthetic Characterization of PCC 6803 Strains.

6.3.1 Pigment Composition of PCC 6803 Strains in Exponential Growth phase.

An aliquot from each of the individual PCC 6803 cultures was analysed during exponential growth to assess oxygen evolution rates at different light intensities using a photoinhibition curve. Cell pigments were analysed by scanning whole cell absorption spectra

(Figure 6-3**Error! Reference source not found.** A-E). The variance was assessed by calculating the phycocyanin:chlorophyll *a* ratio (Figure 6-3**Error! Reference source not found.** F).

The PCC 6803 Δ*hoxW* and Δ*hox* strains showed significantly higher phycocyanin/chlorophyll *a* ratio compared to WT (T-test $p<0.001$ and $p=0.008$ respectively) with no significant difference being observed in Δ*hoxYH* (T-test $p=0.106$). PCC 6803 WT showed no significant difference between the phycocyanin:chlorophyll *a* ratio when compared to the NDH-1 mutants M55, and Δ *ndhD1*/Δ *ndhD2* (T-test $p=0.685$ and $p=0.079$ respectively).

Comparing the PCC 6803, Δ*hoxW* and Δ*hox* cultures, no significant changes in the phycocyanin:chlorophyll *a* ratio were observed (T-test $p=0.447$). PCC Δ*hoxYH* showed a significantly lower phycocyanin:chlorophyll *a* ratio compared to Δ*hoxW* (T-test $p=0.003$) with no significant difference observed compared to the Δ *hox* strain ($p=0.079$).

M55 was shown to have a similar phycocyanin:chlorophyll *a* ratio when compared to Δ *hoxYH*, Δ *hox* and the Δ *ndhD1*/Δ *ndhD2* strain (T-test $p=0.531$, $p=0.067$ and $p=0.157$ respectively). M55 showed significantly less phycocyanin compared to Δ*hoxW* (T-test $p=0.001$). Δ *ndhD1*/Δ *ndhD2* showed a significantly lower phycocyanin:chlorophyll *a* ratio when compared to Δ *hoxYH*, Δ *hoxW* and Δ *hox* (T-test $p=0.007$, $p<0.001$ and $p=0.01$) respectively.

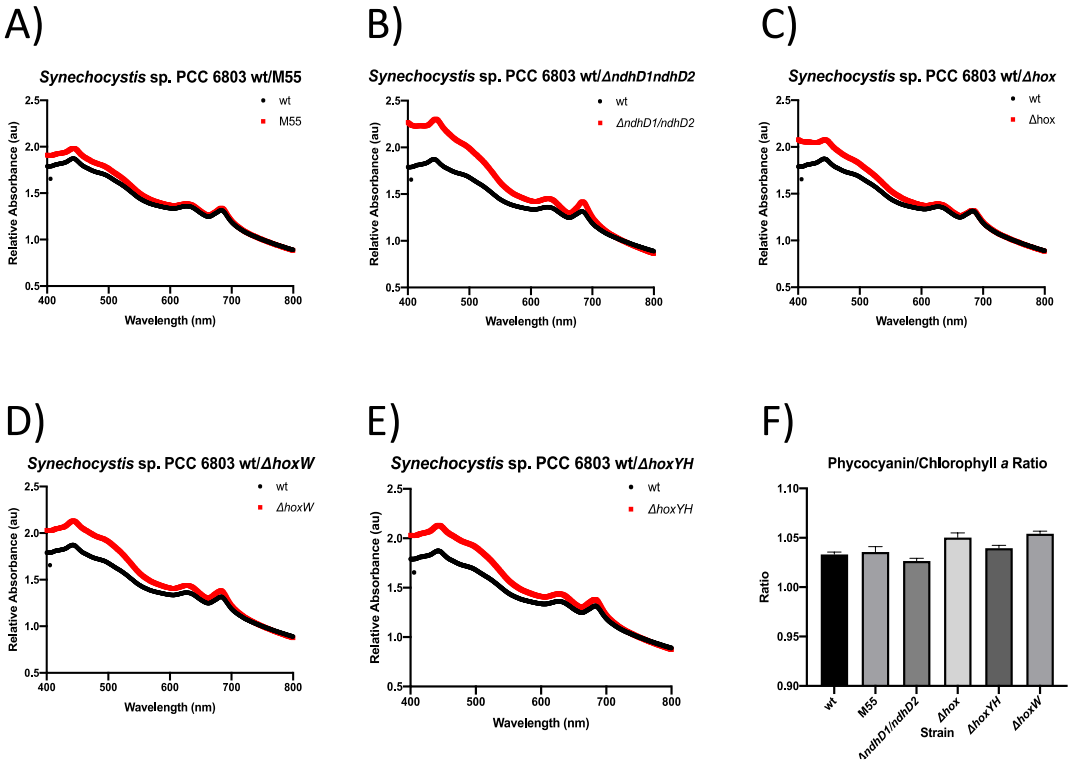

Figure 6-3: Scanning Whole Cell Absorption Spectra of PCC 6803.
Each of the PCC 6803 strains scanning whole cell absorption spectra was measured and compared to wild type (panels A-E) prior to oxygen evolution assessment. A) WT compared to M55, B) WT compared to Δ*ndhD1*/Δ*ndhD2*, C) WT compared to Δ *hox*, D) WT compared to Δ *hoxYH* and E) WT compared to Δ *hoxW*. Panel F depicts the phycocyanin:chlorophyll *a* of all strains. Error bars represent the standard error of the mean (n=6).

6.3.2 Oxygen Evolution Rates of the individual PCC 6803 Strains.

The oxygen evolution rates were measured using the Clark electrode (Figure 6-4**Error! Reference source not found.**). The NDH-1 mutants M55 and Δ *ndhD1*/Δ *ndhD2*, were more susceptible to increased light intensity than the wild type, even at very low light e.g. 13 μE (Figure 6-4**Error! Reference source not found.** A and B). The Hox null mutant had a similar phenotype to the NDH-1 mutant when compared to the wild type (Figure 6-4**Error! Reference source not found.** C-E). The Δ*hoxE* strain was used as a control given localization of the Hox is restricted to the cytoplasm (Burroughs et al., 2014) resulting in a reduction in Hox activity to 70% of the WT (Eckert et al., 2012) (Figure 6-4**Error! Reference source not found.** F). The null phenotype previously seen in the Hox mutant was not observed until the assay reached over 100 μE.

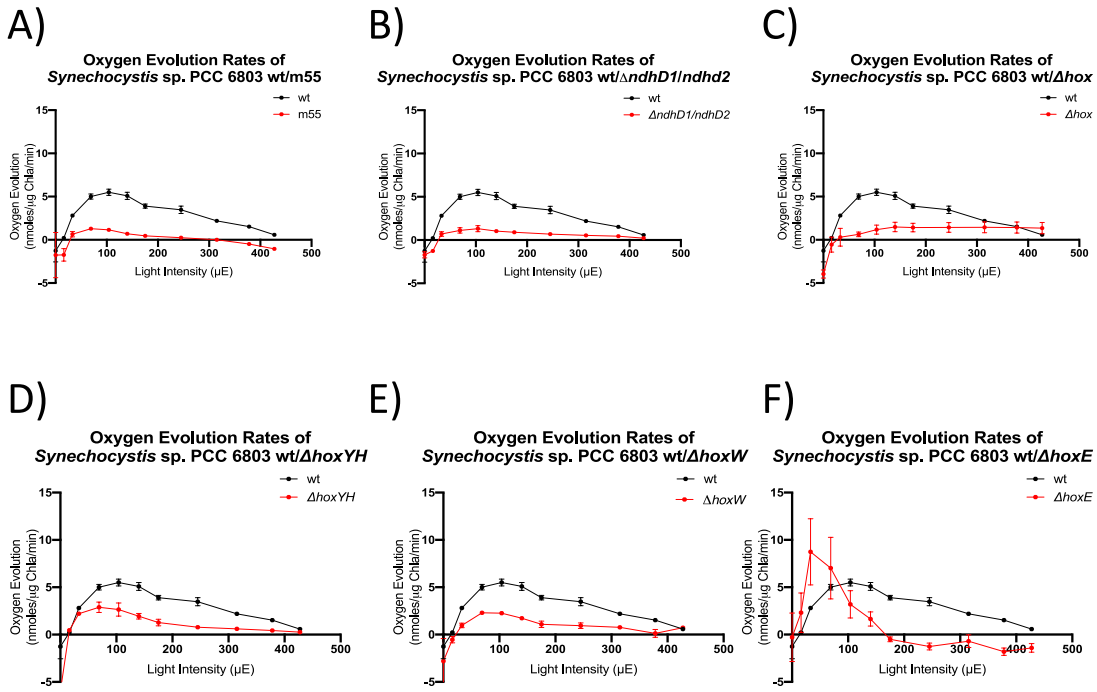

Figure 6-4: Photoinhibition Curve of PCC 6803 Strains.
Oxygen evolution rates were assessed in each of the PCC 6803 strains under increased light intensities and were compared to the wild type (panels A-F). A) WT compared to M55, B) WT compared to Δ*ndhD1*/Δ*ndhD2*, C) WT compared to Δ *hox*, D) WT compared to Δ *hoxYH*, E) WT compared to Δ *hoxW* and F) WT compared to Δ *hoxE*. Error bars represent the standard error of the mean (n=3). Where error bars are not shown, the error bars overlap the data point symbol.

6.4 Metabolomic Profiling of the individual PCC 6803 Strains.

6.4.1 Comparing the Metabolomes of PCC 6803 Wild Type Under Photoautotrophic, Anoxic Dark Adapted and Anoxic Dark Adapted to High Light Conditions.

The above strains were grown under photoautoautotrophic, anoxic dark adapted and anoxic dark adapted followed by highlight exposure. Metabolites were extracted from each strain for untargeted metabolomics. Data was processed and the metabolites were identified using Compound Discoverer 3.1 SP1 (Thermo Fisher Scientific, Hemel Hempstead, UK) using an untargeted workflow. Metabolites were identified using accurate masses, retention times of 268 authentic standards and/or ddMS/MS *mz*Cloud fragmentation database (Thermo Fisher Scientific, Hemel Hempstead, UK), to provide the highest level of confidence on identification.

Both the cell pellet and the supernatant were utilised. Figure 6-5 summarizes the differences in the metabolite profile of the wildtype strain following photoautotrophic growth at 60 $\mu E\ m^{-2}s^{-1}$, anoxic dark adaptation and anoxic dark adaptation and high light exposure (600 $\mu E\ m^{-2}\ s^{-1}$). It is evident that each of the conditions had a significant impact on the wildtype strain and the subsequent metabolic profile, given the clear differences between the points. Similar profiles were seen for each of the other strains tested (data not shown). Metabolite groups were exported from Compound Discovery normalized to OD_{750} for multivariant analysis using Symca +P13 (Umetrics AB, Sweden). Variable importance in the project (VIP) of the OPLS-DA models was used to demonstrate the fitness of the model. Comparing the conditions in PCC 6803 wild type, a fitness of $R^2Y = 0.947$ and predictability of $Q^2=0.823$ was observed in the OPLS-DA model.

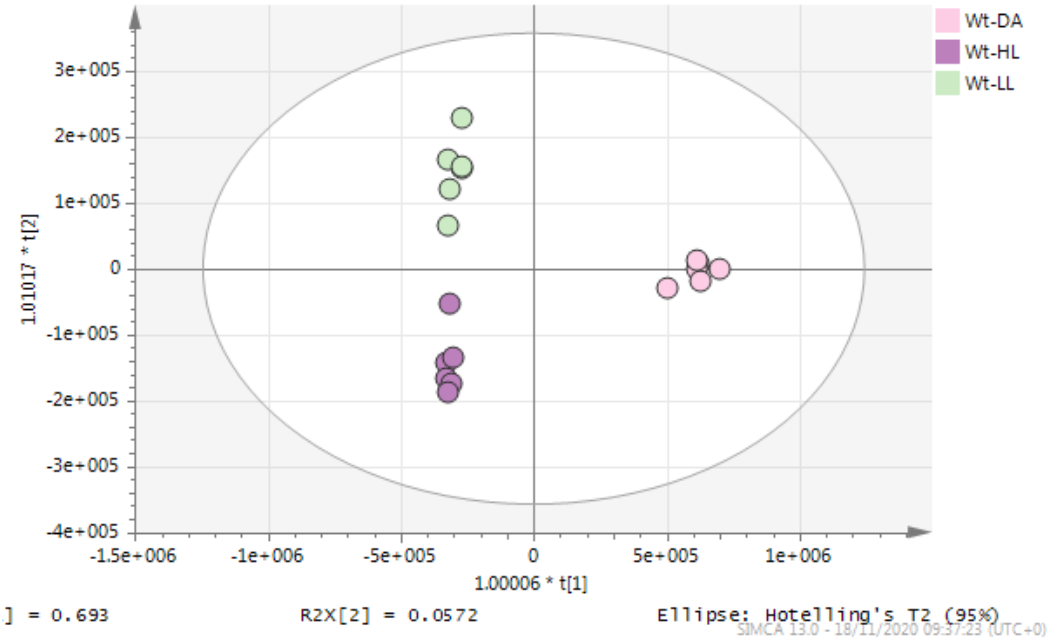

Figure 6-5: OPLSDA Plot Comparing PCC 6803 Wild Type following Photoautotrophic, anoxic dark-adapted and anoxic dark-adapted to high light.
The data displayed shows PCC 6803 strains grown photoautotrophically (green), then anoxically dark adapted (pink) and anoxically dark adapted before high light treatment (magenta). Each of the data points represents 1 biological replicate (n=6).

Table 6-1 highlights the key metabolic changes in wild type PCC6803 grown under the different conditions with significant increases (green) and decreases (red, orange and yellow) detected in the metabolic profile relating to growth e.g., photoautotrophic growth, anoxic dark adaptation and anoxic dark-adaptation and followed by high light treatment. Metabolites highlighted in Table 6-1 all have VIP>1, indicating significant contribution to the model and have log2 fold changes relative to photoautotrophically grown conditions.

As photoautotrophic growth of PCC 6803 does not evolve H_2, whereas anoxic dark adapted and anoxic dark adapted cells treated with high light evolves H_2 (Cournac et al., 2002; Gutthann et al., 2007), the metabolome of wild type in each treatment was

compared to photoautotrophic growth. Following anoxic dark adaptation, lactic acid, 8-hydroxydeoxyguanosine, cytidine and 2’ deoxyadenine was shown to increase significantly. Steric acid, D-pantothenatic acid, valine, serine, threonine and nicotinamide were shown to decrease in abundance.

Given anoxic dark adaptation results in increased H_2 production (Cournac et al., 2004), increased metabolite abundance under these conditions is relevant. Tryptophan and 2’ deoxyadenine were shown to increase in abundance, with no metabolites shown to significantly decrease in abundance.

Table 6-1: Log2 fold Change of Metabolites in PCC 6803 Wild Type Comparing Photoautotrophic Growth with Anoxic Dark Adaptation.
Values displayed are Log2 fold changes in relative peak intensity. Green highlights metabolites with increased relative abundance. Red indicates a decrease in metabolite relative abundance. Scale bar represents changes in relative metabolite abundance.

	Metabolite	DA	DA to HL
Organic acids	DL-Lactic Acid	6.54	-0.27
	Stearic acid	-2.98	1.35
	D-PANTOTHENIC ACID	-2.16	-0.22
	(±)-Malic Acid	1.28	-1.37
	Palmitic Acid	-1.54	0.71
	Succinic acid	-1.14	-1.85
	γ-Aminobutyric acid	-0.63	-0.87
Amino Acids	DL-Glutamic acid	-1.18	0.48
	DL-Glutamine	0.89	0.37
	L-(+)-Valine	-2.19	-1.62
	L-Proline	1.27	1.29
	L-(+)-Leucine	-0.86	-0.92
	DL-Lysine	-0.24	-0.71
	L-(-)-Serine	-2.68	-1.61
	L-(-)-Threonine	-2.09	-1.06
	L-(+)-Alanine	-0.81	-0.60
	DL-Tryptophan	0.52	2.69
Nucleic Acids	8-hydroxy-deoxyguanosine	3.02	1.54
	Cytidine	3.36	0.54
	Nicotinamide	-3.11	-1.75
	2'-Deoxyadenosine	2.86	2.09
	Adenine	-1.76	-1.40

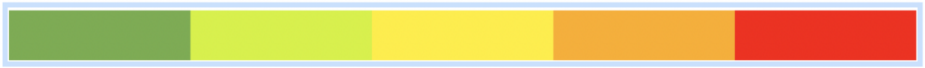

Increase Decrease

6.4.2 Comparing individual PCC 6803 Strains Under Photoautotrophic Growth Conditions.

The metabolome of the different PCC 6803 (Hox mutants and M55) strains was compared directly to the wildtype strain under photoautotrophic growth at 60 μE $m^{-2}s^{-1}$. The M55 strain has been shown to have an increased and sustained rate of H_2 production, the mechanism for this still remains elusive (Cournac et al., 2004). The localised interactions between Hox and NDH-1 have been

clearly highlighted in **Chapters 3 and 4** and therefore NDH1 mutants may impact on Hox metabolism. Figure 6-6summarizes the differences between the wild type and the M55 strain grown photoautotrophically.

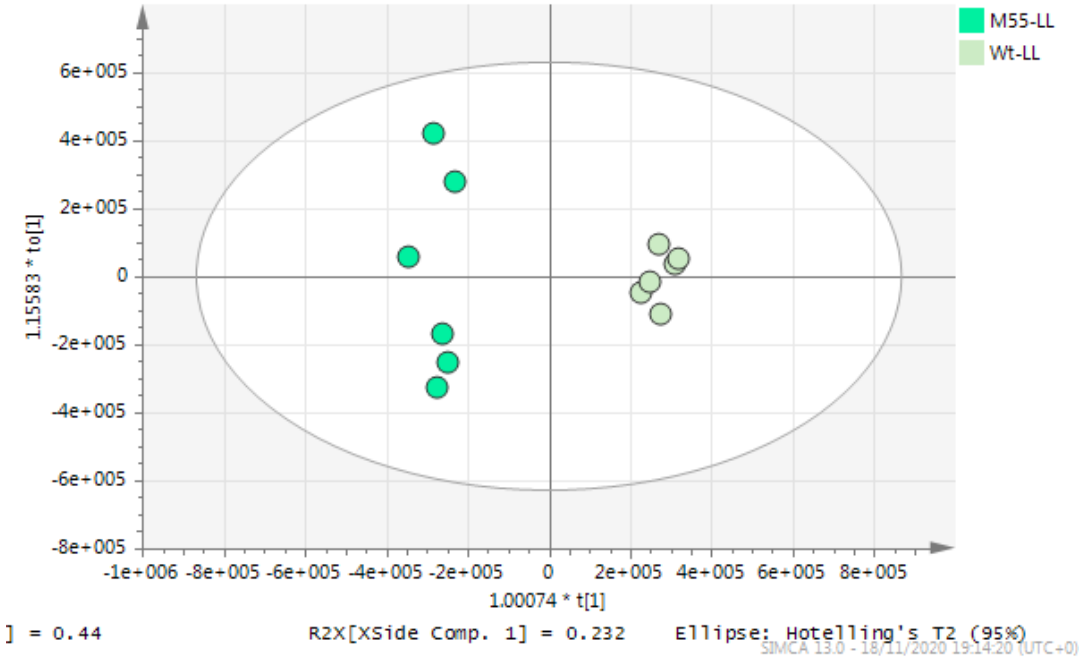

Figure 6-6: OPLSDA Plot Comparing PCC 6803 Wild Type and M55 Strain following Photoautotrophic Growth.
Comparison between PCC 6803 wild type (light green) and M55 (turquoise) grown photoautotrophically. Each of the data points represents 1 biological replicate (n=6).

Table 6-2 highlights the key metabolites which significantly increased (green) and decreased (orange and red) between the different PCC 6803 strains under photoautotrophic growth. In order to highlight pathways associated with H_2 metabolism, all strains were compared to wild type. Metabolites highlighted in Table 6-2 all have VIP>1, indicating significant contribution to the model and have log2 fold changes of strains relative to photoautotrophically grown wild type cultures.

Following photoautotrophic growth M55 showed a significant decrease in leucine, lysine, serine and deoxyadenine. Metabolites with a significant increase in abundance were glutamic acid, proline and alanine.

The Δ*ndhD1/ndhD2* strain showed a relative increase in valine, proline and deoxyadenosine. Metabolites with a significant decrease in relative abundance were D-pantothenic acid, lysine, serine, threonine, cytidine and adenine monophosphate.

The Δ*hox* strain had a significant increase in Glutamine. Stearic acid, malic acid, valine, lysine and 8-hydroxydeoxyguanosine all had a relative decrease in abundance.

No metabolites significantly increased in relative abundance in the Δ*hoxYH* strain. Only lysine showed a relative decrease in abundance. No metabolites significantly increased in relative abundance in the Δ*hoxW* strain. Lysine and D-pantothenic acid were shown to decrease.

Table 6-2: Log2 fold Change of Metabolites in PCC 6803 Strains Grown Photoautotrophically.
Values displayed are 2Log fold changes in relative peak intensity. Green highlights metabolites with increased relative abundance. Red indicates a decrease in metabolite relative abundance. Scale bar represents changes in relative metabolite abundance.

	Metabolite	M55	Δ*ndhD1/ndhD2*	Δ*hox*	Δ*hoxYH*	Δ*hoxW*
Organic acids	DL-Lactic Acid	0.27	0.69	0.35	-1.04	-0.04
	Stearic acid	0.65	1.23	-2.14	0.74	0.71
	D-PANTOTHENIC ACID	0.01	-3.71	-0.35	-0.99	-2.64
	Palmitic Acid	1.96	0.66	-1.86	0.77	0.93
	(±)-Malic Acid	-1.36	-1.76	-2.24	-1.24	-1.35
	γ-aminobutyric acid	1.77	1.17	0.29	-1.68	0.20
	Succinic acid	1.04	1.19	0.44	0.32	0.89
Amino acids	DL-Glutamic acid	4.11	1.29	0.80	1.14	1.26
	DL-Glutamine	0.41	-0.17	3.20	0.33	0.35
	L-(+)-Valine	1.70	2.30	-2.30	-0.96	-0.43
	L-Proline	3.35	2.10	1.53	0.84	1.24
	L-(+)-Leucine	-2.80	0.27	0.16	0.04	-0.23
	DL-Lysine	-2.08	-2.40	-2.05	-2.07	-3.06
	L-(-)-Serine	-3.30	-2.45	-0.03	-0.33	-0.88
	L-(-)-Threonine	-1.62	-2.36	-1.55	-1.18	-0.36
	L-(+)-Alanine	2.05	0.32	-0.85	0.61	0.75
	DL-Tryptophan	1.22	-0.17	-0.85	-0.31	-0.61
	(-)-L-Carnitine	-0.81	0.91	-0.64	-0.22	-0.72
Nucleic acids	8-hydroxy-deoxyguanosine	1.31	0.15	-2.39	-1.16	-0.54
	Cytidine	0.94	-2.82	1.82	1.12	1.73
	Nicotinamide	-1.54	1.04	0.02	0.25	-0.14
	2'-Deoxyadenosine	-2.11	3.04	-0.23	0.65	0.28
	Adenine	-1.54	1.04	0.02	0.25	-0.14
	Adenosine monophosphate	1.40	-2.13	-1.02	-1.44	-1.39

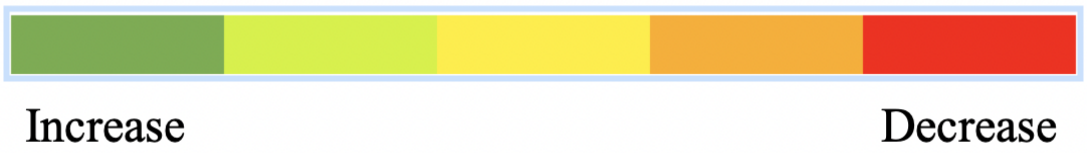

6.4.3 Comparing PCC 6803 Strains following Anoxic Dark Adaptation.

The metabolic data from the PCC 6803 strains was compared under anoxic dark-adapted conditions. H_2 has been shown to be evolved under these conditions (Appel et al., 2020; Cournac et al., 2002, 2004; Gutekunst et al., 2014; Gutthann et al., 2007) and therefore mutants of PCC 6803 that effect H_2 metabolism were investigated. **Error! Reference source not found.**Figure 6-7 summarizes the difference between M55 and the wild type strain following anoxic dark-adaptation. Clear differences can be seen between the two strains. Significant differences were also observed between the other PCC 6803 strains and the wild type (data not shown). Comparing PCC 6803 wild type with the high H_2 producing M55 strain under anoxic dark adaptation after photoautotrophic growth, a fitness of R^2Y = 0.982 and predictability of Q^2=0.971 was observed in the OPLS-DA model.

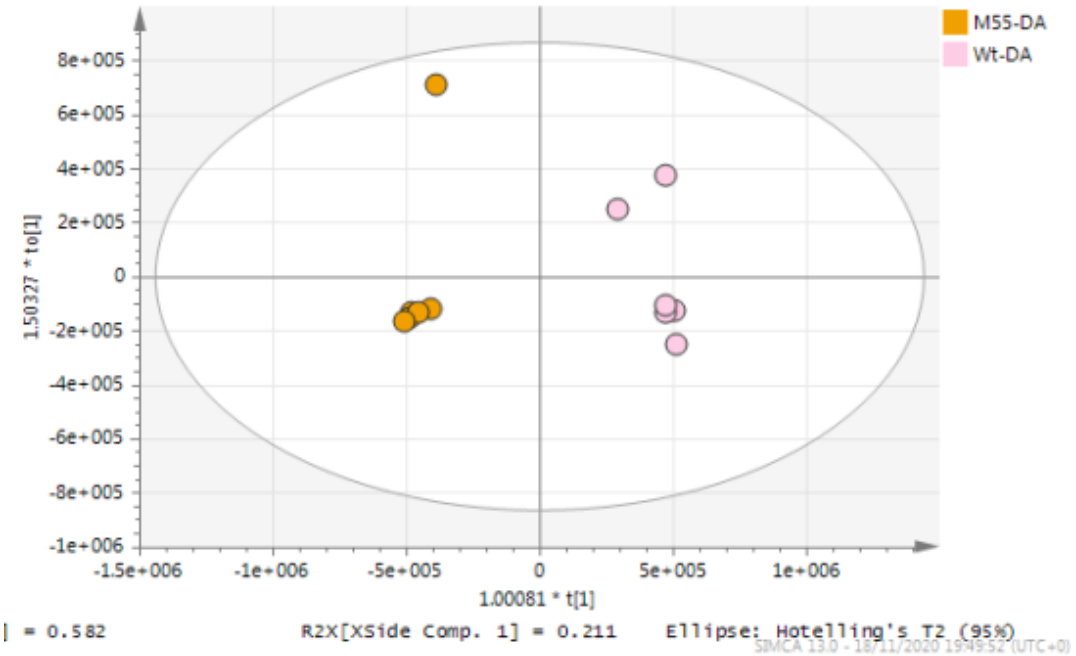

Figure 6-7: OPLSDA Plot Comparing PCC 6803 Wild Type and the M55 Strain following Anoxic Dark Adapted after Photoautotrophic Growth.
Comparison between PCC 6803 WT (pink) and M55 (orange) grown photoautotrophically prior to anoxic dark adaptation. Each of the data points represents 1 biological replicate (n=6).

Table 6-3highlights significant metabolites which either increased (green) or decreased in abundance (orange and red) between the different PCC 6803 strains compared to the wild type following anoxic dark adaptation. Metabolites highlighted in Table 6-3 have VIP>1, indicating significant contribution to the model with the log2 fold changes indicating increased/decreased metabolite abundance in PCC 6803 strains relative to wild type under anoxic dark adapted conditions following photoautotrophic growth.

The M55 strain showed a relative increase in D-pantothenic acid, succinic acid, proline, serine, and alanine. Metabolites that showed a decrease in the relative abundance included lactic acid, malic acid, glutamine, 8-hydroxydeoxyguanosine, cytidine, 2' deoxyadenine and adenine monophosphate.

The Δ*ndhD1/ndhD2* strain had a significant increase in the relative abundance of glutamic acid. The following metabolites showed a decrease in their relative abundance lactic acid, palmitic acid, 8-hydroxydeoxyguanosine and adenine monophosphate.

The Δ*hox* strain showed a relative increase in stearic acid and succinic acid. Metabolites with a decrease in relative abundance included; lactic acid, malic acid, γ-aminobutyric acid, glutamic acid, glutamine, leucine, tryptophan, carnitine, cytidine, 2' deoxyadenine and adenine monosphosphate.

The Δ*hoxYH* strain had a significant increase in the abundance of stearic acid and succinic acid. Metabolites that decreased in relative abundance were lactic acid, malic acid, γ-aminobutyric acid, glutamic acid, glutamine, valine, alanine, tryptophan, carnitine, cytidine and nicotinamide.

The Δ*hoxW* strain showed an increase in the abundance of succinic acid. A decrease in the relative abundance of lactic acid and adenosine monophosphate was observed.

Table 6-3: Log2 fold Change of Metabolites in PCC 6803 Strains In Anoxic Dark Adapted Conditions.
Values displayed are Log2 fold changes in relative peak intensity. Green highlights metabolites with increased relative abundance. Red indicates a decrease in metabolite relative abundance. Scale bar represents changes in relative metabolite abundance.

	Metabolite	M55	Δ*ndhD1/ndhD2*	Δ*hox*	Δ*hoxYH*	Δ*hoxW*
Organic acids	DL-Lactic Acid	-3.87	-5.95	-6.46	-6.37	-5.79
	Stearic acid	0.89	-1.22	2.61	3.29	1.49
	D-PANTOTHENIC ACID	2.59	-0.74	1.54	1.54	1.42
	Palmitic Acid	-1.02	-2.95	-0.42	-0.65	0.03
	(±)-Malic Acid	-2.62	-0.34	-4.80	-3.55	-1.91
	γ-aminobutyric acid	-0.05	1.63	-2.21	-2.56	-1.16
	Succinic acid	2.61	-0.05	2.64	2.70	3.45
Amino acids	DL-Glutamic acid	0.11	2.50	-3.95	-3.71	-1.54
	DL-Glutamine	-2.30	-1.00	-3.54	-2.49	-0.74
	L-(+)-Valine	-0.31	-1.39	0.01	-2.09	-1.25
	L-Proline	3.75	-0.19	0.65	0.51	1.09
	L-(+)-Leucine	2.13	0.11	-2.23	0.26	1.88
	DL-Lysine	0.10	0.62	-0.75	-1.12	-0.68
	L-(-)-Serine	3.00	-0.03	1.86	-0.69	-0.12
	L-(-)-Threonine	1.97	1.82	-1.04	-0.96	-0.01
	L-(+)-Alanine	2.00	-1.52	-0.92	-2.29	-1.10
	DL-Tryptophan	-0.77	-0.38	-4.16	-3.43	-1.15
	(-)-L-Carnitine	-1.95	-1.43	-2.99	-2.19	-1.77
Nucleic acids	8-hydroxy-deoxyguanosine	-4.05	-4.65	1.44	1.51	0.29
	Cytidine	-4.02	-2.64	-3.16	-2.29	-1.14
	Nicotinamide	5.45	0.63	-1.49	-2.12	-0.61
	2'-Deoxyadenosine	-3.16	-4.90	1.49	1.85	0.17
	Adenine	1.34	-1.48	-0.32	-1.17	-0.51
	Adenosine monophosphate	-4.29	-5.25	-2.59	-1.62	-3.14

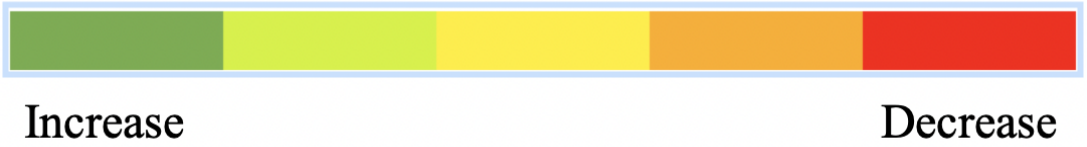

6.4.4 Comparing PCC 6803 Strains following Anoxic Dark Adaptation and Exposure to High Light.

In order to investigate the metabolome of PCC 6803 strains under conditions that have the highest Hox activity (Cournac et al., 2002), The strains were dark adapted for three days and then exposed to high light (600 μE m^{-2} s^{-1}). Figure 6-8demonstrates that there is a clear difference between M55 and the wild type strain following anoxic dark-adaptation and high light exposure. Significant differences were also observed between the individual PCC 6803 strains (data not shown). Comparing PCC 6803 wild type with the high H_2 producing M55 strain grown photoautotrophically, dark adapted and treated with high light (600 μE $m^{-2}s^{-1}$), a fitness of R^2Y = 0.994 and predictability of Q^2=0.98 was observed in the OPLS-DA model.

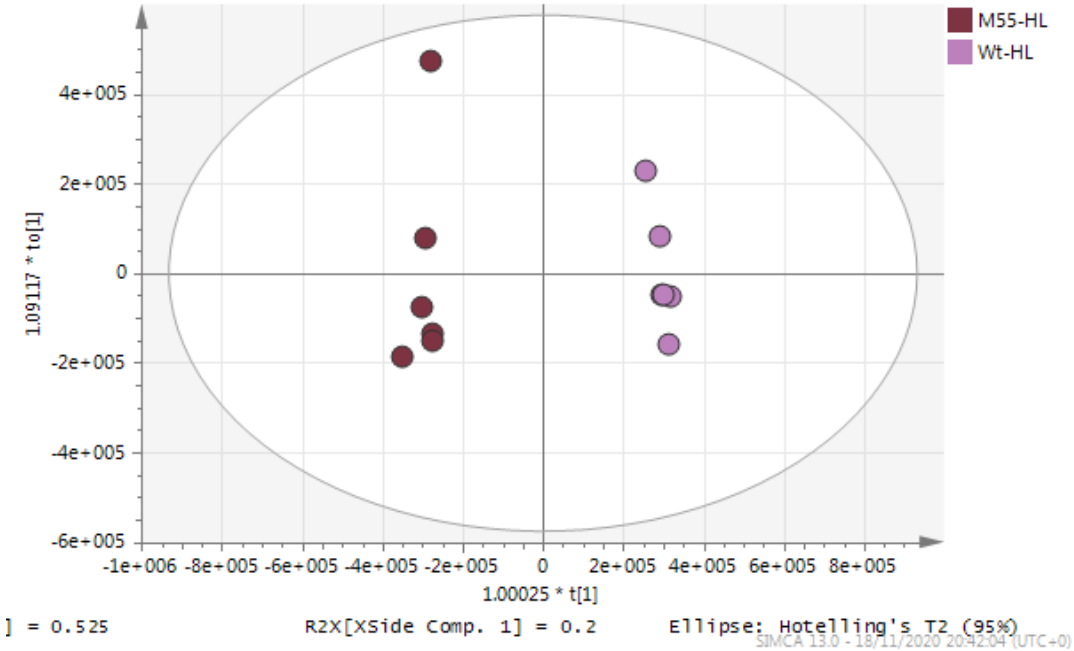

Figure 6-8: OPLSDA Plot Comparing PCC 6803 Wild Type and M55 Strain following Anoxic Dark Adaptation and High Light Treatment.
Comparison between PCC 6803 WT (Purple) and M55 (Brown) grown after anoxic dark adaptation and high light treatment. Each of the data points represents 1 biological replicate (n=6).

Table 6-4 highlights metabolites that significantly increased or (green) decreased (orange and red) between the different PCC 6803 strains following anoxic dark-adaptation and high light. All strains were compared to the wild type. Metabolites highlighted in

Table 6-4 have VIP>1, indicating significant contribution to the model with the log2 fold changes indicating increased/decreased metabolite abundance in PCC 6803 strains relative to wild type under anoxic dark adapted conditions treated with high light following photoautotrophic growth.

M55 showed an increase in the metabolite abundance of valine and carnitine. M55 showed a decrease in relative metabolite abundance of lactic acid and adenosine monophosphate.

The Δ*ndhD1/ndhD2* strain showed an increase in the relative abundance of palmitic acid, γ-aminobutyric acid and malic acid. A decrease was seen in the relative metabolite abundance of lactic acid, D-pantothenic acid, succinic acid, carnitine, nicotinamide and adenosine monophosphate.

The Δ*hox* strain showed an increase in the abundance of carnitine and nicotinamide. Lactic acid, malic acid, glutamic acid, alanine and adenine had a reduced relative abundance.

The Δ*hoxYH* strain showed a relative increase in the abundance of the metabolite adenosine monophosphate. Glutamic acid and alanine showed a relative decrease in abundance.

The Δ*hoxW* strain showed no significant increase in the metabolite abundance. Succinic acid was decreased in abundance.

Table 6-4: Log2 fold Change of Metabolites in PCC 6803 Strains In Anoxic Dark Adapted and Treated with High Light.
Values displayed are Log2 fold changes in relative peak intensity. Green highlights metabolites with increased relative abundance. Red indicates a decrease in metabolite relative abundance. Shades from orange to yellow show increasing relative abundance.

	Metabolite	M55	Δ*ndhD1/ndhD2*	Δ*hox*	Δ*hoxYH*	Δ*hoxW*
Organic acids	DL-Lactic Acid	-2.17	-3.97	-2.83	0.32	0.66
	Stearic acid	0.58	1.74	-1.10	-0.79	1.31
	D-PANTOTHENIC ACID	-1.35	-3.35	-0.26	1.57	1.10
	Palmitic Acid	-0.51	4.23	-0.28	-0.55	1.50
	(±)-Malic Acid	-0.54	2.41	-3.25	-1.88	-1.11
	γ-aminobutyric acid	1.42	3.87	-0.32	-0.46	0.21
	Succinic acid	1.17	-2.77	-0.61	-1.46	-2.74
Amino acids	DL-Glutamic acid	0.05	1.57	-3.91	-2.22	-1.24
	DL-Glutamine	1.17	-0.50	0.04	-0.39	0.96
	L-(+)-Valine	3.59	1.91	-1.09	-0.24	0.94
	L-Proline	0.06	0.90	0.59	-0.42	-0.13
	L-(+)-Leucine	0.89	1.05	0.54	0.51	0.84
	DL-Lysine	1.25	0.85	-1.30	-1.01	-0.57
	L-(-)-Serine	-0.49	-0.02	-1.70	-1.52	-1.28
	L-(-)-Threonine	0.95	1.91	-0.86	-0.71	0.05
	L-(+)-Alanine	-0.95	-0.09	-2.98	-3.75	-1.76
	DL-Tryptophan	0.13	0.67	-1.35	-1.10	-1.08
	(-)-L-Carnitine	2.51	-3.60	2.68	0.71	0.87

Nucleic acids	8-hydroxy-deoxyguanosine	0.86	0.29	1.09	-0.31	0.53
	Cytidine	0.44	1.86	-0.53	-0.27	0.25
	Nicotinamide	0.86	-3.76	2.70	1.95	1.27
	2'-Deoxyadenosine	-0.04	0.45	-0.60	-1.20	-0.96
	Adenine	-0.31	0.05	-2.83	-0.97	-1.15
	Adenosine monophosphate	-2.33	-5.80	1.38	2.70	1.37

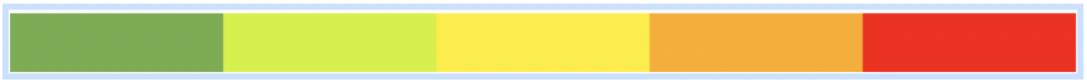

Increase Decrease

6.5 Discussion

In cyanobacteria, it is clear that many electron sinks are present that all compete for reductants (Burrows et al., 2008; Dutta & Vermaas, 2016; Gutthann et al., 2007; McNeely et al., 2010, 2014). This must be addressed to exploit cyanobacteria as a green platform for large-scale bioH_2 production.

The photosynthetic electron transport chain in both the Δ *ndhD1*/Δ *ndhD2* and M55 strains showed increased fluorescent yield (Ohkawa, Pakrasi, et al., 2000) suggesting that plastoquinone reduction is perturbed in this strain by CEF around photosystem I and increased non-photochemical quenching. The increased fluorescent yield observed in PCC 6803 was attributed to the succinate:quinol oxidoreductase (Cooley & Vermaas, 2001), however it is not clear whether the oxidized state of the plastoquinone pool is down to NDH-1 dependant reduction or decreased succinate in the M55 strain (Ohkawa, Pakrasi, et al., 2000). This was observed in the photinhibition curves in this study, where the rate of oxygen evolution was impeded utilizing light intensities above 33 μE $m^{-2}s^{-1}$ in both the *hox* and NDH-1 mutants. This data therefore suggests that mutants investigated in this study have impaired electron transport particularly in acclimatisation to increasing light intensities. These data further highlights the transient and influential role of the Hox as an electron valve under varying growth conditions (Appel et al., 2000) and *in-vitro* oxidoreductase activity of HoxEFU (Artz et al., 2020).

The respiration rate between the PCC 6803 strains was not significantly different from the wild type, previous studies, demonstrated that exogenously applied glucose resulted in a significantly reduced rate of respiration in the Δ *ndhD1*/Δ *ndhD2* strain (Ohkawa, Pakrasi, et al., 2000). This study showed that

there was no significant difference in respiration rate without the addition of glucose.

The growth profiles of the PCC 6803 strains was shown to be consistent with previous publications (Appel et al., 2000; Eckert et al., 2012). PCC 6803 ∆ *hoxH* had a longer lag time when compared to the wild type (Appel et al., 2000). The culturing conditions used in this study were 3% CO_2 enriched air bubbled into cultures with a light intensity of 100 μE $m^{-2}s^{-1}$. Reducing the light intensity to 65 μE $m^{-2}s^{-1}$ and aerating cultures with 2% CO_2 showed that there was no significant difference in specific growth rate with no mention of the extended lag phase previously seen in the ∆ *hox* strain (Eckert 2013). This study showed that there was no significant difference in the growth rates between the strains. The M55, strain has been shown to be severely growth limited and was unable to grow without bicarbonate supplementation (Ohkawa, Dean Price, et al., 2000), in this study there was no significant difference in the growth rate due to supplementation with 10 mM $NaHCO_3$ (Stanier et al., 1971) which circumvented the CO_2 concentrating phenotype observed in previous studies (Ogawa, 1991; Ohkawa, Pakrasi, et al., 2000).

Decreases in the ratio of phycocyanin:Chlorophyll *a* has been suggested to be the mechanism utilized by PCC 6803 ∆ *hoxH* to cope with fluctuations in growth conditions (Appel et al., 2000). In *Synechocystis* sp. PCC 6714, changes in photosystem stoichiometry were observed in response to light intensities, salinity and mixotrophic growth allowing for efficient acclimatization (Murakami et al., 1997). The phycocyanin:chlorophyll *a* ratio increased slightly in the Hox null mutants. This may suggest that another electron sink is compensating for the loss of the electron buffering activity of Hox such as nitrate assimilation or terminal oxidases which have been

shown to be competing pathways for reducing equivalents (Gutthann et al., 2007).

Lactic acid was shown to significantly increase in the wild type strain following photoautotrophic to anoxic dark adaptation and anoxic dark adaptation and high light exposure. The most significant increase was seen following anoxic dak adaptation. In PCC 7002, lactic acid has been shown to be a major competitor for electrons and can act as an electron sink similar to Hox (McNeely et al., 2010). Comparing the relative abundance of lactic acid in the wild type and the M55 strain, there is a significant decrease in the relative abundance of lactic acid in M55, which may suggest more electron flux moving towards Hox. One would expect that if electron flux cannot be dissipated by Hox, that the flux would go through lactic acid (McNeely et al., 2010), however the relative abundance was decreased in *hox* mutants suggesting the excess reducing equivalents are going down an alternative pathway.

An option for diverting electron flux could be nitrate assimilation which is also another competing pathway with Hox (McNeely et al., 2014). The metabolites 2-oxogluterate, glutamic acid and glutamine are pivotal to the assimilation of nitrogen in cyanobacteria (Boyal et al., 2018) and given the high reducing equivalents required for nitrate assimilation coupled to this system (Flores et al., 2005) monitoring these metabolites relative to H_2 metabolism will give insights into this major competing pathway (Gutthann et al., 2007). Nitrate reduction to ammonia and the further processing of the ammonia has been previously highlighted as a significant electron competitor with Hox (Gutthann et al., 2007). Figure 6-9 summarizes the GO/GOGAT ammonium assimilation cycle.

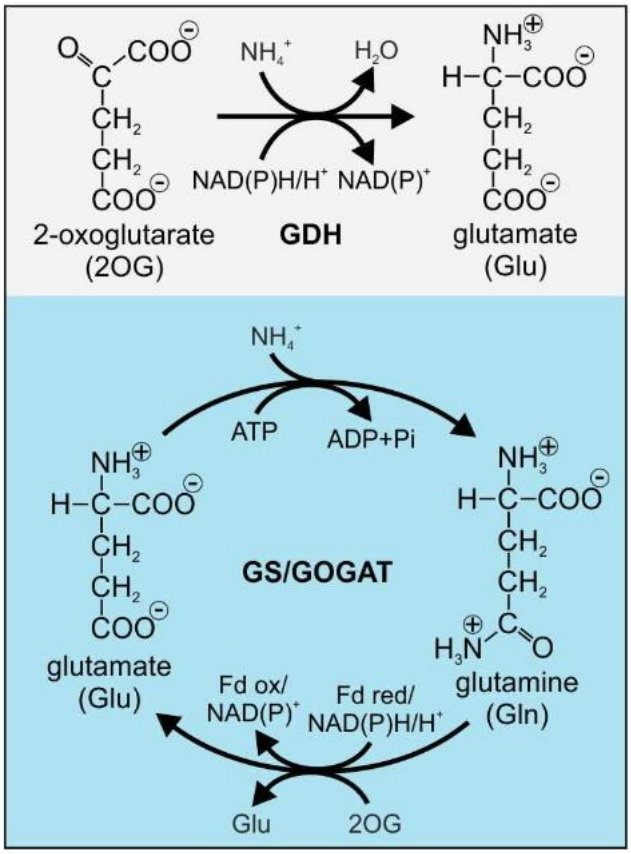

Figure 6-9: Regulation of Nitrogen Assimilation in Cyanobacteria.
Ammonia is transferred to 2-oxoglutarate by using reducing equivalents derived from NAD(P)H in order to generate glutamic acid. The glutamic acid can be converted to glutamine by hydrolysis of ATP. The amine group can be transferred from glutamine by inputting reducing equivalents from either ferredoxin or NAD(P)H. Figure taken from (Boyal et al., 2018).

Comparing photoautotrophic growth and anoxic dark adaptation in the wild type, no significant change in glutamic acid or glutamine was observed. However, when comparing M55 with wild type under anoxic dark-adapted conditions, glutamine significantly decreased. With no significant change in glutamic acid and poor metabolite coverage around this pathway, it is difficult to relate the GS/GOGAT cycle to H_2 metabolism. This may account for the decrease in Hox activity (Gutthann et al., 2007), however, *hox* mutants also showed a similar decrease in glutamine abundance (with the exception of Δ*hoxW*).

Valine was a metabolite that increased in abundance in M55 relative to wild type when anoxic dark-adapted cells were treated with high light. The reaction EC:2.6.1.42 catalyses the conversion of 2-oxoglutarate and valine to glutamic acid and 3-Methyl-2-oxobutanoic acid which may be compensating for the discrepancies in glutamine abundance in M55. 3-Methyl-2-oxobutanoic acid is an intermediate in the D-pantothenic acid biosynthesis pathway, which is critical in the biosynthesis of CoA (Maas & Vogel, 1953). In this study D-pantothenic acid was shown to have a significantly lower relative abundance with valine showing a higher relative abundance, which could account for the reduced H_2 evolution rate observed in M55 (Gutthann et al., 2007) due to the bottleneck of purvate oxidation under fermentative H_2 evolution (Gutekunst et al., 2014).

D-pantothenic acid abundance was shown to increase under anoxic dark adapted conditions in M55 highlighting an outlet for excessive reducing equivalents, through the oxidation of pyruvate followed by the reduction of ferredoxin. There was no significant change in valine abundance relative to wild type under anoxic dark adapted conditions in M55. This suggests that PCC 6803 may increase CoA to divert excess electrons to reduced ferredoxin under anoxic dark adaptation, with PFOR being active only under anoxic conditions (Gutekunst et al., 2014), CoA biosynthesis is downregulated as the main source of reduced ferredoxin from PS I.

Proline was shown to have an increased abundance in M55 under low light and anoxic dark adaptation. The reaction EC:1.5.1.2 catalyses the reduction of pyrrole-5-carboxylate to proline at the expense of NADH. Hox has been demonstrated to carryout reduction of NAD^+ (Artz et al., 2020) and NADH oxidation for H_2 evolution (Gutekunst et al., 2014), therefore this pathway may be competing with Hox for NADH.

The metabolomic data suggests that pathways are enriched in M55 which support the reduction of ferredoxin compared to the wild type. This could account for the increased total H_2 production in M55. With respect to the rate of H_2, the increased abundance of proline suggests a decrease in NADH which could account for decreased rates of H_2 evolution.

7 General Conclusion

Cyanobacteria have been studied extensively for respiratory and photosynthetic electron transport. Since the publication of the PCC 6803 genome, research into the use of cyanobacteria as a chassis for biomanufacturing has increased exponentially due to these organisms being able to utilize CO_2, H_2O, minerals, and light energy for growth, making them an environmentally friendly alternative to fossil fuel processing.

Cyanobacteria offer both a renewable and sustainable platform for H_2 production by the means of acquiring reducing equivalents from H_2O with the aid of light. With advancements in our knowledge of H_2 metabolism in cyanobacteria, we are making strides towards understanding the relationship it has with the photosynthetic and respiratory electron transport chains in these organisms.

The overall aim of this study was to gain a greater understanding of the physiological function of Hox directly linking localization to electron transport complexes and H_2 metabolism. Strains were generated to investigate the localization of Hox and NDH-1 in PCC 6803 and PCC 7002 to visualize the localization of the respective complexes which will give a better understanding of the interaction and therefore giving insights into potential future engineering strategies. The metabolite profiles of high H_2 producers can give insights into the metabolome and engineering cyanobacterial strains for improved H_2 production.

Chapter 3 reported the colocalization between Hox and NDH-1 following photoautotrophic, mixotrophic, nitrate limited mixotrophic growth and anoxic dark adaptation. This work did not answer the question of whether Hox can get electrons directly from NDH-1, however, it clearly shows that Hox and NDH-1 colocalize under a vast range of physiological conditions. It is important to note that the PCC 6803 NDH-1 null mutant (M55) does have a higher yield in total H_2 evolution, however the rate of H_2 evolution is lower compared to wild type PCC 6803 (Gutthann et al., 2007). The data from chapter 3 showed an increase in Hox/NDH-1 colocalization under anoxic dark adapted conditions in mixotrophic and mixotrophic nitrate

limited growth, conditions that improve H_2 productivity (Gutekunst,personal communication), which may suggest that electrons can be donated directly from the plastoquinol pool to Hox via NDH-1. Even when Hox was shown to be primarily localized in the cytoplasm during mixotrophic growth at 60 $\mu E\ m^{-2}\ s^{-1}$ or higher, there does appear to be some colocalization with NDH-1. Current work with Prof. Nigel Burroughs on image analysis is on going to quantify the individual puncta and highlight colocalized populations to give a better understanding on this interaction. Hox puncta has been shown to correlate with hydrogenase activity (Burroughs et al., 2014) with NDH-1 puncta shown to correlate with NDH plastoquinone reduction (L. N. Liu et al., 2012) , it is therefore important to resolve this increased colocalization.

To get a full appreciation for the role of Hox in the electron transport of cyanobacteria, colocalization studies with other complexes in the electron transport chain will be essential. The prime candidate for this would be PSI as this is a plentiful source of reduced ferredoxin which can feed into Hox to improve H_2 productivity. A direct fusion between Hox and PSI was recently generated allowing sustained photobiological H_2 production however, a notable decrease in growth rate was observed in this strain (Appel et al., 2020). A clear picture of Hox localization relative to PSI can pave the way for engineering strategies that can support this interaction without impacting on growth.

Chapter 4 demonstrated that GFP/YFP C-terminal tags on both the diaphorase subunit HoxE and the small Hox subunit HoxY resulted in Hox localization to the cytoplasm. This was very different from the thylakoid localization observed with HoxF. Due to the extensive role that Hox has been demonstrated to play in modulating the redox poise of the soluble electron transport chain, this observation highlights the possibility of sub complexes being localized to other cellular compartments. It was previously demonstrated that the stability of Hox is crucial for maintenance of the fluorescence signal and subcomplex formation often results in decreased stability (fluorescence) in vivo. Both the *hoxEGFP* and *hoxYGFP* strains had detectable levels of fluorescence and therefore can form stable sub complexes in vivo. Although this requires further investigation with 2-D gels

and H_2 measurements to ascertain sub-complex formation and stability *in-vivo*. Multiple tagged subunits will also allow GFP pulldowns to be utilised to address and evaluate potential Hox interaction partners under the different growth conditions assessed in this study. This will provide valuable insight into how Hox interacts with the electron transport chain.

This may have implications on directed evolution strategies in strain and enzyme engineering. As it has been demonstrated that Hox plays a crucial role under nitrate limited mixotrophic growth, it would make sense to use these culturing conditions for directed evolution. However, it has been shown that Hox can use a variety of reducing equivalents and could potentially be modulating the redox poise of the soluble electron transport – which is supported by the change in Hox localization in **Chapter 3** under mixotrophic growth. If there is multiple redox reactions being carried out by Hox they may not all result in H_2 evolution, therefore there is a risk of pushing the selective pressure during adapted evolution to select for mutants that are enhanced in one of these activities as opposed to evolving H_2.

Chapter 5 highlighted the colocalization of Hox with NDH-1 in PCC 7002. This chapter demonstrated that the population of Hox and NDH-1 form dispersed or puncta populations in the thylakoid of 7002 similar to the distribution seen in PCC 6803 and PCC 7942 respectively. What was not observed was the localization of Hox to the cytoplasm in PCC 7002 under mixotrophic growth. Due to the inability of PCC 7002 to fully utilize glucose in the same way that PCC 6803 does, mixotrophic growth in PCC 7002 was carried out using glycerol. Glucose yields more reducing equivalents compared to glycerol and therefore there may still be instances in 7002 where Hox was localized in the cytoplasm and this requires further investigation. Further investigation is also required to assess the components of the soluble electron carriers which Hox utilises as an electron source in PCC 7002 and compare this with PCC 6803. Hox may have a multifunction role in cyanobacteria modulating redox poise within the cell.

Chapter 6 highlighted the differences in H_2 metabolism between different strains of PCC 6803 following various conditions. Both the strain and

the growth condition impacted on metabolism. In this chapter, competing pathways were shown to decrease in abundance. A major observation in this study was highlighting the GO/GOGAT cycle as a potential competing pathway with glutamate and glutamine being key metabolites showing deviations in studied strains compared to wild type. The increased valine abundance also highlights that metabolism may be strain in this strain may be biosynthesising glutamic acid in order to compensate for the lack of NAD(P)H oxidase activity. Proline metabolism was also highlighted as a competing pathway for reducing equivalents to Hox in the form of NADH (Artz et al., 2020; Gutekunst et al., 2014). Overall, this data points towards an overall reductive state of the soluble electron carriers for optimal H_2 evolution.

This study has demonstrated for the first time that Hox and NDH-1 are colocalized *in-vivo* at the thylakoid membrane and that subpopulations exist between the two complexes which do not interact. This study has also clearly demonstrated that Hox can localise to the cytoplasm and this is not dependent on the deletion of the HoxE subunit as previously shown. This is highly significant and has implications for the role Hox plays in the cell.

Furthermore, Hox forms two distinct populations in PCC 7002, both associated with the thylakoid, with puncta being localised to the poles. This is first study to demonstrate this localisation in PCC 7002 and to demonstrate a colocalization between Hox and NDH-1 in this strain.

Finally, this study has highlighted a clear difference in the metabolic profiles of PCC 6803 strains grown under conditions, which relate to colocalization of Hox and NDH-1 and H_2 evolution and is a first step towards linking H2 metabolism to localisation and productivity.

Figure 7-1 summarizes the findings of this thesis in PCC 6803. For exploiting cyanobacteria as a platform for photobiological H_2 production, it is clear that reduced ferredoxin has a stimulatory effect on H_2 production but it remains unclear if Hox can directly oxidise the plastoquinol pool. The decrease in the H_2 evolution rate in M55 coupled with the observation of increased colocalization under conditions that support H_2 evolution suggests

that the plastoquinol pool may play a role in H_2 evolution mediated through NDH-1 which requires further research.

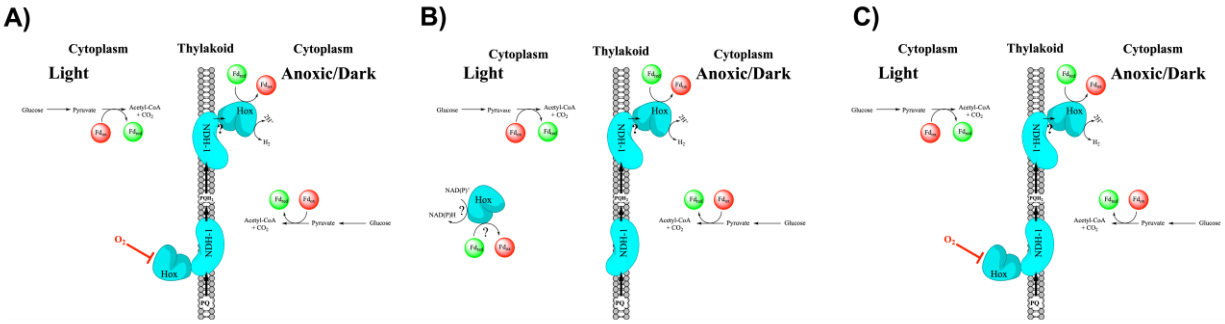

Figure 7-1: Overview of Thesis Findings in PCC 6803
A) Under photoautotrophic growth, NDH-1 and Hox are localized to the thylakoid and show colocalization. Upon anoxic dark adaptation, the degree of Hox and NDH-1 colocalization is lower as shown by the decreased Manders coefficient. Under light, the O_2 evolution from PS II inhibits H_2 evolution from Hox. Under anoxic dark adapted conditions, the oxidation of pyruvate to reduce ferredoxin supports H_2 evolution by Hox (Gutekunst et al., 2014). B) Under photomixotrophic growth, a large proportion of the Hox population is localized to the cytoplasm. Under anoxic dark adapted conditions, Hox is localized to the thylakoid with an increased degree of colocalization with NDH-1. The addition of glucose increases respiratory electron transport which appears to enhance Hox and NDH-1 colocalization. Under light conditions, the Hox does not evolve H_2 and therefore we hypothesise that Hox is functioning to modulate the stoichiometry of soluble electron carriers as has been observed in *in-vitro* studies (Artz et al., 2020). C) PCC 6803 grown photomixotrophically under nitrate limited conditions, Hox localizes to the thylakoid. In the light no H_2 is evolved, with anoxic dark conditions resulting in more H_2 being evolved compared to photoautotrophic and photomixotrophic growth (Gutekunst personal contact) with increased colocalization with NDH-1.

Figure 7-2 summarizes the thesis findings in PCC 7002. Under conditions that support H_2 evolution in PCC 7002, there was colocalization between Hox and NDH-1. When PCC 7002 is grown photomixotrophically with glycerol, there is a decrease in H_2 evolution (McNeely et al., 2011). In **Chapter 5**, mixotrophic growth increased the colocalization between Hox and NDH-1 which suggests that Hox interacts with the electron transport chain slightly differently when compared to PCC 6803. More work is need to understand H_2 metabolism across multiple species of cyanobacteria in order to fully exploit cyanobacteria as a platform for green H_2 production.

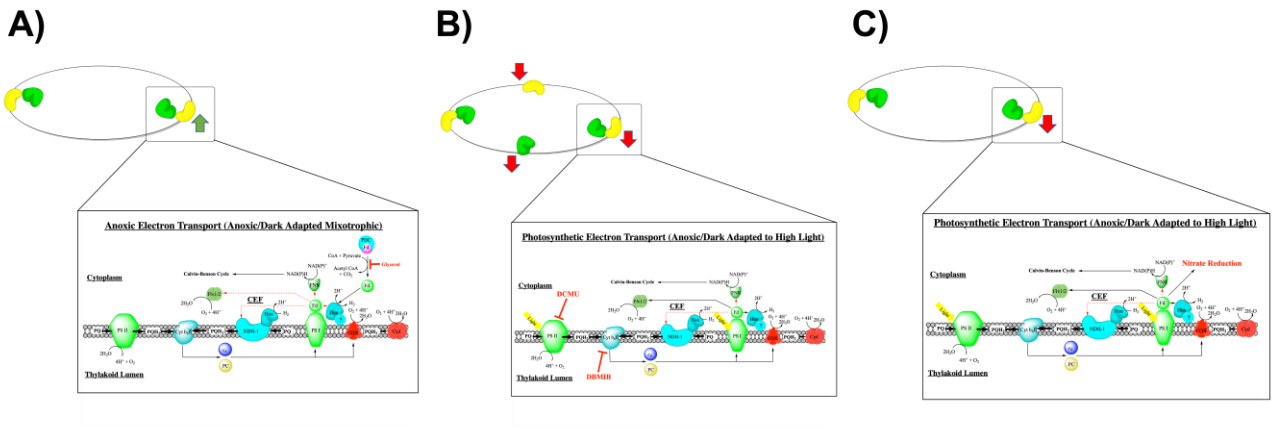

Figure 7-2: Overview of Thesis Findings in PCC 7002
Hox and NDH-1 was localized to the thylakoid with puncta predominantly localized at the poles of the cell. A) Comparing anoxic dark adaptation of photoautotrophically and photomixotrophically grown PCC 7002, photoautotrophic growth showed the highest H_2 productivity. There was a significant increase in Hox and NDH-1 colocalization in photomixotrophic followed by anoxic dark adaptation compared with photoautotrophically grown PCC 7002. B) By limiting the activity of PS II with DCMU, the number of Hox and NDH-1 puncta per cell was shown to decrease resulting in decreased colocalization between Hox and NDH-1. By over reducing the plastoquinone pool with DBMIB, the number of Hox and NDH-1 puncta per cell was shown to decrease resulting in decreased colocalization between Hox and NDH-1.C) By replacing nitrate with urea, a significant electron sink has been removed. There was no significant difference between Hox and NDH-1 colocalization, however there was a significant increase in Hox puncta not colocalized with NDH-1 puncta, which suggests another interaction partner at the thylakoid membrane.

8 References

Appel, J., Hueren, V., Boehm, M., & Gutekunst, K. (2020). Cyanobacterial in vivo solar hydrogen production using a photosystem I–hydrogenase (PsaD-HoxYH) fusion complex. *Nature Energy*. https://doi.org/10.1038/s41560-020-0609-6

Appel, J., Phunpruch, S., Steinmüller, K., & Schulz, R. (2000). The bidirectional hydrogenase of Synechocystis sp. PCC 6803 works as an electron valve during photosynthesis. *Archives of Microbiology*, *173*(5–6), 333–338. https://doi.org/10.1007/s002030000139

Appel, J., & Schulz, R. (1996). Sequence analysis of an operon of a NAD(P)-reducing nickel hydrogenase from the cyanobacterium Synechocystis sp. PCC 6803 gives additional evidence for direct coupling of the enzyme to NAD(P)H-dehydrogenase (complex I). *Biochimica et Biophysica Acta - Protein Structure and Molecular Enzymology*, *1298*(2), 141–147. https://doi.org/10.1016/S0167-4838(96)00176-8

Artz, J. H., Tokmina-Lukaszewska, M., Mulder, D. W., Lubner, C. E., Gutekunst, K., Appel, J., Bothner, B., Boehm, M., & King, P. W. (2020). The structure and reactivity of the HoxEFU complex from the cyanobacterium Synechocystis sp. PCC 6803. *Journal of Biological Chemistry*, *295*(28), 9445–9454. https://doi.org/10.1074/jbc.RA120.013136

Baalen, C. V. A. N. (1961). Studies on Marine Blue-Green Algae. *Botanica Marina*, 130–139.

Baebprasert, W., Jantaro, S., Khetkorn, W., Lindblad, P., & Incharoensakdi, A. (2011). Increased H2 production in the cyanobacterium Synechocystis sp. strain PCC 6803 by redirecting the electron supply via genetic engineering of the nitrate assimilation pathway. *Metabolic Engineering*, *13*(5), 610–616. https://doi.org/10.1016/j.ymben.2011.07.004

Bakenne, A., Nuttall, W., & Kazantzis, N. (2016). Sankey-Diagram-based insights into the hydrogen economy of today. *International Journal of Hydrogen Energy*, *41*(19), 7744–7753. https://doi.org/10.1016/j.ijhydene.2015.12.216

Battchikova, N., Eisenhut, M., & Aro, E. M. (2011). Cyanobacterial NDH-1 complexes: Novel insights and remaining puzzles. *Biochimica et Biophysica Acta - Bioenergetics*, *1807*(8), 935–944. https://doi.org/10.1016/j.bbabio.2010.10.017

Batyrova, K., & Hallenbeck, P. C. (2017). Hydrogen production by a Chlamydomonas reinhardtii strain with inducible expression of photosystem II. *International Journal of Molecular Sciences*, *18*(3). https://doi.org/10.3390/ijms18030647

BERTANI, G. (1951). Studies on lysogenesis. I. The mode of phage liberation by lysogenic Escherichia coli. *Journal of Bacteriology*, *62*(3), 293–300.

Blokesch, M., Paschos, A., Theodoratou, E., Bauer, A., Hube, M., Huth, S., & Böck, A. (2002). Metal insertion into NiFe-hydrogenases. *Biochemical*

Society Transactions, *30*(4), 674–680. https://doi.org/10.1042/BST0300674

Blokesch, Melanie, Paschos, A., Bauer, A., Reissmann, S., Drapal, N., & Böck, A. (2004). Analysis of the transcarbamoylation-dehydration reaction catalyzed by the hydrogenase maturation proteins HypF and HypE. *European Journal of Biochemistry*, *271*(16), 3428–3436. https://doi.org/10.1111/j.1432-1033.2004.04280.x

Blokesch, Melanie, Rohrmoser, M., Rode, S., & Böck, A. (2004). HybF, a Zinc-Containing Protein Involved in NiFe Hydrogenase Maturation. *Journal of Bacteriology*, *186*(9), 2603–2611. https://doi.org/10.1128/JB.186.9.2603-2611.2004

Bock, A. (1995). *t / c*. *138*, 133–138.

Boison, G., Schmitz, O., Schmitz, B., & Bothe, H. (1998). Unusual gene arrangement of the bidirectional hydrogenase and functional analysis of its diaphorase subunit HoxU in respiration of the unicellular cyanobacterium Anacystis nidulans. *Current Microbiology*, *36*(5), 253–258. https://doi.org/10.1007/s002849900305

Bokinsky, G., Peralta-Yahya, P. P., George, A., Holmes, B. M., Steen, E. J., Dietrich, J., Lee, T. S., Tullman-Ercek, D., Voigt, C. A., Simmons, B. A., & Keasling, J. D. (2011). Synthesis of three advanced biofuels from ionic liquid-pretreated switchgrass using engineered Escherichia coli. *Proceedings of the National Academy of Sciences of the United States of America*, *108*(50), 19949–19954. https://doi.org/10.1073/pnas.1106958108

Braga, L. B., Silveira, J. L., Da Silva, M. E., Tuna, C. E., Machin, E. B., & Pedroso, D. T. (2013). Hydrogen production by biogas steam reforming: A technical, economic and ecological analysis. *Renewable and Sustainable Energy Reviews*, *28*, 166–173. https://doi.org/10.1016/j.rser.2013.07.060

Burroughs, N. J., Boehm, M., Eckert, C., Mastroianni, G., Spence, E. M., Yu, J., Nixon, P. J., Appel, J., Mullineaux, C. W., & Bryan, S. J. (2014). Solar powered biohydrogen production requires specific localization of the hydrogenase. *Energy and Environmental Science*, *7*(11), 3791–3800. https://doi.org/10.1039/c4ee02502d

Burrows, E. H., Chaplen, F. W. R., & Ely, R. L. (2008). Optimization of media nutrient composition for increased photofermentative hydrogen production by Synechocystis sp. PCC 6803. *International Journal of Hydrogen Energy*, *33*(21), 6092–6099. https://doi.org/10.1016/j.ijhydene.2008.07.102

Calusinska, M., Happe, T., Joris, B., & Wilmotte, A. (2010). The surprising diversity of clostridial hydrogenases: A comparative genomic perspective. *Microbiology*, *156*(6), 1575–1588. https://doi.org/10.1099/mic.0.032771-0

Cameron, J. C., Wilson, S. C., Bernstein, S. L., & Kerfeld, C. A. (2013). XBiogenesis of a bacterial organelle: The carboxysome assembly pathway. *Cell*, *155*(5), 1131. https://doi.org/10.1016/j.cell.2013.10.044

Casella, S., Huang, F., Mason, D., Zhao, G. Y., Johnson, G. N., Mullineaux, C. W., & Liu, L. N. (2017). Dissecting the Native Architecture and Dynamics of Cyanobacterial Photosynthetic Machinery. *Molecular Plant*, *10*(11), 1434–1448. https://doi.org/10.1016/j.molp.2017.09.019

Chen, C. Y., & Chang, J. S. (2006). Enhancing phototropic hydrogen production by solid-carrier assisted fermentation and internal optical-fiber illumination. *Process Biochemistry*, *41*(9), 2041–2049. https://doi.org/10.1016/j.procbio.2006.05.005

Chen, X., Sun, Y., Xiu, Z., Li, X., & Zhang, D. (2006). Stoichiometric analysis of biological hydrogen production by fermentative bacteria. *International Journal of Hydrogen Energy*, *31*(4), 539–549. https://doi.org/10.1016/j.ijhydene.2005.03.013

Cooley, J. W., & Vermaas, W. F. J. (2001). Succinate dehydrogenase and other respiratory pathways in thylakoid membranes of Synechocystis sp. strain PCC 6803: Capacity comparisons and physiological function. *Journal of Bacteriology*, *183*(14), 4251–4258. https://doi.org/10.1128/JB.183.14.4251-4258.2001

Cournac, L., Guedeney, G., Peltier, G., & Vignais, P. M. (2004). Sustained Photoevolution of Molecular Hydrogen. *Journal of Bacteriology*, *186*(6), 1737–1746. https://doi.org/10.1128/JB.186.6.1737

Cournac, L., Mus, F., Bernard, L., Guedeney, G., Vignais, P., & Peltier, G. (2002). Limiting steps of hydrogen production in Chlamydomonas reinhardtii and Synechocystis PCC 6803 as analysed by light-induced gas exchange transients. *International Journal of Hydrogen Energy*, *27*(11–12), 1229–1237. https://doi.org/10.1016/S0360-3199(02)00105-2

De Rosa, E., Checchetto, V., Franchin, C., Bergantino, E., Berto, P., Szabò, I., Giacometti, G. M., Arrigoni, G., & Costantini, P. (2015). [NiFe]-hydrogenase is essential for cyanobacterium Synechocystis sp. PCC 6803 aerobic growth in the dark. *Scientific Reports*, *5*(February), 1–12. https://doi.org/10.1038/srep12424

Dong, C., Tang, A., Zhao, J., Mullineaux, C. W., Shen, G., & Bryant, D. A. (2009). ApcD is necessary for efficient energy transfer from phycobilisomes to photosystem I and helps to prevent photoinhibition in the cyanobacterium Synechococcus sp. PCC 7002. *Biochimica et Biophysica Acta - Bioenergetics*, *1787*(9), 1122–1128. https://doi.org/10.1016/j.bbabio.2009.04.007

Duman, G., & Yanik, J. (2017). Two-step steam pyrolysis of biomass for hydrogen production. *International Journal of Hydrogen Energy*, *42*(27), 17000–17008. https://doi.org/10.1016/j.ijhydene.2017.05.227

Dutta, I., & Vermaas, W. F. J. (2016). The electron transfer pathway upon H2oxidation by the NiFe bidirectional hydrogenase of Synechocystis sp. PCC 6803 in the light shares components with the photosynthetic electron transfer chain in thylakoid membranes. *International Journal of Hydrogen Energy*, *41*(28), 11949–11959. https://doi.org/10.1016/j.ijhydene.2016.01.172

Eckert, C., Boehm, M., Carrieri, D., Yu, J., Dubini, A., Nixon, P. J., & Maness, P. C. (2012). Genetic analysis of the Hox hydrogenase in the cyanobacterium Synechocystis sp. PCC 6803 reveals subunit roles in association, assembly, maturation, and function. *Journal of Biological Chemistry*, *287*(52), 43502–43515. https://doi.org/10.1074/jbc.M112.392407

Engler, M. J., & Richardson, C. C. (1982). DNA Ligases. *Enzymes*, *15*(C), 3–29. https://doi.org/10.1016/S1874-6047(08)60273-5

Eriksson Johansson, E., Kettaneh-Wold, N., Trygg, J., Wikstr&#xfffd;m, C., Wold,

S., L. (2006). *Multi- and megavariate data analysis : Part I: Basic principles and applications*. Umetrics.
Fereidooni, M., Mostafaeipour, A., Kalantar, V., & Goudarzi, H. (2018). A comprehensive evaluation of hydrogen production from photovoltaic power station. *Renewable and Sustainable Energy Reviews*, *82*(September 2017), 415–423. https://doi.org/10.1016/j.rser.2017.09.060
Flores, E., Frías, J. E., Rubio, L. M., & Herrero, A. (2005). Photosynthetic nitrate assimilation in cyanobacteria. *Photosynthesis Research*, *83*(2), 117–133. https://doi.org/10.1007/s11120-004-5830-9
Forti, G., & Bracale, M. (1984). Ferredoxin-ferredoxin NADP reductase interaction. Catalytic differences between the soluble and thylakoid-bound complex. *FEBS Letters*, *166*(1), 81–84. https://doi.org/10.1016/0014-5793(84)80049-6
Fraser, J. M., Tulk, S. E., Jeans, J. A., Campbell, D. A., Bibby, T. S., & Cockshutt, A. M. (2013). Photophysiological and Photosynthetic Complex Changes during Iron Starvation in Synechocystis sp. PCC 6803 and Synechococcus elongatus PCC 7942. *PLoS ONE*, *8*(3). https://doi.org/10.1371/journal.pone.0059861
Frigaard, N. (2018). Sugar and Sugar Alcohol Production. In *Genetically Engineered Foods* (Issue January). Elsevier Inc. https://doi.org/10.1016/B978-0-12-811519-0/00002-9
Görl, M., Sauer, J., Baier, T., & Forchhammer, K. (1998). Nitrogen-starvation-induced chlorosis in Synechococcus PCC 7942: Adaptation to long-term survival. *Microbiology*, *144*(9), 2449–2458. https://doi.org/10.1099/00221287-144-9-2449
Goswami, R. K., Mehariya, S., Obulisamy, P. K., & Verma, P. (2021). Advanced microalgae-based renewable biohydrogen production systems: A review. *Bioresource Technology*, *320*(PA), 124301. https://doi.org/10.1016/j.biortech.2020.124301
Gray, C. T., & Gest, H. (1965). Biological formation of molecular hydrogen. *Science*, *148*(3667), 186–192. https://doi.org/10.1126/science.148.3667.186
Guo, X. M., Trably, E., Latrille, E., Carrre, H., & Steyer, J. P. (2010). Hydrogen production from agricultural waste by dark fermentation: A review. *International Journal of Hydrogen Energy*, *35*(19), 10660–10673. https://doi.org/10.1016/j.ijhydene.2010.03.008
Gust, B., Challis, G. L., Fowler, K., Kieser, T., & Chater, K. F. (2003). PCR-targeted Streptomyces gene replacement identifies a protein domain needed for biosynthesis of the sesquiterpene soil odor geosmin. *Proceedings of the National Academy of Sciences of the United States of America*, *100*(4), 1541–1546. https://doi.org/10.1073/pnas.0337542100
Gust, B., Chandra, G., Jakimowicz, D., Yuqing, T., Bruton, C. J., & Chater, K. F. (2004). λ Red-mediated genetic manipulation of antibiotic-producing Streptomyces. *Advances in Applied Microbiology*, *54*, 107–128. https://doi.org/10.1016/S0065-2164(04)54004-2
Gutekunst, K. (2018a). Hypothesis on the Synchronistic Evolution of Autotrophy and Heterotrophy. *Trends in Biochemical Sciences*, *43*(6), 402–411. https://doi.org/10.1016/j.tibs.2018.03.008

Gutekunst, K. (2018b). Hypothesis on the Synchronistic Evolution of Autotrophy and Heterotrophy. *Trends in Biochemical Sciences*, *43*(6), 402–411. https://doi.org/10.1016/j.tibs.2018.03.008

Gutekunst, K., Chen, X., Schreiber, K., Kaspar, U., Makam, S., & Appel, J. (2014). The bidirectional NiFe-hydrogenase in synechocystis sp. PCC 6803 Is reduced by flavodoxin and ferredoxin and is essential under mixotrophic, nitrate-limiting conditions. *Journal of Biological Chemistry*, *289*(4), 1930–1937. https://doi.org/10.1074/jbc.M113.526376

Gutekunst, K., Phunpruch, S., Schwarz, C., Schuchardt, S., Schulz-Friedrich, R., & Appel, J. (2005). LexA regulates the bidirectional hydrogenase in the cyanobacterium Synechocystis sp. PCC 6803 as a transcription activator. *Molecular Microbiology*, *58*(3), 810–823. https://doi.org/10.1111/j.1365-2958.2005.04867.x

Gutthann, F., Egert, M., Marques, A., & Appel, J. (2007). Inhibition of respiration and nitrate assimilation enhances photohydrogen evolution under low oxygen concentrations in Synechocystis sp. PCC 6803. *Biochimica et Biophysica Acta - Bioenergetics*, *1767*(2), 161–169. https://doi.org/10.1016/j.bbabio.2006.12.003

Hallenbeck, P. C. (2011). Microbial paths to renewable hydrogen production. *Biofuels*, *2*(3), 285–302. https://doi.org/10.4155/bfs.11.6

Hart, S. E., Schlarb-Ridley, B. G., Bendall, D. S., & Howe, C. J. (2005). Terminal oxidases of cyanobacteria. *Biochemical Society Transactions*, *33*(4), 832–835. https://doi.org/10.1042/BST0330832

Helman, Y., Barkan, E., Eisenstadt, D., Luz, B., & Kaplan, A. (2005). Fractionation of the three stable oxygen isotopes by oxygen-producing and oxygen-consuming reactions in photosynthetic organisms. *Plant Physiology*, *138*(4), 2292–2298. https://doi.org/10.1104/pp.105.063768

Helman, Y., Tchernov, D., Reinhold, L., Shibata, M., Ogawa, T., Schwarz, R., Ohad, I., & Kaplan, A. (2003). Genes encoding A-type flavoproteins are essential for photoreduction of O2 in cyanobacteria. *Current Biology*, *13*(3), 230–235. https://doi.org/10.1016/S0960-9822(03)00046-0

Hill, N. C., Tay, J. W., Altus, S., Bortz, D. M., & Cameron, J. C. (2020). Life cycle of a cyanobacterial carboxysome. *Science Advances*, *6*(19), 1–9. https://doi.org/10.1126/sciadv.aba1269

Hoffmann, D., Gutekunst, K., Klissenbauer, M., Schulz-Friedrich, R., & Appel, J. (2006). Mutagenesis of hydrogenase accessory genes of Synechocystis sp. PCC 6803: Additional homologues of hypA and hypB are not active in hydrogenase maturation. *FEBS Journal*, *273*(19), 4516–4527. https://doi.org/10.1111/j.1742-4658.2006.05460.x

Hussy, I., Hawkes, F. R., Dinsdale, R., & Hawkes, D. L. (2005). Continuous fermentative hydrogen production from sucrose and sugarbeet. *International Journal of Hydrogen Energy*, *30*(5), 471–483. https://doi.org/10.1016/j.ijhydene.2004.04.003

Ingram, L. O., Calder, J. A., van Baalen, C., Plucker, F. E., & Parker, P. L. (1973). Role of reduced exogenous organic compounds in the physiology of the blue green bacteria (Algae): Photoheterotrophic growth of a “heterotrophic” blue green bacterium. *Journal of Bacteriology*, *114*(2), 695–700. https://doi.org/10.1128/JB.114.2.695-700.1973

Joerger, R. D., Jacobson, M. R., Premakumar, R., Wolfinger, E. D., & Bishop, P. E. (1989). Nucleotide sequence and mutational analysis of the

structural genes (anfHDGK) for the second alternative nitrogenase from Azotobacter vinelandii. *Journal of Bacteriology*, *171*(2), 1075–1086. https://doi.org/10.1128/jb.171.2.1075-1086.1989

Kaneko, T., Sato, S., Kotani, H., Tanaka, A., Asamizu, E., Nakamura, Y., Miyajima, N., Hirosawa, M., Sugiura, M., Sasamoto, S., Kimura, T., Hosouchi, T., Matsuno, A., Muraki, A., Nakazaki, N., Naruo, K., Okumura, S., Shimpo, S., Takeuchi, C., … Tabata, S. (1996). Sequence analysis of the genome of the unicellular cyanobacterium synechocystis sp. strain PCC6803. II. Sequence determination of the entire genome and assignment of potential protein-coding regions. *DNA Research*, *3*(3), 109–136. https://doi.org/10.1093/dnares/3.3.109

Kapoor, K., Cashman, D. J., Nientimp, L., Bruce, B. D., & Baudry, J. (2018). Binding Mechanisms of Electron Transport Proteins with Cyanobacterial Photosystem I: An Integrated Computational and Experimental Model. *Journal of Physical Chemistry B*, *122*(3), 1026–1036. https://doi.org/10.1021/acs.jpcb.7b08307

Khanna, N., & Lindblad, P. (2015). Cyanobacterial hydrogenases and hydrogen metabolism revisited: Recent progress and future prospects. *International Journal of Molecular Sciences*, *16*(5), 10537–10561. https://doi.org/10.3390/ijms160510537

Khosravitabar, F., & Hippler, M. (2019). A new approach for improving microalgal biohydrogen photoproduction based on safe & fast oxygen consumption. *International Journal of Hydrogen Energy*, *44*(33), 17835–17844. https://doi.org/10.1016/j.ijhydene.2019.05.038

Kumar, A., Jones, D. D., & Hanna, M. A. (2009). Thermochemical biomass gasification: A review of the current status of the technology. *Energies*, *2*(3), 556–581. https://doi.org/10.3390/en20300556

Lacasse, M. J., & Zamble, D. B. (2016). [NiFe]-Hydrogenase Maturation. *Biochemistry*, *55*(12), 1689–1701. https://doi.org/10.1021/acs.biochem.5b01328

Lea-Smith, D. J., Ross, N., Zori, M., Bendall, D. S., Dennis, J. S., Scott, S. A., Smith, A. G., & Howe, C. J. (2013). Thylakoid terminal oxidases are essential for the cyanobacterium Synechocystis sp. PCC 6803 to survive rapidly changing light intensities. *Plant Physiology*, *162*(1), 484–495. https://doi.org/10.1104/pp.112.210260

Lee, H. S., & Rittmann, B. E. (2010). Characterization of energy losses in an upflow single-chamber microbial electrolysis cell. *International Journal of Hydrogen Energy*, *35*(3), 920–927. https://doi.org/10.1016/j.ijhydene.2009.11.040

Lee, H. S., Vermaas, W. F. J., & Rittmann, B. E. (2010). Biological hydrogen production: Prospects and challenges. *Trends in Biotechnology*, *28*(5), 262–271. https://doi.org/10.1016/j.tibtech.2010.01.007

Li, Y., Alaimo, C. P., Kim, M., Kado, N. Y., Peppers, J., Xue, J., Wan, C., Green, P. G., Zhang, R., Jenkins, B. M., Vogel, C. F. A., Wuertz, S., Young, T. M., & Kleeman, M. J. (2019). Composition and Toxicity of Biogas Produced from Different Feedstocks in California. *Environmental Science and Technology*. https://doi.org/10.1021/acs.est.9b03003

Liu, H., Grot, S., & Logan, B. E. (2005). Electrochemically assisted microbial production of hydrogen from acetate. *Environmental Science and Technology*, *39*(11), 4317–4320. https://doi.org/10.1021/es050244p

Liu, L. N., Bryan, S. J., Huang, F., Yu, J., Nixon, P. J., Rich, P. R., & Mullineaux, C. W. (2012). Control of electron transport routes through redox-regulated redistribution of respiratory complexes. *Proceedings of the National Academy of Sciences of the United States of America*, *109*(28), 11431–11436. https://doi.org/10.1073/pnas.1120960109

Lo, Y. C., Lee, K. S., Lin, P. J., & Chang, J. S. (2009). Bioreactors configured with distributors and carriers enhance the performance of continuous dark hydrogen fermentation. *Bioresource Technology*, *100*(19), 4381–4387. https://doi.org/10.1016/j.biortech.2009.04.024

Löscher, S., Zebger, I., Andersen, L. K., Hildebrandt, P., Meyer-Klaucke, W., & Haumann, M. (2005). The structure of the Ni-Fe site in the isolated HoxC subunit of the hydrogen-sensing hydrogenase from Ralstonia eutropha. *FEBS Letters*, *579*(20), 4287–4291. https://doi.org/10.1016/j.febslet.2005.06.063

Ludwig, M., & Bryant, D. A. (2012a). Acclimation of the global transcriptome of the cyanobacterium Synechococcus sp. strain PCC 7002 to nutrient limitations and different nitrogen sources. *Frontiers in Microbiology*, *3*(APR), 1–15. https://doi.org/10.3389/fmicb.2012.00145

Ludwig, M., & Bryant, D. A. (2012b). Synechococcus sp. Strain PCC 7002 transcriptome: Acclimation to temperature, salinity, oxidative stress, and mixotrophic growth conditions. *Frontiers in Microbiology*, *3*(OCT), 1–14. https://doi.org/10.3389/fmicb.2012.00354

MAAS, W. K., & VOGEL, H. J. (1953). alpha-Ketoisovaleric acid, a precursor of pantothenic acid in. *Journal of Bacteriology*, *65*(4), 388–393. https://doi.org/10.1128/jb.65.4.388-393.1953

Mackinney, G. (1941). Absorption of light by chlorophyll solutions. *The Journal of Biological Chemistry*, *140*(2), 315–322.

Maier, T., Jacobi, A., Sauter, M., & Bock, A. (1993). The product of the hypB gene, which is required for nickel incorporation into hydrogenases, is a novel guanine nucleotide-binding protein. *Journal of Bacteriology*, *175*(3), 630–635. https://doi.org/10.1128/jb.175.3.630-635.1993

Mannan, R. M., & Pakrasi, H. B. (1993). Dark heterotrophic growth conditions result in an increase in the content of Photosystem II units in the filamentous cyanobacterium Anabaena variabilis ATCC 29413. *Plant Physiology*, *103*(3), 971–977. https://doi.org/10.1104/pp.103.3.971

Marreiros, B. C., Batista, A. P., Duarte, A. M. S., & Pereira, M. M. (2013). A missing link between complex i and group 4 membrane-bound [NiFe] hydrogenases. *Biochimica et Biophysica Acta - Bioenergetics*, *1827*(2), 198–209. https://doi.org/10.1016/j.bbabio.2012.09.012

McDowall, J. S., Murphy, B. J., Haumann, M., Palmer, T., Armstrong, F. A., & Sargent, F. (2014). Bacterial formate hydrogenlyase complex. *Proceedings of the National Academy of Sciences of the United States of America*, *111*(38), E3948–E3956. https://doi.org/10.1073/pnas.1407927111

McKinlay, J. B., & Harwood, C. S. (2010). Carbon dioxide fixation as a central redox cofactor recycling mechanism in bacteria. *Proceedings of the National Academy of Sciences of the United States of America*, *107*(26), 11669–11675. https://doi.org/10.1073/pnas.1006175107

McNeely, K., Kumaraswamy, G. K., Guerra, T., Bennette, N., Ananyev, G., & Dismukes, G. C. (2014). Metabolic switching of central carbon

metabolism in response to nitrate: Application to autofermentative hydrogen production in cyanobacteria. *Journal of Biotechnology*, *182–183*(1), 83–91. https://doi.org/10.1016/j.jbiotec.2014.04.004

McNeely, K., Xu, Y., Ananyev, G., Bennette, N., Bryant, D. A., & Dismukes, G. C. (2011). Synechococcus sp. strain PCC 7002 nifJ mutant lacking pyruvate:Ferredoxin oxidoreductase. *Applied and Environmental Microbiology*, *77*(7), 2435–2444. https://doi.org/10.1128/AEM.02792-10

McNeely, K., Xu, Y., Bennette, N., Bryant, D. A., & Dismukes, G. C. (2010). Redirecting reductant flux into hydrogen production via metabolic engineering of fermentative carbon metabolism in a cyanobacterium. *Applied and Environmental Microbiology*, *76*(15), 5032–5038. https://doi.org/10.1128/AEM.00862-10

Melis, A., Zhang, L., Forestier, M., Ghirardi, M. L., & Seibert, M. (2000). Sustained photobiological hydrogen gas production upon reversible inactivation of oxygen evolution in the green alga Chlamydomonas reinhardtii. *Plant Physiology*, *122*(1), 127–135. https://doi.org/10.1104/pp.122.1.127

Metz, J. G., Pakrasi, H. B., Seibert, M., & Arntzer, C. J. (1986). Evidence for a dual function of the herbicide-binding D1 protein in photosystem II. *FEBS Letters*, *205*(2), 269–274. https://doi.org/10.1016/0014-5793(86)80911-5

Mondal, J., & Bruce, B. D. (2018). Ferredoxin: the central hub connecting photosystem I to cellular metabolism. *Photosynthetica*, *56*(1), 279–293. https://doi.org/10.1007/s11099-018-0793-9

Mullineaux, C. W. (1994). Excitation energy transfer from phycobilisomes to Photosystem I in a cyanobacterial mutant lacking Photosystem II. *BBA - Bioenergetics*, *1184*(1), 71–77. https://doi.org/10.1016/0005-2728(94)90155-4

Murakami, A., Kim, S. J., & Fujita, Y. (1997). Changes in Photosystem Stoichiometry in Response to Environmental Conditions for Cell Growth Observed with the Cyanophyte Synechocystis PCC 6714. *Plant and Cell Physiology*, *38*(4), 392–397. https://doi.org/10.1093/oxfordjournals.pcp.a029181

Nagarajan, D., Lee, D. J., Kondo, A., & Chang, J. S. (2017). Recent insights into biohydrogen production by microalgae – From biophotolysis to dark fermentation. *Bioresource Technology*, *227*(1), 373–387. https://doi.org/10.1016/j.biortech.2016.12.104

Nguyen, T., Abdin, Z., Holm, T., & Mérida, W. (2019). Grid-connected hydrogen production via large-scale water electrolysis. *Energy Conversion and Management*, *200*(October), 112108. https://doi.org/10.1016/j.enconman.2019.112108

Nikolaidis, P., & Poullikkas, A. (2017). A comparative overview of hydrogen production processes. *Renewable and Sustainable Energy Reviews*, *67*, 597–611. https://doi.org/10.1016/j.rser.2016.09.044

Ogawa, T. (1991). A gene homologous to the subunit-2 gene of NADH dehydrogenase is essential to inorganic carbon transport of Synechocystis PCC6803. *Proceedings of the National Academy of Sciences of the United States of America*, *88*(10), 4275–4279. https://doi.org/10.1073/pnas.88.10.4275

Ohkawa, H., Dean Price, G., Badger, M. R., & Ogawa, T. (2000). Mutation of

ndh genes leads to inhibition of CO2 uptake rather than HCO3- uptake in Synechocystis sp. strain PCC 6803. *Journal of Bacteriology*, *182*(9), 2591–2596. https://doi.org/10.1128/JB.182.9.2591-2596.2000

Ohkawa, H., Pakrasi, H. B., & Ogawa, T. (2000). Two types of functionally distinct NAD(P)H dehydrogenases in Synechoeystis sp. strain PCC6803. *Journal of Biological Chemistry*, *275*(41), 31630–31634. https://doi.org/10.1074/jbc.M003706200

Okolie, J. A., Rana, R., Nanda, S., Dalai, A. K., & Kozinski, J. A. (2019). Supercritical water gasification of biomass: A state-of-the-art review of process parameters, reaction mechanisms and catalysis. *Sustainable Energy and Fuels*, *3*(3), 578–598. https://doi.org/10.1039/c8se00565f

Ortega-Ramos, M., Jittawuttipoka, T., Saenkham, P., Czarnecka-Kwasiborski, A., Bottin, H., Cassier-Chauvat, C., & Chauvat, F. (2014). Engineering synechocystis PCC6803 for hydrogen production: Influence on the tolerance to oxidative and sugar stresses. *PLoS ONE*, *9*(2), 1–13. https://doi.org/10.1371/journal.pone.0089372

Pan, X., Cao, D., Xie, F., Xu, F., Su, X., Mi, H., Zhang, X., & Li, M. (2020). Structural basis for electron transport mechanism of complex I-like photosynthetic NAD(P)H dehydrogenase. *Nature Communications*, *11*(1). https://doi.org/10.1038/s41467-020-14456-0

Paschos, A., Bauer, A., Zimmermann, A., Zehelein, E., & Böck, A. (2002). HypF, a carbamoyl phosphate-converting enzyme involved in [NiFe] hydrogenase maturation. *Journal of Biological Chemistry*, *277*(51), 49945–49951. https://doi.org/10.1074/jbc.M204601200

Pimentel, D., Berger, B., Filiberto, D., Newton, M., Wolfe, B., Karabinakis, E., Clark, S., Poon, E., Abbett, E., & Nandagopal, S. (2007). Water resources: Agricultural and environmental issues. *Food, Energy, and Society, Third Edition*, *54*(10), 183–200. https://doi.org/10.1201/9781420046687

Poudel, J., Choi, J. H., & Oh, S. C. (2019). Process design characteristics of syngas (CO/H 2) separation using composite membrane. *Sustainability (Switzerland)*, *11*(3). https://doi.org/10.3390/su11030703

Prasannan, C. B., Jaiswal, D., Davis, R., & Wangikar, P. P. (2018). An improved method for extraction of polar and charged metabolites from cyanobacteria. *PLoS ONE*, *13*(10), 1–16. https://doi.org/10.1371/journal.pone.0204273

Price, G. D., & Badger, M. R. (1991). Evidence for the role of carboxysomes in the cyanobacterial CO 2 -concentrating mechanism . *Canadian Journal of Botany*, *69*(5), 963–973. https://doi.org/10.1139/b91-124

Qian, X., Kumaraswamy, G. K., Zhang, S., Gates, C., Ananyev, G. M., Bryant, D. A., & Dismukes, G. C. (2016). Inactivation of nitrate reductase alters metabolic branching of carbohydrate fermentation in the cyanobacterium Synechococcus sp. strain PCC 7002. *Biotechnology and Bioengineering*, *113*(5), 979–988. https://doi.org/10.1002/bit.25862

Regensburg, D.-, & Freiburg, U. (1991). *alnstitut fi~r Biophysik und Physikalische Biochemie, Universitgit Regensburg, D-93040 Regensburg, Germany; blnstitut fi~r Botanik II, Universitgit Freiburg, D-79104 Freiburg, Germany*. *17838*, 17838.

Rezaei, M., Mostafaeipour, A., Qolipour, M., & Arabnia, H. R. (2018). Hydrogen production using wind energy from sea water: A case study on

Southern and Northern coasts of Iran. *Energy and Environment*, *29*(3), 333–357. https://doi.org/10.1177/0958305X17750052

Sacharz, J., Bryan, S. J., Yu, J., Burroughs, N. J., Spence, E. M., Nixon, P. J., & Mullineaux, C. W. (2015). Sub-cellular location of FtsH proteases in the cyanobacterium Synechocystis sp: PCC 6803 suggests localised PSII repair zones in the thylakoid membranes. *Molecular Microbiology*, *96*(3), 448–462. https://doi.org/10.1111/mmi.12940

Sakamoto, T., Delgaizo, V. B., & Bryant, D. A. (1998). Growth on urea can trigger death and peroxidation of the cyanobacterium Synechococcus sp. strain PCC 7002. *Applied and Environmental Microbiology*, *64*(7), 2361–2366. https://doi.org/10.1128/aem.64.7.2361-2366.1998

Sambrook, J., Fritsch, E. F., & Maniatis, T. (1989). *Molecular Cloning: A Laboratory Manual*. Cold Spring Harbor Laboratory.

Sancheti, S. V., & Burange, A. S. (2015). An Understanding of Gasification and Applications of Catalytic Materials in Hydrogen Production: Mini Review. *Asian Journal of Research in Chemistry*, *8*(3), 201. https://doi.org/10.5958/0974-4150.2015.00036.x

Sánchez-Bastardo, N., Schlögl, R., & Ruland, H. (2020). Methane Pyrolysis for CO2-Free H2 Production: A Green Process to Overcome Renewable Energies Unsteadiness. *Chemie-Ingenieur-Technik*, *92*(10), 1596–1609. https://doi.org/10.1002/cite.202000029

Schuchmann, K., Chowdhury, N. P., & Müller, V. (2018). Complex multimeric [FeFe] hydrogenases: Biochemistry, physiology and new opportunities for the hydrogen economy. *Frontiers in Microbiology*, *9*(DEC), 1–22. https://doi.org/10.3389/fmicb.2018.02911

Schütz, K., Happe, T., Troshina, O., Lindblad, P., Leitão, E., Oliveira, P., & Tamagnini, P. (2004). Cyanobacterial H2 production - A comparative analysis. *Planta*, *218*(3), 350–359. https://doi.org/10.1007/s00425-003-1113-5

Schwarz, R., & Forchhammer, K. (2005). Acclimation of unicellular cyanobacteria to macronutrient deficiency: Emergence of a complex network of cellular responses. *Microbiology*, *151*(8), 2503–2514. https://doi.org/10.1099/mic.0.27883-0

Shima, S., Pilak, O., Vogt, S., Schick, M., Stagni, M. S., Meyer-Klaucke, W., Warkentin, E., Thauer, R. K., & Ermler, U. (2008). The crystal structure of [Fe]-hydrogenase reveals the geometry of the active site. *Science*, *321*(5888), 572–575. https://doi.org/10.1126/science.1158978

Shimmori, Y., Kanesaki, Y., Nozawa, M., Yoshikawa, H., & Ehira, S. (2018). Transcriptional activation of glycogen catabolism and the oxidative pentose phosphate pathway by NrrA facilitates cell survival under nitrogen starvation in the Cyanobacterium Synechococcus sp. Strain PCC 7002. *Plant and Cell Physiology*, *59*(6), 1225–1233. https://doi.org/10.1093/pcp/pcy059

Shomura, Y., & Higuchi, Y. (2013). Structural aspects of [NiFe]-hydrogenases. *Reviews in Inorganic Chemistry*, *33*(4), 173–192. https://doi.org/10.1515/revic-2013-0005

Siemann, S., Schneider, K., Oley, M., & Müller, A. (2003). Characterization of a tungsten-substituted nitrogenase isolated from Rhodobacter capsulatus. *Biochemistry*, *42*(13), 3846–3857. https://doi.org/10.1021/bi0270790

Stanier, R. Y., Kunisawa, R., Mandel, M., & Cohen-Bazire, G. (1971). Purification and properties of unicellular blue-green algae (order Chroococcales). *Bacteriological Reviews*, *35*(2), 171–205. https://doi.org/10.1128/mmbr.35.2.171-205.1971

Stevens, S. E., Patterson, C. O. P., & Myers, J. (1973). the Production of Hydrogen Peroxide By Blue-Green Algae: a Survey. In *Journal of Phycology* (Vol. 9, Issue 4, pp. 427–430). https://doi.org/10.1111/j.1529-8817.1973.tb04116.x

Sytar, O., Cai, Z., Brestic, M., Kumar, A., Prasad, M. N. V, Taran, N., Iryna, S., & Faculty, A. (2013). Accept e d Article. *October*, 1–22.

Tamagnini, P., Axelsson, R., Lindberg, P., Oxelfelt, F., Wünschiers, R., & Lindblad, P. (2002). Hydrogenases and Hydrogen Metabolism of Cyanobacteria. *Microbiology and Molecular Biology Reviews*, *66*(1), 1–20. https://doi.org/10.1128/mmbr.66.1.1-20.2002

Tran, K. T., Maeda, T., & Wood, T. K. (2014). Metabolic engineering of Escherichia coli to enhance hydrogen production from glycerol. *Applied Microbiology and Biotechnology*, *98*(10), 4757–4770. https://doi.org/10.1007/s00253-014-5600-3

Veaudor, T., Ortega-Ramos, M., Jittawuttipoka, T., Bottin, H., Cassier-Chauvat, C., & Chauvat, F. (2018). Overproduction of the cyanobacterial hydrogenase and selection of a mutant thriving on urea, as a possible step towards the future production of hydrogen coupled with water treatment. *PLoS ONE*, *13*(6), 1–16. https://doi.org/10.1371/journal.pone.0198836

Vignais, P. M., & Billoud, B. (2007). Occurrence, classification, and biological function of hydrogenases: An overview. *Chemical Reviews*, *107*(10), 4206–4272. https://doi.org/10.1021/cr050196r

Vignais, P. M., Billoud, B., & Meyer, J. (2001). Classification and phylogeny of hydrogenases. *FEMS Microbiology Reviews*, *25*(4), 455–501. https://doi.org/10.1016/S0168-6445(01)00063-8

Vuksic, M., Zorica, S., & Zulim, I. (2014). Evaluation of DC-DC Resonant Converters for Solar Hydrogen Production Evaluation of DC-DC resonant converters for solar hydrogen production based on load current characteristics. *Contemporary Issues in Economy and Technology*, *June 2014*, 121–133. https://www.researchgate.net/publication/263470190_Evaluation_of_DC-DC_Resonant_Converters_for_Solar_Hydrogen_Production_Based_on_Load_Current_Characteristics

Want, E. J., Wilson, I. D., Gika, H., Theodoridis, G., Plumb, R. S., Shockcor, J., Holmes, E., & Nicholson, J. K. (2010). Global metabolic profiling procedures for urine using UPLC-MS. *Nature Protocols*, *5*(6), 1005–1018. https://doi.org/10.1038/nprot.2010.50

Williams, J. G. K. (1988). Construction of Specific Mutations in Photosystem II Photosynthetic Reaction Center by Genetic Engineering Methods in Synechocystis 6803. *Methods in Enzymology*, *167*(C), 766–778. https://doi.org/10.1016/0076-6879(88)67088-1

Winkler, M., Esselborn, J., & Happe, T. (2013). Molecular basis of [FeFe]-hydrogenase function An insight into the complex interplay between protein and catalytic cofactor. *Biochimica et Biophysica Acta - Bioenergetics*, *1827*(8–9), 974–985.

https://doi.org/10.1016/j.bbabio.2013.03.004
Winter, G., Buhrke, T., Lenz, O., Jones, A. K., Forgber, M., & Friedrich, B. (2005). A model system for [NiFe] hydrogenase maturation studies: Purification of an active site-containing hydrogenase large subunit without small subunit. *FEBS Letters*, *579*(20), 4292–4296. https://doi.org/10.1016/j.febslet.2005.06.064
Yao, L., Shabestary, K., Björk, S. M., Asplund-Samuelsson, J., Joensson, H. N., Jahn, M., & Hudson, E. P. (2020). Pooled CRISPRi screening of the cyanobacterium Synechocystis sp PCC 6803 for enhanced industrial phenotypes. *Nature Communications*, *11*(1). https://doi.org/10.1038/s41467-020-15491-7
Yu, J., & Takahashi, P. (2007). *Biophotolysis-based Hydrogen Production by Cyanobacteria and Green Microalgae*. *June*, 79–89.
Zavřel, T., Sinetova, M. A., Búzová, D., Literáková, P., & Červený, J. (2015). Characterization of a model cyanobacterium Synechocystis sp: PCC 6803 autotrophic growth in a flat-panel photobioreactor. *Engineering in Life Sciences*, *15*(1), 122–132. https://doi.org/10.1002/elsc.201300165
Zhang, C., Shuai, J., Ran, Z., Zhao, J., Wu, Z., Liao, R., Wu, J., Ma, W., & Lei, M. (2020). Structural insights into NDH-1 mediated cyclic electron transfer. *Nature Communications*, *11*(1), 1–13. https://doi.org/10.1038/s41467-020-14732-z
Zhang, P., Battchikova, N., Jansen, T., Appel, J., Ogawa, T., & Aro, E. M. (2004). Expression and functional roles of the two distinct NDH-1 complexes and the carbon acquisition complex NdhD3/NdhF3/CupA/SII1735 in Synechocystis sp PCC 6803. *Plant Cell*, *16*(12), 3326–3340. https://doi.org/10.1105/tpc.104.026526
Zhang, Y. H. P., Evans, B. R., Mielenz, J. R., Hopkins, R. C., & Adams, M. W. W. (2007). High-yield hydrogen production from starch and water by a synthetic enzymatic pathway. *PLoS ONE*, *2*(5), 2–7. https://doi.org/10.1371/journal.pone.0000456

9 Appendix

Table S1: Primer Table

Primer	Sequence
	***Synechococystis* sp. PCC 6803**
	Fluorescent Protein Tagging Primers
6803PsbA2UYFPF	tgaattcgcggccgcctgcaACCTTACTTGGATGCCGG
6803PsbA2UYFPR	CGCCCTtgctcaccatTTGGTTATAATTCCTTATGTATTTGTCGATGTTC
6803psbA2YFPF	TACATAAGGAAttataaccaaATGGTGAGCAAGGGCGAGgag
6803PsbA2YFPR	ccgggcccggcagTCTAGATCCGGTGGATCCC
6803PsbA2ORFYFPF	cggatctagactgccgggcccggagctgccgggtccggagATGACAACGACTCTCCAAC
6803PsbA2ORFYFPR	GGTCGACGGAtccccggaatTTAACCGTTGACAGCAGG
6803PsbA2SpecF	GCTGTcaacggttaaATTCCGGGGATCCGTCGAC
6803PsbA2SpecR	CATTAcaccaaggaaTGTAGGCTGGAGCTGCTTC
6803PsbA2DYFPF	CAGCTccagcctacaTTCCTTGGTGTAATGCCAAC
6803PsbA2DYFPR	catccaacgcgttgggagctGAAGCATTTTCAGGCAATC
6803PsaFYUpF	actagtgaattcgcggccgcctgcaGACTATTGGCGGCCACCC
6803PsaFYUpr	ccgggcccggcagGCGGGGGGAAGTGGGGAT

6803PsaFYFPF	cacttccccccgcCTGCCGGGCCCGGAGCTG
6803PsaFYFPR	aatgcccaactaaGAAGTTCCTATTCTCTAGAAAGTATAGGAACTTCGAAGTTCCCGCC
6803PsaFYdwnF	gaataggaacttcTTAGTTGGGCATTGACTG
6803PsaFYdwnR	ctatgcatccaacgcgttgggagctGAAGCCATCGTCAGTTTTAC
6803NdhMYupF	actagtgaattcgcggccgcctgcaCCCCAGCTTGGGCACTGT
6803NdhMYupR	ccgggcccggcagGTTATCCAGCCAATATTTTCCTGCAGTTTC
6803NdhMYFPF	ttggctggataacCTGCCGGGCCCGGAGCTG
6803NdhMYFPR	aattgataccaagGAAGTTCCTATTCTCTAGAAAGTATAGGAACTTCGAAGTTCCCGCC
6803NdhMYdwnF	gaataggaacttcCTTGGTATCAATTGACCATAACTGGAGGGAG
6803NdhMYdwnR	ctatgcatccaacgcgttgggagctAAGGGGCGGTCCAAGCCG
6803SdhACCupF	actagtgaattcgcggccgcctgcaGGGCTTTGGAAAATCATATTTTTG
6803SdhACCupR	ccgggcccggcagATGGCTAAAGTGGGAACC
6803SdhACFPF	ccactttagccatCTGCCGGGCCCGGAGCTG
6803SdhACFPR	atgattatgatgcGAAGTTCCTATTCCGAAGTTCCTATTCTCTAGAAAGTATAGGAACTTCTTTATACTCGAGC
6803SdhACCdwnF	gaataggaacttcGCATCATAATCATTCACAATG
6803SdhACCdwnR	ctatgcatccaacgcgttgggagctTATATCTGCATATTTTTTTCTTTGTAAAAC

6803PetFCupF	actagtgaattcgcggccgcctgcaTTTGTCGATTGTCCCATTG
6803PetFCupR	ccgggcccggcagGTAGAGGTCTTCTTCTTTG
683PetFCFPF	agaagacctctacCTGCCGGGCCCGGAGCTG
6803PetFCFPR	agcattattacccGAAGTTCCTATTCCGAAGTTCCTATTCTCTAGAAAGTATAGGAACTTCTTTATACTCGAGC
6803PetFCdwnF	gaataggaacttcGGGTAATAATGCTGGCCATG
6803PetFCdwnR	ctatgcatccaacgcgttgggagctATTTAAAAACTAATCCCATTGATTTGTTAG
6803 HoxE up R	CTCCGggcccggcagACTGTTACTTAACCAAGGTTG
6803HoxEGFPF	TGGTTaagtaacagtCTGCCGGGCCCGGAGCTG
6803HoxEGFPR	ACGGAtccccggaatttaCTTGTACAGCTCGTCCATGCCGAGAGTG
6803HoxESpecF	GAgctgtacaagtaaATTCCGGGGATCCGTCGAC
6803HoxESpecR	GATACttaatatccgTGTAGGCTGGAGCTGCTTC
6803HoxEDwnF	ccagcctacaCGGATATTAAGTATCAGGTGATTGCTTGATCTTTTCTAGTTGATTTTTTGATTTGTTGTTATTG
6803HoxEdwnR	catccaacgcgttgggagctTGGTCGGGGCGTTCCCCG
6803HoxFUpF	tgaattcgcggccgcctgcaAATGTACAAAATCCCACC
6803HoxFUpR	ggcccggcagGACTTTGAGTAATTCTTCATATTC
6803HoxFGFPF	actcaaagtcCTGCCGGGCCCGGAGCTG

6803HoxFGFPR	aattaccgaaATTCCGGGGATCCGTCGACCTG
6803HoxFdwnF	tccccggaatTTCGGTAATTTATCCACTCAG
6803HoxFdwnR	catccaacgcgttgggagctCATGATTGCCTTCGGAAAAAAG
6803HoxYCUpF	actagtgaattcgcggccgcctgcaATGAAGAGTTAGGCGTTAAAG
6803HoxYCUpR	ccgggcccggcagACCAAATTTGATCATTGCTC
6803HoxYCGFPF	gatcaaatttggtCTGCCGGGCCCGGAGCTG
6803HoxYCGFPR	gaaaacttgaattATTCCGGGGATCCGTCGACCTG
6803HoxYCdwnF	ggatccccggaatAATTCAAGTTTTCTAAACAGTTTG
6803HoxYCdwnR	ctatgcatccaacgcgttgggagctCGACCTTCGCAAAATTTTTC

Mutagenesis Primers

6803MutHoxUF	ATTCATTTTC*AACGTT*AAAGGAGTTTTTGGCCA
6803MutHoxUR	TAGAAATGAT*GGATCC*GTTAAAAGTTCTTAAAAGTTCAAC
6803MutHoxYF	TACAAG*CCTGAA*CGTTTTTTGGAAAATGATTTTTAGGT
6803MutHoxYR	TATAGAAAGC*GGATCC*CGGATCTTGTAATAAATATTCAGG
8803MutHoxHF	AAAAAATATC*AACGTT*TAAATCAACAATAATCAATCCC
6803MutHoxHR	ATTTTTTTGA*GGATCC*CGTCTGAATGTTTTTTGT

Screening Primers	
6803PsbA2SCF	GATTGCGGCTTTAGCGTTCC
6803PsbA2SCR	CAAGGTACCGAACCAACCGA
6803PsaFSCF	CAAGGGCAAATGTGCCTAGC
6803PsaFSCR	GGTGAATACACCTCCGGCAA
6803NdhMSCF	TGGCTCGGATTTGGAGCATT
6803NdhMSCR	GCACAGTGTTAAGCCTCCCT
6803SdhASCF	CGATCGCCTATTTTGCCAGC
6803SdhASCR	GAATTCACTGCACTCGGGGA
6803PetFSCF	ATTGTCCACGGCAGGGTTTA
6803PetFSCR	GAAGCATTAGGGGAACCGGG
6803HoxEscF	TGAAGGGGAGACGGTGAAAA
6803HoxEscR	AATGACGAAGCGGTATTGGC
6803HoxFSCF	TGTGGATTGGGGATGAGTGC
6803HoxFSCR	TCCCAATGACCGGGTTTACG
6803HoxYCSCF	TGTCAGCCGCCTATGATGTC

6803HoxYCSCR	TGGAGATTTTGGCATGGCCT
***Synechococcus* sp. PCC 7002**	
Deletion Primers	
7002HoxHupF	tgaattcgcggccgcctgcaTTCGCAATCAAAAGGGAG
7002HoxHupR	ggtcgacggatccccggaatCATTTTTTACTCCTAGATGATTTTTC
7002HoxHSpecF	tcatctaggagtaaaaaatgATTCCGGGGATCCGTCGAC
7002HoxHSpecR	cattaaagtttgtttcattaTGTAGGCTGGAGCTGCTTC
7002HoxHdwnF	cgaagcagctccagcctacaTAATGAAACAAACTTTAATGATTGG
7002HoxHdwn R	catccaacgcgttgggagctTAAATCTTTCGCCAAAAAATAG
Fluorescent Protein Tagging Primers	
7002PsbA2NCupF	actagtgaattcgcggccgcctgcaGCGAGGAGGAGTTGCAATTG
7002PsbA2NCupR	ccttgctcaccatATCGTTATGATTGCTATGAAATTATCAAGG
7002PsbA2NCFPF	caatcataacgatATGGTGAGCAAGGGCGAG
7002PsbA2NCFPR	tgccgggtccggagCTTGTACAGCTCGTCCATGC
7002PsbA2NorfF	cgagctgtacaagctccggacccggcagctccgggcccggcagATGACTACTACACTACAACAG
7002PsbA2NorfR	gaataggaacttcTTAACCGTTGATTGCAGG

7002PsbA2NKmF	aatcaacggttaaGAAGTTCCTATTCTCTAGAAAG
7002PsbA2NKmR	actcaaacagttaGAAGTTCCTATTCCGAAG
7002PsbA2NdwnF	gaataggaacttcTAACTGTTTGAGTCTTCGGG
7002PsbA2NdwnR	ctatgcatccaacgcgttgggagctAACCGCACCGTATGGAAATTTTG
7002PsaFCupF	actagtgaattcgcggccgcctgcaAAACCACTGTTTGCTGCC
7002PsaFCupR	ccgggcccggcagGCGAGGAGAGATGGGGAC
7002PsaFCFPF	catctctcctcgcCTGCCGGGCCCGGAGCTG
7002PsaFCFPR	taaaaatgaaaacGAAGTTCCTATTCCGAAGTTCCTATTCTCTAGAAAGTATAGGAACTTCTTTATACTCGAGC
7002PsaFCdwnF	gaataggaacttcGTTTTCATTTTTAAGTATTTATCATTCTTTTTGGAGTAAATAAATGG
7002PsaFCdwnR	ctatgcatccaacgcgttgggagctAAAAGCGGGGATCACGGTG
7002PsaFYupF	actagtgaattcgcggccgcctgcaAAACCACTGTTTGCTGCC
7002PsaFYupR	ccgggcccggcagGCGAGGAGAGATGGGGAC
7002PsaFYFPF	catctctcctcgcCTGCCGGGCCCGGAGCTG
7002PsaFYFPR	taaaaatgaaaacGAAGTTCCTATTCTCTAGAAAGTATAGGAACTTCGAAGTTCCCGCC
7002PsaFYdwnF	gaataggaacttcGTTTTCATTTTTAAGTATTTATCATTCTTTTTGGAGTAAATAAATGG
7002PsaFYdwnR	ctatgcatccaacgcgttgggagctAAAAGCGGGGATCACGGTG

7002NdhMCYupF	actagtgaattcgcggccgcctgcaGGGGAGAGATTAACAAAATCAAAG
7002NdhMCYupR	ccgggcccggcagCTGGAGGTAAGCGCCTTG
7002NdhMCYFPF	cgcttacctccagCTGCCGGGCCCGGAGCTG
7002NdhMCYFPR	tctagactaaaccGAAGTTCCTATTCTCTAGAAAGTATAGGAACTTCGAAGTTCCCGCC
7002NdhMCYdwnF	gaataggaacttcGGTTTAGTCTAGACTTAGAATTC
7002NdhMCYdwnR	ctatgcatccaacgcgttgggagctCGCATCTATAAATTTGGGG
7002SdhACCupF	actagtgaattcgcggccgcctgcaTCAATAGACCAAGATGTCG
7002SdhACCupR	ccgggcccggcagATACTTGCGCTCTTTGGG
7002SdhACCFPF	agagcgcaagtatCTGCCGGGCCCGGAGCTG
7002SdhACCFPR	agggctgagggctGAAGTTCCTATTCCGAAGTTCCTATTCTCTAGAAAGTATAGGAACTTCTTTATACTCGAGC
7002SdhACCdwnF	gaataggaacttcAGCCCTCAGCCCTTCTCAAAG
7002SdhACCdwnR	ctatgcatccaacgcgttgggagctGGCGCAACTGTGGGAGCG
7002HoxFCGupF	actagtgaattcgcggccgcctgcaTACAATGCCAACGCCCGC
7002HoxFCGupR	ccgggcccggcagATCGGCGTTACTCCCCAC
7002HoxFCGFPF	gagtaacgccgatCTGCCGGGCCCGGAGCTG
7002HoxFCGFPR	attaaaaaaaaatATTCCGGGGATCCGTCGACCTG

7002HoxFCdwnF	ggatccccggaatATTTTTTTTTAATTCCCATGCAG
7002HoxFCdwnR	ctatgcatccaacgcgttgggagctAATTCCAAATTTTCTTGGTTAG

Screening Primers

7002PsbA2NSCF	CTAGACGAGCTTGGGCAGTC
7002PsbA2NSCR	ACTTCTCCCACAAGGAAGCG
7002PsaFSCF	TCTGATCGCAGTCCGTGATG
7002PsaFSCR	AACACCGGCGCAGAAGATAA
7002NdhMSCF	ATCTCGTCCTCGCCCTTAGT
7002NdhMSCR	GGATCACCCCGATAGCCAAG
7002SdhASCF	TTACCTCTGCTTACCACCGC
7002SdhASCR	TCTTGGGGAACATGCCACAG
7002HoxHintF	TGATCCCATGACTCGCATCG
7002HoxHintR	CGGATCACTGTCCCAACCAA
7002HoxHextF	CCCCCGTCATGACTGACAAA
7002HoxHextR	ATCGCCACGGTTTCTGTCAT
7002HoxFSCF	CCGGCGGACTACCTTGATAC

7002HoxFSCR	TCAAGGATCGTTTCCCCAGC

***Synechococcus* sp. PCC 7942**

Fluorescent Protein Tagging Primers

7942PsbA2UF	tgaattcgcggccgcctgcaCCGTAGACCGCTAGTCCTTG
7942PsbA2UR	GCTCCTCGCccttgctcacTTTGCGATGAGTCCTTAGTTG
7942PsbA2GFPF	AGGACtcatcgcaaaGTGAGCAAGGGCGAGGAG
7942PsbA2GFPR	ccgggcccggcagCTTGTACAGCTCGTCCATGC
7942PsbA2ORFF	GACGAgctgtacaagctgccgggcccggagctgccgggtccggagATGACGACTGCATTGCAG
7942PsbA2ORFR	ACGgatccccggaatcTTAGCCGTTGATTGCAGG
7942PsbA2ApraF	TGCAATcaacggctaaGATTCCGGGGATCCGTCG
7942PsbA2ApraR	CGCATcagccggcaaGAATAGGAACTTCGGAATAGGAACTTCATG
7942PsbA2DGFPF	ATTCCGAAgttcctattcTTGCCGGCTGATGCGGAACAG
7942PsbA2DGFPR	catccaacgcgttgggagctTTGTGGCCGAGACTGATTTGC
7942HoxFCGUpF	actagtgaattcgcggccgcctgcaCAATTTTCAGTTCACAGACGTAG
7942HoxFCGUpR	ccgggcccggcagATGAGTCAGTGCGATCGC
7942HoxFCGFPF	cgcactgactcatCTGCCGGGCCCGGAGCTG

7942HoxFCGFPR	ctaaatcgatcgcATTCCGGGGATCCGTCGACCTG
7942HoxFCGdwnF	ggatccccggaatGCGATCGATTTAGGTCAAATTCAGCAGC
7942HoxFCGdwnR	ctatgcatccaacgcgttgggagctGCCCTTGGCTGAACGCCC
7942NdhMCYUpF	actagtgaattcgcggccgcctgcaTCCGGCAACAGTAGCTTGAG
7942NdhMCYUpR	ccgggcccggcagGACAACGGCTTGCGGCAC
7942NdhMCYFPF	gcaagccgttgtcCTGCCGGGCCCGGAGCTG
7942NdhMCYFPR	ctcaacgcctgcaGAAGTTCCTATTCTCTAGAAAGTATAGGAACTTCGAAGTTCCCGCC
7942NdhMCYdwnF	gaataggaacttcTGCAGGCGTTGAGTCTAC
7942NdhMYdwnR	ctatgcatccaacgcgttgggagctTTCATTGCCCTTGATTCTCAATC
7942PsaFCYUpF	actagtgaattcgcggccgcctgcaCGCCCCCCACGGCGATCG
7942PsaFCYUpR	ccgggcccggcagGCGGGGCGAGACGGTGATTTC
7942PsaFCYFPF	cgtctcgccccgcCTGCCGGGCCCGGAGCTG
7942PsaFCYFPR	aacgacagaaatcGAAGTTCCTATTCTCTAGAAAGTATAGGAACTTCGAAGTTCCCGCC
7942PsaFCYdwnF	gaataggaacttcGATTTCTGTCGTTTTACGGAGC
7942PsaFCYdwnR	ctatgcatccaacgcgttgggagctCCGCTATCCCACCTGGTG
7942Fdx1CCUpF	actagtgaattcgcggccgcctgcaTACCGAAGCCATGCGTCTG

7942Fdx1CCUpR	ccgggcccggcagGCCGGGCTGACCAAATTG
7942Fdx1CCFPF	tggtcagcccggcCTGCCGGGCCCGGAGCTG
7942Fdx1CCFPR	aattgggtctgcaGAAGTTCCTATTCCGAAGTTCCTATTCTCTAGAAAGTATAGGAACTTCTTTATACTCGAGC
7942Fdx1CCdwnF	gaataggaacttcTGCAGACCCAATTTGTCAGTCTG
7942Fdx1CCdwnR	ctatgcatccaacgcgttgggagctGCCGCCGATCGCAGTCTC
7942SdhACCUpF	actagtgaattcgcggccgcctgcaCCCATAGGCTTTTAACATCTG
7942SdhACCUpR	ccgggcccggcagTTGATAGTTTCGCTGGCTG
7942SdhACCFPF	gcgaaactatcaaCTGCCGGGCCCGGAGCTG
7942SdhACCFPR	ttaaatggaggcgGAAGTTCCTATTCCGAAGTTCCTATTCTCTAGAAAGTATAGGAACTTCTTTATACTCGAGC
7942SdhACCdwnF	gaataggaacttcCGCCTCCATTTAAGCAATAAG
7942SdhACCdwnR	ctatgcatccaacgcgttgggagctGTCGAGCGACTGGTCTTC

Screenin Primers

7942PsbA2SCF	GCCGAACCAACCCACATAGA
7942PsbA2SCR	TATTCACTTACTGGGCGGGC
7942PsaFSCF	CCAAGAGTTCAGCAGCGGTA
7942PsaFSCR	TGACGCTTTCCTAGAGGGGA

7942NdhMSCF	ATCAAGAGCGGGTAGGAGGT
7942NdhMSCR	TTGAGTGCCGTTAGGACGAC
7942SdhASCF	CCCAGCCAGCGAAACTATCA
7942SdhASCR	ACAGTTGGAGGAACTCTGCG
Fdx1CSCF	CTCAGCGGTGAAGTGGATCA
Fdx1CSCR	AGACTCGCCCCATTCATCAC
7942HoxFSCF	TGGGAATGTCTGCTCCCAAC
7942HoxFSCR	GCACCAAAACGACTGGTGTC

YFP Vector Primers

eYFPF	CAATCAACATactagt*CTGCCGGGCCCGGAGCTGCCGGGTCCGGAG*ATGGTGAGCAAGGGCGAG
eYFPR	AGTTGATCAGtgatcaTTATCTAGATCCGGTGGATCC

CFP Vector Primers

CFPF	tgaattcgcggccgcctgcactgcc*gggcccggagctgccgggtccggag*ATGGTGAGCAAGGGCGAG
CFPR	CCTTCGGGTGGGCCTTTCTGCGTTATTACTTGTACAGCTCGTCCA
KmF	GTACAAGTAATAACGCAGAAAGGCCCACCCGAAGGTGAGCCGAAGTTCCTATTCTCTAGAAAGTATAGGAACTTCTTAGAAAAACTCATCGAGCA
KmR	catccaacgcgttgggagctgaagttcctattccgaagttcctattctctagaaagtataggaacttcTTTATACTCGAGCTGATCC

Table S2: Metabolite Standards

Index	Compound Name	Abbr	synonyms	Formula	Monoisopopic mass	[M+H]+	[M-H]-	Conc (mM)	Mix vol
1	(+) Epinephrine			$C_9H_{13}NO_3$	183.0895	184.0968	182.0822	100	1.00
2	(+)-α-Lipoamide	Lipm	Thioctic acid amide	$C_8H_{15}NOS_2$	205.0595	206.0668	204.0522	10	10.00
3	(+)-α-Lipoic acid	LipA	Lipoic acid_alpha-Lipoic acid_Thioctic acid	$C_8H_{14}O_2S_2$	206.0435	207.0508	205.0362	10	10.00
4	(3-Carboxypropyl)trimethylammonium chloride (γ-Butyrobetaine hydrochloride, Deoxycarnitine hydrochloride)	4TMAB	4-Trimethylammoniobutanoate	$C_7H_{16}NO_2$	146.1181	147.1254	145.1108	100	1.00
5	1- Aminopropan-2-ol		1-AMINO-2-PROPANOL; 1-Aminopropan-2-ol; Monoisopropanolamine; Amino-2-propanol; Isopropanolamine; Threamine	C_3H_9NO	75.0684	76.0757	74.0611	100	1.00
6	1- Methylguanidine			$C_2H_7N_3$	73.0640	74.0713	72.0567	100	1.00
7	1,3-Diaminopropane	DaP	Trimethylenediamine_1,3-Propanediamine_Propane-1,3-diamine	$C_3H_{10}N_2$	74.0844	75.0917	73.0771	100	1.00
8	1-Aminocyclopropanecarboxylic acid		1-Aminocyclopropanecarboxylic acid; 1-Aminocyclopropane-1-carboxylic acid; 22059-21-8; 1-Amino-1-cyclopropanecarboxylic acid; Cyclopropanecarboxylic acid, 1-amino-; Carboxycyclopropylamine	$C_4H_7NO_2$	101.0477	102.0550	100.0404	100	1.00

9	1-Butanol	1BN	1-Butyl alcohol	$C_4H_{10}O$	74.0732	75.0805	73.0659	10	10.00
10	2,3-Diphospho-D-glyceric acid	23BPG	2,3-Disphospho-D-glycerate_D-Greenwald ester_DPG__2-3-Diphosphoglycericacid	$C_3H_8O_{10}P_2$	265.9593	266.9666	264.9520	10	10.00
11	2′-Deoxyuridine	dUri	2-Deoxyuridine_2'-Deoxyuridine	$C_9H_{12}N_2O_5$	228.0746	229.0819	227.0673	10	10.00
12	2'-Deoxyadenosine	dAds	2'-Deoxyadenosine	$C_{10}H_{13}N_5O_3$	251.1018	252.1091	250.0945	10	10.00
13	2'-Deoxyadenosine 5'-monophosphate (dAMP)	dAMP	2'-Deoxyadenosine 5'-phosphate_2'-Deoxyadenosine 5'-monophosphate_Deoxyadenylic acid_Deoxyadenosine monophosphate	$C_{10}H_{14}N_5O_6P$	331.0682	332.0755	330.0609	10	10.00
14	2-Deoxy-D-glucose	2DOG	2-Deoxy-D-arabino-hexose_D-arabino-2-Deoxyhexose	$C_6H_{12}O_5$	164.0685	165.0758	163.0612	10	10.00
15	2-Deoxy-D-ribose	dRi	2-Deoxy-D-erythro-pentose_Thyminose_2-Deoxy-D-ribose	$C_5H_{10}O_4$	134.0579	135.0652	133.0506	100	1.00
16	2'-Deoxyguanosine 5'-monophosphate (dGMP)	dGMP	2'-Deoxyguanosine 5'-monophosphate_2'-Deoxyguanosine 5'-phosphate_Deoxyguanylic acid_Deoxyguanosine monophosphate	$C_{10}H_{14}N_5O_7P$	347.0631	348.0704	346.0558	100	1.00
17	2'-Deoxyinosine 5'-monophosphate (dIMP)	dIMP	2'-deoxy-IMP; CHEBI:61194; 2'-deoxy-5'-O-phosphonatoinosine	$C_{10}H_{13}N_4O_7P$	332.0522	333.0595	331.0449	100	1.00
18	2'-Deoxyuridine 5'-monophosphate (dUMP)	dUMP	Deoxyuridylic acid_Deoxyuridine monophosphate_Deoxyuridine 5'-phosphate_2'-Deoxyuridine 5'-phosphate	$C_9H_{13}N_2O_8P$	308.0410	309.0483	307.0337	100	1.00

19	2-Hydroxyethyldisulfide		2-Hydroxyethyl disulfide; 2,2'-Dithiodiethanol; Bis(2-hydroxyethyl) disulfide; Ethanol, 2,2'-dithiobis-; 1892-29-1; Hydroxyethyl disulfide	$C_4H_{10}O_2S_2$	154.0122	155.0195	153.0049	100	1.00
20	2-Hydroxyhippuric acid			$C_9H_9NO_4$	195.0532	196.0605	194.0459	50	2.00
21	2-Hydroxyisobutyric acid			$C_4H_8O_3$	104.0473	105.0546	103.0400	100	1.00
22	2-Hydroxyisocaproic acid (Leucinic acid)			$C_6H_{12}O_3$	132.0786	133.0859	131.0713	100	1.00
23	2-Methylcitric acid	2mc	2-Hydroxybutane-1,2,3-tricarboxylate_(2R,3S)-2-Hydroxybutane-1,2,3-tricarboxylate	$C_7H_{10}O_7$	206.0427	207.0500	205.0354	100	1.00
24	2-oxobutyrate (2-Oxobutanoic acid)	2oBA	2-Ketobutyric acid_2-Oxobutyric acid_2-Oxobutyrate_2-Oxobutanoic acid_alpha-Ketobutyric acid_alpha-Ketobutyrate	$C_4H_6O_3$	102.0317	103.0390	101.0244	100	1.00
25	2-Oxoglutaric acid	2OGA	Oxoglutaric acid_2-Ketoglutaric acid_alpha-Ketoglutaric acid	$C_5H_6O_5$	146.0215	147.0288	145.0142	100	1.00
26	2-Picolinic acid		picolinic acid; Pyridine-2-carboxylic acid; 2-Pyridinecarboxylic acid; 2-Picolinic acid; 98-98-6; 2-Carboxypyridine	$C_6H_5NO_2$	123.0320	124.0393	122.0247	100	1.00
27	3 -Phospho-D-glycerate	3PGA	D-Glycerate 3-phosphate_3-Phospho-(R)-glycerate_3-Phosphoglycerate	$C_3H_7O_7P$	185.9929	187.0002	184.9856	100	1.00
28	3,4-Dihydroxyphenylacetic acid	DHPA	3,4-Dihydroxyphenylacetic acid_3,4-Dihydroxyphenyl acetate_3,4-Dihydroxyphenyl acetic acid_Homoprotocatechuate	$C_8H_8O_4$	168.0423	169.0496	167.0350	100	1.00

29	3-Hydroxyphenylacetic acid	3HPA	3-Hydroxyphenylacetic acid	$C_8H_8O_3$	152.0473	153.0546	151.0400	10	10.00
30	3-Methyl-2-oxabutanoic acid			$C_6H_{12}O_2$	116.0837	117.0910	115.0764	100	1.00
31	3-Methyl-L-histidine	NMH	N(pi)-Methyl-L-histidine	$C_7H_{11}N_3O_2$	169.0851	170.0924	168.0778	100	1.00
32	4-Aminobenzoic acid	PABA	ABEE_4-Aminobenzoic acid_p-Aminobenzoate	$C_9H_{11}NO_2$	165.0790	166.0863	164.0717	10	10.00
33	4-Aminobutanoate (GABA)	GABA	4-Aminobutanoic acid_4-Aminobutyrate_4-Aminobutyric acid_gamma-Aminobutyric acid	$C_4H_9NO_2$	103.0633	104.0706	102.0560	100	1.00
34	4-Aminohippuric acid			$C_9H_{10}N_2O_3$	194.0691	195.0764	193.0618	100	1.00
35	4-Hydroxy-3-methoxyphenylglycol sulfate			$C_9H_{12}O_7S$	264.0304	265.0377	263.0231	10	10.00
36	4-Hydroxyphenyl acetic acid			$C_8H_8O_3$	152.0473	153.0546	151.0400	100	1.00
37	4-Hydroxyphenylpyruvic acid	4HPP	4-Hydroxyphenylpyruvic acid; Testacid; 3-(4-Hydroxyphenyl)-2-oxopropanoic acid; p-Hydroxyphenylpyruvic acid; 156-39-8; 4-hydroxyphenylpyruvate	$C_9H_8O_4$	180.0423	181.0496	179.0350	10	10.00
38	4-Imidazole acetic acid	ImAc	Imidazoleacetic acid_4-Imidazoleacetate	$C_5H_6N_2O_2$	126.0429	127.0502	125.0356	100	1.00
39	5-Aminolevulinic acid	AmLvu	5-Amino-4-oxopentanoate_5-Amino-4-oxovaleric acid	$C_5H_9NO_3$	131.0582	132.0655	130.0509	100	1.00

40	5-Hydroxyindole-3-acetic acid			$C_{10}H_9NO_3$	191.0582	192.0655	190.0509	10	10.00
41	5-Methoxytryptamine	5mT	5-MeOT	$C_{11}H_{14}N_2O$	190.1106	191.1179	189.1033	100	1.00
42	5'-Methylthioadenosine (5'-Deoxy-5'-(methylthio) adenosine)	5MTA	(methylthio)adenosine_Thiomethyladenosine_MTA	$C_{11}H_{15}N_5O_3S$	297.0896	298.0969	296.0823	10	10.00
43	6-Biopterin	BPt	2-Amino-6-(1,2-dihydroxypropyl)-4(1H)-pteridinone	$C_9H_{11}N_5O_3$	237.0862	238.0935	236.0789	100	1.00
44	6-Phosphogluconic acid	6PGA	6-Phosphogluconic acid, D-Gluconic acid 6-phosphate	$C_6H_{13}O_{10}P$	276.0246	277.0319	275.0173	10	10.00
45	Acetaldehyde			C_2H_4O	44.0262	45.0335	43.0189	100	1.00
46	Acetoin (3-hydroxy-2-butanone)			$C_4H_8O_2$	88.0524	89.0597	87.0451	100	1.00
47	Acetyl coenzyme A	AcCoA	Acetyl coenzyme A	$C_{23}H_{38}N_7O_{17}P_3S$	809.1258	810.1331	808.1185	10	10.00
48	Adenine	Adn	Adenin, Ade	$C_5H_5N_5$	135.0545	136.0618	134.0472	1	100.00
49	Adenosine	Ads	adenosine; Adenocard; Adenoscan; 58-61-7; Adenosin; Adenine riboside	$C_{10}H_{13}N_5O_4$	267.0968	268.1041	266.0895	10	10.00
50	Adenosine 2',5'-diphosphate (ADP)	A2P5P	adenosine-2'-5'-diphosphate; A2P5P; Adenosine 2',5'-bisphosphate; 2,5-ADP; Adenosine 2',5'-diphosphate; adenosine-2',5'-bisphosphate	$C_{10}H_{15}N_5O_{10}P_2$	427.0294	428.0367	426.0221	10	10.00

51	Adenosine 3',5'-cyclic monophosphate(cyclic AMP)	cAMP	Cyclic adenylic acid_Cyclic AMP_Adenosine 3',5'-phosphate_cAMP	$C_{10}H_{12}N_5O_6P$	329.0525	330.0598	328.0452	10	10.00
52	Adenosine 5' monophosphate (AMP)	AMP	Adenosine 5'-monophosphate_Adenylic acid_Adenylate_5'-AMP_5'-Adenylic acid_5'-Adenosine monophosphate_Adenosine 5'-phosphate	$C_{10}H_{14}N_5O_7P$	347.0631	348.0704	346.0558	10	10.00
53	Adenosine 5'-diphosphate (ADP)	ADP		$C_{10}H_{15}N_5O_{10}P_2$	427.0294	428.0367	426.0221	10	10.00
54	Agmatine	Agm	(4-Aminobutyl) guanidine	$C_5H_{14}N_4$	130.1218	131.1291	129.1145	100	1.00
55	Allantoin	All	5-Ureidohydantoin_Glyoxyldiureide	$C_4H_6N_4O_3$	158.0440	159.0513	157.0367	10	10.00
56	Amino-2-propanol			C_3H_9NO	75.0684	76.0757	74.0611	100	1.00
57	Ascorbate	Asc	Ascorbic acid_L-Ascorbate_L-Ascorbic acid_Vitamin C	$C_6H_8O_6$	176.0321	177.0394	175.0248	10	10.00
58	ATP	ATP	Adenosine 5'-triphosphate	$C_{10}H_{16}N_5O_{13}P_3$	506.9957	508.0030	505.9884	10 μM	100.00
59	Benzoate	Bz	Benzoic acid_Benzenecarboxylic acid_Phenylformic acid_Dracylic acid	$C_7H_6O_2$	122.0368	123.0441	121.0295	10	10.00
60	Betaine	Bet	Trimethylaminoacetate_Glycine betaine_N,N,N-Trimethylglycine_Trimethylammonioacetate	$C_5H_{11}NO_2$	117.0790	118.0863	116.0717	100	1.00
61	Biotin	Biot	D-Biotin_Vitamin H_Coenzyme R	$C_{10}H_{16}N_2O_3S$	244.0882	245.0955	243.0809	1	100.00

62	Chenodeoxycholic acid			$C_{24}H_{40}O_4$	392.2927	393.3000	391.2854	100	1.00
63	Coenzyme A	CoA	Coenzyme A_CoA-SH	$C_{21}H_{36}N_7O_{16}P_3S$	767.1152	768.1225	766.1079	10	10.00
64	Creatine			$C_4H_9N_3O_2$	131.0695	132.0768	130.0622	100	1.00
65	Creatinine	crtn	alpha-Methylguanidino acetic acid_Methylglycocyamine	$C_4H_7N_3O$	113.0589	114.0662	112.0516	100	1.00
66	Cytidine	Cyt	Cytosine riboside	$C_9H_{13}N_3O_5$	243.0855	244.0928	242.0782	100	1.00
67	Cytidine 5' monophosphate (CMP)	CMP	Cytidine-5'-monophosphate_Cytidylic acid	$C_9H_{14}N_3O_8P$	323.0519	324.0592	322.0446	10	10.00
68	Cytidine 5'-diphosphate (CDP)			$C_9H_{15}N_3O_{11}P_2$	403.0182	404.0255	402.0109	10	10.00
69	Cytidine 5'-triphosphate (CTP)	CTP	Cytidine 5'-triphosphate_Cytidine triphosphate	$C_9H_{16}N_3O_{14}P_3$	482.9845	483.9918	481.9772	10	10.00
70	Cytosine	Csn	cytosine; 71-30-7; 4-Amino-2-hydroxypyrimidine; Cytosinimine; 2(1H)-Pyrimidinone, 4-amino-; 4-Amino-2(1H)-pyrimidinone	$C_4H_5N_3O$	111.0433	112.0506	110.0360	10	10.00
71	D-(-)-Arabinose	Dara	D-(-)-Arabinose; arabinose; 10323-20-3; DL-Arabinose; Arabinose,d; aldehydo-D-arabinose	$C_5H_{10}O_5$	150.0528	151.0601	149.0455	100	1.00

72	D-(-)-Ribose	Rib	D-ribose; 50-69-1; (2R,3R,4R)-2,3,4,5-tetrahydroxypentanal; aldehydo-D-ribose; Ribose, D-; aldehydo-D-ribo-pentose	$C_5H_{10}O_5$	150.0528	151.0601	149.0455	100	1.00
73	D-(-)-Threose		L-Threose; UNII-MHH79K1BVR; (2R,3S)-2,3,4-trihydroxybutanal; Threose; L-Threofuranose; L-threo-tetrose	$C_4H_8O_4$	120.0423	121.0496	119.0350	100	1.00
74	D-(+)-Galactose			$C_6H_{12}O_6$	180.0634	181.0707	179.0561	100	1.00
75	D-(+)-Galacturonic acid	GtnA	D-Galacturonic acid__D(+)-Galacturoic acid	$C_6H_{10}O_7$	194.0427	195.0500	193.0354	10	10.00
76	Dehydroascorbic acid	dAsc	Dehydroascorbate_Dehydroascorbic acid_L-Dehydroascorbic acid	$C_6H_6O_6$	174.0164	175.0237	173.0091	100	1.00
77	Deoxycholic acid			$C_{24}H_{40}O_4$	392.2927	393.3000	391.2854	100	1.00
78	D-Erythrose	Ery	D-erythro-tetrose	$C_4H_8O_4$	120.0423	121.0496	119.0350	100	1.00
79	D-Erythrose 4-phosphate	E4P	D-Erythrose 4-phosphate; erythrose 4-phosphate; threose 4-phosphate; D-erythrose-4-phosphate; erythrose-4P; erythrose-4-P	$C_4H_9O_7P$	200.0086	201.0159	199.0013	100	1.00
80	D-Fructose	Fruc	Levulose_Fruit sugar_D-arabino-Hexulose	$C_6H_{12}O_6$	180.0634	181.0707	179.0561	100	1.00
81	D-Fructose 1,6-disphosphate	F16BP	Fructose 1,6-bisphosphate	$C_6H_{14}O_{12}P_2$	339.9960	341.0033	338.9887	10	10.00

82	D-Fructose 6-phosphate	F6P	D-Fructose 6-phosphoric acid_Neuberg ester	$C_6H_{13}O_9P$	260.0297	261.0370	259.0224	100	1.00
83	D-Gluconic acid	GlcA	D-Gluconate_D-gluco-Hexonic acid	$C_6H_{12}O_7$	196.0583	197.0656	195.0510	100	1.00
84	D-Glucono-1,4-lactone (D(+)-Gluconic acid gamma lactone)	Glu4L	D(+)-Gluconic acid gamma lactone	$C_{12}H_{20}O_2$	196.1463	197.1536	195.1390	100	1.00
85	D-Glucosamine	Glcn	Chitosamine_2-Amino-2-deoxy-D-glucose__D(+)-Glucosamine	$C_6H_{13}NO_5$	179.0794	180.0867	178.0721	100	1.00
86	D-Glucosamine 6-phosphate	Gln6P	D-Glucosamine phosphate	$C_6H_{14}NO_8P$	259.0457	260.0530	258.0384	100	1.00
87	D-Glucose	Gluc	beta-D-Glucose	$C_6H_{12}O_6$	180.0634	181.0707	179.0561	100	1.00
88	D-glucose 6-phosphate	G6P	Glucose 6-phosphate_Robison ester	$C_6H_{13}O_9P$	260.0297	261.0370	259.0224	100	1.00
89	DL-2,3-Diaminopropionic acid	L-2,3-Diaminopropanoic acid		$C_3H_8N_2O_2$	104.0586	105.0659	103.0513	100	1.00
90	DL-3,4-Dihyhroxymandelic acid			$C_8H_8O_5$	184.0372	185.0445	183.0299	100	1.00
91	DL-4-Hydroxy-3-methoxymandelic acid (Vanillylmandelic acid)			$C_9H_{10}O_5$	198.0528	199.0601	197.0455	10	10.00
92	DL-Carnitine	Car	Carnitine_gamma-Trimethyl-hydroxybutyrobetaine_3-Hydroxy-4-trimethylammoniobutanoate	$C_7H_{15}NO_3$	161.1052	162.1125	160.0979	100	1.00

93	DL-Citrulline	citn	2-Amino-5-ureidovaleric acid_Citrulline	$C_6H_{13}N_3O_3$	175.0957	176.1030	174.0884	100	1.00
94	DL-Glyceraldehyde	Glal	2,3-Dihydroxypropionaldehyde_2,3-Dihydroxypropanal_Glycerose_Aldotriose	$C_3H_6O_3$	90.0317	91.0390	89.0244	100	1.00
95	DL-Glyceraldehyde-3-phosphate	GA3P	(2R)-2-Hydroxy-3-(phosphonooxy)-propanal	$C_3H_7O_6P$	169.9980	171.0053	168.9907	10	10.00
96	DL-Homocysteine	Hcys	L-2-Amino-4-mercaptobutyric acid	$C_4H_9NO_2S$	135.0354	136.0427	134.0281	100	1.00
97	DL-Homocystine	DL-Homocystine; HOMOCYSTINE; 870-93-9; 462-10-2; L-Homocystine; Oxidized DL-Homocysteine		$C_8H_{16}N_2O_4S_2$	268.0551	269.0624	267.0478	100	1.00
98	DL-Lactic acid	Lact	D-Lactate_D-Lactic acid_D-2-Hydroxypropanoic acid_D-2-Hydroxypropionic acid	$C_3H_6O_3$	90.0317	91.0390	89.0244	100	1.00
99	DL-Metanephrine			$C_{10}H_{15}NO_3$	197.1052	198.1125	196.0979	10	10.00
100	DL-Norleucine			$C_6H_{13}NO_2$	131.0946	132.1019	130.0873	100	1.00
101	DL-Ornithine	Orn	(S)-2,5-Diaminovaleric acid_(S)-2,5-Diaminopentanoic acid_(S)-2,5-Diaminopentanoate	$C_5H_{12}N_2O_2$	132.0899	133.0972	131.0826	100	1.00
102	D-Mannitol			$C_6H_{14}O_6$	182.0790	183.0863	181.0717	100	1.00

103	Dopamine	dop	4-(2-Aminoethyl)-1,2-benzenediol_4-(2-Aminoethyl)benzene-1,2-diol_3,4-Dihydroxyphenethylamine_2-(3,4-	$C_9H_{11}NO_4$	197.0688	198.0761	196.0615	100	1.00
104	D-Pantothenic acid	Pant	Pantothenic acid_(R)-Pantothenate	$C_9H_{17}NO_5$	219.1107	220.1180	218.1034	100	1.00
105	D-Ribose 5-phosphate	R5P	Ribose 5-phosphate	$C_5H_{11}O_8P$	230.0192	231.0265	229.0119	100	1.00
106	Flavin adenine dinucleotide (FAD)	FAD	Flavin adenine dinucleotide	$C_{27}H_{33}N_9O_{15}P_2$	785.1571	786.1644	784.1498	10	10.00
107	Folate	FolA	Pteroylglutamic acid_Folic acid	$C_{19}H_{19}N_7O_6$	441.1397	442.1470	440.1324	5	20.00
108	Fumaric acid	FuA	Fumaric acid_trans-Butenedioic acid	$C_4H_4O_4$	116.0110	117.0183	115.0037	100	1.00
109	Gallate	GLA	Gallic acid	$C_7H_6O_5$	170.0215	171.0288	169.0142	10	10.00
110	Glutathione reduced form (Glutathione)	GSH	5-L-Glutamyl-L-cysteinylglycine_N-(N-gamma-L-Glutamyl-L-cysteinyl)glycine_gamma-L-Glutamyl-L-cysteinyl-glycine_GSH_Reduced glutathione	$C_{10}H_{17}N_3O_6S$	307.0838	308.0911	306.0765	100	1.00
111	Glycerol	Gol	Glycerin_1,2,3-Trihydroxypropane_1,2,3-Propanetriol	$C_3H_8O_3$	92.0473	93.0546	91.0400	100	1.00
112	Glycine	Gly	Aminoacetic acid_Gl	$C_2H_5NO_2$	75.0320	76.0393	74.0247	100	1.00
113	Glycolate	GCA	Glycolic acid_2-Hydroxyacetic acid	$C_2H_4O_3$	76.0160	77.0233	75.0087	100	1.00

114	Glycyl-glycine	GG	Glycylglycine; N-GLYCYLGLYCINE; Diglycine; 556-50-3; Gly-Gly; Glycyl-glycine	$C_4H_8N_2O_3$	132.0535	133.0608	131.0462	100	1.00
115	Glyoxylate	GxA	Glyoxalate_Glyoxylic acid	$C_2H_2O_3$	74.0004	75.0077	72.9931	100	1.00
116	Guanidine			CH_5N_3	59.0483	60.0556	58.0410	10	10.00
117	Guanidineacetic acid			$C_3H_7N_3O_2$	117.0538	118.0611	116.0465	10	10.00
118	Guanine	Guan	2-Amino-6-hydroxypurine	$C_5H_5N_5O$	151.0494	152.0567	150.0421	10	10.00
119	Guanosine			$C_{10}H_{13}N_5O_5$	283.0917	284.0990	282.0844	1	100.00
120	Guanosine 3',5'-cyclic monophosphate (cyclic GMP)			$C_{10}H_{12}N_5O_7P$	345.0474	346.0547	344.0401	1	100.00
121	Guanosine 5'-diphosphate (GDP)	GDP	Guanosine 5'-diphosphate_Guanosine diphosphate	$C_{10}H_{15}N_5O_{11}P_2$	443.0243	444.0316	442.0170	10	10.00
122	Guanosine 5'-monophophate (GMP)	GMP	Guanosine 5'-phosphate_Guanosine monophosphate_Guanosine 5'-monophosphate_Guanylic acid	$C_{10}H_{14}N_5O_8P$	363.0580	364.0653	362.0507	10	10.00
123	Guanosine 5'-triphosphate (GTP)	GTP	Guanosine 5'-triphosphate	$C_{10}H_{16}N_5O_{14}P_3$	522.9907	523.9980	521.9834	10	10.00
124	HEPES	Gsn	guanosine; guanine riboside; 118-00-3; Guanozin; vernine; Guanosin	$C_8H_{18}N_2O_4S$	238.0987	239.1060	237.0914	10	10.00

125	Hippuric acid	HEPES	HEPES; 7365-45-9; 4-(2-Hydroxyethyl)-1-piperazineethanesulfonic acid; 4-(2-Hydroxyethyl)piperazine-1-ethanesulfonic acid; CHEBI:42334; 2-(4-(2-Hydroxyethyl)piperazin-1-yl)ethanesulfonic acid	$C_9H_9NO_3$	179.0582	180.0655	178.0509	100	1.00
126	Homovanillic acid	Hx	Purine-6-ol	$C_9H_{10}O_4$	182.0579	183.0652	181.0506	10	10.00
127	Hypoxanthine			$C_5H_4N_4O$	136.0385	137.0458	135.0312	1	100.00
128	Imidazole	Imz	Glyoxaline_1,3-Diazole	$C_3H_4N_2$	68.0374	69.0447	67.0301	10	10.00
129	Inosine			$C_{10}H_{12}N_4O_5$	268.0808	269.0881	267.0735	10	10.00
130	Inosine 5'-diphosphate (IDP)	IDP	Inosine 5'-diphosphate_Inosine diphosphate	$C_{10}H_{14}N_4O_{11}P_2$	428.0134	429.0207	427.0061	10	10.00
131	Inosine 5'-monophosphate (IMP)	IMP	Inosinic acid_Inosine monophosphate_Inosine 5'-monophosphate_Inosine 5'-phosphate_5'-Inosinate_5'-Inosinic acid_5'-Inosine	$C_{10}H_{13}N_4O_8P$	348.0471	349.0544	347.0398	10	10.00
132	Isobutyraldehyde (2-Methylpropanal)			C_4H_8O	72.0575	73.0648	71.0502	100	1.00
133	Isonicotinic acid	ISONICOTINIC ACID; 4-Pyridinecarboxylic acid; Pyridine-4-carboxylic acid; 55-22-1; 4-Picolinic acid; 4-Carboxypyridine		$C_6H_5NO_2$	123.0320	124.0393	122.0247	10	10.00

134	Itaconic acid	Itaconic acid; 2-Methylenesuccinic acid; 97-65-4; METHYLENESUCCINIC ACID; Methylenebutanedioic acid; Butanedioic acid, methylene		$C_5H_6O_4$	130.0266	131.0339	129.0193	100	1.00
135	L-(-)-Malic acid	MaA	L-Malate_L-Apple acid_L-Malic acid_L-2-Hydroxybutanedioic acid	$C_4H_6O_5$	134.0215	135.0288	133.0142	10	10.00
136	L-2,4-Diaminobutyric Acid	AmBu	alpha,gamma-Diaminobutyrate_L-2,4-Diaminobutyrate__2,4-Diaminobutyricacid	$C_4H_{10}N_2O_2$	118.0742	119.0815	117.0669	100	1.00
137	L-2-Aminoadipate	Am.Ad	L-alpha-Aminoadipate_L-alpha-Aminoadipic acid_L-2-Aminoadipic acid_L-2-Aminohexanedioate	$C_6H_{11}NO_4$	161.0688	162.0761	160.0615	1	100.00
138	L-2-Hydroxyglutaric acid	2HG	d-alpha-hydroxyglutarate	$C_5H_8O_5$	148.0372	149.0445	147.0299	100	1.00
139	L-Alanine	Ala	L-2-Aminopropionic acid_L-alpha-Alanine	$C_3H_7NO_2$	89.0477	90.0550	88.0404	100	1.00
140	L-Arginine	Arg	(S)-2-Amino-5-guanidinovaleric acid	$C_6H_{14}N_4O_2$	174.1117	175.1190	173.1044	100	1.00
141	L-Asparagine	Asn	2-Aminosuccinamic acid	$C_4H_8N_2O_3$	132.0535	133.0608	131.0462	100	1.00
142	L-Aspartic acid	Asp	D-Aspartate_D-Aspartic acid	$C_4H_7NO_4$	133.0375	134.0448	132.0302	100	1.00
143	L-Cystathionine	Cnn	L-cystathionine; cystathionine; L-(+)-Cystathionine; Cystathionine, L-; (R)-S-(2-Amino-2-carboxyethyl)-L-homocysteine; 56-88-2	$C_7H_{14}N_2O_4S$	222.0674	223.0747	221.0601	10	10.00

144	L-Cysteic acid	CysA	L-Cysteic acid_3-Sulfoalanine_2-Amino-3-sulfopropionic acid	$C_3H_7NO_5S$	169.0045	170.0118	167.9972	100	1.00
145	L-Cysteine	Cys	L-2-Amino-3-mercaptopropionic acid	$C_3H_7NO_2S$	121.0197	122.0270	120.0124	100	1.00
146	L-Cysteine methyl ester			$C_4H_9NO_2S$	135.0354	136.0427	134.0281	10	10.00
147	L-Cystine		L-cystine; Cystine acid; L-Cystin; Cysteine disulfide; Dicysteine; L-Dicysteine	$C_6H_{12}N_2O_4S_2$	240.0238	241.0311	239.0165	1	100.00
148	L-Glutamic acid	Glu	L-Glutamic acid_L-Glutaminic acid_Glutamate	$C_5H_9NO_4$	147.0532	148.0605	146.0459	100	1.00
149	L-Glutamine	Gln	L-2-Aminoglutaramic acid	$C_5H_{10}N_2O_3$	146.0691	147.0764	145.0618	100	1.00
150	L-Glutathione oxidized		glutathione disulfide; oxiglutatione; GSSG; oxidized glutathione; Glutathione disulphide; Glutathione-ssg	$C_{20}H_{32}N_6O_{12}S_2$	612.1520	613.1593	611.1447	10	10.00
151	L-Gulonic acid γ-lactone (L-Gulonolactone)		L-Gulonolactone; L-Gulono-1,4-lactone; gamma-Gulonolactone; 1128-23-0; L-Gulonic acid gamma-lactone; L-Gulono-gamma-lactone	$C_6H_{10}O_6$	178.0477	179.0550	177.0404	100	1.00
152	L-Histidine	His	(S)-alpha-Amino-1H-imidazole-4-propionic acid	$C_6H_9N_3O_2$	155.0695	156.0768	154.0622	100	1.00
153	L-Homoserine	hSer	2-Amino-4-hydroxybutyric acid	$C_4H_9NO_3$	119.0582	120.0655	118.0509	100	1.00
154	L-Homoserine lactone		2-Aminobutan-4-olide	$C_4H_7NO_2$	102.0555	103.0628	101.0482	100	1.00

155	L-Isoleucine	ILE	2-Amino-3-methylvaleric acid	$C_6H_{13}NO_2$	131.0946	132.1019	130.0873	100	1.00
156	L-Kynurenine	Kyn	3-Anthraniloyl-L-alanine	$C_{10}H_{12}N_2O_3$	208.0848	209.0921	207.0775	10	10.00
157	L-Leucine	Leu	2-Amino-4-methylvaleric acid_(2S)-alpha-2-Amino-4-methylvaleric acid_(2S)-alpha-Leucine	$C_6H_{13}NO_2$	131.0946	132.1019	130.0873	100	1.00
158	L-Lysine	Lys	Lysine acid_2,6-Diaminohexanoic acid	$C_6H_{15}N_2O_2$	146.1055	147.1128	145.0982	100	1.00
159	L-Methionine	Met	Methionine_L-2-Amino-4methylthiobutyric acid	$C_5H_{11}NO_2S$	149.0510	150.0583	148.0437	100	1.00
160	L-Methionine sulfone			$C_5H_{11}NO_4S$	181.0409	182.0482	180.0336	50	2.00
161	L-Phenylalanine	Phe	(S)-alpha-Amino-beta-phenylpropionic acid	$C_9H_{11}NO_2$	165.0790	166.0863	164.0717	100	1.00
162	L-Proline	Pro	2-Pyrrolidinecarboxylic acid	$C_5H_9NO_2$	115.0633	116.0706	114.0560	100	1.00
163	L-Rhamnose	Lrha	6-Deoxy-L-mannose_L-Mannomethylose__a-L-Rhamnose	$C_6H_{12}O_5$	164.0685	165.0758	163.0612	100	1.00
164	L-Serine	Ser	L-2-Amino-3-hydroxypropionic acid_L-3-Hydroxy-alanine_Serine	$C_3H_7NO_3$	105.0426	106.0499	104.0353	100	1.00
165	L-Threonine	Thr	2-Amino-3-hydroxybutyric acid	$C_4H_9NO_3$	119.0582	120.0655	118.0509	100	1.00

166	L-Tryptophan	Trp	Tryptophan_(S)-alpha-Amino-beta-(3-indolyl)-propionic acid	$C_{11}H_{12}N_2O_2$	204.0899	205.0972	203.0826	10	10.00
167	L-Tyrosine	Tyr	(S)-3-(p-Hydroxyphenyl)alanine_(S)-2-Amino-3-(p-hydroxyphenyl)propionic acid_Tyrosine	$C_9H_{11}NO_3$	181.0739	182.0812	180.0666	10	10.00
168	L-Valine	Val	2-Amino-3-methylbutyric acid	$C_5H_{11}NO_2$	117.0790	118.0863	116.0717	10	10.00
169	Maleic acid	MeA	Maleate_cis-Butenedioic acid	$C_4H_4O_4$	116.0110	117.0183	115.0037	100	1.00
170	Malonic acid	Mln	Malonic acid_Propanedioic acid	$C_3H_4O_4$	104.0110	105.0183	103.0037	100	1.00
171	Melatonin	Mel	N-Acetyl-5-methoxytryptamine	$C_{13}H_{16}N_2O_2$	232.1212	233.1285	231.1139	5	20.00
172	Menadione		menadione; Vitamin K3; 2-Methyl-1,4-naphthoquinone; 58-27-5; Menaphthone; 2-Methylnaphthoquinone	$C_{11}H_8O_2$	172.0524	173.0597	171.0451	10	10.00
173	Mercaptoethanol		2-mercaptoethanol; Mercaptoethanol; Beta-Mercaptoethanol; Ethanol, 2-mercapto-; Thioglycol; 2-Thioethanol	C_2H_6OS	78.0139	79.0212	77.0066	100	1.00
174	Mesaconic acid		mesaconic acid; Methylfumaric acid; mesaconate; 2-Methylfumaric acid; Fumaric acid, methyl-; trans-2-Methyl-2-butenedioic acid	$C_5H_6O_4$	130.0266	131.0339	129.0193	100	1.00
175	meso-2,6-Diaminopimelic acid	dapA	meso-2,6-Diaminopimelate_meso-2,6-Diaminopimelic acid_meso-Diaminoheptanedioate__meso diaminopimelate	$C_7H_{14}N_2O_4$	190.0954	191.1027	189.0881	10	10.00

176	methylglyoxal	MGX	Pyruvaldehyde_2-oxopropanal	$C_3H_4O_2$	72.0211	73.0284	71.0138	100	1.00
177	Methylguanidine		N-Methylguanidine	$C_2H_7N_3$	73.0640	74.0713	72.0567	100	1.00
178	Methylmalonic acid	mma	Methylmalonic acid	$C_4H_6O_4$	118.0266	119.0339	117.0193	100	1.00
179	MOPS	MOPS	3-(N-Morpholino)propanesulfonic acid, 4-Morpholinepropanesulfonic acid	$C_7H_{15}NO_4S$	209.0722	210.0795	208.0649	100	1.00
180	Mucic acid (Galactaric acid)	Glct	D-Mucic acid_D-Galactaric acid	$C_6H_{10}O_8$	210.0376	211.0449	209.0303	1	100.00
181	Myoinositol			$C_6H_{12}O_6$	180.0634	181.0707	179.0561	100	1.00
182	N-Acetyl-D-glucosamine	NAGlc	N-Acetylchitosamine_2-Acetamido-2-deoxy-D-glucose_GlcNAc	$C_8H_{15}NO_6$	221.0899	222.0972	220.0826	100	1.00
183	N-Acetyl-L-cysteine		N-Acetyl-L-cysteine; acetylcysteine; N-Acetylcysteine; Acetadote; 616-91-1; Fluimucil	$C_5H_9NO_3S$	163.0303	164.0376	162.0230	100	1.00
184	N-acetyl-L-glutamic acid	NAGln	Acetyl-glutamine	$C_7H_{11}NO_5$	189.0637	190.0710	188.0564	10	10.00
185	N-Acetylneuraminic acid	AcNam	N-Acetylneuraminic acid_5-Acetamido-3,5-dideoxy-D-glycero-D-galacto-2-nonulosonic acid_Neu5Ac	$C_{11}H_{19}NO_9$	309.1060	310.1133	308.0987	100	1.00
186	Nicotinamide (Niacinamide)	Nicd	Nicotinic acid amide_Niacinamide_Vitamin PP	$C_6H_6N_2O$	122.0480	123.0553	121.0407	100	1.00

187	Noradenaline (Norepinephrine)		norepinephrine; noradrenaline; Levarterenol; Arterenol; Levophed; (-)-Norepinephrine	$C_8H_{11}NO_3$	169.0739	170.0812	168.0666	100	1.00
188	Normetanephrine			$C_9H_{13}NO_3$	183.0895	184.0968	182.0822	100	1.00
189	Nα-Acetyl-L-glutamine	NAGln	Acetyl-glutamine	$C_7H_{12}N_2O_4$	188.0797	189.0870	187.0724	10	10.00
190	Nα-Acetyl-L-ornithine	NAO	N2-Acetyl-L-ornithine	$C_7H_{14}N_2O_3$	174.1004	175.1077	173.0931	10	10.00
191	Nε-Acetyl-L-lysine	N2AL	Nalpha-Acetyl-L-lysine	$C_8H_{16}N_2O_3$	188.1161	189.1234	187.1088	5	20.00
192	O-Acetyl-L-carnitine		Acetyl-L-carnitine; Nicetile; O-acetylcarnitine; L-O-Acetylcarnitine; (R)-Acetylcarnitine; (-)-Acetylcarnitine	$C_9H_{17}NO_4$	203.1158	204.1231	202.1085	100	1.00
193	O-Acetyl-L-serine		O-acetyl-L-serine; O-acetylserine; O3-acetyl-L-serine; 5147-00-2; (S)-3-Acetoxy-2-aminopropanoic acid; L-Serine, acetate (ester)	$C_5H_9NO_4$	147.0532	148.0605	146.0459	10	10.00
194	O-Phosphorylethanolamine	OPE	O-Phosphorylethanolamine_Phosphoethanolamine_O-Phosphoethanolamine	$C_2H_8NO_4P$	141.0191	142.0264	140.0118	100	1.00
195	Orotic acid	OroA	Orotic acid_Uracil-6-carboxylic acid	$C_5H_4N_2O_4$	156.0171	157.0244	155.0098	5	20.00
196	Orotidine	Ordn	Orotidine; 6-Carboxyuridine; 3-Ribofuranosylorotic acid; UNII-B350MC02GZ; 314-50-1; orotidin	$C_{10}H_{12}N_2O_8$	288.0594	289.0667	287.0521	10	10.00

197	Oxalic acid	OxA	Oxalic acid_Ethanedioic acid	$C_2H_2O_4$	89.9953	91.0026	88.9880	50	2.00
198	Oxaloacetic acid	OxAc	Oxalacetic acid_Oxaloacetic acid_2-Oxobutanedioic acid_Oxosuccinic acid_keto-Oxaloacetate	$C_4H_4O_5$	132.0059	133.0132	130.9986	100	1.00
199	p-Coumaric acid	pCou	p-Coumaric acid_trans-4-Hydroxycinnamate_trans-p-Hydroxycinnamate_4-Hydroxycinnamic acid_4-Hydroxycinnamate	$C_9H_8O_3$	164.0473	165.0546	163.0400	100	1.00
200	Phenolsulfonphthalein		Phenol Red	$C_{19}H_{14}O_5S$	354.0562	355.0635	353.0489	100	1.00
201	Phenylacetylglycine	PAG	Phenylacetylglycine; Phenaceturic acid; N-Phenylacetylglycine; Phenacetylglycine; N-Phenacetylglycine; N-(Phenylacetyl)glycine	$C_{10}H_{11}NO_3$	193.0739	194.0812	192.0666	100	1.00
202	Phenylhydrazine		Hydrazinobenzene	$C_6H_8N_2$	108.0687	109.0760	107.0614	100	1.00
203	Phenylpyruvate	pPyr	Phenylpyruvic acid_alpha-Ketohydrocinnamic acid_keto-Phenylpyruvate_3-Phenyl-2-oxopropanoate	$C_9H_8O_3$	164.0473	165.0546	163.0400	100	1.00
204	Phosphate	PO4	Orthophosphate	O_4P	94.9534	95.9607	93.9461	100	1.00
205	Phospho(enol)pyruvic acid	PEP	Phosphoenolpyruvic acid_PEP	$C_3H_5O_6P$	167.9824	168.9897	166.9751	10	10.00
206	Phosphocholine	ChoP	Phosphorylcholine_Phosphocholine_O-Phosphocholine	$C_5H_{15}NO_4P$	184.0739	185.0812	183.0666	100	1.00

207	Putrescine	PuT	1,4-Butanediamine_1,4-Diaminobutane_Tetramethylenediamine	$C_4H_{12}N_2$	88.1000	89.1073	87.0927	100	1.00
208	pyrazinoate		Pyrazinecarboxylic acid	$C_5H_4N_2O_2$	124.0273	125.0346	123.0200	10	10.00
209	Pyridoxal	Pxl	pyridoxal; Pyridoxaldehyde; 66-72-8; 3-Hydroxy-5-(hydroxymethyl)-2-methylisonicotinaldehyde; 4-Pyridinecarboxaldehyde, 3-hydroxy-5-(hydroxymethyl)-2-methyl-; Vitamin B6 hydrochloride	$C_8H_9NO_3$	167.0582	168.0655	166.0509	100	1.00
210	Pyridoxal 5'-phosphate	PxlP	Pyridoxal 5-phosphate_Pyridoxal 5'-phosphate	$C_8H_{10}NO_6P$	247.0246	248.0319	246.0173	10	10.00
211	Pyridoxine	Pdxn	Pyridoxol	$C_8H_{11}NO_3$	169.0739	170.0812	168.0666	100	1.00
212	Pyroglutamic acid	5oxP	5-Oxoproline	$C_5H_7NO_3$	129.0426	130.0499	128.0353	100	1.00
213	Pyrophosphate	PP	Pyrophosphoric acid_Diphosphate_Ppi	O_7P_2	173.9119	174.9192	172.9046	100	1.00
214	Pyruvic acid	Pyr	Pyruvic acid_2-Oxopropanoate_2-Oxopropanoic acid_Pyroracemic acid	$C_3H_4O_3$	88.0160	89.0233	87.0087	100	1.00
215	Riboflavin 5' monophosphate (Flavin mononucleotide)	FMN	Riboflavin-5-phosphate_Flavin mononucleotide	$C_{17}H_{21}N_4O_9P$	456.1046	457.1119	455.0973	10	10.00
216	S-Adenosyl-L-homocysteine	SAH	S-Adenosylhomocysteine	$C_{14}H_{20}N_6O_5S$	384.1216	385.1289	383.1143	10	10.00

217	S-Adenosylmethioninamine	SAM	S-Adenosylmethionine_Acylcarnitine	$C_{14}H_{23}N_6O_3S$	355.1552	356.1625	354.1479	10	10.00
218	Sarcosine			$C_3H_7NO_2$	89.0477	90.0550	88.0404	100	1.00
219	Seleno-L-methionine	SeMet	2-amino-4-methylselanylbutanoic acid	$C_5H_{11}NO_2Se$	196.9955	198.0028	195.9882	100	1.00
220	Serotonin	5HT	3-(2-Aminoethyl)-1H-indol-5-ol_5-Hydroxytryptamine_Enteramine	$C_{10}H_{12}N_2O$	176.0950	177.1023	175.0877	10	10.00
221	S-Methyl-L-cysteine		Methylcysteine	$C_4H_9NO_2S$	135.0354	136.0427	134.0281	100	1.00
222	sn-Glycero-3-Phosphocholine	GPC	Glycerophosphocholine	$C_8H_{20}NO_6P$	257.1028	258.1101	256.0955	100	1.00
223	sn-Glycerol 3-phosphate	G3P	Glycerophosphoric acid_D-Glycerol 1-phosphate_Glycerol-3-phosphate	$C_3H_9O_6P$	172.0137	173.0210	171.0064	10	10.00
224	Spermidine	Spdn	N-(3-Aminopropyl)-1,4-butane-diamine	$C_7H_{19}N_3$	145.1579	146.1652	144.1506	100	1.00
225	Spermine	Spmn	N,N'-Bis(3-aminopropyl)-1,4-butanediamine	$C_{10}H_{26}N_4$	202.2157	203.2230	201.2084	100	1.00
226	Stearic acid			$C_{18}H_{36}O_2$	284.2715	285.2788	283.2642	100	1.00
227	Succinic acid	SuA	Succinic acid_Butanedionic acid_Ethylenesuccinic acid	$C_4H_6O_4$	118.0266	119.0339	117.0193	100	1.00

228	Sucrose	Scrs	Cane sugar_Saccharose_1-alpha-D-Glucopyranosyl-2-beta-D-fructofuranoside	$C_{12}H_{22}O_{11}$	342.1162	343.1235	341.1089	100	1.00
229	Taurine	Tau	2-Aminoethanesulfonic acid_Aminoethylsulfonic acid	$C_2H_7NO_3S$	125.0147	126.0220	124.0074	100	1.00
230	Taurocholate	Tch	Taurocholic acid_Cholyltaurine	$C_{26}H_{45}NO_7S$	515.2917	516.2990	514.2844	10	10.00
231	Thiamine	Thia	Thiamine_Vitamin B1_Aneurin_Antiberiberi factor	$C_{12}H_{17}N_4OS$	265.1123	266.1196	264.1050	100	1.00
232	Thiaminepyrophosphate	ThPP	Thiamine diphosphate_Thiamin pyrophosphate_TPP_ThPP	$C_{12}H_{19}N_4O_7P_2S$	425.0450	426.0523	424.0377	100	1.00
233	Thymidine	Tdn	Deoxythymidine	$C_{10}H_{14}N_2O_5$	242.0903	243.0976	241.0830	100	1.00
234	Thymine	Thym	5-Methyluracil	$C_5H_6N_2O_2$	126.0429	127.0502	125.0356	10	10.00
235	trans-Aconitic acid			$C_6H_6O_6$	174.0164	175.0237	173.0091	100	1.00
236	UDP			$C_9H_{14}N_2O_{12}P_2$	404.0022	405.0095	402.9949	100	1.00
237	UDP-Glucose	UDPG	UDPglucose_UDP-D-glucose_Uridine diphosphate glucose_UDP-alpha-D-glucose__Uridine 5′-diphosphoglucose	$C_{15}H_{24}N_2O_{17}P_2$	566.0550	567.0623	565.0477	100	1.00
238	UMP	UMP	Uridylic acid_Uridine monophosphate_Uridine 5'-monophosphate_5'Uridylic acid	$C_9H_{13}N_2O_9P$	324.0359	325.0432	323.0286	10	10.00

239	Uracil	Ur	uracil; 2,4-Dihydroxypyrimidine; 2,4(1H,3H)-Pyrimidinedione; 66-22-8; 2,4-Pyrimidinediol; 2,4-Dioxopyrimidine	$C_4H_4N_2O_2$	112.0273	113.0346	111.0200	5	20.00
240	Urea			CH_4N_2O	60.0324	61.0397	59.0251	100	1.00
241	Uric acid			$C_5H_4N_4O_3$	168.0283	169.0356	167.0210	100	1.00
242	Uridine	Uri	uridine; Uridin; 1-beta-D-Ribofuranosyluracil; 58-96-8; Uracil riboside; beta-Uridine	$C_9H_{12}N_2O_6$	244.0695	245.0768	243.0622	10	10.00
243	UTP			$C_9H_{15}N_2O_{15}P_3$	483.9685	484.9758	482.9612	100	1.00
244	Xanthine	Xan	xanthine; 2,6-Dihydroxypurine; Xanthin; 69-89-6; 2,6-dioxopurine; Pseudoxanthine	$C_5H_4N_4O_2$	152.0334	153.0407	151.0261	10	10.00
245	Xanthosine			$C_{10}H_{12}N_4O_6$	284.0757	285.0830	283.0684	50	2.00
246	α-Naphthaleneacetic acid			$C_{12}H_{10}O_2$	186.0681	187.0754	185.0608	100	1.00
247	β-Nicotinamide adenine dinucleotide (NAD)	NAD+	NAD_Nicotinamide adenine dinucleotide_DPN_Diphosphopyridine nucleotide_Nadide	$C_{21}H_{28}N_7O_{14}P_2$	664.1169	665.1242	663.1096	100	1.00
248	β-Nicotinamide adenine dinucleotide phosphate(NADP)	NADP	NADP_Nicotinamide adenine dinucleotide phosphate_beta-Nicotinamide adenine dinucleotide phosphate_TPN_Triphosphopyridine nucleotide	$C_{21}H_{29}N_7O_{17}P_3$	744.0833	745.0906	743.0760	10	10.00

249	β-Nicotinamide adenine dinucleotide phosphate, reduced (NADPH)		NADPH; Dihydronicotinamide-adenine dinucleotide phosphate; TPNH; CHEBI:16474; Reduced Nicotinamide Adenine Dinucleotide Phosphate; [(2r,3r,4r,5r)-5-(6-aminopurin-9-yl)-3-hydroxy-4-phosphonooxy-tetrahydrofuran-2-yl]methyl[[(2r,3s,4r,5r)-5-(3-carbamoyl-4h-pyridin-1-yl)-3,4-dihydroxy-tetrahydrofuran-2-yl]methoxy-hydroxy-phosphoryl] hydrogen phosphate	$C_{21}H_{30}N_7O_{17}P_3$	745.0911	746.0984	744.0838	20	5.00
250	β-Nicotinamide adenine dinucleotide reduced (NADH)	NADH	DPNH	$C_{21}H_{29}N_7O_{14}P_2$	665.1248	666.1321	664.1175	10	10.00

Table S3: Cross-Validation of the Multivariate models

Model	Type	A	N	R2X(cum)	R2Y(cum)	Q2(cum)	R2 and Q2 validation	Classes in the model
Figure 1	PCA-X	14	120	0.892		0.583	≥0.5	All samples
Figure 2	PLS-DA	34	108	0.961	0.897	0.333	≤0.5	All samples no QC

Figure 3	OPLS-DA	12+1+0	108	0.867	0.532	0.363	≤0.5	All samples no QC
Figure 4	OPLS-DA	2+2+0	18	0.792	0.981	0.943	≥0.5	D1
Figure 4	OPLS-DA	2+2+0	18	0.795	0.918	0.697	≥0.5	Hox
Figure 4	OPLS-DA	2+2+0	18	0.822	0.962	0.773	≥0.5	M55
Figure 4	OPLS-DA	2+2+0	18	0.711	0.853	0.469	≤0.5	W
Figure 4	OPLS-DA	2+2+0	18	0.859	0.947	0.823	≥0.5	Wt
Figure 4	OPLS-DA	2+2+0	18	0.769	0.838	0.588	≥0.5	YH

Figure 5	OPLS-DA	1+1+0	12	0.825	0.986	0.97	≥0.5	wt da vwt ll
Figure 5	OPLS-DA	1+1+0	12	0.845	0.989	0.978	≥0.5	wt da v wt hl
Figure 5	OPLS-DA	1+1+0	12	0.503	0.912	0.698	≥0.5	wt hl v wt ll
Figure 5	OPLS-DA	1+1+0	12	0.636	0.885	0.745	≥0.5	yhda v yh ll
Figure 5	OPLS-DA	1+1+0	12	0.584	0.797	0.429	≤0.5	YH HL v YH LL
Figure 5	OPLS-DA	1+1+0	12	0.592	0.9	0.797	≥0.5	YH DA v YHHL
Figure 5	OPLS-DA	1+1+0	12	0.544	0.93	0.814	≥0.5	W DA v W LL

Figure 5	OPLS-DA	1+1+0	12	0.505	0.895	0.2	≤0.5	W HL v WLL
Figure 5	OPLS-DA	1+1+0	12	0.528	0.911	0.576	≥0.5	W DA v W HL
Figure 5	OPLS-DA	1+1+0	12	0.689	0.932	0.855	≥0.5	Hox DA v Hox LL
Figure 5	OPLS-DA	1+1+0	12	0.695	0.942	0.815	≥0.5	Hox HL v Hox LL
Figure 5	OPLS-DA	1+1+0	12	0.388	0.967	0.679	≥0.5	Hox DA v Hox HL
Figure 5	OPLS-DA	1+1+0	12	0.606	0.976	0.912	≥0.5	D1DA v D1 LL
Figure 5	OPLS-DA	1+1+0	12	0.759	0.961	0.915	≥0.5	D1HL v D1LL

Figure 5	OPLS-DA	1+1+0	12	0.647	0.988	0.961	≥0.5	D1DA v D1HL
Figure 5	OPLS-DA	1+1+0	12	0.735	0.884	0.725	≥0.5	M55 DA v M55 LL
Figure 5	OPLS-DA	1+1+0	12	0.62	0.97	0.832	≥0.5	M55 HL v M55 LL
Figure 5	OPLS-DA	1+1+0	12	0.724	0.978	0.956	≥0.5	M55 DAv M55 HL
Figure 6	OPLS-DA	1+1+0	12	0.627	0.757	0.54	≥0.5	Wt LL v YH LL
Figure 6	OPLS-DA	1+1+0	12	0.649	0.897	0.79	≥0.5	Wt LL v W LL

Figure 6	OPLS-DA	1+1+0	12	0.515	0.969	0.877	≥0.5	Wt LL v Hox LL
Figure 6	OPLS-DA	1+1+0	12	0.552	0.985	0.947	≥0.5	Wt LL v D1 LL
Figure 6	OPLS-DA	1+1+0	12	0.673	0.984	0.945	≥0.5	Wt LL v M55 LL
Figure 6	OPLS-DA	1+1+0	12	0.527	0.805	0.491	≤0.5	YH LL v W LL
Figure 6	OPLS-DA	1+1+0	12	0.657	0.968	0.916	≥0.5	YH LL v Hox LL
Figure 6	OPLS-DA	1+1+0	12	0.62	0.98	0.878	≥0.5	YH LL v D1 LL
Figure 6	OPLS-DA	1+1+0	12	0.599	0.987	0.961	≥0.5	YH LL v M55 LL

Figure 6	OPLS-DA	1+1+0	12	0.656	0.98	0.868	≥0.5	W LL v Hox LL
Figure 6	OPLS-DA	1+1+0	12	0.671	0.976	0.897	≥0.5	W LL v D1 LL
Figure 6	OPLS-DA	1+1+0	12	0.75	0.97	0.94	≥0.5	W LL v M55 LL
Figure 6	OPLS-DA	1+1+0	12	0.734	0.964	0.921	≥0.5	Hox LL v M55 LL
Figure 6	OPLS-DA	1+1+0	12	0.738	0.979	0.958	≥0.5	D1 LL v Hox LL
Figure 7	OPLS-DA	1+1+0	12	0.86	0.975	0.963	≥0.5	Wt DA v YH DA
Figure 7	OPLS-DA	1+1+0	12	0.757	0.982	0.963	≥0.5	Wt DA v W DA

Figure 7	OPLS-DA	1+1+0	12	0.858	0.974	0.96	≥0.5	Wt DA v Hox DA
Figure 7	OPLS-DA	1+1+0	12	0.795	0.985	0.963	≥0.5	Wt DA v D1 D1
Figure 7	OPLS-DA	1+1+0	12	0.793	0.982	0.971	≥0.5	Wt DA v M55 DA
Figure 7	OPLS-DA	1+1+0	12	0.585	0.717	0.472	≤0.5	W DA v YH DA
Figure 7	OPLS-DA	1+1+0	12	0.688	0.901	0.73	≥0.5	YH DA v Hox DA
Figure 7	OPLS-DA	1+1+0	12	0.78	0.982	0.957	≥0.5	D1 DA v YH DA
Figure 7	OPLS-DA	1+1+0	12	0.632	0.957	0.824	≥0.5	YH DA v M55 DA

Figure 7	OPLS-DA	1+1+0	12	0.528	0.866	0.63	≥0.5	W DA v Hox |DA
Figure 7	OPLS-DA	1+1+0	12	0.669	0.979	0.935	≥0.5	W DA v D1 DA
Figure 7	OPLS-DA	1+1+0	12	0.619	0.967	0.874	≥0.5	W DA v M55 DA
Figure 7	OPLS-DA	1+1+0	12	0.58	0.966	0.799	≥0.5	Hox DA v M55 DA
Figure 7	OPLS-DA	1+1+0	12	0.762	0.988	0.957	≥0.5	D1 DA v Hox DA
Figure 8	OPLS-DA	1+1+0	12	0.694	0.84	0.57	≥0.5	Wt HL v YH HL
Figure 8	OPLS-DA	1+1+0	12	0.576	0.895	0.554	≥0.5	Wt HL v W HL

Figure 8	OPLS-DA	1+1+0	12	0.706	0.988	0.944	≥0.5	Wt HL v Hox HL
Figure 8	OPLS-DA	1+1+0	12	0.808	0.997	0.98	≥0.5	Wt HL v D1 HL
Figure 8	OPLS-DA	1+1+0	12	0.725	0.994	0.98	≥0.5	Wt HL v M55 HL
Figure 8	OPLS-DA	1+1+0	12	0.518	0.592	0.681	≥0.5	W HL v YH HL
Figure 8	OPLS-DA	1+1+0	12	0.595	0.938	0.837	≥0.5	YH HL v Hox HL
Figure 8	OPLS-DA	1+1+0	12	0.804	0.985	0.969	≥0.5	YH HL v D1 HL
Figure 8	OPLS-DA	1+1+0	12	0.718	0.969	0.888	≥0.5	YH HL v M55 HL

Figure 8	OPLS-DA	1+1+0	12	0.608	0.912	0.845	≥0.5	Hox HL v M55 HL
Figure 8	OPLS-DA	1+1+0	12	0.844	0.989	0.977	≥0.5	D1 HL v Hox HL
Figure 8	OPLS-DA	1+1+0	12	0.535	0.936	0.713	≥0.5	Hox HL v W HL
Figure 8	OPLS-DA	1+1+0	12	0.748	0.985	0.943	≥0.5	W HL v D1 HL
Figure 8	OPLS-DA	1+1+0	12	0.635	0.976	0.926	≥0.5	W HL v M55 HL
Figure 9	Permutation test (intercept)	12	108		0.099	-0.39	Q2≤0	All samples, no QC

Table S 1
Table S 2